2023

Theoretical Framework of Exchange Coupled Tripartite Spin Systems with Magnetic Anisotropy and Predictions of Spin and Electronic Transport Properties for Their Use in Quantum Architectures

Eric Switzer
University of Central Florida

THEORETICAL FRAMEWORK OF EXCHANGE COUPLED TRIPARTITE SPIN SYSTEMS WITH MAGNETIC ANISOTROPY AND PREDICTIONS OF SPIN AND ELECTRONIC TRANSPORT PROPERTIES FOR THEIR USE IN QUANTUM ARCHITECTURES

by

ERIC D. SWITZER
M.S. University of Central Florida, 2021
B.S. Portland State University, 2010

A dissertation submitted in partial fulfilment of the requirements
for the degree of Doctor of Philosophy
in the Department of Physics
in the College of Sciences
at the University of Central Florida
Orlando, Florida

Summer Term
2023

Major Professor: Talat Shahnaz Rahman

ABSTRACT

There has been significant interest in spin systems involving two or more coupled spins as a single logical qubit, particularly for scalable quantum computing architectures. Recent realizations include the so-called singlet-triplet qubits and coupled magnetic molecules. An important class of coupled-spin systems, the three-spin paradigm for spin greater than 1/2, has not yet been fully realized in scalable qubit architectures. In this thesis, I develop the theoretical framework to investigate a class of tripartite spin models for realistic systems. First, I model a spin 1/2 particle (e.g., an electron) and two spin 1 particles (in a dimer arrangement) coupled with an exchange interaction. I find that if the two spin particles possess zero-field magnetic anisotropy, there exists resonance conditions that enable read, manipulate, and write operations on the representative qubit using the electron. Next, I generalize this result for any spin S, and describe how the resonance conditions change based on the type of exchange coupling, magnetic anisotropy, and magnitude of applied magnetic fields. The rest of the thesis is dedicated to utilizing the tools described in the framework to uncover the properties of potential scalable quantum architectures. To guide the correspondence between experiment and model Hamiltonians of effective tripartite spin systems connected to leads, I investigate the transport properties of a three-terminal quantum dot coupled to a magnetic molecular dimer using the generalized master equation. I then model both steady state and transient phenomena using equilibrium and non-equilibrium Green's functions (NEGF), and comment on the applicability of a newly-developed NEGF-derived quantum master equation. Finally, I characterize two examples of novel quantum systems: the spin qubit candidate h-BN $V_B{}^-$ and the thin film $Fe[H_2B(Pz)_2]_2(bipy)$ spin-crossover molecule.

EXTENDED ABSTRACT

There has been significant interest in spin systems involving two or more coupled spins as a single logical qubit, particularly for scalable quantum computing architectures. Recent realizations include the so-called singlet-triplet qubits, many-electron quantum dots, coupled atom qubits utilizing scanning tunneling electron microscopy and electron spin resonance, and coupled magnetic molecules. An important class of coupled-spin systems, the three-spin paradigm for spin greater than 1/2, has not yet been fully realized in scalable qubit architectures. A theoretical framework is needed to characterize these novel systems and provide guidance on the constituents for new devices.

In this thesis, I develop the theoretical framework to investigate a class of tripartite spin models for realistic systems. First, I model a spin 1/2 particle (e.g., an electron) and two spin 1 particles (in a dimer arrangement) coupled with an exchange interaction. I find that if the two spin particles possess zero-field magnetic anisotropy, there exists resonance conditions that enable read, manipulate, and write operations on the representative qubit using the electron. Next, I generalize this result for any spin S, and describe how the resonance conditions change based on the type of exchange coupling, magnetic anisotropy, and magnitude of applied magnetic fields. The rest of the thesis is dedicated to utilizing the tools described in the framework to uncover the properties of potential scalable quantum architectures.

To guide the correspondence between experiment and model Hamiltonians of effective tripartite spin systems connected to leads, I investigate the transport properties of a three-terminal quantum dot coupled to a magnetic molecular dimer using the generalized master equation. The results show signatures of each term of the model Hamiltonian in differential conductance measurements. I then model a toy model of a steady state two magnetic impurity system anisotropically exchange-coupled with electrons in a 1D wire us-

ing first-quantized Green's functions. I extend these results with a representative three-site tight-binding model to predict transient phenomena using non-equilibrium Green's functions (NEGF), and comment on the applicability of a newly-developed NEGF-derived quantum master equation. Finally, I characterize two examples of novel quantum systems: the spin qubit candidate h-BN V_B^- using first-principles calculations and quantum defect embedding theory, and the thin film $Fe[H_2B(Pz)_2]_2(bipy)$ spin-crossover molecule, a candidate for spintronics applications, using the latest generation *ab initio* + NEGF software.

I dedicate this thesis to the countless individuals who have guided, inspired, and supported me throughout my life journey. To my parents, your timeless lessons of honesty, grit, and determination shaped my mind. Your unwavering support and love shaped my heart. Your words of encouragement to explore the unknown shaped my passion. I love you both. To my siblings Ryan, Brittain, and Skyler, your efforts and love enabled all of our families to thrive and achieve our dreams. To my wife, your laughter and care reminded me that life is meant to be jovial. And finally, to my son William Alexander, the kindness you have shown to all others, the strength of your convictions, and your wonder and unabashed curiosity of the natural world continue to inspire me.

ACKNOWLEDGMENTS

I would like to thank the following people for their support on the research projects that comprise this thesis. First and foremost, my advisor Dr. Talat Rahman for her guidance and patience. I have experienced tremendous growth under her leadership. Her infectious drive for new science inspired me to keep "turning rocks" and find novel ways to solve problems, both academic and professional. Next, Dr. Duy Le for his constant availability and willingness to help. His fresh perspectives on the processes in academia and life, his uncanny chemical intuition, and insights on raising a child while being a researcher has been useful. Next, Dr. Volodymyr Turkowski for his experience and insights in field theory and condensed matter. It was invaluable to my development as a scientist, and I am appreciative of the nudges and advice on careers in our field.

I want to acknowledge my committee members Dr. Enrique del Barco, Dr. Luca Argenti, and Dr. Parag Banerjee for their efforts and support on both the dissertation proposal and this thesis. Next, I thank Dr. Xiaoguang Zhang for guiding me through several years of exploring the spin systems detailed in this thesis, and encouraging me to continue probing and discovering. I am grateful to Dr. Peter Dowben for his insights on molecular spin systems and deep expertise in both experiment and theory, which have more than inspired me to continue researching. I am thankful to Dr. Nicolás Lorente for opening my eyes to a much wider world and opportunity in quantum science. Next I acknowledge Dr. Christian Vorwerk and Dr. Giulia Galli for the opportunity to explore novel defect qubits and the QDET approach. I am also grateful to Andreas Heinrich, Michelle Randall, Christoph Wolf, Deung-Jang Choi, and Jose Reina Gálvez for their support and hospitality during my stay at the Center for Quantum Nanoscience.

I would not have made it this far without the continued friendship and support (and the cups of coffee and tea) from my group mate Dave Austin. It has been a joy to explore

physics with him. I am grateful to several of those from the Rahman research group who directly aided me when I first started: Dr. Naseem Ud Din, Dr. Tao Jiang, and Dr. Jia Shi. I want to acknowledge the social support of my UCF Physics cohort, notably Eric Rende whose walk-and-talks were instrumental to discovering new ideas. For two years, I had the privilege to lead (and be led by!) the American Physical Society UCF chapter officers Stephanie Lough and Rebecca Reddin. Our talks and fellowship gave me energy to keep me going, and it both humbled and grounded me when I listened to the reality of their experimental work. Last, I would like to acknowledge several sources of funding: the Center for Molecular Magnetic Quantum Materials, an Energy Frontier Research Center funded by the U.S. Department of Energy, Office of Science, Basic Energy Sciences under Award No. DE-SC0019330, and the U.S. Department of Energy though Grant No. DE-FG02-07ER46354.

TABLE OF CONTENTS

LIST OF FIGURES

LIST OF TABLES

CHAPTER 1: INTRODUCTION

Multipartite spin systems are an attractive option as a building block of scalable quantum computer architectures for use in quantum information science (QIS). Recent two-spin realizations include the so-called singlet-triplet qubit which utilize two quantum dots exchange coupled together, and whose Bloch sphere representation involves the singlet and triplet spin states [1–3]. The use of three-spin particle scenarios for QIS is growing, like the recent work on triple quantum dots using a singlet-triplet qubit coupled with a Loss-DiVincenzo qubit [4, 5], and effective three-center molecular magnet qubits [6]. In this introduction, I will describe a theoretical approach for characterizing a class of three-spin systems, the exchange-coupled three-spin system with magnetic anisotropy (MA), in the context of their use in QIS and other quantum architectures such as spintronics. First I will summarize key concepts in QIS architectures and provide some physical examples. The model Hamiltonian derived from these physical examples will then be explained, along with a brief exploration into the origins of the spin parameters used in the model. I will then comment on the use of *ab initio* and non-equilibrium Green's function techniques to uncover properties of tripartite spin systems, before providing an outline for the rest of the thesis.

1.1 Principles of QIS Architectures

To understand why different spin systems have been explored for QIS applications, one must examine the principal unit in quantum computing: the qubit. In classical computing, the principal unit (the computational bit) possesses the ability to switch between an off (0) and on (1) state. In modern computational architectures, the states of a bit often correspond to fine-tuned voltages operated at the nanoscale. Qubits are the quantum extension of the classic bit, and in principle can be made from any two-level system, provided that the states

of the qubit can span any superposition of the two levels, $|\psi\rangle = \alpha\,|0\rangle + \beta\,|1\rangle$, where $\alpha, \beta \in \mathbb{C}$ describe the mixing and relative phase of the two states. The magnitudes of the coefficients are bounded by $|\alpha|^2 + |\beta|^2 = 1$ for a two-state system without decoherence, and are in general bounded by $0 \leq |\alpha|^2 + |\beta|^2 \leq 1$ if other unwanted states are energetically accessible.

The prototypical example of a qubit system is the spin qubit using quantum dots, or the "Loss and DiVincenzo" qubit [7]. The two levels of the Loss and DiVincenzo qubit are the two possibilities of the magnetic quantum number associated with the spin of an electron $|m_s = \pm\hbar/2\rangle$ trapped in a quantum dot. For the Loss and DiVincenzo qubit, it was theorized that the use of applied fields, such as a pulsed magnetic field, could enable access to a particular superposition of states for a single qubit, i.e., to perform a single qubit operation. In general, quantum computing exploits the properties of entanglement between two or more qubits, using qubit operations to access a particular entanglement state [8]. Entanglement is a feature of composite quantum systems. Composite quantum systems are those in which the composite Hilbert space H_{comp} is a tensor product of the Hilbert spaces belonging to each object: $H_{comp} = H_1 \otimes H_2 \otimes ...H_n$. The general state $|\chi\rangle$ belonging to the composite system can then be expressed as a complex superposition of components of the Kronecker outer product of each state $|\psi\rangle_i$, e.g., for a two object system $|\chi\rangle = \sum_{ij} c_{ij}\,|i\rangle_1 \otimes |j\rangle_2$ for $c_{ij} \in \mathbb{C}$. If the composite system state cannot be decomposed into a product state of two objects, i.e., $|\chi\rangle \neq |\psi\rangle_1 \otimes |\psi\rangle_2$, then the $|\chi\rangle$ state is considered an entangled state.

For useful quantum computers, David P. DiVincenzo developed criteria for scalable quantum architectures [9]. The five criteria are a scalable and well-defined Hilbert space control, a state preparation method, low decoherence (i.e., long qubit lifetimes), controlled unitary transformations through universal quantum gates, and a state-specific quantum measurement mechanism. Several quantum architectures have been explored, with some better suited to particular DiVincenzo criteria than others. For example, optical cavity quantum computers have coherence times on the order of 10 μs and qubit operation times on the order

of 10 fs, while quantum dots have coherence times on the order of 10 μs and operation times on the order of ns [8].

One limitation of the spin qubits is the factors that destroy the entanglement between the qubits. The primary sources of this decoherence are spin-lattice interactions and spin-spin interactions. These interactions are characterized by relaxation times, T_1 and T_2 respectively. If one chooses to utilize spin qubits, one must perform a quantum operation before either sources of decoherence win over. Several schemes, such as coupled magnetic molecules, and coupled quantum dots, have been developed to tackle spin decoherence for single logic qubits to prolong their lifetimes, but there is still much work needed to find a specific platform that both protects against decoherence and maintains the ability to scale the architecture to large number of coupled qubits.

1.2 Examples of Physical Systems

As mentioned in the introduction paragraph, there has been recent progress in realizing three-spin particle scenarios. There are several candidates for the class of exchange-coupled tripartite spin systems with MA that may be useful for quantum architectures. Magnetic molecules have been identified as a possible qubit because of the possible protection from decoherence due to the surrounding spin environment [10]. Magnetic molecules have also been a focus for quantum devices beyond QIS. Some useful properties for those other applications include tailorable ligands which offer chemical customization, slow relaxation of magnetization below a critical block temperature, large MA, and magnetic hysteresis that is statistically protected against thermal excitations [11]. Dimer molecular magnet systems, composed of two metal centers, in principle should combine the desirable magnetic properties of single molecular magnets with tailored asymmetry of either the magnetic centers or choice of ligands. The creation of asymmetry is important to implementing controllable

time-irreversible operations. There has been some work on exploring dimer molecules for this purpose, such as two Cr_7Ni rings [6, 12]. The effective tripartite spin molecular magnet consisting of two Cr_7Ni rings and a Cu ion has also been synthesized [6].

The effective exchange-coupled tripartite model, however, is not just constrained to magnetic molecules. Examples include three magnetic atom structures accessed using scanning tunneling microscopy and electron spin resonance [13] and triple quantum dots [4, 14]. A combination of these physical models, such as a quantum dot or addressable magnetic atom connected to a molecular magnetic dimer, could provide the necessary spin ingredients to utilize the resonance conditions important to QIS found in Chapter 2 and 3. As a step towards identifying which systems would work best, I next explore the properties of the mentioned physical systems that can be predicted using model Hamiltonians.

1.3 Model Spin Hamiltonians and Origin of Spin Parameters

One has the option of several model Hamiltonians to describe the physical scenarios of the prior section. As a starting point for this thesis, I first choose the popular Hamiltonian model for magnetic molecules that incorporates the effective exchange coupling and effective MA for each giant-spin approximated molecular metal center [10],

$$\hat{\mathcal{H}}_{\text{dimer}} = D\left(\hat{S}_2^z\hat{S}_2^z + \hat{S}_3^z\hat{S}_3^z\right) + J_z\hat{S}_2^z\hat{S}_3^z + J_{xy}\left(\hat{S}_2^x\hat{S}_3^x + \hat{S}_2^y\hat{S}_3^y\right) + \sum_{i=2}^{3}\mathbf{g}_i\mu_B\hat{\mathbf{S}}_i\cdot\mathbf{B}. \qquad (1.1)$$

Here $\mathbf{S}_i$ is the spin moment of particle i, D is the effective axial MA of each spin, J_z is the exchange coupling between the spins along their z axis projection (aligned with respect to the MA axis), and J_{xy} is the exchange coupling between the spins in the plane perpendicular to the MA axis. The last term in Eq. (1.1) is easily identified as the Zeeman term, with effective g-tensor $\mathbf{g}_i$ for spin particle i, μ_B is the Bohr magneton and $\mathbf{B}$ is a state magnetic field. The origins of the first two terms will be described in the next two sections. The

electron is then added to this dimer, and looking only at the spin space of the electron, interacts initially to the applied magnetic field,

$$\hat{\mathcal{H}}_{\text{electron}} = \mathbf{g}_1 \mu_B \hat{\mathbf{S}}_1 \cdot \mathbf{B}. \tag{1.2}$$

The last ingredient in the model spin Hamiltonian is the interactions of the electron with the dimer through an exchange term that initially neglects the momentum components of the electron,

$$\hat{\mathcal{H}}_{\text{dimer-electron}} = \frac{1}{2} \sum_{\mu,\mu'} J_{1i} \hat{\mathbf{S}}_i \cdot \hat{d}^{\dagger}_{\mu,i} \hat{\boldsymbol{\sigma}}_{\mu,\mu'} \hat{d}_{\mu',i}, \tag{1.3}$$

where μ is a spin index for particle 1, $\hat{\boldsymbol{\sigma}}_{\mu,\mu'}$ is the corresponding μ, μ' matrix element of the $s = \frac{1}{2}$ Pauli matrix, and $\hat{d}^{\dagger}_{\mu,i}/\hat{d}_{\mu,i}$ represents (in second quantization language) the creation/annihilation operator of a state in which particle 1 is bound to particle i. The total spin Hamiltonian is,

$$\hat{\mathcal{H}}_{\text{total}} = \hat{\mathcal{H}}_{\text{dimer}} + \hat{\mathcal{H}}_{\text{electron}} + \hat{\mathcal{H}}_{\text{dimer-electron}} \tag{1.4}$$

Next, I will describe the origins for two classes of terms: exchange coupling and MA.

1.3.1 Exchange Coupling

The second and third term in Eq. (1.1) and Eq. (1.3) describe a spin exchange interaction between two spin particles. At its core, the exchange interaction is a quantum mechanical one that originates from the indistinguishability of localized particles. There are different types of exchange coupling that can manifest in an atomic system [15]. As an example, one can construct a wave function that is built from two one-electron eigenstates $\psi(\mathbf{r})\chi(m_s)$ (i.e., a two-electron Slater determinant) for spatial part ψ and spin part χ with eigenvalues α and

β,

$$\Psi_{\alpha\beta}(\mathbf{r}_1, m_{s\alpha}; \mathbf{r}_2, m_{s\beta}) = \frac{1}{\sqrt{2}} \begin{vmatrix} \psi_\alpha(\mathbf{r}_1)\chi(m_{s\alpha}) & \psi_\alpha(\mathbf{r}_2)\chi(m_{s\alpha}) \\ \psi_\beta(\mathbf{r}_1)\chi(m_{s\beta}) & \psi_\beta(\mathbf{r}_2)\chi(m_{s\beta}) \end{vmatrix}. \tag{1.5}$$

When the Coulomb interaction,

$$\hat{\mathcal{H}}_U = \frac{1}{|\hat{\mathbf{r}}_1 - \hat{\mathbf{r}}_2|}, \tag{1.6}$$

is expressed in this basis, one finds two types of integrals that appear in the Hamiltonian representation. The first integral type is the Coulomb integral,

$$U_{\alpha\beta} = \int \mathrm{d}\mathbf{r}_1 \int \mathrm{d}\mathbf{r}_2 \, \frac{|\psi_\alpha(\mathbf{r}_1)|^2 |\psi_\beta(\mathbf{r}_2)|^2}{|\mathbf{r}_1 - \mathbf{r}_2|}, \tag{1.7}$$

while the second type is the exchange integral,

$$J_{\alpha\beta} = \int \mathrm{d}\mathbf{r}_1 \int \mathrm{d}\mathbf{r}_2 \, \frac{\psi^*_\alpha(\mathbf{r}_1)\psi_\beta(\mathbf{r}_1)\psi^*_\beta(\mathbf{r}_2)\psi_\alpha(\mathbf{r}_2)}{|\mathbf{r}_1 - \mathbf{r}_2|}. \tag{1.8}$$

Diagonalizing the interaction Hamiltonian expressed in the two-electron Slater determinant results in four eigenstates, one that is triply degenerate (the so-called "triplet" states) with eigenenergy $U_{\alpha\beta} - J_{\alpha\beta}$ and another eigenstate (the "singlet" state) with eigenenergy $U_{\alpha\beta} + J_{\alpha\beta}$. In this way, the interaction of the two electrons will always result in a shift of the energy by the Coulomb integral $U_{\alpha\beta}$ and the exchange integral $\pm J_{\alpha\beta}$.

One can also extend the idea of interacting electron orbitals to electrons moving between localized "sites", e.g., the Hubbard model [16]. In the Hubbard model, the kinetic movement of the electron between the sites are accounted for by "hopping" terms that are parameterized by the tunneling parameter t. A localized onsite Coulomb repulsion U is also

included. In the two-site spin Hubbard model, ignoring the onsite chemical potential, the Hamiltonian has the form,

$$\hat{\mathcal{H}}_{SH} = -t \sum_{\sigma} \left(\hat{c}^{\dagger}_{1\sigma} \hat{c}_{2\sigma} + \hat{c}^{\dagger}_{2\sigma} \hat{c}_{1\sigma} \right) + U \left(\hat{n}_{1\uparrow} \hat{n}_{1\downarrow} + \hat{n}_{2\uparrow} \hat{n}_{2\downarrow} \right), \tag{1.9}$$

where $\hat{c}^{\dagger}_{i\sigma}$ creates an electron with spin σ at site i, and $\hat{n}_{i\sigma} \equiv \hat{c}^{\dagger}_{i\sigma} \hat{c}_{i\sigma}$ is the number operator. The eigenenergies of this Hamiltonian are $\varepsilon = 0$, U, and $(U \pm \sqrt{U^2 + 16t^2})/2$. By assuming U is very large, one can downfold onto a low energy Hilbert space by projecting out the high energy states (in a manner similar to what is done for the three-spin Kondo model in Appendix A). The two lowest eigenenergies in this downfolded space are $\varepsilon = 0$ and $-4t^2/U$ which correspond to the triplet and singlet states, respectively. The exchange energy due to the singlet-triplet splitting is thus $J = 4t^2/U$. Additionally, the downfolded Hamiltonian, upon using a suitable transformation of the electron operators to spin $1/2$ operators $\mathbf{S}_i \equiv \hat{c}^{\dagger}_{\mu,i} \hat{\boldsymbol{\sigma}}_{\mu,\mu'} \hat{c}_{\mu',i}$ and using the definition of the exchange energy, is,

$$\hat{\mathcal{H}}_{SH,\text{downfold}} = J \left(\hat{\mathbf{S}}_1 \cdot \hat{\mathbf{S}}_2 - \frac{1}{4} \hat{n}_1 \hat{n}_2 \right). \tag{1.10}$$

This form of the exchange interaction is derived from the direct interactions of the electrons between orbitals, and is referred to as "direct" exchange. One can also start with the Anderson model [17] of electrons interacting with the d orbitals of metal impurities, and perform a Schrieffer-Wolff transformation [18] to recover a Kondo Hamiltonian [19] of the form,

$$\hat{\mathcal{H}}_K = \sum_{\mathbf{k}\sigma} \varepsilon_{\mathbf{k}} \hat{c}^{\dagger}_{\mathbf{k}\sigma} \hat{c}_{\mathbf{k}\sigma} - J \hat{\mathbf{S}} \cdot \hat{\mathbf{s}}, \tag{1.11}$$

where J is the Kondo exchange coupling constant, $\mathbf{S}$ is the spin of the impurity, and $\mathbf{s}$ is the

electron spin density at the impurity site. There are other exchange mechanisms that are possible such as superexchange and ferromagnetic superexchange, which involves an electron hopping through an intermediate orbital, and double exchange, which is a combination of the direct exchange and Coulomb exchange detailed previously [15]. Extending the two-spin particle results of this section to periodic systems enriches the physics that can be explored, resulting in a full Hubbard model, and the well-known Heisenberg model (which is the downfolded Hubbard model in the limit of large U). In all of these models, an effective exchange coupling constant is present that quantifies the exchange interaction.

It is important to note that the exchange constants have been derived in this section to be isotropic because of the one-dimensional nature of the hopping elements and spherical potential in the case of the Coulomb exchange. In principle, the interactions need not be isotropic. In certain materials, such as α-Fe_2O_3, one may need complex exchange terms such as the Dzyaloshinski-Moriya interaction [20, 21] to model their energetics. In the next section, I will explore one kind of anisotropy in magnetic systems: an intrinsic magnetic zero-field anisotropy.

1.3.2 Magnetic Anisotropy

The MA in Eq. (1.1) describes the energetic preference of each spin to a magnetic axis. In general, MA in a solid material is a description of how that material's magnetic properties differ depending on the axis chosen from a fixed frame within the solid. For example, if the solid is known to be more easily magnetized along a single axis, the material is said to possess MA along this "easy" axis. This property is intrinsic to the material, and exists without an applied magnetic field. If the solid is easily magnetized along two axes, the material is said to possess an "easy" plane.

The origins of MA can differ depending on the spin system. Jahn-Teller distortions are sometimes responsible for the MA in magnetic molecules [22, 23]. On-site interactions

between atoms in two states in ultra-cold optical lattices [24] can also induce an effective MA. This thesis utilizes a form of MA whose origin is most likely to be found for molecular magnets connected to metallic leads or on surfaces, defected periodic solids, and atoms on surfaces: spin-orbit coupling.

MA in periodic solids arises from the coupling between the orbital motion of the solid's electrons in a potential gradient (such as the atomic lattice potential) and the spin of those electrons [25]. This spin-orbit coupling leads to symmetry breaking where certain directions of the magnetization is preferred. In the atomic energy point of view, e.g., an electron in the spherically symmetric potential of the hydrogen atom, the spin-orbit coupling Hamiltonian is,

$$\hat{\mathcal{H}}_{so} = (g_e - 1)\frac{\mu_B}{\hbar m_e c^2}\frac{1}{r}\frac{\partial V(\mathbf{r})}{\partial r}\hat{\mathbf{L}} \cdot \hat{\mathbf{S}}, \tag{1.12}$$

where g_e is the g-factor of the electron, μ_B is the Bohr magneton, $\hbar$ is the Plank constant, m_e is the mass of the electron, e the charge of the electron, c is the speed of light, $V(\mathbf{r})$ is the electric potential of the electron, $\hat{\mathbf{L}}$ is the angular momentum of the electron, and $\hat{\mathbf{S}}$ is the spin angular vector of the electron. In extended systems, the potential gradient $\frac{\partial V(\mathbf{r})}{\partial r}$ is derived from the atomic lattice potential, and the spin-orbit interaction takes the form of,

$$\hat{\mathcal{H}}_{so;\text{extended}} = \xi\hat{\mathbf{L}} \cdot \hat{\mathbf{S}} \tag{1.13}$$

where ξ is a spin-orbit parameter, $\hat{\mathbf{L}}$ is the orbital angular momentum operator, and $\hat{\mathbf{S}}$ is the spin operator. By expanding the spin-orbit Hamiltonian in an extended system in the basis of orbital, spin, and momentum quantum numbers, the change of total energy of the system

is calculated in second-order perturbation theory (and neglecting spin flip terms) to be [26],

$$\Delta E \approx \frac{1}{4}\xi\hat{\mathbf{S}} \cdot [\langle \mathbf{L}_\uparrow \rangle - \langle \mathbf{L}_\downarrow \rangle], \tag{1.14}$$

where $\mathbf{L}_\sigma$ is the orbital moment vector for the spin band σ, and it has been projected onto the magnetization direction $\hat{\mathbf{S}}$ (not to be confused with the spin operator $\hat{\mathbf{S}}$).

The notion of energetic preference along a direction within the solid can be generalized and described by the effective spin Hamiltonian,

$$\hat{\mathcal{H}}_{ma} = \sum_{k\in\mathbb{Z}} \sum_{q=-k}^{k} A_k^q \hat{O}_k^q(\hat{\mathbf{S}}), \tag{1.15}$$

where $A_k^q \in \mathbb{R}$ is an associated coefficient to the hermitian operator $\hat{O}_k^q$ of rank k for spin operator $\hat{\mathbf{S}}$, with q-fold symmetry about the axial direction [27]. The collection of these operators are called the extended Stevens operators (ESOs). The components of these spherical and tesseral tensor operators A_k^q has been explored for arbitrary rank k and spin S. As an example, the MA Hamiltonian term of Eq. (1.1) is related to the component of the second-order ESO B_2^0 minus a constant,

$$B_2^0 \hat{O}_2^0 = 3\hat{S}_z^2 - S(S+1). \tag{1.16}$$

The use of ESOs is ubiquitous in model Hamiltonians for molecular magnets, for example in the giant spin description of single molecule magnets [28, 29].

1.4 Application of Ab Initio and Transport Theories to Tripartite Spin Systems

Beyond the implicit inclusion of spin-orbit coupling in the magnetic anisotropy terms, so far there is no other information on the *electronic* aspects of the spin Hamiltonian in Eq. (1.1)

and Eq. (1.3). These missing elements may be necessary for an accurate description of physical systems. There is also no identification of the source of the electron. Even with the aforementioned toy spin model, there are significant physics that can be teased out for QIS purposes, as is investigated in Chapter 2 and 3. Once one determines the physical scenario, the natural progression of questions are 1. how to obtain the parameters for the model Hamiltonian so that it appropriately predicts magnetic properties, and 2. how does one take into account the orbital and electronic degrees of freedom, which will undoubtedly impact the dynamics of a realistic qubit? While the former is not investigated in this thesis, I explore the latter through several methods, including generalized master equations (GMEs), *ab initio* density-functional theory (DFT), and both Green's function and non-equilibrium Green's function (NEGF) techniques.

1.4.1 Master Equation Methods

To uncover transport properties, one can use the GME; of which a formal derivation and the assumptions used is given in Appendix B. GMEs in general offer a method to predict the dynamics of open quantum systems embedded in an environmental "bath". This method is used in Chapter 4 to explore a three-spin system (a quantum dot coupled to a magnetic dimer), connected to biased leads and influenced by both a gate and applied magnetic fields. The inclusion of the density of states in the GME, and the hopping terms that play a role in the transfer rates via the electrode-molecule coupling, account for the electronic degrees of freedom. Recent progress has been made to incorporate non-equilibrium Green's function-derived transfer rates into similar types of master equations, called quantum master equations [30, 31]. The use of NEGF-derived transfer rates offer another method to more realistically treat exchange-coupled tripartite spin systems with magnetic anisotropy coupled to leads; this advancement is commented on in Chapter 6.

1.4.2 Density Functional Theory

DFT is used in Chapter 7 to identify important spin excitation properties in the qubit candidate h-BN $V_B{}^-$. Standard DFT has its origins in the Hohenberg and Kohn theorem [32]. DFT primarily works with the ground-state number density distribution $n(\mathbf{r})$ (which is the electron number density upon multiplication of the electron charge e) and the effective single-particle Schrödinger equation in the Born approximation called the Kohn-Sham (KS) equation (in atomic units),

$$\left[-\frac{1}{2}\nabla^2 + \int \mathrm{d}\mathbf{r}' \, \frac{n(\mathbf{r}')}{|\mathbf{r}-\mathbf{r}'|} + v(\mathbf{r}) + V_{xc}(\mathbf{r})\right] \psi_i^{\mathrm{KS}}(\mathbf{r}) = \varepsilon_i^{\mathrm{KS}} \psi_i^{\mathrm{KS}}(\mathbf{r}), \tag{1.17}$$

where $\psi_i^{\mathrm{KS}}(\mathbf{r})$ is the i'th KS state, $v(\mathbf{r})$ is the external potential, e.g., from nuclei-electron interactions, V_{xc} the exchange correlation potential defined by $\delta E_{xc}[n(\mathbf{r})]/\delta n(\mathbf{r})$, $E_{xc}[n(\mathbf{r})]$ is the exchange correlation energy functional, $\varepsilon_i^{\mathrm{KS}}$ is the i'th KS eigenvalue, and the number density is defined as $n(\mathbf{r}) = \sum_{i=1}^{N} \left|\psi_i^{\mathrm{KS}}(\mathbf{r})\right|^2$ with the sum over N electrons. The KS wave functions are properly normalized to reproduce the total number of electrons within the volume spanned by the KS equation, and the number density satisfies the Pauli-exclusion principle for fermions. The KS equation is solved self-consistently because the exchange-correlation energy E_{xc} is a functional of the number density, which is dependent on the KS wave functions, which in turn is dependent on the exchange-correlation potential and thus the exchange-correlation energy. The exchange-correlation energy functional is not known *a priori*, and suitable approximations must be made to this functional in order to accurately model properties of a chosen system.

Standard DFT must be extended in order to predict the electronic structure of spin-polarized systems. The first extension is the spin-dependent version of DFT, which in the

collinear form [33] uses spinor KS wave functions,

$$\phi_i^{\mathrm{KS}}(\mathbf{r}) \to \begin{pmatrix} \phi_{i,\uparrow}^{\mathrm{KS}}(\mathbf{r}) \\ \phi_{i,\downarrow}^{\mathrm{KS}}(\mathbf{r}) \end{pmatrix}. \tag{1.18}$$

Naturally, collinear spin-polarized DFT must use the number density matrix $\rho_{\alpha\beta}$ with components indexed by spin,

$$\rho_{\alpha\beta} = \phi_\alpha^{*\mathrm{KS}}(\mathbf{r})\phi_\beta^{\mathrm{KS}}(\mathbf{r}). \tag{1.19}$$

The KS equation is then modified as,

$$\left[\left(-\frac{1}{2}\nabla^2 + \int \mathrm{d}\mathbf{r}' \, \frac{n(\mathbf{r}')}{|\mathbf{r}-\mathbf{r}'|}\right)\mathbf{I} + \boldsymbol{v}(\mathbf{r}) + \boldsymbol{V}_{xc}(\mathbf{r})\right] \begin{pmatrix} \phi_{i,\uparrow}^{\mathrm{KS}}(\mathbf{r}) \\ \phi_{i,\downarrow}^{\mathrm{KS}}(\mathbf{r}) \end{pmatrix} = \varepsilon_i^{\mathrm{KS}} \begin{pmatrix} \phi_{i,\uparrow}^{\mathrm{KS}}(\mathbf{r}) \\ \phi_{i,\downarrow}^{\mathrm{KS}}(\mathbf{r}) \end{pmatrix}, \tag{1.20}$$

where $\mathbf{I}$ is the identity matrix in the spin basis and $\boldsymbol{v}$ now allows for external spin potentials like magnetic fields. This form of the KS equation requires that the exchange correlation energy is a functional of the number density matrix, i.e. $E_{xc} \equiv E_{xc}[\rho(\mathbf{r})]$.

As will be shown in Chapter 7, DFT can be used to explore the ground-state properties of a quantum architecture. To more accurately describe the excited states needed for quantum architectures, other methods are needed. I provide a brief synopsis of one such method, quantum defect embedding theory (QDET), in Chapter 7. While these methods can help guide parameterization of transport models, numerical descriptions of read, manipulate, and write operations on a representative qubit or spintronic state cannot be completely described using DFT or QDET because the processes are inherently time and frequency dependent. For this problem, one can turn to NEGF methods.

1.4.3 Non-Equilibrium Green's Functions

The inherently non-equilibrium problem of excited state dynamics can be explored with NEGF methods. As described in reference [34], Green's functions are a method to solve inhomogeneous differential equations such as the inhomogeneous Schrödinger equation. In essence, the many-body Green's functions describe the correlations of operators. Measurable quantities, such as average particle number, can be extracted once one solves for the many-body Green's function. There are several types of many-body Green's functions, each with their own advantages and linked to different observables. A review of the Green's functions that are used in this thesis are given in Appendix D. In equilibrium (in the sense that the dynamics does not depend on time, but the difference in times), one can use the fluctuation-dissipation theorem and a perturbation expansion to solve for energy dependent quantities, such as the density of states. Solving such problems can be difficult as the problem needs an identification of the self-energy of a system, which requires choosing which Feynman diagrams to include in the possibly infinite perturbation expansion.

Assuming that a scheme for the self energy has been determined, predicting the output of operations on quantum architectures in the time domain is needed. The seminal work of Yigal Meir and Ned Wingreen brought forth a tractable method to solve the nonequilibrium problem using nonequilibrium Green's functions [35]. Their work serves the basis and/or inspiration of many NEGF codes, including TranSiesta [36–38]. Other methods utilizing the Meir and Wingreen equations are typically reserved for tractable Hubbard-like models, like double QDs connected to leads [39]. TranSiesta allows one to use the wave functions derived from *ab initio* in a localized basis set and solve the non-equilibrium problem. I use TranSiesta in Chapter 8 to uncover important properties of the thin film spintronics candidate $Fe[H_2B(Pz)_2]_2(bipy)$. The aim in the future is to use a combination of DFT+NEGF tools to adequately characterize quantum operations for the exchange-coupled tripartite spin

system with MA.

1.5 Outline of Thesis

In this introduction, I have detailed a general theory behind exchange-coupled tripartite spin systems that contain MA and addressed the problem of how one can implement such a scheme with a realistic system. The theoretical framework built in this chapter are the jumping point for the next chapters. In chapter 2, I examine the spin space for one of the simplest exchange-coupled tripartite spin systems that contains MA: the spin 1 dimer coupled with an electron. I extend our coupled dimer-electron result to dimer of general spin S in chapter 3. The results from both chapters prove that there exists necessary, but not sufficient, resonance conditions for optimal qubit operations utilizing the MA of each monomer in the dimer, and the exchange coupling of the electron with the dimer. Chapter 4 in effect takes the tripartite spin system and connects it to leads. Utilizing the generalized master equation approach, I predict signatures of the dimer system within transport spectra, which can aid in the construction and verification of such a spin system for QIS purposes. In chapter 5, I describe the first-quantized Green's function and Lippman-Schwinger approach to transport for two magnetic impurities. This is contrasted with the two and three-site tight-binding model NEGF results in chapter 6. Chapter 7 investigates a negatively-charged boron vacancy in bulk hexagonal boron nitride, a potential spin qubit, using first-principles calculations and quantum defect embedding theory to identify useful excited states. I then highlight the utility of transport models such as non-equilibrium Green's Functions paired with density functional theory for use in characterizing spin systems such as spin-crossover molecules in chapter 8, which have been predicted as candidates for spintronics applications.

1.6 List of References

[1] J. Levy, Physical Review Letters **89**, 147902 (2002).

[2] J. R. Petta, A. C. Johnson, J. M. Taylor, E. A. Laird, A. Yacoby, M. D. Lukin, C. M. Marcus, M. P. Hanson, and A. C. Gossard, Science **309**, 2180 (2005).

[3] A. C. Johnson, J. R. Petta, J. M. Taylor, A. Yacoby, M. D. Lukin, C. M. Marcus, M. P. Hanson, and A. C. Gossard, Nature **435**, 925 (2005).

[4] A. Noiri, T. Nakajima, J. Yoneda, M. R. Delbecq, P. Stano, T. Otsuka, K. Takeda, S. Amaha, G. Allison, K. Kawasaki, Y. Kojima, A. Ludwig, A. D. Wieck, D. Loss, and S. Tarucha, Nature Communications **9**, 5066 (2018).

[5] A. Noiri, K. Takeda, T. Nakajima, T. Kobayashi, A. Sammak, G. Scappucci, and S. Tarucha, Nature **601**, 338 (2022).

[6] G. A. Timco, S. Carretta, F. Troiani, F. Tuna, R. J. Pritchard, C. A. Muryn, E. J. L. McInnes, A. Ghirri, A. Candini, P. Santini, G. Amoretti, M. Affronte, and R. E. P. Winpenny, Nature Nanotechnology **4**, 173 (2009).

[7] D. Loss and D. P. DiVincenzo, Physical Review A **57**, 120 (1998).

[8] M. A. Nielsen and I. L. Chuang, *Quantum Computation and Quantum Information: 10th Anniversary Edition* (Cambridge University Press, Cambridge, 2010).

[9] D. P. DiVincenzo and D. Loss, Superlattices and Microstructures **23**, 419 (1998).

[10] S. Hill, R. S. Edwards, N. Aliaga-Alcalde, and G. Christou, Science **302**, 1015 (2003).

[11] L. Bogani and W. Wernsdorfer, Nature Materials **7**, 179 (2008).

[12] A. Ardavan, A. M. Bowen, A. Fernandez, A. J. Fielding, D. Kaminski, F. Moro, C. A. Muryn, M. D. Wise, A. Ruggi, E. J. L. McInnes, K. Severin, G. A. Timco, C. R. Timmel, F. Tuna, G. F. S. Whitehead, and R. E. P. Winpenny, npj Quantum Information **1**, 1 (2015).

[13] S.-h. Phark, H. T. Bui, A. Ferrón, J. Fernández-Rossier, J. Reina-Gálvez, C. Wolf, Y. Wang, K. Yang, A. J. Heinrich, and C. P. Lutz, Electric-field-driven spin resonance by on-surface exchange coupling to a single-atom magnet (2023).

[14] M. Russ and G. Burkard, Journal of Physics: Condensed Matter **29**, 393001 (2017).

[15] E. Pavarini, E. Koch, R. Scalettar, and R. Martin, eds., *The Physics of Correlated Insulators, Metals, and Superconductors*, Schriften des Forschungszentrums Jülich. Reihe Modeling and Simulation, Vol. 7 (Forschungszentrum Jülich GmbH Zentralbibliothek, Verlag, Jülich, 2017) p. 450 S.

[16] J. Hubbard, Proceedings of the Royal Society of London. Series A. Mathematical and Physical Sciences **276**, 238 (1963).

[17] P. W. Anderson, Physical Review **124**, 41 (1961).

[18] J. R. Schrieffer and P. A. Wolff, Physical Review **149**, 491 (1966).

[19] J. Kondo, Progress of Theoretical Physics **32**, 37 (1964).

[20] T. Moriya, Physical Review **120**, 91 (1960).

[21] I. Dzyaloshinsky, Journal of Physics and Chemistry of Solids **4**, 241 (1958).

[22] R. Sessoli, D. Gatteschi, A. Caneschi, and M. A. Novak, Nature **365**, 141 (1993).

[23] D. Gatteschi and R. Sessoli, Angewandte Chemie International Edition **42**, 268 (2003).

[24] W. C. Chung, J. de Hond, J. Xiang, E. Cruz-Colón, and W. Ketterle, Physical Review Letters **126**, 163203 (2021).

[25] G. Bihlmayer, in *Handbook of Materials Modeling: Methods: Theory and Modeling* (Springer, 2020) pp. 895–917.

[26] G. v. d. Laan, Journal of Physics: Condensed Matter **10**, 3239 (1998).

[27] C. Rudowicz and C. Y. Chung, Journal of Physics: Condensed Matter **16**, 5825 (2004).

[28] D. Gatteschi, R. Sessoli, and J. Villain, *Molecular nanomagnets*, Vol. 5 (Oxford University Press on Demand, 2006).

[29] A. L. Barra, D. Gatteschi, and R. Sessoli, Physical Review B **56**, 8192 (1997).

[30] B. Bhandari, R. Fazio, F. Taddei, and L. Arrachea, Physical Review B **104**, 035425 (2021).

[31] J. Reina-Gálvez, N. Lorente, F. Delgado, and L. Arrachea, Physical Review B **104**, 245435 (2021).

[32] P. Hohenberg and W. Kohn, Physical Review **136**, B864 (1964).

[33] U. v. Barth and L. Hedin, Journal of Physics C: Solid State Physics **5**, 1629 (1972).

[34] H. Haug and A. P. Jauho, *Quantum Kinetics in Transport and Optics of Semiconductors* (Springer Berlin Heidelberg, 2007).

[35] Y. Meir and N. S. Wingreen, Physical Review Letters **68**, 2512 (1992).

[36] M. Brandbyge, J.-L. Mozos, P. Ordejón, J. Taylor, and K. Stokbro, Physical Review B **65**, 165401 (2002).

[37] N. Papior, N. Lorente, T. Frederiksen, A. García, and M. Brandbyge, Computer Physics Communications **212**, 8 (2017).

[38] A. García, N. Papior, A. Akhtar, E. Artacho, V. Blum, E. Bosoni, P. Brandimarte, M. Brandbyge, J. I. Cerdá, F. Corsetti, R. Cuadrado, V. Dikan, J. Ferrer, J. Gale, P. García-Fernández, V. M. García-Suárez, S. García, G. Huhs, S. Illera, R. Korytár, P. Koval, I. Lebedeva, L. Lin, P. López-Tarifa, S. G. Mayo, S. Mohr, P. Ordejón, A. Postnikov, Y. Pouillon, M. Pruneda, R. Robles, D. Sánchez-Portal, J. M. Soler, R. Ullah, V. W.-z. Yu, and J. Junquera, The Journal of Chemical Physics **152**, 204108 (2020).

[39] A. Dey, D. S. Bhakuni, B. K. Agarwalla, and A. Sharma, Journal of Physics: Condensed Matter **32**, 075603 (2019).

CHAPTER 2: ANISOTROPY-EXCHANGE RESONANCE AS A MECHANISM FOR ENTANGLED STATE SWITCHING

(Adapted from Eric D. Switzer, Xiao-Guang Zhang, and Talat S. Rahman, "Anisotropy-exchange resonance as a mechanism for entangled state switching." Phys. Rev. A 104, 052434 (2021))

2.1 Introduction

Spin state entanglement plays a key role in many systems, including those considered within quantum information science (QIS). For example, spin qubits, the coherent superposition of spin states within quantum objects, make use of entangled spin states for quantum gate operations [1]. Spin qubits have been explored theoretically and experimentally, notably in the application of confined electrons in quantum dots fabricated in semiconductors [2–9] and the search for robust QIS-applicable magnetic molecule systems [10–17]. Molecular magnets in particular possess an onsite magnetic anisotropy which gives rise to their unique magnetic properties. Molecular magnets are viable candidates for spin state switching for QIS purposes because of their long coherence times, the ability to tunnel between spin states resulting from their magnetic anisotropy, and tailorable ligands [18]. For example, the single molecule magnet $TbPc_2$ possesses a nuclear spin that is electrically controllable and has long coherence times [15, 17]. In both of these QIS approaches, the Kondo effect has been found [19–21], and thus the Kondo or Anderson impurity model [22, 23] is applicable to predict some features of these systems.

With these considerations, a QIS system that contains onsite magnetic anisotropy is expected to have a complex interaction between the system's anisotropy and effective exchange coupling. While some studies have examined the interplay of exchange coupling

and onsite magnetic anisotropy for two particles [24], the three-particle case is a qualitatively different system that has not been fully explored. Some experimental and theoretical studies have realized multiple-quantum dot scenarios [5–7, 25], or studied the two magnetic impurity entanglement state dependency of contact exchange interactions with incident electrons [26–28]. As described in the effectively three spin particle setup in Ref. [29], the strong-coupling Kondo exchange regime and the weak-coupling spin-orbit interaction regime compete with each other, resulting in a non-trivial interaction. Outside QIS, a similar balance between exchange coupling and magnetic anisotropy has been recently found experimentally in a Mott insulator composed of an ultra-cold optical lattice of ^{87}Rb atoms [30]. In all of these studies, the exchange coupling mechanism plays a significant role in controlling the system of interest. Unintended variations in this exchange can cause undesirable effects, and thus a system must be correspondingly robust against them.

In this work, we explore a general spin model with exchange and magnetic anisotropy that encompasses these scenarios and investigates the robustness of the spin system by extending the two-particle case of Ref. [24] to the three-particle paradigm. We consider two magnetic sites of either $S_{2,3} = \frac{1}{2}$ or $S_{2,3} = 1$ in which an exchange interaction is applied either isotropically or anisotropically between them and the $S_1 = \frac{1}{2}$ particle. Because we do not treat the electronic degrees of freedom and instead focus solely on the model's spin degrees of freedom, our model is a general one with physical analogs in the recently realized experiments of three quantum dots [5–7] and ultra-cold optical lattices [30]. As we will show, we find that for the $\mathbb{C}^{18}$ state space model corresponding to $S_{2,3} = 1$, the exchange and anisotropy interactions lead to a set of necessary conditions on the exchange and magnetic anisotropy strengths that correspond with perfect non-entangled to entangled state switching in four smaller SO(2) representation subgroups. We find that at these special resonance conditions, which we designate as "DJ resonances," measurement of the coupled particle entanglement states is possible by measurement of the $S_1 = \frac{1}{2}$ particle's spin. We also show the conditions

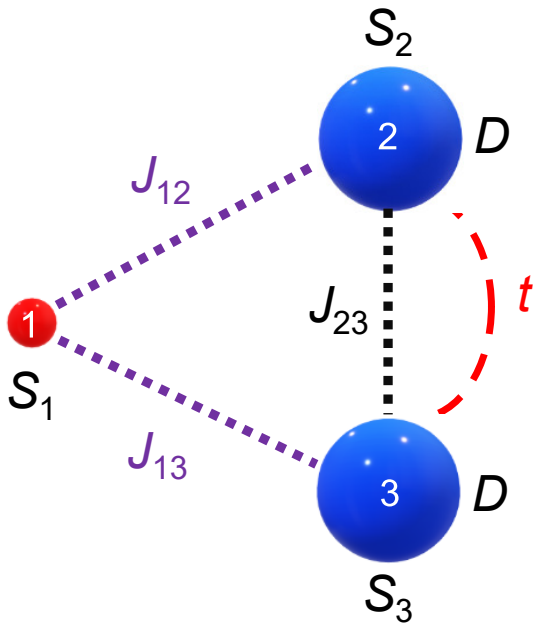

Figure 2.1: Schematic of the spin model considered in this work. Particle 2 and 3 are coupled by an exchange interaction J_{23}. Particle 1 is also coupled to particle 2 and 3 by an exchange interaction, J_{12} and J_{13}, respectively. Particle 1 is allowed to hop between particle 2 and particle 3 with hopping strength t.

in which these DJ resonances allow for complete control of appropriately-chosen Bloch vectors within a subspace of the coupled particles' total spin space, which is not found for the $S_{2,3} = \frac{1}{2}$ model. We demonstrate conditions for full control of this Bloch vector, and that for a relevant molecular magnet example, state coherence is robust against anisotropic application of the exchange coupling.

A representative schematic of the resulting spin model is shown in Fig. 2.1. The spin Hamiltonian ($\hbar = 1$) is then,

$$\mathcal{H} = \mathcal{H}_{12} + \mathcal{H}_{13} + \mathcal{H}_{23} + \mathcal{H}_{\mathrm{A}} + \mathcal{H}_{\mathrm{t}}, \tag{2.1}$$

where each term in the Hamiltonian is explained as follows. Motivated by the application

of exchange coupling between two coupled dimers [31], the exchange interaction of the two $S_{2,3}$ particles is represented by

$$\mathcal{H}_{23} = J_z \hat{S}_2^z \hat{S}_3^z + J_{xy} \left(\hat{S}_2^x \hat{S}_3^x + \hat{S}_2^y \hat{S}_3^y \right), \tag{2.2}$$

where $\hat{\mathbf{S}}_i = (\hat{S}_i^x, \hat{S}_i^y, \hat{S}_i^z)$ is the spin operator for the ith particle, J_z is the strength of the exchange interaction between particle 2 and 3 parallel to the direction of the magnetic anisotropy axis, and J_{xy} is the strength of the exchange interaction between particle 2 and 3 perpendicular to the direction of the magnetic anisotropy axis. When this interaction is taken to be isotropic, i.e. $J_z = J_{xy} \equiv J_{23}$, this equation simplifies to $\mathcal{H}_{23} = J_{23} \hat{\mathbf{S}}_2 \cdot \hat{\mathbf{S}}_3$. The interaction of the $S_1 = \frac{1}{2}$ particle with the $S_{2,3}$ particles is closely related to the spin portion of the Kondo interaction, and may be represented by,

$$\mathcal{H}_{1i} = \frac{J_{1i}}{2} \sum_{\mu,\mu'} \hat{\mathbf{S}}_i \cdot \hat{d}^\dagger_{\mu,i} \hat{\boldsymbol{\sigma}}_{\mu,\mu'} \hat{d}_{\mu',i}, \tag{2.3}$$

where μ is a spin index for particle 1, $\hat{\boldsymbol{\sigma}}_{\mu,\mu'}$ is the corresponding μ, μ' matrix element of the $s = \frac{1}{2}$ Pauli matrix, and $\hat{d}^\dagger_{\mu,i}/\hat{d}_{\mu,i}$ represents (in second quantization language) the creation/annihilation operator of a state in which particle 1 is bound to particle i. In our general treatment, we allow J_{12} and J_{13} to take all values, i.e., we consider both ferromagnetic and anti-ferromagnetic possibilities.

Additionally, we consider situations in which $S_{2,3} = 1$ particles possess an anisotropic response to applied magnetic fields,

$$\mathcal{H}_{\mathrm{A}} = D \left(\hat{S}_2^z \hat{S}_2^z + \hat{S}_3^z \hat{S}_3^z \right), \tag{2.4}$$

where D is a uniaxial anisotropy strength. Our general treatment permits D to span all values, which allows one to consider both "easy-axis" and "hard-axis" anisotropies. The

physical origin of the magnetic anisotropy, also called "zero-field splitting", is dependent on the manifestation of the $S_{2,3}$ particles. For example, if the two spin particles refer to magnetic molecules, the primary source of magnetic anisotropy could be from geometric distortions (Jahn-Teller distortions) of constituent ions [32]. In the ultra-cold optical lattice context, an effective magnetic anisotropy is created by direct on-site interactions between atoms in two states [30].

While we consider the spin interactions of three particles in this work, one can in principle pursue a more realistic treatment of the three-particle problem by incorporating the spatial degrees of freedom. If one were to extend our model spatially, the movement of the particles will impact the time-dependent dynamics of the system non-trivially. The purpose of this work, however, is to elucidate the spin dynamics of the three-particle model, which may serve as a necessary, but not sufficient, picture to realize useful control of the system's spin states. We balance these considerations by accommodating for Hamiltonian terms that may not play a key role in spin dynamics, but ultimately may be pivotal in more realistic contexts. In this light, we follow in the footsteps of other models (such as the Hubbard model), and include a term that describes the movement of the S_1 particle hopping from the S_2 particle to S_3 and vice versa. In spin space, this hopping term takes the form,

$$\mathcal{H}_{\mathrm{t}} = \sum_{\mu} \left\{ t\hat{d}^{\dagger}_{\mu,2}\hat{d}_{\mu,3} + h.c. \right\}, \tag{2.5}$$

where μ is the spin index for particle 1, and t is the hopping strength.

Incorporating each of the aforementioned Hamiltonian terms, we provide a representative example of Fig. 2.1. One could imagine a scenario of a magnetic molecule dimer (e.g., coupled Tb^{III} ions in a molecular complex) placed on a weakly interacting substrate next to a quantum dot. Exchange interactions could then be achieved by appropriate gating. The dynamics of the system, which may involve entangled particle scenarios, is described by the

density operator ρ in the Schrödinger picture,

$$i\frac{\partial \rho}{\partial t} = [\mathcal{H}, \rho]\,, \tag{2.6}$$

where the brackets denote the commutator.

There are various basis sets that uncover different aspects of the dynamics of the three-spin system. One convenient representation of the Hamiltonian and density operator can be built from the basis $|s, m_s\rangle$, where $\mathbf{S} = \mathbf{S}_1 + \mathbf{S}_2 + \mathbf{S}_3$. Because we also need to examine the possible entangled states of the $S_{2,3}$ particles in anticipation of correlating states within a qubit representation, we designate a "device" basis with states $|s_1, m_1\rangle\,|s_{23}, m_{23}\rangle$. In this representation, the $|s_{23}, m_{23}\rangle$ states are designated the "coupled particle" basis states.

2.2 Results

We first consider the $S_{2,3} = 1$ model and the impact of each term within the total Hamiltonian of Eq. (2.1) on the states of the system. We find that the hopping term given in Eq. (2.5) is diagonal in the spin space, and can therefore be ignored for purposes of examining the spin dynamics of the system. We remove the hopping term in what follows, though one may not be able to ignore it when considering a spatial extension of the considered model. Next, when the exchange Hamiltonians involving S_1 are applied anisotropically (i.e., $J_{12} \neq J_{13}$), the Hamiltonian connects states between different s_{23} subspaces in the device representation and can no longer be block-diagonalized by the s_{23} subspaces. Instead, the effective exchange Hamiltonian can be block diagonalized by m values, where $\mathcal{H}_m$ is the block Hamiltonian corresponding to m, and $\mathcal{H}_{\pm 5/2}$ are diagonal. In the $\mathcal{H}_{\pm 3/2}$ subspaces, the $|m_1\rangle\,|s_{23}, m_{23}\rangle = \left|\pm\frac{1}{2}\right\rangle|2, \pm 1\rangle$, $\left|\pm\frac{1}{2}\right\rangle|1, \pm 1\rangle$, and $\left|\mp\frac{1}{2}\right\rangle|2, \pm 2\rangle$ states participate, forming three-dimensional subspaces. Similarly, the $\mathcal{H}_{\pm 1/2}$ subspaces contain the interactions of the $\left|\pm\frac{1}{2}\right\rangle|2, 0\rangle$, $\left|\pm\frac{1}{2}\right\rangle|1, 0\rangle$, $\left|\pm\frac{1}{2}\right\rangle|0, 0\rangle$, $\left|\mp\frac{1}{2}\right\rangle|2, \pm 1\rangle$, and $\left|\mp\frac{1}{2}\right\rangle|1, \pm 1\rangle$ states, making the

subspaces five dimensional. These forms of the effective exchange Hamiltonian will play a pivotal role in transitions between states with the same m value.

In the $S_{2,3} = 1$ model, resonant transitions between states are found in several of the m subspaces. By inspecting the $m = \frac{3}{2}$ subspace, which corresponds with the dynamics of the $|m_1\rangle |s_{23}, m_{23}\rangle = \{|\uparrow\rangle |2,1\rangle, |\uparrow\rangle |1,1\rangle, |\downarrow\rangle |2,2\rangle\}$ states, the block Hamiltonian takes the form (a common $t + t^* + J_{xy} + D + \frac{1}{4}\Sigma_1$ is removed from the diagonal),

$$\mathcal{H}_{3/2} = \frac{1}{4}\begin{pmatrix} 0 & \Delta_1 & 2\Sigma_1 \\ \Delta_1 & -8J_{xy} & -2\Delta_1 \\ 2\Sigma_1 & -2\Delta_1 & -3\Sigma_1 + 4D + 4\Delta_{23} \end{pmatrix}, \tag{2.7}$$

where the notation $\Delta_1 \equiv J_{12} - J_{13}$, $\Sigma_1 \equiv J_{12} + J_{13} \equiv 2J_1$, and $\Delta_{23} \equiv J_z - J_{xy}$ has been introduced. When the application of the S_1 exchange coupling is isotropic by choosing $J_{12} = J_{13} = J_1$ and $\Delta_1 = 0$, the $|\uparrow\rangle |1,1\rangle$ state is no longer coupled to the other states within this block. Under these conditions, the total Hamiltonian takes the form,

$$\begin{aligned} \mathcal{H}_{eff} = {} & J_z \hat{S}_2^z \hat{S}_3^z + J_{xy}\left(\hat{S}_2^x \hat{S}_3^x + \hat{S}_2^y \hat{S}_3^y\right) \\ & + J_1\left(\hat{\mathbf{S}}_1 \cdot \hat{\mathbf{S}}_2 + \hat{\mathbf{S}}_1 \cdot \hat{\mathbf{S}}_3\right) + D\left(\hat{S}_2^z \hat{S}_2^z + \hat{S}_3^z \hat{S}_3^z\right). \end{aligned} \tag{2.8}$$

Inspecting the $m = 3/2$ subspace again, the effective Hamiltonian block becomes,

$$-\frac{1}{2}\left(D - \frac{3}{2}J_1 + \Delta_{23}\right)\begin{pmatrix} 1 & 0 \\ 0 & -1 \end{pmatrix} + J_1\begin{pmatrix} 0 & 1 \\ 1 & 0 \end{pmatrix}. \tag{2.9}$$

For comparison, the same procedure is repeated for the $m = 1/2$ subspace, where the effective

Hamiltonian corresponding with the $|\uparrow\rangle|1,0\rangle$ and $|\downarrow\rangle|1,1\rangle$ basis takes the form,

$$\frac{1}{2}\left(D+\frac{1}{2}J_1-\Delta_{23}\right)\begin{pmatrix}1 & 0\\ 0 & -1\end{pmatrix}+\frac{1}{\sqrt{2}}J_1\begin{pmatrix}0 & 1\\ 1 & 0\end{pmatrix}. \tag{2.10}$$

If one prepares the initial density matrix of the system to represent a pure $|\downarrow\rangle|2,2\rangle$ state (e.g., by utilizing a setup similar to Ref. [6, 7] to prepare a particular spin state), an application of the Rabi formula results in the probability of measuring the $|\uparrow\rangle|2,1\rangle$ state as,

$$P_{|\uparrow\rangle|2,+1\rangle}(t)=\left(\frac{J_1}{\Omega}\right)^2\sin^2(\Omega t), \tag{2.11}$$

with Rabi frequency,

$$\Omega=\sqrt{J_1^2+\frac{1}{4}\left(D-\frac{3}{2}J_1+\Delta_{23}\right)^2}. \tag{2.12}$$

Transforming between the considered device basis states and their site-basis representation ($|m_1\rangle|s_{23},m_{23}\rangle\rightarrow|m_1\rangle|m_2\rangle|m_3\rangle$),

$$|\downarrow\rangle|2,2\rangle=|\downarrow\rangle|1\rangle|1\rangle, \tag{2.13}$$

$$|\uparrow\rangle|2,1\rangle=\frac{1}{\sqrt{2}}\left(|\uparrow\rangle|0\rangle|1\rangle+|\uparrow\rangle|1\rangle|0\rangle\right), \tag{2.14}$$

one can see that the $|\downarrow\rangle|2,2\rangle$ state corresponds with a non-entangled coupled particle state, and the $|\uparrow\rangle|2,1\rangle$ corresponds with a maximally entangled coupled particle state. A single measurement of particle 1's spin orientation determines the entanglement state of particle 2 and 3. This demonstrates the read out of the entanglement state if the measurement of the S_1 spin polarization is taken at any general time t. This also demonstrates preparation of the entanglement state if the S_1 spin polarization is measured at a specific time t corresponding

Table 2.1: Pure state transitions for the $S_{2,3} = 1$ model, where J_{R} is the condition on J_1 to reach resonance, P_R is the maximum transition probability amplitude at resonance, and Ω_R is the Rabi frequency at resonance.

State Transitions	J_{R}	P_{R}	Ω_{R}
$\|\uparrow\rangle \|2,+1\rangle$, $\|\downarrow\rangle \|2,+2\rangle$	$\frac{2}{3}(D + \Delta_{23})$	1	$\frac{2}{3}\|D + \Delta_{23}\|$
$\|\uparrow\rangle \|2,-2\rangle$, $\|\downarrow\rangle \|2,-1\rangle$	$\frac{2}{3}(D + \Delta_{23})$	1	$\frac{2}{3}\|D + \Delta_{23}\|$
$\|\uparrow\rangle \|1,0\rangle$, $\|\downarrow\rangle \|1,+1\rangle$	$-2(D - \Delta_{23})$	1	$\sqrt{2}\|D - \Delta_{23}\|$
$\|\uparrow\rangle \|1,-1\rangle$, $\|\downarrow\rangle \|1,0\rangle$	$-2(D - \Delta_{23})$	1	$\sqrt{2}\|D - \Delta_{23}\|$

with a peak in the Rabi oscillation.

As shown in Eq. (2.9) and Eq. (2.10), the magnetic anisotropy D, average exchange interaction strength J_1, and the anisotropy of the $S_2 - S_3$ exchange interaction Δ_{23} determine the Rabi frequency and transition amplitudes of the system. When the Rabi frequencies and amplitudes are calculated for the other possible two state systems in the $S_{2,3} = 1$ model, we see that particular conditions on the magnitude and sign of J_1, Δ_{23}, and D result in resonant transition probabilities, i.e., each state's transition probability oscillates with a maximum amplitude of 1. Table 2.1 lists these possible magnetic anisotropy and exchange strength resonance conditions, i.e., DJ resonances, for two-state switching. To see the physical consequence of these DJ resonances, we turn to a representation of the states involved in a transition, where one can project the two-state systems onto a Bloch sphere. For the $m = 3/2$ case, Eq. (2.9) is written suggestively to highlight the effect of the unitary operator $U(t) = e^{-i\mathcal{H}t}$ on the Bloch vector $\mathbf{V}$ prepared as $(|\mathbf{V}|, \theta, \phi) = (1, 0, 0)$. In the case of Eq. (2.9), the Bloch vector's poles are defined by the $|\downarrow\rangle |2,2\rangle$ and $|\uparrow\rangle |2,1\rangle$ states. The first term in Eq. (2.9) corresponds with a rotation (up to a global phase) of the Bloch vector about the z-axis with a frequency $D - \frac{3}{2}J_1 + \Delta_{23}$ and the second with a rotation about the x-axis with a frequency of $2J_1$.

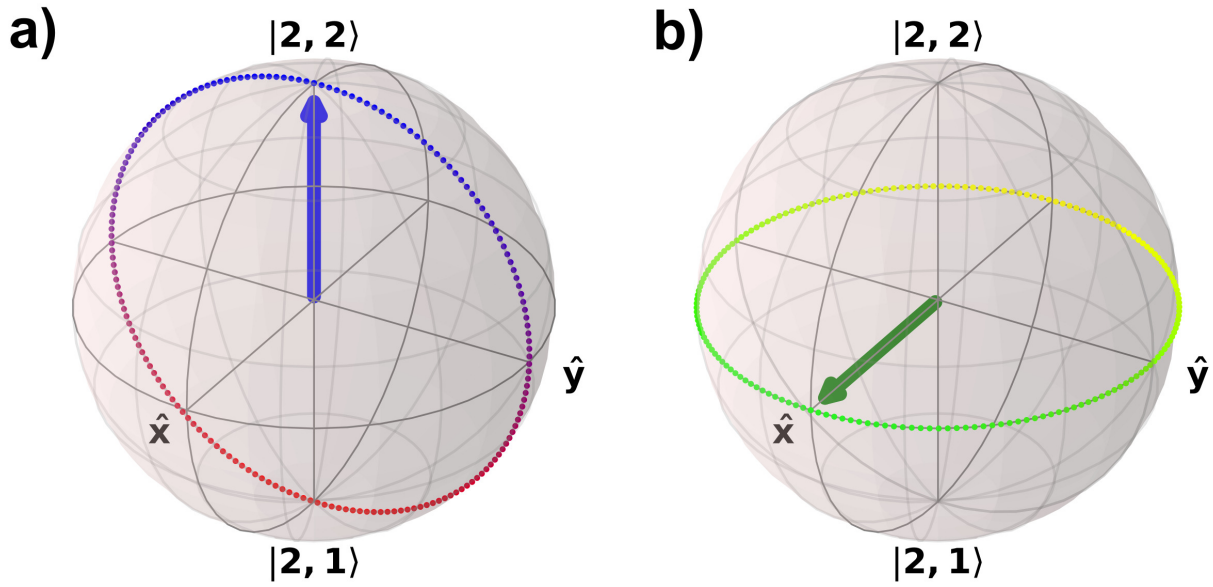

Figure 2.2: Bloch sphere representation of the states within the $|\downarrow\rangle |2,2\rangle, |\uparrow\rangle |2,1\rangle$, $m = \frac{3}{2}$ subspace when $J_{12} = J_{13} = J_1$. (a) When J_1 is tuned to a DJ resonance, rotation about the x-axis is realized. (b) When $J_1 = 0$, $(D + \Delta_{23})$-modulated rotation about the z-axis is possible.

As shown in Fig. 2.2, at the DJ resonance condition of $J_1 = \frac{2}{3}D + \Delta_{23}$, the z-axis rotation vector is 0, and the Bloch vector is rotated solely about the x-axis. In this way, with appropriate pulsing of the DJ resonance condition, control of the Bloch vector in the $x = 0$ plane is realized. Physically, the magnitude of the exchange couplings and magnetic anisotropy determine the contribution of the device states that are energetically favorable for that parameter. At the DJ resonance, these state contributions are equally balanced. In other words, there is equal probability to collapse the device state upon measurement to one that favors the S_1 exchange coupling or to one that favors some sort of anisotropy (magnetic or between S_2 and S_3).

Similarly, by turning off the exchange coupling between S_1 and the two $S_{2,3}$ particles, the x-axis rotation is suppressed, leading to rotation solely about the z-axis with frequency

$D + \Delta_{23}$. Combinations of these rotations, accomplished by appropriate tuning of J_1, can realize any point on the Bloch sphere. By turning off these interactions, or utilizing another type of anisotropy (e.g., if one can control Δ_{23}), the dynamics can be stopped after a desired rotation operation after a given time t. Any relevant operation in the qubit representation on the Bloch sphere, and by extension any equivalent SU(2) operation, can be accomplished by utilizing the DJ resonance.

Next, we find that when small values of anisotropy of the exchange coupling are included, the numerical calculation of the Bloch vector's projection on the x-axis oscillates, resulting in a correspondingly small deviation in its z-axis projection. This originates from the inclusion of additional off-diagonal states (e.g., see Eq. (2.7)) that correspond with one of the azimuthal axes in the Bloch sphere. Moreover, these additional states include contributions of the exchange interaction between particle 2 and 3, so that five parameters now control the rotation of the Bloch vector. Despite these contributions, we find that for certain parameters, the projection of the Bloch vector onto the z-axis (which directly corresponds with the switching behavior as measured by the electron) results in a maximal transition probability above $P = 0.995$ even when using significant ratios of anisotropy in the application of the exchange coupling, in our case $\Delta_1/J_1 = 0.072$, as shown in Fig. 2.3. When the anisotropic application of the exchange coupling is larger than the $\Delta_1/J_1 = 0.072$ ratio for the set of parameters considered, the projection onto the Bloch sphere's z-axis is more distorted, as additional rotations about axes lying in the azimuthal plane are included.

We also do not find a simple relationship between the distortions and the strength of J_{23}. For example, using the same parameters as Fig. 2.3 and setting $J_{23} = 0.60$ cm^{-1}, we find that the maximal transition probability remains above $P = 0.995$. When $J_{23} = -0.20$ cm^{-1}, the maximal transition probability falls below $P = 0.995$, but again rises above $P = 0.995$ when $J_{23} = -0.40$ cm^{-1}. The Δ_{23} parameter, on the other hand, provides a target from which to maintain fidelity. Inspection of the DJ resonance conditions indicate that modulating J_1 to

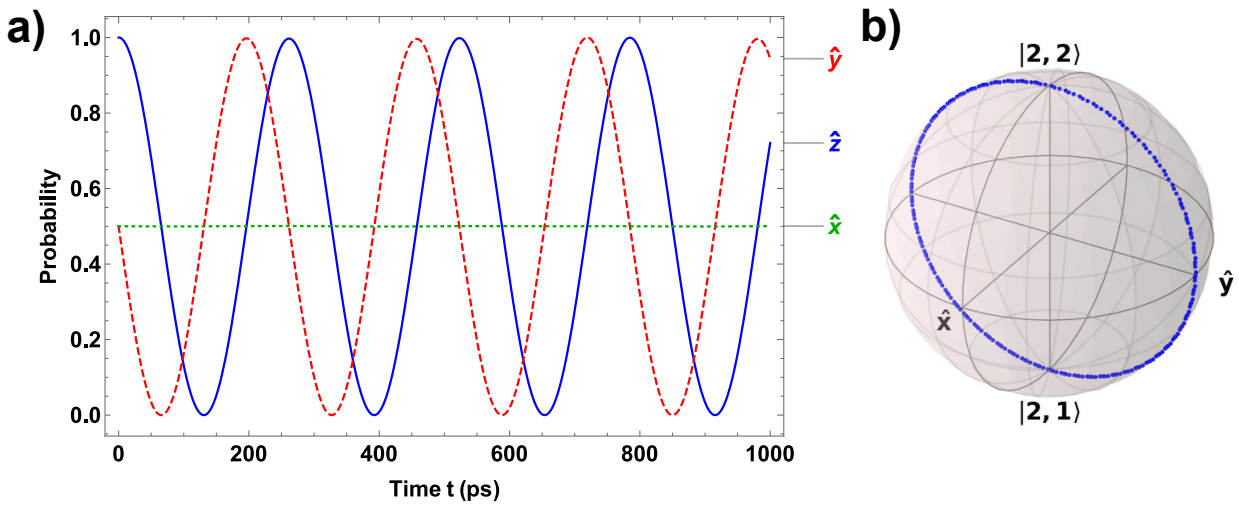

Figure 2.3: (a) Probability of measuring a state corresponding with the $\hat{x}$ (dotted), $\hat{y}$ (dashed), and $\hat{z}$ (solid) unit vectors on the Bloch sphere defined in Fig. 2.2, as a function of time. The Bloch vector is initially prepared in the state $|\downarrow\rangle\,|2,2\rangle$, and an anisotropic application of the exchange coupling strength has been used ($\Delta_1/J_1 = 0.072$). The parameter set has been prepared around the DJ resonance. (b) The corresponding Bloch sphere representation of the path traced by the Bloch vector over the same time interval considered. In units of cm^{-1}, the parameters are: $J_{23} = -0.05$, $J_1 = -0.40$, $D = -0.60$, $t = 0.05$.

account for Δ_{23} allows one to reach resonance. By looking at the variables that participate in the dynamics in each block of the Hamiltonian (e.g., Eq. (2.7), we find that these distortions of the Rabi-like oscillations are enhanced by larger values of J_{xy} and Δ_1, and thus the relative magnitudes of the five parameters (Σ_1, Δ_1, J_{xy}, Δ_{23}, and D) dictate the limit of robustness of a particular resonance scenario.

The behavior of the $S_{2,3} = 1$ model is not possible for $S_{2,3} = \frac{1}{2}$ without additional spin selection methods. Repeating the same type of procedure and analysis for the $S_{2,3} = \frac{1}{2}$ model, and noting that magnetic anisotropy is not expected for $S = \frac{1}{2}$ particles, we find that the maximum probability amplitude is 8/9 for both transition types. When the two states involved in a transition are mapped onto a Bloch sphere, the effect of the unitary operator as a rotation is not about an axis solely on the azimuthal plane, but instead contains a

component in the polar plane.

2.3 Discussion

Fig. 2.3 forms the primary consequence of the main result of this work, namely that resonance conditions exist in the $S_{2,3} = 1$ model in which preparation and measurement of the coupled particles' degree of entanglement can be accomplished by appropriate measurement of the $S_1 = \frac{1}{2}$ particle. Furthermore, realization of these DJ resonances is robust against anisotropy of the exchange coupling between the coupled particles. This is found to not be the case for the $S_{2,3} = \frac{1}{2}$ model. In particular, as shown in Table 2.1, the DJ resonance conditions for maximal transitions between non-entangled and entangled states is controlled by the non-trivial interaction of the exchange coupling, J_{12} and J_{13}, between particle 1 and 2/3, the anisotropic exchange coupling interaction Δ_{23}, and the magnetic anisotropy D of particle 2 and 3 in the $S_{2,3} = 1$ paradigm.

The DJ resonance conditions indicate a possible avenue for investigating complex spin spaces and the conditions required to simplify complicated spin Hamiltonians, such as those that represent the interactions of magnetic monomers or dimers with an electron, or when applied to three-particle Bose-Hubbard-like spin models such as in ultra-cold optical lattices. It is interesting to note that because our model has not required particular physical mechanisms for the exchange coupling and magnetic anisotropy, it is possible that outside of condensed matter physics, the block diagonalization of similar $\mathbb{C}^{18}$ state systems could result in isolated SO(2) representation subgroups. The DJ resonance feature introduces a different level of control in Bloch vector rotation operations. The inclusion of the $S_1 = \frac{1}{2}$ particle allows for preparation, manipulation, and reading of the entangled coupled particles.

In quantum dot QIS systems, states are often prepared with applied magnetic fields. Electrically-controlled methods, however, are attractive because of the relative ease of ma-

nipulating electric fields within a variety of environmental conditions. The results of our model predict that single-electron control of entangled particles without any use of applied magnetic fields is possible. Furthermore, an important conclusion to be drawn from Fig. 2.3 is that the Bloch vector, in time, is forgiving against misalignment, so that this scheme does not actually require impossible experimental perfection to work.

Last, we note that if the resonances are used for QIS applications, several additional factors must be incorporated that have not been considered in this paper. As an illustrative example, the parameters chosen in Fig. 2.3 are inspired by a scenario involving $[Mn_3]_2$ [33]. The $[Mn_3]_2$ dimer, however, has higher spin, and thus a formula to determine the resonance conditions for higher $S_{2,3}$ is desired. For general QIS scenarios, the order of parameters used in Fig. 2.3 imply that several oscillations have completed within 1 ns. This time is smaller than relevant spin-lattice and spin-spin relaxation times in most novel molecular magnets and quantum dots. Tuning the magnitudes of the D, Δ_{23}, and J_1 parameters can lead to faster oscillations. In this way, one can identify the T_1 and T_2 times for a particular system, and tailor the search of DJ resonance conditions based on those parameters.

Determining a more complete picture of a transient S_1 particle requires the incorporation of additional degrees of freedom not considered here, such as the S_1 particle's source and drain. We note, however, that while the source of the S_1 particle has not been explicitly identified, some generalizations of the source (e.g., to a conduction band of a metal) will not substantially change the overall model or results. On the other hand, if the S_1 particle is not transient, but instead is confined on a surface or within bulk material, additional exchange coupling interactions between the particle and the confinement source may need to be accounted for. Regardless of the physical mechanism chosen to realize this model, the use of these DJ resonances provides an exciting avenue to uncover interesting highly-correlated spin phenomena.

2.4 List of References

[1] M. A. Nielsen and I. L. Chuang, *Quantum Computation and Quantum Information: 10th Anniversary Edition* (Cambridge University Press, Cambridge, 2010).

[2] D. Loss and D. P. DiVincenzo, Physical Review A **57**, 120 (1998).

[3] J. R. Petta, A. C. Johnson, J. M. Taylor, E. A. Laird, A. Yacoby, M. D. Lukin, C. M. Marcus, M. P. Hanson, and A. C. Gossard, Science **309**, 2180 (2005).

[4] R. Hanson, L. P. Kouwenhoven, J. R. Petta, S. Tarucha, and L. M. K. Vandersypen, Reviews of Modern Physics **79**, 1217 (2007).

[5] A. Noiri, J. Yoneda, T. Nakajima, T. Otsuka, M. R. Delbecq, K. Takeda, S. Amaha, G. Allison, A. Ludwig, A. D. Wieck, and S. Tarucha, Applied Physics Letters **108**, 153101 (2016).

[6] A. Noiri, T. Nakajima, J. Yoneda, M. R. Delbecq, P. Stano, T. Otsuka, K. Takeda, S. Amaha, G. Allison, K. Kawasaki, Y. Kojima, A. Ludwig, A. D. Wieck, D. Loss, and S. Tarucha, Nature Communications **9**, 5066 (2018).

[7] T. Nakajima, A. Noiri, J. Yoneda, M. R. Delbecq, P. Stano, T. Otsuka, K. Takeda, S. Amaha, G. Allison, K. Kawasaki, A. Ludwig, A. D. Wieck, D. Loss, and S. Tarucha, Nature Nanotechnology **14**, 555 (2019).

[8] C. H. Yang, R. C. C. Leon, J. C. C. Hwang, A. Saraiva, T. Tanttu, W. Huang, J. Camirand Lemyre, K. W. Chan, K. Y. Tan, F. E. Hudson, K. M. Itoh, A. Morello, M. Pioro-Ladrière, A. Laucht, and A. S. Dzurak, Nature **580**, 350 (2020).

[9] R. C. C. Leon, C. H. Yang, J. C. C. Hwang, J. C. Lemyre, T. Tanttu, W. Huang, K. W.

Chan, K. Y. Tan, F. E. Hudson, K. M. Itoh, A. Morello, A. Laucht, M. Pioro-Ladrière, A. Saraiva, and A. S. Dzurak, Nature Communications **11**, 797 (2020).

[10] M. N. Leuenberger and D. Loss, Nature **410**, 789 (2001).

[11] L. M. K. Vandersypen, M. Steffen, G. Breyta, C. S. Yannoni, M. H. Sherwood, and I. L. Chuang, Nature **414**, 883 (2001).

[12] R. Vincent, S. Klyatskaya, M. Ruben, W. Wernsdorfer, and F. Balestro, Nature **488**, 357 (2012).

[13] M. Ganzhorn, S. Klyatskaya, M. Ruben, and W. Wernsdorfer, Nature Nanotechnology **8**, 165 (2013).

[14] M. Urdampilleta, S. Klyatskaya, M. Ruben, and W. Wernsdorfer, Physical Review B **87**, 195412 (2013).

[15] S. Thiele, F. Balestro, R. Ballou, S. Klyatskaya, M. Ruben, and W. Wernsdorfer, Science **344**, 1135 (2014).

[16] K. S. Pedersen, A.-M. Ariciu, S. McAdams, H. Weihe, J. Bendix, F. Tuna, and S. Piligkos, Journal of the American Chemical Society **138**, 5801 (2016).

[17] K. Najafi, A. L. Wysocki, K. Park, S. E. Economou, and E. Barnes, The Journal of Physical Chemistry Letters **10**, 7347 (2019).

[18] L. Bogani and W. Wernsdorfer, Nature Materials **7**, 179 (2008).

[19] S. M. Cronenwett, T. H. Oosterkamp, and L. P. Kouwenhoven, Science **281**, 540 (1998).

[20] M. N. Leuenberger and E. R. Mucciolo, Physical Review Letters **97**, 126601 (2006).

[21] G. González, M. N. Leuenberger, and E. R. Mucciolo, Physical Review B **78**, 054445 (2008).

[22] J. Kondo, Progress of Theoretical Physics **32**, 37 (1964).

[23] P. W. Anderson, Physical Review **124**, 41 (1961).

[24] R. Žitko, R. Peters, and T. Pruschke, Physical Review B **78**, 224404 (2008).

[25] S. Mehl and D. P. DiVincenzo, Physical Review B **92**, 115448 (2015).

[26] A. T. Costa, S. Bose, and Y. Omar, Physical Review Letters **96**, 230501 (2006).

[27] F. Ciccarello, G. M. Palma, M. Zarcone, Y. Omar, and V. R. Vieira, New Journal of Physics **8**, 214 (2006).

[28] F. Ciccarello, G. Massimo Palma, M. Paternostro, M. Zarcone, and Y. Omar, Solid State Sciences **11**, 931 (2009).

[29] R. Hiraoka, E. Minamitani, R. Arafune, N. Tsukahara, S. Watanabe, M. Kawai, and N. Takagi, Nature Communications **8**, 16012 (2017).

[30] W. C. Chung, J. de Hond, J. Xiang, E. Cruz-Colón, and W. Ketterle, Physical Review Letters **126**, 163203 (2021).

[31] S. Hill, R. S. Edwards, N. Aliaga-Alcalde, and G. Christou, Science **302**, 1015 (2003).

[32] D. Gatteschi and R. Sessoli, Angewandte Chemie International Edition **42**, 268 (2003).

[33] J.-X. Yu, G. Christou, and H.-P. Cheng, The Journal of Physical Chemistry C **124**, 14768 (2020).

CHAPTER 3: ELECTRONIC CONTROL AND SWITCHING OF ENTANGLED SPIN STATE USING ANISOTROPY AND EXCHANGE IN THE THREE-PARTICLE PARADIGM

(Adapted from Eric D. Switzer, Xiao-Guang Zhang, and Talat S. Rahman, "Electronic control and switching of entangled spin state using anisotropy and exchange in the three-particle paradigm." J. Phys. Commun. 6, 075007 (2022))

3.1 Introduction

The ability to generate and stabilize entanglement within qubits is a prerequisite for usable quantum information devices. Spin qubits, which are the coherent superposition of spin states within quantum objects, make use of entangled spin states for quantum gate operations [1]. This general class of qubits has had much success and is seen as a promising candidate for scalable quantum information science (QIS) technologies [2]. Some applications, like those utilizing confined electrons in quantum dots fabricated in semiconductors, use manipulation of electrostatic gates, electric dipole spin resonance, and applied magnetic fields to generate, stabilize, and manipulate the entangled states [3–10].

Some of these preparation methods have also been applied to QIS approaches that utilize molecular magnets [11–18]. Molecular magnets, such as $TbPc_2$ [15] and Mn_{12} [19], are complex molecules that possess an onsite magnetic anisotropy because of their larger magnetic moments that distinguishes them from the $S = \frac{1}{2}$ Ising spins. The long coherence times, the ability to tunnel between spin states enabled by their magnetic anisotropy, and tailorable ligands [20] make molecular magnets desirable candidates for QIS systems.

In several QIS approaches, exchange coupling plays a key role [21–23], including the use of the Kondo effect [24] in the switching of entanglement states [25]. Considering

magnetic anisotropy in molecular molecules, it is important to incorporate both exchange coupling and magnetic anisotropy within models to predict and realize spin entanglement scenarios. For example, the study of an electron scattering off of two magnetic impurities under a contact exchange interaction found coherent transmission scenarios based on the entangled state of the impurities [26–28]. The study of the interplay of exchange coupling and magnetic anisotropy goes beyond QIS, and has applications in systems which contain both of these dynamical interactions, as in ultra-cold optical lattices [29]. While the study of these two effects has been explored for two particles [30], the community's drive to realize scalable QIS devices may require the investigation of multi-particle models similar to those explored in Ref. [31]. Work that incorporates multiple sites/particles, exchange coupling, and magnetic anisotropy is ongoing [32, 33].

In this work, we further investigate a general model introduced in Ref. [33] that incorporates the interplay of exchange coupling with magnetic anisotropy for three stationary spin particles. In the interest of maintaining wide applicability to contexts outside QIS, we consider a general model in which two of the spin particles can possess any spin magnitude. Similar to the concepts used in quantum dot technologies and ultra-cold optical lattices, we neglect the kinetic components of the physical system, and concentrate solely on the spin degree of freedom.

As we will show, we find the interactions of the exchange coupling and magnetic anisotropy terms leads to a set of conditions that correspond with perfect (lossless) switching between non-entangled and entangled states, named as "DJ resonances," for any spin $S_{2,3} > \frac{1}{2}$. These resonances allow for full control of appropriately chosen Bloch vectors. We contrast these resonances for two applications of the general model: one in which all three particles possess a spin $S_{1,2,3} = \frac{1}{2}$, and another in which two of the particles possess a spin $S_{2,3} = 1$. We also demonstrate that control of the entanglement state can be accomplished by appropriate spin filtering of the S_1 particle for any spin $S_{2,3}$.

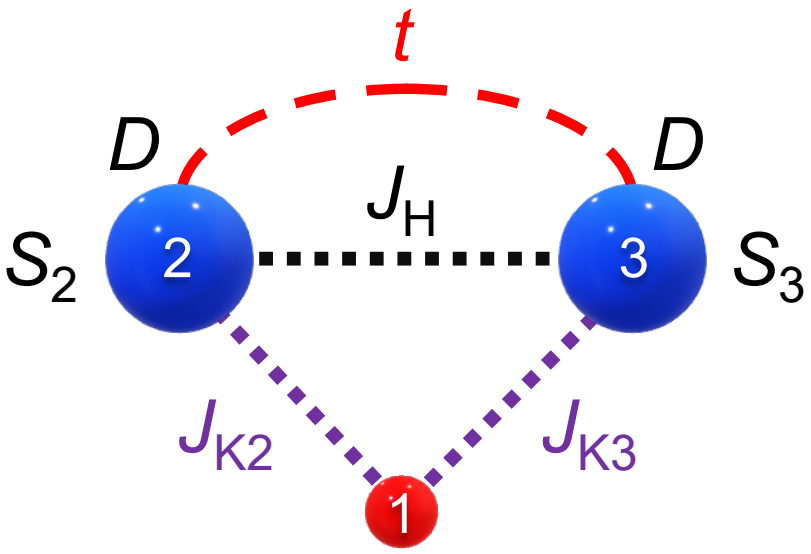

Figure 3.1: Schematic of the three particle spin model. Particle 2 and 3 are coupled via an exchange interaction J_{H}, and possess magnetic anisotropy D. Each couple with particle 1 with an exchange interaction J_{K2} and J_{K3}, respectively. Particle 1 may hop between particle 2 and 3 with hopping strength t.

3.2 Theoretical Method

As shown in the schematic in Fig. 3.1, we consider four interactions: the similar uniaxial magnetic anisotropy possessed by particle 2 and 3, the Heisenberg-like exchange interaction between particle 2 and 3, a Kondo-like interaction between particle 1 and 2 and particle 1 and 3, and a hopping term which describes the movement of particle 1 between particle 2 and 3. We also allow the parameters of the system to generically encompass all available regimes. This is achieved by both allowing the exchange interaction and magnetic anisotropy parameters to take on all values. In other words, the exchange interactions are allowed to be ferromagnetic ($J < 0$) or antiferromagnetic ($J > 0$), and both hard ($D > 0$) or easy ($D < 0$) magnetic anisotropy axes are permitted.

3.2.1 Model Hamiltonian

The total Hamiltonian is,

$$\mathcal{H} = \mathcal{H}_{\mathrm{H}} + \mathcal{H}_{\mathrm{K}} + \mathcal{H}_{\mathrm{A}} + \mathcal{H}_{\mathrm{t}}, \tag{3.1}$$

where $\mathcal{H}_{\mathrm{H}}$ is the Heisenberg-like Hamiltonian, $\mathcal{H}_{\mathrm{K}}$ is the Kondo-like Hamiltonian, $\mathcal{H}_{\mathrm{A}}$ is the magnetic anisotropy Hamiltonian, and $\mathcal{H}_{\mathrm{T}}$ is the hopping Hamiltonian. From this point forward, $\hbar = 1$. The Heisenberg-like interaction takes the form,

$$\mathcal{H}_{\mathrm{H}} = J_z \hat{S}_2^z \hat{S}_3^z + J_{xy} \left(\hat{S}_2^x \hat{S}_3^x + \hat{S}_2^y \hat{S}_3^y \right), \tag{3.2}$$

where $\hat{\mathbf{S}}_i = (\hat{S}_i^x, \hat{S}_i^y, \hat{S}_i^z)$ is the spin operator for the ith particle, J_z is the strength of the exchange interaction between particle 2 and 3 parallel to the direction of the magnetic anisotropy axis, and J_{xy} is the strength of the exchange interaction between particle 2 and 3 perpendicular to the direction of the magnetic anisotropy axis. This exchange term is similar to those used to describe the exchange interaction between two coupled dimers with a Heisenberg XXY model [34]. When this interaction is taken to be isotropic, i.e. $J_z = J_{xy} \equiv J_{\mathrm{H}}$, this equation simplifies to $\mathcal{H}_{\mathrm{H}} = J_{\mathrm{H}} \hat{\mathbf{S}}_2 \cdot \hat{\mathbf{S}}_3$. The exchange interaction of the S_1 particle with the $S_{2,3}$ particles is closely related to the spin portion of the Kondo interaction, and may be represented by,

$$\mathcal{H}_{\mathrm{K}} = \frac{1}{2} \sum_{\mu,\mu',i=2,3} J_{\mathrm{Ki}} \hat{\mathbf{S}}_i \cdot \hat{d}_{\mu,i}^{\dagger} \hat{\boldsymbol{\sigma}}_{\mu,\mu'} \hat{d}_{\mu',i}, \tag{3.3}$$

where μ is a spin index for particle 1, $\boldsymbol{\sigma}_{\mu,\mu'}$ is the corresponding μ, μ' matrix element of the $s = \frac{1}{2}$ Pauli matrix, and $\hat{d}_{\mu,k}^{\dagger}/\hat{d}_{\mu,i}$ represents (in second quantization language) the creation/annihilation operator of a state in which particle 1 is bound to particle i.

The magnetic anisotropy term is given as,

$$\mathcal{H}_{\mathrm{A}} = D\left(\hat{S}_2^z\hat{S}_2^z + \hat{S}_3^z\hat{S}_3^z\right), \tag{3.4}$$

where D is a uniaxial anisotropy strength. This Hamiltonian term is derived differently depending on the context of the spin particle type. For example, if the two spin particles refer to magnetic molecules, magnetic anisotropy is explained by geometric distortions of constituent ions [19]. Conversely, in ultra-cold optical lattices, an effective magnetic anisotropy is created by direct on-site interactions between atoms in two states [29]. We note that the magnetic anisotropy Hamiltonian term is only meaningful for $S_{2,3} > \frac{1}{2}$.

Last, the hopping Hamiltonian is described by,

$$\mathcal{H}_{\mathrm{t}} = \sum_{\mu}\left\{t\hat{d}_{\mu,2}^{\dagger}\hat{d}_{\mu,3} + h.c.\right\}, \tag{3.5}$$

where μ is the spin index for particle 1. This term describes kinetic motion of the S_1 particle between S_2 and S_3 and vice versa. As will be shown later, the hopping term does not play a significant role in the spin dynamics of the system. This, however, does not mean that the hopping term serves no role. We show later that the spin dynamics form a necessary condition in measuring the entanglement state of the coupled particles, but this condition is not a sufficient one. To realize the results of this work in an experimental setup, one should also include the spatial degrees of freedom of the spin particles. For example, we give a derivation of this term as an extension of the two-site Anderson impurity model in Appendix A, in which the momentum components of this term will certainly contribute to the overall dynamics of that system. While not vital for those systems that do not fit the impurity model, we conclude that it is important to keep the hopping term due to the possible role that the S_1 particle will play as a transient carrier of information of the coupled

particles' entanglement state. Because of the diagonal nature of the term when projected onto spin space, one may remove the term if it is not needed.

3.2.2 Dynamics and Choice of Basis

To examine the dynamics of the system, we use the language of density operators to analytically and numerically solve the Liouville-von Neumann equation (the density operator equivalent of the time-dependent Schrödinger equation),

$$i\frac{\partial \rho}{\partial t} = [\mathcal{H}, \rho]\,, \tag{3.6}$$

where ρ is the density operator in the Schrödinger picture, and the brackets denote the commutator. In general, the solution for Eq. (3.6) is,

$$\rho(t) = U(t)\rho(0)U^{\dagger}(t), \tag{3.7}$$

where $U(t)$ is the unitary time evolution operator,

$$U(t) = \mathcal{T}\left[\exp\left(-i\int_0^t \mathcal{H}(\tau)\,\mathrm{d}\tau\right)\right], \tag{3.8}$$

and $\mathcal{T}$ is the time-ordered operator. For the familiar case in which the Hamiltonian is time-independent, like in all of our applications to our model considered in this paper, the unitary time evolution operator simplifies to,

$$U(t) = e^{-i\mathcal{H}t}. \tag{3.9}$$

Thus, in principle, the time-dependent behavior of our model's density matrix can be solved exactly.

It is important to consider specific choices of three-particle basis sets to uncover the spin dynamics of our model. The natural choice are states that are aligned to the action of the $\hat{S}^z = \hat{S}^z_1 \otimes \hat{S}^z_2 \otimes \hat{S}^z_3$ operator, i.e., the Hamiltonian and density operator are represented in the product basis $|s, m_s\rangle = |s_1, m_{s_1}\rangle \otimes (|s_2, m_{s_2}\rangle \otimes |s_3, m_{s_3}\rangle)$, where $\mathbf{S} = \mathbf{S}_1 + \mathbf{S}_2 + \mathbf{S}_3$. Because the $S_{2,3}$ particle states are anticipated to be correlated within a Bloch sphere representation, we designate a "device" basis which is given by $|s_1, m_1\rangle \otimes |s_{23}, m_{23}\rangle$. In this representation, $|s_{23}, m_{23}\rangle = |s_2, m_2\rangle \otimes |s_3, m_3\rangle$ is designated the "coupled particle" basis.

3.3 Results

3.3.1 Condition for DJ Resonance

Switching is a dynamic process in which the exchange coupling (J) and the onsite anisotropy (D) act as competing interactions. Maximum switching occurs when these two interactions are perfectly balanced, a condition we call the DJ resonance [33]. Such resonance has been observed experimentally in an ultra-cold atom system [29].

We first demonstrate that for general $S_{2,3} > \frac{1}{2}$ and $S_1 = \frac{1}{2}$, at least two DJ resonances exist. We begin by noting that for two particles with similar spin s, the following coupled particle basis states can be written in $|s_i, m_{s_i}\rangle$ spin basis notation,

$$|2s, 2s\rangle = |s, s\rangle\,|s, s\rangle\,, \tag{3.10}$$

$$|2s, 2s-1\rangle = \frac{1}{\sqrt{2}}\big(\,|s, s\rangle\,|s, s-1\rangle + |s, s-1\rangle\,|s, s\rangle\,\big). \tag{3.11}$$

We couple the S_1 particle to these coupled particle states, while maintaining spin angular momentum conservation. We choose, as will be apparent later, the two device states $\{|\downarrow\rangle\,|2s, 2s\rangle\,, |\uparrow\rangle\,|2s, 2s-1\rangle\}$. Forming a subspace with these two states, one can easily see that the isotropic Heisenberg-like exchange Eq. (3.2) and hopping Eq. (3.5) terms are diag-

onal in the subspace, and can be neglected when considering the transition dynamics. We again do not restrict the range of the other exchange term, nor of the magnetic anisotropy. We thus concentrate on a reduced spin Hamiltonian of the form (dropping the K subscript in the exchange term for notational ease),

$$\mathcal{H} = J\hat{\mathbf{S}}_1 \cdot \left(\hat{\mathbf{S}}_2 + \hat{\mathbf{S}}_3\right) + D\left(\hat{S}_2^z\hat{S}_2^z + \hat{S}_3^z\hat{S}_3^z\right). \tag{3.12}$$

Applying this Hamiltonian to the chosen states within the device basis, we find that no other device states participate in the dynamics within this subspace. The Hamiltonian is then,

$$\mathcal{H} = \begin{pmatrix} 2Ds^2 - Js & J\sqrt{s} \\ J\sqrt{s} & J\left(s-\frac{1}{2}\right) + D\left(s^2 + (s-1)^2\right). \end{pmatrix} \tag{3.13}$$

Expressing it in a convenient form by removing a constant diagonal offset, we arrive at,

$$\mathcal{H} = J\sqrt{s}\sigma_x + \left[D\left(s-\frac{1}{2}\right) - J\left(s-\frac{1}{4}\right)\right]\sigma_z, \tag{3.14}$$

where σ_z and σ_x are the spin $\frac{1}{2}$ Pauli rotation matrices about the $\hat{z}$ and $\hat{x}$ axis, respectively. Applying the Rabi formula [35] to this Hamiltonian sub-block results in a Rabi frequency,

$$\Omega = \sqrt{\left(D\left(s-\frac{1}{2}\right) - J\left(s-\frac{1}{4}\right)\right)^2 + \left(J\sqrt{s}\right)^2}. \tag{3.15}$$

If the system is prepared as a pure $|\downarrow\rangle\,|2s, 2s\rangle$ state, the transition probability amplitude takes the form,

$$P(t) = \left(\frac{J\sqrt{s}}{\Omega}\right)^2 \sin^2(\Omega t). \tag{3.16}$$

Resonance is achieved when Eq. (3.16) is maximized to unity. This occurs when the rotation

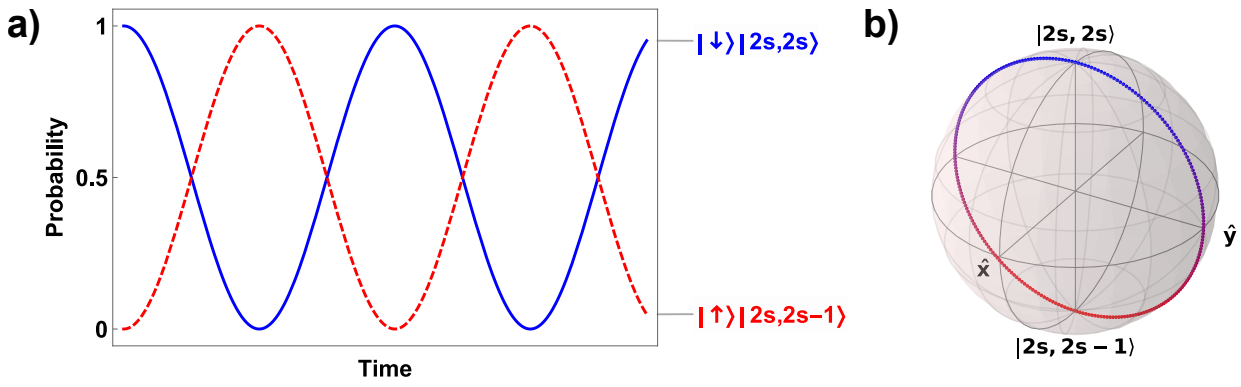

Figure 3.2: Representations of the DJ resonance for (a) the transition probability amplitudes between the $|\downarrow\rangle |2s, 2s\rangle$ state (solid) and the $|\uparrow\rangle |2s, 2s-1\rangle$ state (dashed), and (b) the corresponding Bloch sphere representation of the system.

about the z-axis in this subspace is stopped, or when,

$$J = \frac{\left(s - \frac{1}{2}\right)}{\left(s - \frac{1}{4}\right)} D. \tag{3.17}$$

Performing a similar procedure on the subspace corresponding with the $\{|\uparrow\rangle |2s, -2s\rangle, |\downarrow\rangle |2s, -2s+1\rangle\}$ states results in the same condition. There are at least two DJ resonances, one for each block described, for every value of $S_{2,3} > \frac{1}{2}$. A representation of the transition probability amplitudes and a corresponding Bloch sphere representation for any DJ resonance is given in Fig. 3.2.

3.3.2 Generalized DJ Resonances

The analysis of the last section can be extended by considering a Hamiltonian with additional terms that contribute to an anisotropic spin response. Our new general spin Hamiltonian incorporates Eq. (3.2), Eq. (3.12), and an applied magnetic field along the same axis as the

magnetic anisotropy Hamiltonian term. The general Hamiltonian is then,

$$\mathcal{H} = J\hat{\mathbf{S}}_1 \cdot \left(\hat{\mathbf{S}}_2 + \hat{\mathbf{S}}_3\right) + D\left(\hat{S}_2^z \hat{S}_2^z + \hat{S}_3^z \hat{S}_3^z\right) \\ + J_z \hat{S}_2^z \hat{S}_3^z + J_{xy}\left(\hat{S}_2^x \hat{S}_3^x + \hat{S}_2^y \hat{S}_3^y\right) + \sum_{i=1}^{3} g_i \mu_B \hat{S}_i^z B_0, \tag{3.18}$$

where g_i is spin particle i's g-factor, and B_0 is the applied static magnetic field strength for a field directed along the axis of particle 2 and 3's magnetic anisotropy. We assume that particle 2 and 3 have the same g-factor, i.e. $g_2 = g_3 = g_{23}$. Repeating the same procedure, one finds that when the Hamiltonian is expressed in the device basis, two blocks have the form,

$$\mathcal{H}_a = \Omega_x \sigma_x - \Omega_z \sigma_z - \frac{1}{2}\left(g_1 - g_{23}\right)\mu_B B_0 \sigma_z \tag{3.19}$$

$$\mathcal{H}_b = \Omega_x \sigma_x + \Omega_z \sigma_z - \frac{1}{2}\left(g_1 - g_{23}\right)\mu_B B_0 \sigma_z, \tag{3.20}$$

where the "a" block corresponds with the dynamics of the $\{|\downarrow\rangle |2s, 2s\rangle, |\uparrow\rangle |2s, 2s-1\rangle\}$ states, the "b" block corresponds with the dynamics of the $\{|\downarrow\rangle |2s, -2s+1\rangle, |\uparrow\rangle |2s, -2s\rangle\}$ states, $\Omega_x = J\sqrt{s}$, and $\Omega_z = J\left(s - 1/4\right) - D\left(s - 1/2\right) + \left(J_{xy} - J_z\right)s/2$. Comparing the two blocks, one sees that the "a" block rotates an appropriate Bloch vector in that space clockwise about the z-axis. The applied magnetic field acts in concert with this rotation. Conversely, the "b" block rotates a corresponding Bloch vector counter-clockwise, with the applied magnetic field acting in competition with this rotation. This changes the resonance conditions, leading

to two generalized DJ resonances,

$$J_a = D\frac{\left(s-\frac{1}{2}\right)}{\left(s-\frac{1}{4}\right)} + \frac{1}{2}\frac{s}{\left(s-\frac{1}{4}\right)}\left(J_z - J_{xy}\right) - \frac{1}{2}\frac{\mu_B B_0}{\left(s-\frac{1}{4}\right)}\left(g_1 - g_{23}\right), \tag{3.21}$$

$$J_b = D\frac{\left(s-\frac{1}{2}\right)}{\left(s-\frac{1}{4}\right)} + \frac{1}{2}\frac{s}{\left(s-\frac{1}{4}\right)}\left(J_z - J_{xy}\right) + \frac{1}{2}\frac{\mu_B B_0}{\left(s-\frac{1}{4}\right)}\left(g_1 - g_{23}\right) \tag{3.22}$$

We next analyze the eigenvectors of the simpler Hamiltonian in Eq. (3.12) for the two two-dimensional blocks considered so far in order to uncover the physical meaning behind these resonance conditions.

3.3.3 Physical Meaning of the DJ Resonance

We begin by examining which device basis states that participate in the block given in Eq. (3.14) are energetically preferred. In the following discussion, we neglect the $s = \frac{1}{2}$ case, as we give results for that case in another section. Within that subspace, if $J = 0$, and the magnetic anisotropy axis is hard, i.e. $D > 0$, the $|\uparrow\rangle\,|2s, 2s-1\rangle$ state is preferred. If the magnetic anisotropy axis is easy, i.e. $D < 0$, the $|\downarrow\rangle\,|2s, 2s\rangle$ state is preferred. A proof of this is easily shown by examining the eigensystem of the block when $J = 0$. The eigenvalues are $\mp D\left(s-\frac{1}{2}\right)$ which are matched to the eigenvectors $|\uparrow\rangle\,|2s, 2s-1\rangle$ and $|\downarrow\rangle\,|2s, 2s\rangle$, respectively.

The opposite preference occurs when $D = 0$ and $J \neq 0$. If J represents antiferromagnetic exchange coupling (i.e., when J is positive in our sign convention), then the $|\downarrow\rangle\,|2s, 2s\rangle$ is favored. If J represents ferromagnetic exchange coupling (i.e., J is negative), then the $|\uparrow\rangle\,|2s, 2s-1\rangle$ is favored. When inspecting the regime of the DJ resonance (when J and D have the same sign and $s > \frac{1}{2}$), one can see that the magnetic anisotropy and exchange

terms of the total Hamiltonian act in competition.

Next, we examine the eigensystem of the block for relevant conditions for $s > \frac{1}{2}$. The eigenvalues are $\alpha = \mp\sqrt{\beta^2 + \left(J\sqrt{s}\right)^2}$, where $\beta \equiv D\left(s - \frac{1}{2}\right) - J\left(s - \frac{1}{4}\right)$. The corresponding eigenvectors are,

$$|\phi_1\rangle = \rightarrow A\left(\frac{\beta - \alpha}{J\sqrt{s}}\right)|\downarrow\rangle\,|2s, 2s\rangle + A\,|\uparrow\rangle\,|2s, 2s-1\rangle\,, \tag{3.23}$$

$$|\phi_2\rangle = \rightarrow A\left(\frac{\beta + \alpha}{J\sqrt{s}}\right)|\downarrow\rangle\,|2s, 2s\rangle + A\,|\uparrow\rangle\,|2s, 2s-1\rangle\,, \tag{3.24}$$

where A is a normalization constant. It is apparent that the $|\phi_1\rangle$ eigenstate is always preferred, except when $\alpha = 0$. The latter condition is never satisfied for $J \neq 0$, i.e., there is no condition in which the $|\phi_2\rangle$ state is energetically favorable.

Armed with the energetically favorable eigenvector, we now uncover the balance of device basis states around the DJ resonance. This can be done by examining the relative proportions of the two device basis states within the $|\phi_1\rangle$ eigenvector. For example, if the eigenvector contains a larger proportion of the $|\downarrow\rangle\,|2s, 2s\rangle$ basis state for positive D and J, then one can infer from the prior analysis that the exchange coupling Hamiltonian term plays a stronger role in the dynamics than the magnetic anisotropy term. The test is then to compare the modulus squared values of the components of the eigenvector. When both components are balanced (and noting that both components are always real), the condition is,

$$\left(J\sqrt{s}\right)^2 = (\beta - \alpha)^2\,. \tag{3.25}$$

This condition holds exactly at the DJ resonance given in Eq. (3.17). We repeat this analysis for off resonance conditions, i.e., when $J = J_{\mathrm{R}} + \epsilon$ for appropriate ϵ. We also enforce conditions that lie within the DJ resonance regime, i.e., $J \in (0, \infty)$ when $D > 0$ and

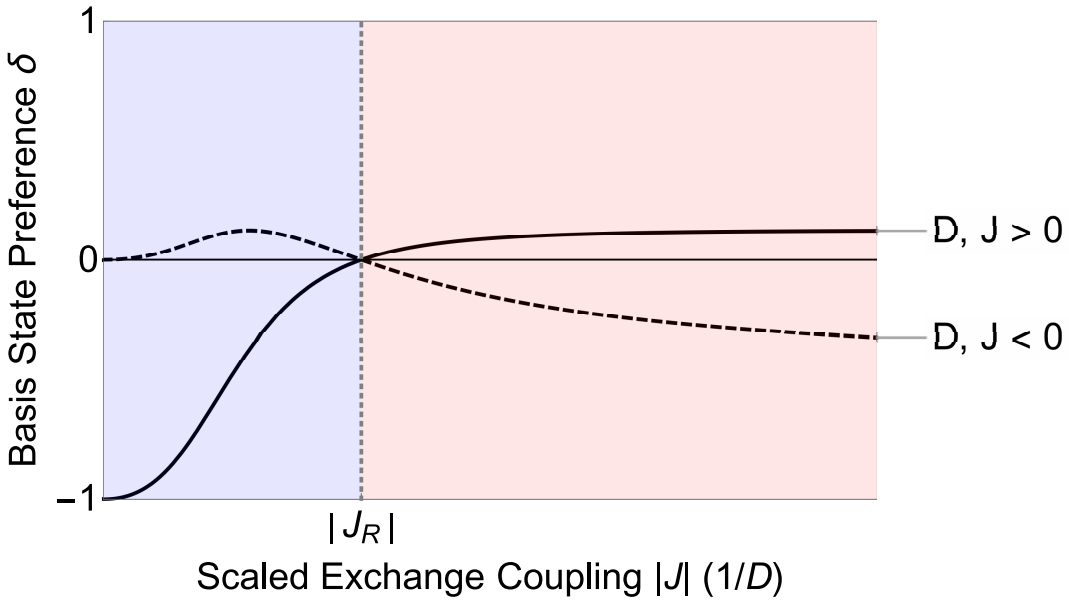

Figure 3.3: Representation of basis set mixture in the energetically-favored eigenvector $|\phi_1\rangle$ when D and $J > 0$ (solid) and when D and $J < 0$ (dashed). The difference between the modulus squared coefficients $\delta \equiv |c_1|^2 - |c_2|^2$ is plotted for $s = 1$, where c_1 is the coefficient of the $|\downarrow\rangle |2s, 2s\rangle$ basis state within the $|\phi_1\rangle$ eigenvector, and c_2 the coefficient of the $|\uparrow\rangle |2s, 2s-1\rangle$ state. Basis state mixtures that are favorable to magnetic anisotropy are shaded blue, while those that favor exchange coupling are shaded red.

$J \in (-\infty, 0)$ when $D < 0$. A representation of these conditions, and the results, are shown in Fig. 3.3. We find that when $|J| < |J_{\mathrm{R}}|$, there is a higher proportion of the basis states within the eigenvector that are energetically favorable to magnetic anisotropy. Conversely, when $|J| > |J_{\mathrm{R}}|$, there is a lower proportion of those same basis states in the eigenvector. The DJ resonance is the inflection point in which the action of the two terms in the total Hamiltonian are in perfect balance. We next explore the $S_{2,3} = \frac{1}{2}$ model, in light of the condition that Eq. (3.17) takes at that value of s, and compare to the $S_{2,3} = 1$ model.

3.3.4 Coupled Particles with $S_{2,3} = \frac{1}{2}$ Model

For the $S_{2,3} = \frac{1}{2}$ model, when the Hamiltonian of Eq. (3.1) is expressed in the product basis, the two $s = \frac{1}{2}$ subspaces are coupled to each other by anisotropic application of the exchange term J_{K}, while the $s = \frac{3}{2}$ subspace is diagonal and remains uncoupled. The Heisenberg-like exchange, given in Eq. (3.2), is diagonal in both the product and device basis if $J_z = J_{xy} = J_{\mathrm{H}}$, i.e., the interaction is isotropic between particle 2 and 3. While it's important to consider the situation in which the Heisenberg-like exchange is applied anisotropically (i.e., $J_z \neq J_{xy}$), we first consider the isotropic case. The tunneling Hamiltonian in Eq. (3.5) is also diagonal in both the product and device basis. In the device basis, the tunneling Hamiltonian carries the same eigenvalue across all s_{23} subspaces in the device basis, and the isotropic Heisenberg exchange Hamiltonian has the same eigenvalue in each subspace. As a result, the total Hamiltonian in the product basis takes the form,

$$\begin{pmatrix} \left[\mathcal{H}^0_{3/2}\right] & & \\ & \left[\mathcal{H}^1_{1/2}\right] & \\ & & \left[\mathcal{H}^2_{1/2}\right] \end{pmatrix}, \tag{3.26}$$

where $\mathcal{H}^n_{1/2}$ refers to the Hamiltonian block that corresponds with the n'th interaction of the two spin $s = \frac{1}{2}$ subspaces, and $\mathcal{H}^0_{3/2}$ is the diagonal $s = \frac{3}{2}$ subspace. When the Hamiltonian is expressed in the device basis, the anisotropic application of the exchange term couples the different $s_{2,3}$ subspaces. This leads to a block Hamiltonian of the form,

$$\begin{pmatrix} \left[\mathcal{H}^0_{\pm 3/2}\right] & & \\ & \left[\mathcal{H}_{1/2}\right] & \\ & & \left[\mathcal{H}_{-1/2}\right] \end{pmatrix}, \tag{3.27}$$

where $\mathcal{H}_m$ refers to a 3-dimensional Hamiltonian block that corresponds with the m subspace, and $\mathcal{H}^0$ refers to a 2-dimensional diagonal block of spin $s_{23} = 1$.

We further explore the $m = \pm 1/2$ blocks corresponding with the $|m_1\rangle |s_{23}, m_{23}\rangle = |\uparrow\rangle |1,0\rangle$, $|\uparrow\rangle |0,0\rangle$, $|\downarrow\rangle |1,1\rangle$ and $|\uparrow\rangle |1,-1\rangle$, $|\downarrow\rangle |1,0\rangle$, $|\downarrow\rangle |0,0\rangle$ states, respectively. They take the form (with a common $t + t^* + \frac{1}{4}J_{\mathrm{H}}$ removed from the diagonal),

$$\mathcal{H}_{1/2} = \frac{1}{4}\begin{pmatrix} 0 & \Delta_{\mathrm{K}} & \sqrt{2}\Sigma_{\mathrm{K}} \\ \Delta_{\mathrm{K}} & -4J_H & -\sqrt{2}\Delta_{\mathrm{K}} \\ \sqrt{2}\Sigma_{\mathrm{K}} & -\sqrt{2}\Delta_{\mathrm{K}} & -\Sigma_{\mathrm{K}} \end{pmatrix}, \tag{3.28}$$

$$\mathcal{H}_{-1/2} = \frac{1}{4}\begin{pmatrix} -\Sigma_{\mathrm{K}} & \sqrt{2}\Sigma_{\mathrm{K}} & \sqrt{2}\Delta_{\mathrm{K}} \\ \sqrt{2}\Sigma_{\mathrm{K}} & 0 & -\Delta_{\mathrm{K}} \\ \sqrt{2}\Delta_{\mathrm{K}} & -\Delta_{\mathrm{K}} & -4J_H \end{pmatrix}, \tag{3.29}$$

where $\Delta_{\mathrm{K}} \equiv J_{\mathrm{K}2} - J_{\mathrm{K}3}$ and $\Sigma_{\mathrm{K}} \equiv J_{\mathrm{K}2} + J_{\mathrm{K}3} \equiv 2J_{\mathrm{K}}$. When the exchange term is isotropically applied, i.e. $\Delta_{\mathrm{K}} = 0$, the corresponding $|0,0\rangle$ states no longer interact with the others. The Hamiltonian blocks then become,

$$\mathcal{H}^{eff}_{\pm 1/2} = \pm\frac{1}{4}J_{\mathrm{K}}\sigma_z + \frac{1}{\sqrt{2}}J_{\mathrm{K}}\sigma_x. \tag{3.30}$$

Applying the Rabi formula to the case in which the system is initially prepared in either the pure $|\downarrow\rangle |1,1\rangle$ or $|\uparrow\rangle |1,-1\rangle$ state, we find,

$$P(t) = \frac{8}{9}\sin^2(\Omega t), \tag{3.31}$$

with Rabi frequency,

$$\Omega = \frac{3}{4}|J_{\mathrm{K}}|. \tag{3.32}$$

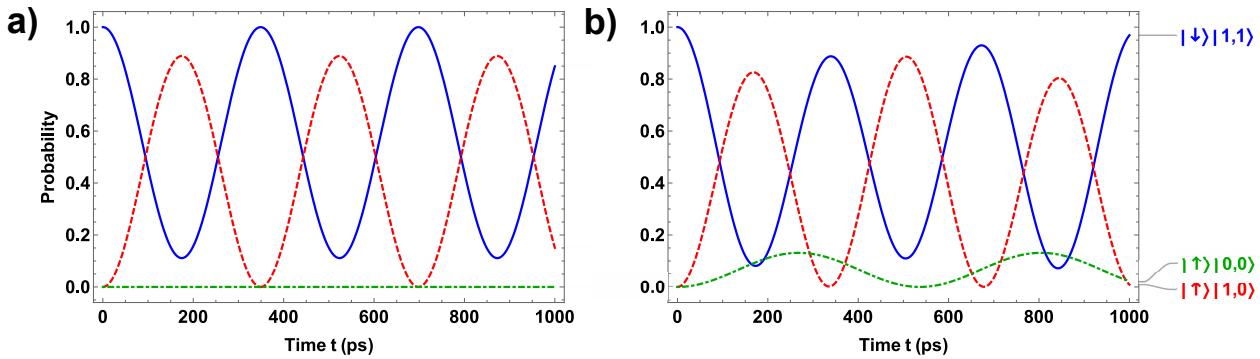

Figure 3.4: Transition probability amplitudes for the $S_{2,3} = \frac{1}{2}$ model, for the $|\downarrow\rangle\,|1,1\rangle$ (solid), $|\uparrow\rangle\,|1,0\rangle$ (dashed), and $|\uparrow\rangle\,|0,0\rangle$ (dot-dashed) states as a function of time. The exchange strength is (a) isotropically-applied J_{K} and (b) anisotropically-applied J_{K} (i.e., $J_{\mathrm{K2}} \neq J_{\mathrm{K3}}$). The system is initially prepared as a pure $|\downarrow\rangle\,|1,1\rangle$ state. In units of cm^{-1}, exchange parameters are (a) $J_{\mathrm{K2}} = J_{\mathrm{K3}} = -0.40$ and (b) $\Delta_{\mathrm{K}}/J_{\mathrm{K}} = 0.5$. The shared parameters are: $J_{\mathrm{H}} = -0.05$ and $t = 0.05$.

In this case, and as shown in Fig. 3.4, there are no resonance conditions in which the maximum transition probability amplitude is unity, even when considering anisotropic application of the exchange coupling.

To check for scenarios in which a maximum transition probability of unity can be achieved in the $S_{2,3} = \frac{1}{2}$ model, we explore applications of spin filtering on the system. To do this, first an appropriate change of basis of the device states is needed. The states, originally expressed in the $|s_1, m_{s_1}\rangle \otimes \left|s_{2,3}, m_{s_{2,3}}\right\rangle$, are changed by transforming $|s_1, m_{s_1}\rangle$ states to $|\theta, \phi\rangle$ spinor states. In general, the spinor takes the form,

$$\chi = \begin{pmatrix} \cos\frac{\theta}{2} e^{-i\frac{\phi}{2}} \\ \sin\frac{\theta}{2} e^{i\frac{\phi}{2}} \end{pmatrix}, \tag{3.33}$$

where θ is the polar angle and ϕ is the azimuthal angle. Because the reduced Hamiltonian blocks will no longer be two-dimensional, we numerically solve Eq. (3.7) to obtain the relative transition probabilities from one state to the next.

We choose to monitor those states that are coupled in the Hamiltonian and correspond with transitions between non-entangled to maximally entangled states. The transition $|1,1\rangle \rightarrow |1,0\rangle$ fits this description, as the device-to-spin correspondence is,

$$|1,1\rangle = |\uparrow\rangle\,|\uparrow\rangle\,, \tag{3.34}$$

$$|1,0\rangle = \frac{1}{\sqrt{2}}\left(|\uparrow\rangle\,|\downarrow\rangle + |\downarrow\rangle\,|\uparrow\rangle\right). \tag{3.35}$$

Fig. 3.5 investigates the orientations of particle 1's spin that will lead to maximum probability between these two states at a given snapshot of the Rabi-like oscillations, with the azimuthal orientation angle chosen to be 0. Peaks of transition probability are found for several combinations of preparation and measurement orientations. Taking Fig. 3.5 as guidance to explore a higher transition probability scenario for a given spin filter, particle 1's prepared polar angle is chosen to be $\theta_{\text{in}} = \pi$ and the measured polar angle to be $\theta_{\text{out}} = \frac{\pi}{8}$. The resulting transition probability oscillations are shown in Fig. 3.6. It is clear from this result that the maximum amplitude has indeed been raised from 8/9, calculated to be $P = 0.995$. Fig. 3.6 demonstrates the same feature of the spin dynamics for the three-particle system as found in Ref. [33], namely that a single measurement of particle 1's spin orientation determines the entanglement state of particle 2 and 3. This demonstrates the read out of the entanglement state if the measurement of the S_1 spin polarization is taken at any general time t. This also demonstrates preparation of the entanglement state if the S_1 spin polarization is measured at a specific time t corresponding with a peak in the Rabi oscillation.

Finally, another method may be used to prepare the entanglement state. Looking to Eq. (3.21) and Eq. (3.22), the resonance condition for $S_{2,3} = \frac{1}{2}$ without an applied magnetic field is,

$$J_{\text{K}} = J_z - J_{xy}. \tag{3.36}$$

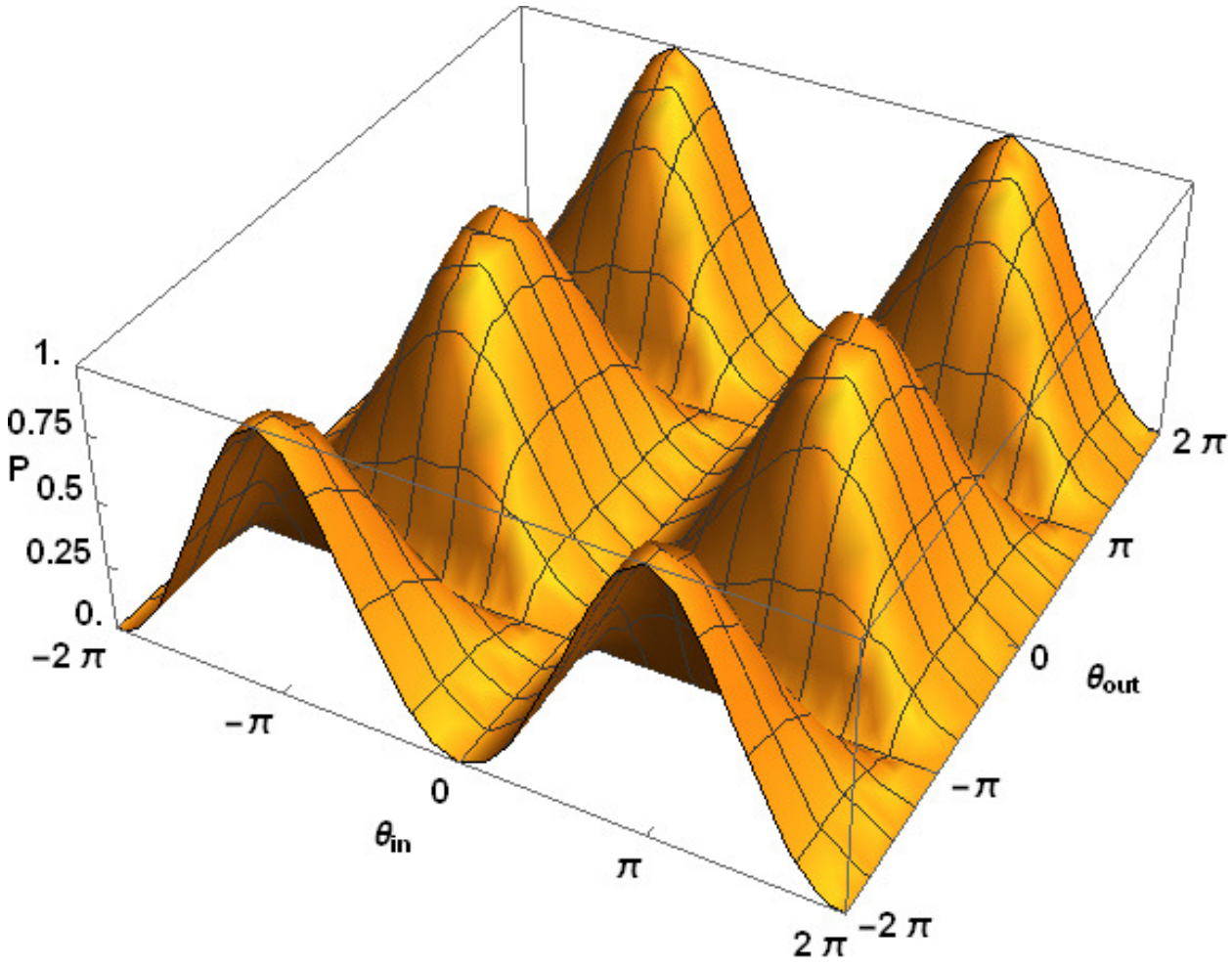

Figure 3.5: Relative transition probability (z axis) of the $|\theta,\phi\rangle\,|s_{23},m_{23}\rangle = |\theta_{\rm in},0\rangle\,|1,1\rangle \rightarrow |\theta_{\rm out},0\rangle\,|1,0\rangle$ with respect to the total probability of finding the system with the chosen S_1 particle's measured polar spin orientation (y axis), as a function of the chosen S_1 particle's prepared polar spin orientation (x axis). The snapshot of probabilities was calculated for $t = 133$ ps. In units of cm^{-1}, the parameters are $J_{\rm K2} = J_{\rm K3} = -0.40$, $J_{\rm H} = -0.05$, $t = 0.05$.

When this resonance condition (which we designate as the "JJ resonance") is applied to the system considered in Fig. 3.4(a), the maximum transition probability amplitude is unity. While the $S_{2,3} = \frac{1}{2}$ model does not contain a DJ resonance as indicated in Eq. (3.17), a JJ resonance could be used to achieve the same transition probability behavior. As we will next show, and in comparison to the $S_{2,3} = \frac{1}{2}$ model, this resonance switching mechanism is

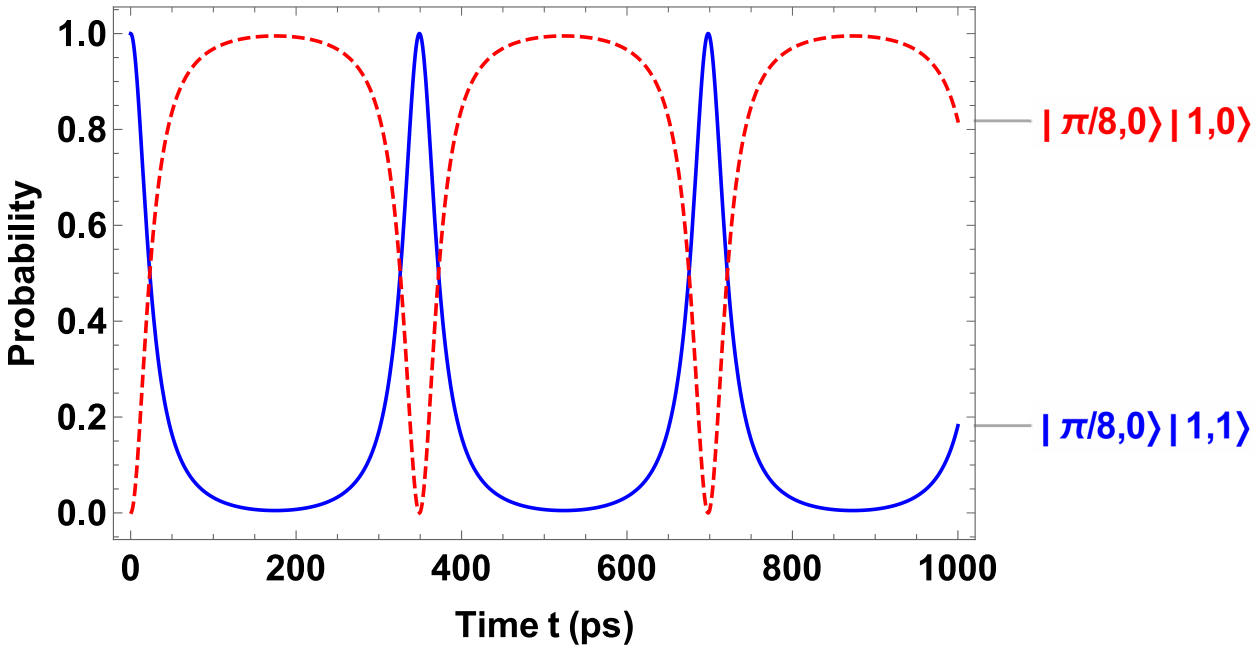

Figure 3.6: Relative transition probability amplitudes in the $S_{2,3} = \frac{1}{2}$ model, for the $|\pi/8\rangle\,|1,1\rangle$ (solid) and $|\pi/8\rangle\,|1,0\rangle$ (dashed) states, as a function of time. The system is initially prepared in the pure $|\pi,0\rangle\,|1,1\rangle$ state, with the same parameter state as Fig. 3.5.

maximized in the $S_{2,3} = 1$ model without the use of spin filtering mechanisms or anisotropy of the exchange interaction between particle 2 and 3.

3.3.5 Comparison to the Coupled Particles $S_{2,3} = 1$ Model

We next compare the $S_{2,3} = 1$ model as explored in [33] by identifying the role of each Hamiltonian term given in Eq. (3.1) in that model. Similar to the $S_{2,3} = \frac{1}{2}$ model, the Heisenberg-like exchange and tunneling Hamiltonians are diagonal in the device basis. Because the magnetic anisotropy term is no longer diagonal like in the $S_{2,3} = \frac{1}{2}$ model, the $s = 2$ and $s = 0$ subspaces are connected. As shown in Ref. [33], because the magnetic anisotropy and exchange Hamiltonians have off-diagonal terms in similar m subspaces, there is a complicated interplay of these interactions that influence the transition dynamics of

systems prepared for a given value of m.

We next summarize the blocks of the $S_{2,3} = 1$ model Hamiltonian. The $m = \frac{3}{2}$ subspace, which corresponds with the dynamics of the $|m_1\rangle |s_{23}, m_{23}\rangle = \{|\uparrow\rangle |2,1\rangle , |\uparrow\rangle |1,1\rangle , |\downarrow\rangle |2,2\rangle\}$ states, takes the form (after removing a common $t + t^* + J_{\rm H} + D + \frac{1}{4}\Sigma_{\rm K}$ from the diagonal),

$$\mathcal{H}_{3/2} = \frac{1}{4}\begin{pmatrix} 0 & \Delta_{\rm K} & 2\Sigma_{\rm K} \\ \Delta_{\rm K} & -8J_H & -2\Delta_{\rm K} \\ 2\Sigma_{\rm K} & -2\Delta_{\rm K} & -3\Sigma_{\rm K} + 4D \end{pmatrix}. \tag{3.37}$$

Similarly, the $m = -\frac{3}{2}$ block (corresponding with the dynamics of the $\{|\uparrow\rangle |2,-2\rangle , |\downarrow\rangle |2,-1\rangle , |\downarrow\rangle |1,-1\rangle\}$ states) with the same diagonal values removed has the form,

$$\mathcal{H}_{-3/2} = \frac{1}{4}\begin{pmatrix} -3\Sigma_{\rm K} + 4D & 2\Sigma_{\rm K} & 2\Delta_{\rm K} \\ 2\Sigma_{\rm K} & 0 & -\Delta_{\rm K} \\ 2\Delta_{\rm K} & -\Delta_{\rm K} & -8J_H \end{pmatrix}. \tag{3.38}$$

When the exchange coupling is instead isotropically applied, and similar to the $S_{2,3} = \frac{1}{2}$ model, the $|\uparrow\rangle |1,1\rangle$ state in Eq. (3.37) and the $|\downarrow\rangle |1,1\rangle$ state in Eq. (3.38) are no longer coupled to the other states within their respective block Hamiltonians. For the other two states in the $m = \pm\frac{3}{2}$ blocks, the effective Hamiltonians (with the appropriate diagonal entries removed) become,

$$\mathcal{H}^{eff}_{\pm 3/2} = \mp\frac{1}{2}\left(D - \frac{3}{2}J_{\rm K}\right)\sigma_z + J_{\rm K}\sigma_x. \tag{3.39}$$

While the anisotropic case of exchange coupling is more complicated for the $m = \pm\frac{1}{2}$ subspaces, a similar reduction in the corresponding block Hamiltonians is found when the ex-

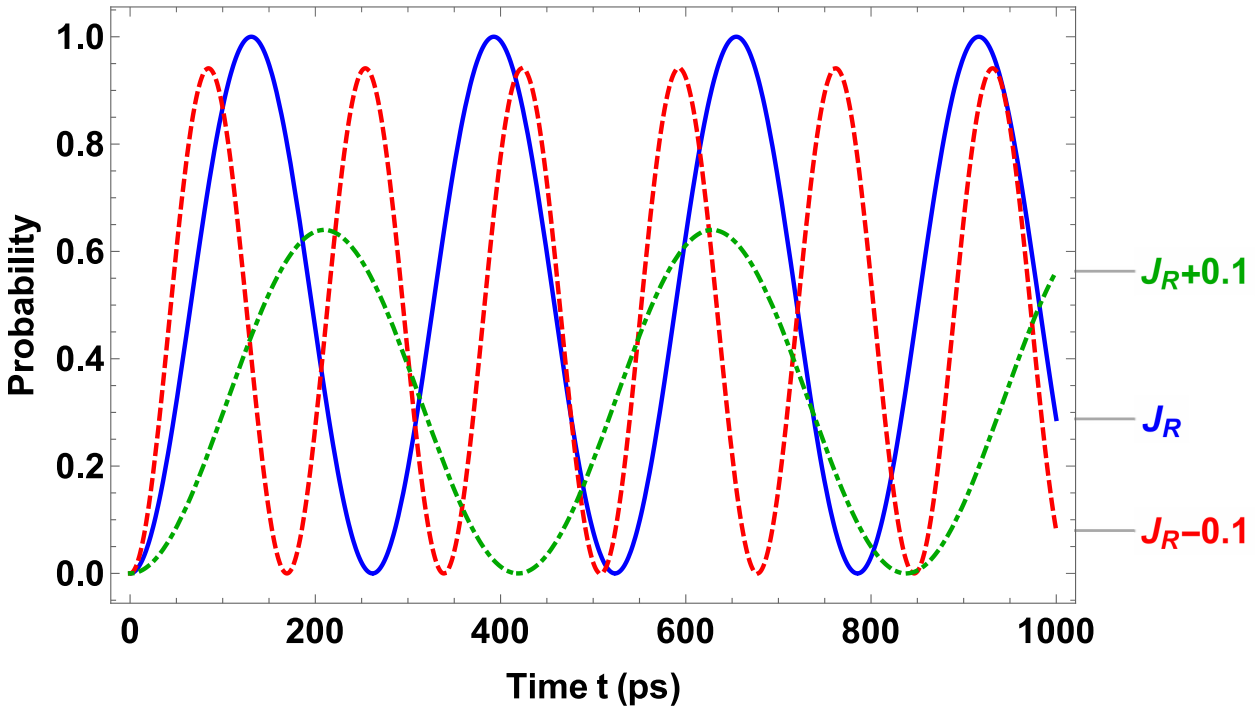

Figure 3.7: Transition probability amplitudes as a function of time for the $S_{2,3} = 1$ model, for the $|m_1\rangle |s_{23}, m_{23}\rangle = |\uparrow\rangle |2, 1\rangle$ state when the initial state is prepared as a pure $|\downarrow\rangle |2, 2\rangle$ state. Several values of the isotropically-applied $J_{\rm K}$ (i.e. $J_{\rm K2} = J_{\rm K3}$) are given. The exchange strengths correspond with the DJ resonance condition of $J_K = \frac{2}{3}D$ (solid) and off resonance by ± 0.1 (dot-dashed and dashed, respectively). In units of cm^{-1}, the parameters are: $J_{\rm H} = -0.05$, $J_{\rm R} = -0.40$, $D = -0.60$, $t = 0.05$.

change coupling is applied isotropically. Repeating the same procedure, we find,

$$\mathcal{H}^{eff}_{\pm 1/2} = \pm \frac{1}{2}\left(D + \frac{1}{2}J_{\rm K}\right)\sigma_z + \frac{1}{\sqrt{2}}J_{\rm K}\sigma_x. \tag{3.40}$$

Thus the same procedure to analyze the Rabi frequency of the m sub-blocks can be used. As shown in Fig. 3.7, if $J_{\rm K}$ is chosen to minimize the Rabi frequency, e.g., when $J_{\rm K} = \frac{2}{3}D$ for $m = \pm\frac{3}{2}$, the maximum transition probability amplitude is unity. When $J_{\rm K}$ is chosen off of the resonance condition, the denominator in the Rabi formula increases and the maximum transition probability amplitude decreases.

Table 3.1: Pure state transitions for the $S_{2,3} = 1$ and $S_{2,3} = 1/2$ model, where J_{R} is the condition on J_{K} to reach resonance, P is the maximum transition probability amplitude, and Ω is the Rabi frequency for this maximum amplitude.

$S_{2,3}$	State Transitions	J_{R}	P	Ω
$\frac{1}{2}$	$\|\uparrow\rangle\|1,0\rangle$, $\|\downarrow\rangle\|1,+1\rangle$	-	$\frac{8}{9}$	$\frac{3}{4}\|J_{\mathrm{K}}\|$
$\frac{1}{2}$	$\|\downarrow\rangle\|1,0\rangle$, $\|\uparrow\rangle\|1,-1\rangle$	-	$\frac{8}{9}$	$\frac{3}{4}\|J_{\mathrm{K}}\|$
1	$\|\uparrow\rangle\|2,+1\rangle$, $\|\downarrow\rangle\|2,+2\rangle$	$\frac{2}{3}D$	1	$\frac{2}{3}\|D\|$
1	$\|\uparrow\rangle\|2,-2\rangle$, $\|\downarrow\rangle\|2,-1\rangle$	$\frac{2}{3}D$	1	$\frac{2}{3}\|D\|$
1	$\|\uparrow\rangle\|1,0\rangle$, $\|\downarrow\rangle\|1,+1\rangle$	$-2D$	1	$\sqrt{2}\|D\|$
1	$\|\uparrow\rangle\|1,-1\rangle$, $\|\downarrow\rangle\|1,0\rangle$	$-2D$	1	$\sqrt{2}\|D\|$

3.4 Discussion and Summary

3.4.1 Control of Degree of Entanglement and Vectors on the Bloch Sphere

The main result of this work, demonstrated effectively through Eq. (3.17), is that for any value of $S_{2,3} > \frac{1}{2}$, with no restriction on half-integer versus integer spin, at least two DJ resonances exist. Taking the classical limit as $s \to \infty$, the resonance condition tends towards $J_K = D$. As is shown in Table 3.1, Fig. 3.6, and Fig. 3.7, both the $S_{2,3} = \frac{1}{2}$ and $S_{2,3} = 1$ models demonstrate preparation and measurement of the coupled particles' degree of entanglement by appropriate measurement of the $S_1 = \frac{1}{2}$ particle.

We find that the physical interplay between the exchange and anisotropy terms in the Hamiltonian are vital for realizing the DJ resonance. As shown in the $S_{2,3} = \frac{1}{2}$ model, the lack of anisotropy in particle 2 and 3 result in no DJ resonances. We also find that at each DJ resonance, the system has achieved a perfect balance of states that balance the effect of the exchange coupling and magnetic anisotropy terms in the total Hamiltonian. In other words, if $|J_{\mathrm{K}}| = |J_R|$, where J_R is a DJ resonance, the most energetically favorable eigenvector of the

Hamiltonian sub block contains an equal mixture of states that favor magnetic anisotropy and exchange coupling.

For the $S_{2,3} = \frac{1}{2}$ model, the non-maximal probability amplitude indicates in the language of the Bloch sphere that the rotation is not about an axis solely on the azimuthal plane, but instead contains a rotation axis component in the polar plane, as shown in Fig. 3.8. By searching for appropriate spin filtering conditions, as shown in Fig. 3.5, one could find rotations in the Bloch sphere that maximizes the amount of time spent near the non-entangled to entangled transition is possible. The DJ resonances as found in [33], however, is a feature for the $S_{2,3} > \frac{1}{2}$ model. Rather than relying on either the use of an extra spin filtering step to maximize transition probabilities, or the use of other anisotropies such as the anisotropic application of the Heisenberg-like term, the DJ resonance allows for full control of the Bloch sphere representation with appropriate control of the exchange coupling strength on and off resonance.

Control of the rotation of a general Bloch vector within the appropriate Bloch sphere is important in QIS contexts. Looking to Eq. (3.19) and Eq. (3.20), the exchange coupling J gives one control over rotations of the Bloch vector about the x-axis, and the resonance condition allows control of rotations about the z-axis. With appropriate pulsing of the parameters, one can realize any point on the corresponding Bloch sphere. It's precisely because of the resonance condition that all points on the sphere are accessible, which implies that all single qubit operations are possible. This can be seen by inspecting the effective Hilbert spin space. The isolated sub blocks of Eq. (3.19) and Eq. (3.20) belong to the SO(2) group. When substituted into the unitary propagator of Eq. (3.9), the resulting operation is SU(2). The adjoint representation of SU(2) is isomorphic to SO(3). If one is able to realize all SO(3) operations on the Bloch vector, as has been shown, all relevant SU(2) operations can be realized.

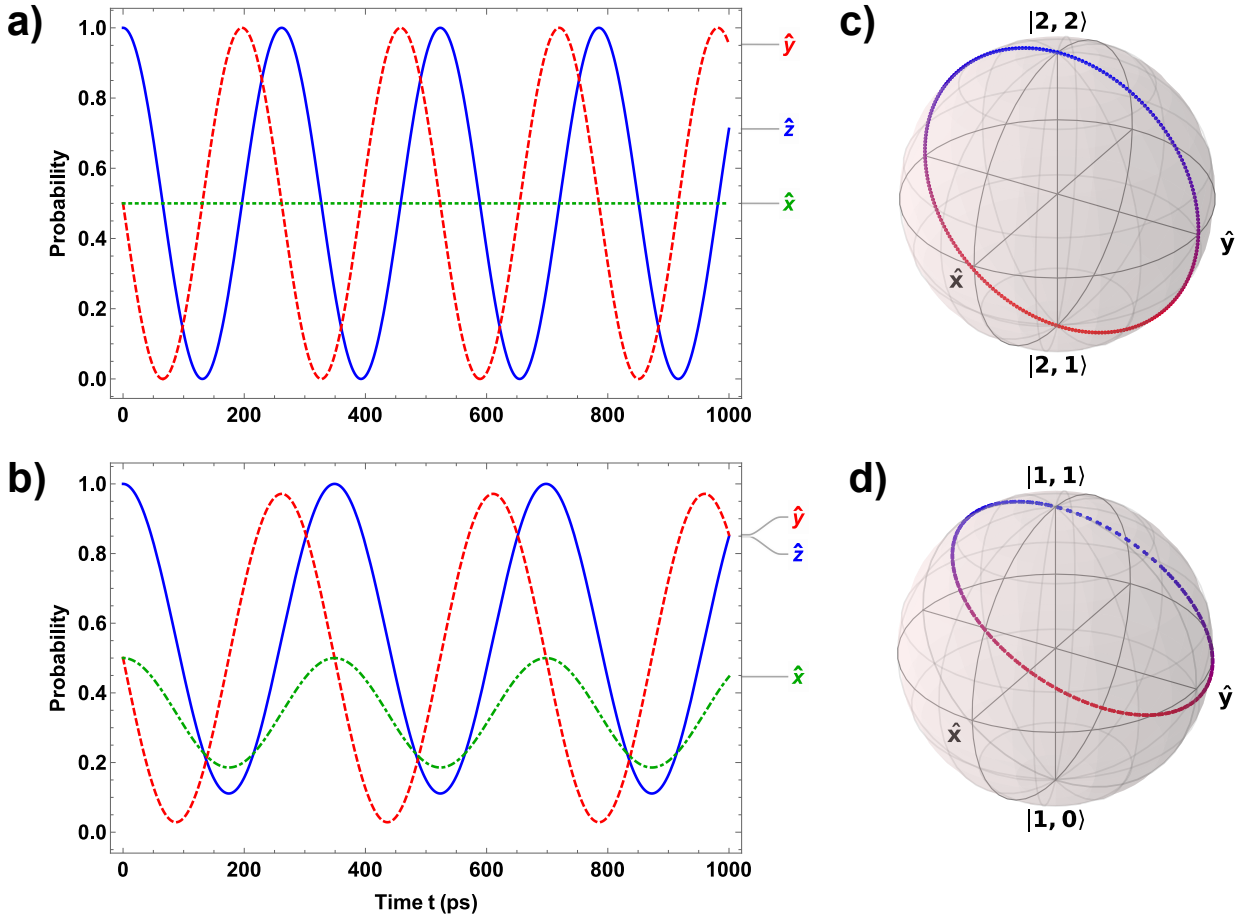

Figure 3.8: Probability of measuring a state corresponding with the $\hat{x}$ (dotted), $\hat{y}$ (dashed), and $\hat{z}$ (solid) unit vectors as a function of time for the (a) $S_{2,3} = 1$ and (b) $S_{2,3} = \frac{1}{2}$ models on the Bloch sphere as defined in (c) and (d), respectively. The Bloch vector for (a)/(c) and (b)/(d) is initially prepared in the $|\downarrow\rangle|2,2\rangle$ and $|\downarrow\rangle|1,1\rangle$ states, respectively. The corresponding Bloch sphere representation of the path traced by the Bloch vector for the (c) $S_{2,3} = 1$ and (d) $S_{2,3} = \frac{1}{2}$ model is given for the same interval considered. In units of cm^{-1}, the shared parameters are: $J_{\text{K2}} = J_{\text{K3}} = -0.40$, $J_{\text{H}} = -0.05$, $t = 0.05$. The $S_{2,3} = 1$ model additionally has $D = -0.60$.

3.4.2 Application to Ultra-Cold Optical Lattices

Because of the general nature of the total Hamiltonian considered in this paper, there are several immediate applications within the condensed matter context. For example, Ref. [29] recently found experimentally-realized resonance conditions of magnetic anisotropy and ex-

change coupling for a Mott insulator composed of an ultra-cold optical lattice of ^{87}Rb atoms. The authors uncover an oscillation in an observable parameter A, which represents the longitudinal spin alignment, that is maximized for the resonance condition of $J = \pm\frac{2}{3}D$. Recovering the authors' form of the two-site Bose-Hubbard Hamiltonian used to explain these resonances from our model is trivial, and is accomplished by setting $J_{K2} = J_{K3} = 0$, while noting the difference in the sign convention of J. We use the experimental example to uncover another possible resonance, but also highlight a constraint within DJ resonances. Using the Hamiltonian $m = 0$ sub-block in Ref. [29], if one were to prepare the system as a pure mixture of either state within the block, i.e., either state in $\{(|1,-1\rangle + |-1,1\rangle)/\sqrt{2}, |0,0\rangle\}$, one finds a resonance condition of $J = 2D$. If one were to choose instead the product basis, a single sub block of the Hamiltonian would emerge associated with the $\{|2,0\rangle, |0,0\rangle\}$ product states. Preparation of a pure mixture of one of these states results in a different DJ resonance condition, namely $J = \frac{2}{9}D$. Whether any particular resonance is important experimentally, however, is the constraint on whether a measurement of the oscillations between states is feasible.

It is interesting to note that applying our three-particle model with similar conditions leads to strikingly different behavior than the two-site Bose-Hubbard model. To do this, one should first modify our model by matching the particle type across all three particles, i.e., change S_1 so that $S_1 = S_2 = S_3 \equiv S_{1,2,3} = 1$, and extend magnetic anisotropy to particle 1. In doing so, and assuming an isotropic coupling between nearest neighbors (i.e., $J_{K2} = J_H = J$ and $J_{K3} = 0$), the effective Hamiltonian becomes,

$$\mathcal{H}_{\mathrm{BH3}} = J\left(\hat{\mathbf{S}}_1 \cdot \hat{\mathbf{S}}_2 + \hat{\mathbf{S}}_2 \cdot \hat{\mathbf{S}}_3\right) + D\sum_{i=1}^{3} \hat{S}_i^z \hat{S}_i^z. \tag{3.41}$$

Within this total Hamiltonian, there are three two-dimensional blocks that correspond with transitions between different state phases: $\{|2,2\rangle_A, |2,2\rangle_B\}$, $\{|2,0\rangle_A, |2,0\rangle_B\}$, and

$\{|2,-2\rangle_A, |2,-2\rangle_B\}$. These blocks share the same form,

$$\mathcal{H} = \frac{1}{2}\left(J\sigma_z + \sqrt{3}J\sigma_x\right). \tag{3.42}$$

Application of the Rabi formula on this block gives a Rabi frequency $\Omega = |J|$, and a transition probability amplitude of,

$$P(t) = \frac{3}{4}\sin^2(\Omega t). \tag{3.43}$$

Thus in the extension of the approximate form of the two-site Bose-Hubbard Hamiltonian to three sites, there is no DJ resonance within that basis, and the transition probability maxima is 3/4. In contrast, we have found that the DJ resonances appear when considering exchange interactions that extend either to next-nearest neighbor exchange interactions (in the linear chain geometry) or in trimer geometries for $S = 1$.

3.4.3 Application to Magnetic Molecules and Quantum Dots

The results of this work can be applied to magnetic molecule models. In single-molecule quantum dots, like those explored in Ref. [32], the source of magnetic anisotropy is from spin-orbit interactions and the geometry of the system resembles a two-terminal molecular transistor. Even so, the spin model approximation of the system resembles the spin model considered here. Competing effects such as additional exchange coupling interactions with the substrate and decay mechanisms such as spin lattice vibrations could mask these DJ resonances. As found in Ref. [33], however, significant anisotropic application of the exchange coupling between particle 1 and the others still allows for usable entangled state switching (up to P=0.995) around a DJ resonance. This is important when considering the experimental uncertainties inherent in a scenario of coupling an electron to a magnetic dimer on a

substrate. Furthermore, the existence of a DJ resonance for any value of $S_{2,3}$ via Eq. (3.17) opens the application of this model to larger spin magnetic molecules coupled together, such as coupled Mn_3 monomers.

When considering a trimer geometry for the $S_{1,2,3} = 1$ model, or equivalently a next-nearest neighbor exchange interaction in a chain geometry, the preceding section's assumption of $J_{K3} = 0$ is modified. Assuming an isotropic application of the exchange strength coupling between each particle in the three-particle system, the $S_{1,2,3} = 1$ model's effective spin Hamiltonian is

$$\begin{aligned}\mathcal{H}_{\text{trimer}} = J\left(\hat{\mathbf{S}}_1 \cdot \hat{\mathbf{S}}_2 + \hat{\mathbf{S}}_2 \cdot \hat{\mathbf{S}}_3 + \hat{\mathbf{S}}_3 \cdot \hat{\mathbf{S}}_1\right) \\ + D\sum_{i=1}^{3} \hat{S}_i^z \hat{S}_i^z. \end{aligned} \tag{3.44}$$

In the device basis, this Hamiltonian contains four two-dimensional blocks corresponding with the conserved spin transitions of $m = \pm 1$ and $m = \pm 2$. The $m = \pm 1$ blocks contain the interactions of the $\{|1\rangle|1,0\rangle, |0\rangle|1,1\rangle\}$ and $\{|0\rangle|1,-1\rangle, |-1\rangle|1,0\rangle\}$ states, respectively. The $m = \pm 1$ block's effective form is,

$$\mathcal{H}_{m=\pm 1}^{\text{trimer}} = \pm D\sigma_z + J\sigma_x. \tag{3.45}$$

The $m = \pm 2$ blocks involve the $\{|1\rangle|2,1\rangle, |0\rangle|2,2\rangle\}$ and $\{|0\rangle|2,-2\rangle, |-1\rangle|2,-1\rangle\}$ states, respectively, and have the form,

$$\mathcal{H}_{m=\pm 2}^{\text{trimer}} = \pm\frac{1}{2} J\sigma_z + \sqrt{2} J\sigma_x. \tag{3.46}$$

Application of the Rabi formula to both the $m = \pm 1$ and $m = \pm 2$ blocks yields two cases. When the state transition is in the $m = \pm 1$ block, the Rabi frequency is $\Omega_{\pm 1} = \sqrt{D^2 + J^2}$

with a transition probability amplitude of,

$$P_{\pm 1}(t) = \left(\frac{J}{\Omega_{\pm 1}}\right)^2 \sin^2(\Omega_{\pm 1} t). \tag{3.47}$$

In other words, the two state system possesses a DJ resonance at $D = \pm J$. If instead the state transition is in the $m = \pm 2$ block, the Rabi frequency is $\Omega_{\pm 2} = \frac{3}{2}|J|$ with an amplitude of,

$$P_{\pm 2}(t) = \frac{8}{9} \sin^2(\Omega_{\pm 2} t). \tag{3.48}$$

Thus in the $m = \pm 2$ block, there is no DJ resonance, and the maximum transition probability amplitude is 8/9. This maximum matches the maximum amplitude in the $S_{1,2,3} = \frac{1}{2}$ model where anisotropy does not play a role. We also note that in the trimer model, another DJ resonance exists within a different basis: the product basis. In that basis, there are two two-dimensional blocks that contain the transitions between the $|2, \pm 1\rangle_B$ and $|1, \pm 1\rangle_B$ states. They take the form,

$$\mathcal{H}_{\pm 1}^{\text{trimer}} = J\sigma_z \pm D\sigma_x. \tag{3.49}$$

We note the similarity to Eq. (3.45), but with the reversed role of D and J on Bloch vectors within the corresponding Bloch sphere. The Rabi frequency is the same ($\Omega_{\pm 1} = \sqrt{D^2 + J^2}$), and the transition probability amplitude reflects the D and J role reversal,

$$P_{\pm 1}(t) = \left(\frac{D}{\Omega_{\pm 1}}\right)^2 \sin^2(\Omega_{\pm 1} t). \tag{3.50}$$

3.4.4 Summary

In summary, we have demonstrated the general existence formula for DJ resonances and how these resonances enable full control of the Bloch vector in an appropriately chosen Bloch sphere representation. We also contrasted the difference in entanglement switching mechanisms for the spin $S_{2,3} = \frac{1}{2}$ and $S_{2,3} = 1$ models. We have shown that in order to achieve acceptable control of a Bloch vector within the $S_{2,3} = \frac{1}{2}$ model, additional mechanisms such as outgoing spin filters for particle 1 or anisotropy of the exchange interaction between particle 2 and 3 is required. Last, we have indicated several systems of interest where DJ resonances could be used to explore qubit scenarios and to discover fundamental phenomena.

3.5 List of References

[1] M. A. Nielsen and I. L. Chuang, *Quantum Computation and Quantum Information: 10th Anniversary Edition* (Cambridge University Press, Cambridge, 2010).

[2] A. Chatterjee, P. Stevenson, S. De Franceschi, A. Morello, N. P. de Leon, and F. Kuemmeth, Nature Reviews Physics **3**, 157 (2021).

[3] D. Loss and D. P. DiVincenzo, Physical Review A **57**, 120 (1998).

[4] J. R. Petta, A. C. Johnson, J. M. Taylor, E. A. Laird, A. Yacoby, M. D. Lukin, C. M. Marcus, M. P. Hanson, and A. C. Gossard, Science **309**, 2180 (2005).

[5] R. Hanson, L. P. Kouwenhoven, J. R. Petta, S. Tarucha, and L. M. K. Vandersypen, Reviews of Modern Physics **79**, 1217 (2007).

[6] A. Noiri, J. Yoneda, T. Nakajima, T. Otsuka, M. R. Delbecq, K. Takeda, S. Amaha, G. Allison, A. Ludwig, A. D. Wieck, and S. Tarucha, Applied Physics Letters **108**, 153101 (2016).

[7] A. Noiri, T. Nakajima, J. Yoneda, M. R. Delbecq, P. Stano, T. Otsuka, K. Takeda, S. Amaha, G. Allison, K. Kawasaki, Y. Kojima, A. Ludwig, A. D. Wieck, D. Loss, and S. Tarucha, Nature Communications **9**, 5066 (2018).

[8] T. Nakajima, A. Noiri, J. Yoneda, M. R. Delbecq, P. Stano, T. Otsuka, K. Takeda, S. Amaha, G. Allison, K. Kawasaki, A. Ludwig, A. D. Wieck, D. Loss, and S. Tarucha, Nature Nanotechnology **14**, 555 (2019).

[9] C. H. Yang, R. C. C. Leon, J. C. C. Hwang, A. Saraiva, T. Tanttu, W. Huang, J. Camirand Lemyre, K. W. Chan, K. Y. Tan, F. E. Hudson, K. M. Itoh, A. Morello, M. Pioro-Ladrière, A. Laucht, and A. S. Dzurak, Nature **580**, 350 (2020).

[10] R. C. C. Leon, C. H. Yang, J. C. C. Hwang, J. C. Lemyre, T. Tanttu, W. Huang, K. W. Chan, K. Y. Tan, F. E. Hudson, K. M. Itoh, A. Morello, A. Laucht, M. Pioro-Ladrière, A. Saraiva, and A. S. Dzurak, Nature Communications **11**, 797 (2020).

[11] M. N. Leuenberger and D. Loss, Nature **410**, 789 (2001).

[12] L. M. K. Vandersypen, M. Steffen, G. Breyta, C. S. Yannoni, M. H. Sherwood, and I. L. Chuang, Nature **414**, 883 (2001).

[13] R. Vincent, S. Klyatskaya, M. Ruben, W. Wernsdorfer, and F. Balestro, Nature **488**, 357 (2012).

[14] M. Ganzhorn, S. Klyatskaya, M. Ruben, and W. Wernsdorfer, Nature Nanotechnology **8**, 165 (2013).

[15] M. Urdampilleta, S. Klyatskaya, M. Ruben, and W. Wernsdorfer, Physical Review B **87**, 195412 (2013).

[16] S. Thiele, F. Balestro, R. Ballou, S. Klyatskaya, M. Ruben, and W. Wernsdorfer, Science **344**, 1135 (2014).

[17] K. S. Pedersen, A.-M. Ariciu, S. McAdams, H. Weihe, J. Bendix, F. Tuna, and S. Piligkos, Journal of the American Chemical Society **138**, 5801 (2016).

[18] K. Najafi, A. L. Wysocki, K. Park, S. E. Economou, and E. Barnes, The Journal of Physical Chemistry Letters **10**, 7347 (2019).

[19] D. Gatteschi and R. Sessoli, Angewandte Chemie International Edition **42**, 268 (2003).

[20] L. Bogani and W. Wernsdorfer, Nature Materials **7**, 179 (2008).

[21] S. M. Cronenwett, T. H. Oosterkamp, and L. P. Kouwenhoven, Science **281**, 540 (1998).

[22] M. N. Leuenberger and E. R. Mucciolo, Physical Review Letters **97**, 126601 (2006).

[23] G. González, M. N. Leuenberger, and E. R. Mucciolo, Physical Review B **78**, 054445 (2008).

[24] J. Kondo, Progress of Theoretical Physics **32**, 37 (1964).

[25] S. B. Tooski, B. R. Bułka, R. Žitko, and A. Ramšak, The European Physical Journal B **87**, 145 (2014).

[26] A. T. Costa, S. Bose, and Y. Omar, Physical Review Letters **96**, 230501 (2006).

[27] F. Ciccarello, G. M. Palma, M. Zarcone, Y. Omar, and V. R. Vieira, New Journal of Physics **8**, 214 (2006).

[28] F. Ciccarello, G. Massimo Palma, M. Paternostro, M. Zarcone, and Y. Omar, Solid State Sciences E-MRS symposium N and R, **11**, 931 (2009).

[29] W. C. Chung, J. de Hond, J. Xiang, E. Cruz-Colón, and W. Ketterle, Physical Review Letters **126**, 163203 (2021).

[30] R. Žitko, R. Peters, and T. Pruschke, Physical Review B **78**, 224404 (2008).

[31] S. Mehl and D. P. DiVincenzo, Physical Review B **92**, 115448 (2015).

[32] R. Hiraoka, E. Minamitani, R. Arafune, N. Tsukahara, S. Watanabe, M. Kawai, and N. Takagi, Nature Communications **8**, 16012 (2017).

[33] E. D. Switzer, X.-G. Zhang, and T. S. Rahman, Physical Review A **104**, 052434 (2021).

[34] S. Hill, R. S. Edwards, N. Aliaga-Alcalde, and G. Christou, Science **302**, 1015 (2003).

[35] I. I. Rabi, Physical Review **51**, 652 (1937).

CHAPTER 4: MAPPING SPIN INTERACTIONS FROM CONDUCTANCE PEAK SPLITTING IN COULOMB BLOCKADE

(Adapted from Eric D. Switzer, Xiao-Guang Zhang, Volodymyr Turkowski, and Talat S. Rahman, "Mapping Spin Interactions from Conductance Peak Splitting in Coulomb Blockade." arXiv:2301.05370 (2023))

4.1 Introduction

Determining the internal structure of a spin complex is important in both quantum information science (QIS) and spintronics. Examples of useful spin complexes include molecular magnets (MMs) [1–5], coupled quantum dots (QDs) [6–8], and many-electron QDs [9] because they possess properties like magnetic hysteresis, long spin-relaxation times, and protection against spin decoherence. A complete description of their eigenspectrum involves mapping the properties of their internal structure onto effective spin model Hamiltonians. Four common parameterized spin Hamiltonian terms for this purpose are magnetic anisotropy, exchange coupling between spin centers, exchange coupling of the spin centers with transitory electrons when the spin centers are placed between biased leads, and response to an applied magnetic field.

There is significant work, utilizing a combination of theory and experiment, to match model spin Hamiltonian terms to experimentally-accessible transport measurements. Several commonly used techniques to characterize magnetic systems are electron paramagnetic resonance spectra measurements for crystalline MM complexes [10–12], magnetic susceptibility measurements [13], neutron inelastic scattering [14], and magnetic circular dichroism spectroscopy [15]. Characterizing systems important to QIS and spintronics involves the use

of differential conductance measurements that exploit the Coulomb blockade (CB). Examples include probing exchange coupling and magnetic anisotropy for MM transistors such as $N@C_{60}$ [4] and Fe_4 [5], the exchange coupling of two or more coupled QDs [16–20], and the detection and manipulation of spin states [6–8] for QD qubits. In the blockade, the flow of electrons is blocked by their Coulomb repulsion at low temperature and small bias voltage applied across leads connected through a central region [21]. By constraining the dynamics to a single electron interacting with a complicated spin system, one can extract parameters based on repeated transport measurements.

Model approximations are often used for MMs, such as ignoring internal exchange coupling between spin centers and assuming a single spin S (giant spin approximation). For a certain class of spin complexes, this enables a tractable measurement scheme of some of the spin Hamiltonian terms [4, 5]. Other spin complexes, however, may not be described accurately by those approximations, such as Ni_4 single MMs (SMM) [1, 2] and Mn_3 dimer complexes [3]. In some molecular cases, and in general with qubit read/write operations for tripartite spin systems [22, 23], one must characterize all exchange couplings that are energetically relevant. Some approximations, such as ignoring a particular Hamiltonian term in MMs (e.g., between exchange coupling or magnetic anisotropy) cannot be made because they are both defined by the overlap of atomic orbitals belonging to the spin centers. Changing one of the aforementioned parameters inevitably means that the other parameter also changes.

Accurate measurements of all four parameters is then necessary in those cases to help screen materials for quantum architectures. In this paper we propose a scheme to map the four parameters of a particular class of spin complexes, namely exchange coupled spin dimers possessing magnetic anisotropy and coupled to an "indirect measurement" QD, using differential conductance and three experimentally-controlled parameters: anisotropically-applied magnetic field, bias voltage, and gate voltage. We rely on a rate equation-based

theoretical approach of an electron transiting through a QD in the CB, as rate equations have been successful at identifying conductance peak features in transport spectra for systems consisting of an SMM placed between leads [24–29]. By including all four parameters in our spin model, we find that one can use the number and location of the peaks in differential conductance to determine each of the model's Hamiltonian parameters.

The paper is organized as follows. In Sec. 4.2, we describe our model, write down the Hamiltonian and solve the generalized master equation to obtain closed equations for electronic current. In Sec. 4.3 we describe the role of the Hamiltonian terms in predicted differential conductance peaks. Last, in Sec. 4.4 and Sec. 4.5, we summarize the results and discuss the experimental scheme to measure the parameters for each Hamiltonian term.

4.2 Model and Hamiltonian

A three-terminal setup consisting of a source and drain electrode, and a gate, is found in many nanosized devices, including three-terminal coupled QDs [6–8], nuclear and molecular spin qubit transistors [30–32], and magnetic molecule tunneling junctions [33–36]. We consider a hybrid of the aforementioned setups by modeling a central region consisting of a QD influenced by two spin particles, connected to three terminals. This model is functionally equivalent to the models explored in [37, 38], but instead of exploring timescales in which coherence can be tracked, we focus on timescales in which incoherent transport is measured. The source and drain electrodes enable transport of an itinerant electron into the QD where it interacts with other spins via a spin exchange interaction. The energy levels of the central region are adjusted by the third terminal to bring the system into the CB regime. The overall model is shown schematically in Fig. 4.1.

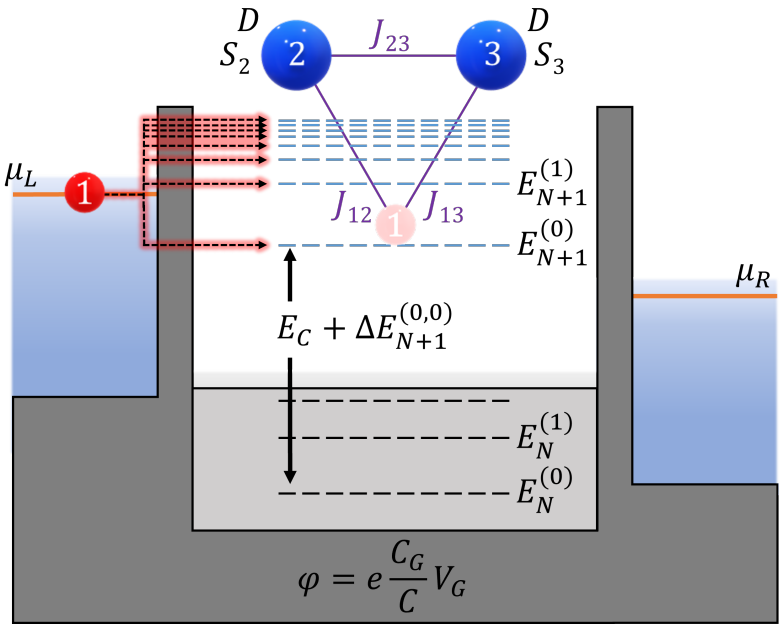

Figure 4.1: Schematic of the system consisting of a central scattering region, containing an $S_{2,3} = 1$ spin dimer complex interacting through an exchange interaction J_{23}, coupled to polarized leads at temperature T. The central region's eigenenergy levels are tuned via gate voltage V_G so that the charged ground state energy $E_{N+1}^{(0)}$ with $N+1$ electrons is aligned with the unbiased leads, i.e., $E_{N+1}^{(0)} = \mu_L = \mu_R = 0$ eV. Applying a symmetric bias voltage as shown enables transport of a single electron (particle 1) through the $N+1$ electron states. Once the electron has transported into the central region, and prior to leaving the central region, additional exchange interactions J_{1i} couples the electron's spin to the dimer.

4.2.1 Hamiltonian

The total Hamiltonian is,

$$\mathcal{H} = \mathcal{H}_{\text{leads}} + \mathcal{H}_{\text{leads-C}} + \mathcal{H}_{\text{C}}, \tag{4.1}$$

where each term in Eq. (4.1) is explained as follows. The energy of the electrons on the leads $\mathcal{H}_{\text{leads}}$ is,

$$\mathcal{H}_{\text{leads}} = \sum_{\alpha k\sigma} \left(\epsilon_{\alpha k} + \mu_\alpha\right) \hat{c}^\dagger_{\alpha k\sigma} \hat{c}_{\alpha k\sigma}, \tag{4.2}$$

where $\hat{c}^\dagger_{\alpha k\sigma}$ creates an electron in the left and right lead, $\alpha = L, R$, respectively, with energy $\epsilon_{\alpha k}$ relative to the chemical potential of the lead μ_α, momentum $k \equiv \mathbf{k}$, and spin state σ projected on the z-axis set by the easy-axis of the zero-field splitting term described later. We set the zero of the lead's chemical potential to the ground-state of the $N+1$ electron manifold of the central region, and the bias voltage is applied symmetrically such that $\mu_L = V_b/2$ and $\mu_R = -V_b/2$. The coupling of the leads to the central region can be described by the hybridization term $\mathcal{H}_{\text{leads}-\text{C}}$,

$$\mathcal{H}_{\text{leads}-\text{C}} = \sum_{\alpha k\sigma n} \left(t_{\alpha k\sigma} \hat{c}^\dagger_{\alpha k\sigma} \hat{d}_{n\sigma} + h.c. \right), \tag{4.3}$$

where $t_{\alpha k\sigma}$ is the tunneling amplitude of an electron with momentum k at lead α to level n, $\hat{d}^\dagger_{n\sigma}$ creates an electron with spin σ on the central region's eigenstate n, and we have assumed that the hopping rate is independent of n.

The central region Hamiltonian has the form,

$$\mathcal{H}_{\text{C}} = \mathcal{H}_{eS} + \mathcal{H}_{23} + \mathcal{H}_A + \mathcal{H}_Z + \mathcal{H}_E + \mathcal{H}_G. \tag{4.4}$$

$\mathcal{H}_{eS}$ refers to the exchange interaction of the electron in the QD with the two spin particles in the central region,

$$\mathcal{H}_{eS} = \delta_{N_e,1} \frac{1}{2} J_{1i} \sum_{in\mu\mu'} \hat{\mathbf{S}}_i \cdot \hat{d}^\dagger_{n\mu} \hat{\boldsymbol{\sigma}}_{\mu\mu'} \hat{d}_{n\mu'}, \tag{4.5}$$

where N_e is the number of extra electrons in the central region (i.e., the charge state), J_{1i} is the exchange interaction between an electron and the spin particles (assumed to be the same strength for each spin particle i), $\mathbf{S}_i$ is the spin operator for spin particle i, and $\hat{\boldsymbol{\sigma}}_{\mu\mu'}$ is the corresponding μ, μ' matrix element of the $s = \frac{1}{2}$ Pauli matrix. This form of the exchange interaction is derived by extending the single impurity Anderson model [39] to a two-impurity Anderson model, and transforming into the low energy regime by means of the Schrieffer-Wolff transformation [40]. The $\mathcal{H}_{23}$ term similarly refers to interactions between the two spin centers,

$$\mathcal{H}_{23} = J_{23}\hat{\mathbf{S}}_2 \cdot \hat{\mathbf{S}}_3, \tag{4.6}$$

where J_{23} characterize the exchange interaction between spin particle 2 and 3.

Next, the $\mathcal{H}_{\mathrm{A}}$ term originates from the spin-orbit interaction of one or more unpaired electrons in spin $S > \frac{1}{2}$ impurities, and describes the effective zero-field splitting (and magnetic anisotropy), of spin particle 2 and 3,

$$\mathcal{H}_A = D\left(\hat{S}_2^z\hat{S}_2^z + \hat{S}_3^z\hat{S}_3^z\right). \tag{4.7}$$

Here D is the magnitude of the uniaxial anisotropy strength, with the z direction determined by the preferential direction of the easy axis, and in general is dependent on the charge state. The $\mathcal{H}_Z$ term represents the applied magnetic field,

$$\mathcal{H}_Z = \mu_B\left(\delta_{N_e,1}g_1\hat{\boldsymbol{\sigma}} + g_2\hat{\mathbf{S}}_2 + g_3\hat{\mathbf{S}}_3\right)\cdot\mathbf{B}, \tag{4.8}$$

where g_i is the isotropic g factor for spin particle i, μ_B is the Bohr magneton, and $\mathbf{B} = B_x\hat{x} + B_y\hat{y} + B_z\hat{z}$ is an applied magnetic field. As indicated in this Hamiltonian term, the magnetic field is locally applied within the central region, and applies to the electron only if

it transits the central region.

The last two Hamiltonian terms are electrostatic in nature and describe the charging energy of the central region and the applied gate voltage [41],

$$\mathcal{H}_E + \mathcal{H}_G = \frac{N_e^2}{2} E_C - N_e e \frac{C_G}{C} V_G, \tag{4.9}$$

where E_C is the charging energy $e^2/2C$, e is the charge of the electron, C is the total capacitance across the barriers, C_G is the capacitance of the central region connected to the gate, and V_G is the gate voltage. In this work, we do not include $N+2$ and $N-1$ electron manifolds (i.e., $N_e = 2$ and $N_e = -1$, respectively) because those manifolds are assumed to be energetically unfavorable. We also rescale V_G to highlight the net effect of the gate voltage on transport properties by performing the transformation $\frac{C_G}{C} V_G \to V_G$. Under the manifold assumption, the electrostatic terms become,

$$\mathcal{H}_E + \mathcal{H}_G = \frac{1}{2} E_C - e V_G, \tag{4.10}$$

for the $N+1$ electron manifold, and zero for the N electron manifold. As will be useful later, we define $\Delta E^{(i,j)}_{N,N+1} \equiv E^i_N - E^j_{N+1}$ as the energy difference of the i'th and j'th eigenstate of the N and $N+1$ manifold, where $i = 0$ defines the ground state of that manifold. The magnetic parameters chosen for our model are on the order of cm^{-1}, as is common with MM systems. Similarly, for parameters that can be easily tuned experimentally, the fields are on the order of T, while the electrostatics are on the order of mV to access useful transport properties.

4.2.2 Model Details

We work in the regime appropriate for single-charge dynamics, i.e., the CB regime, along with weak lead-central region interactions. As a result, third-order and higher terms of the lead-central region perturbation will not contribute much to the dynamics of the system's density matrix. This allows consideration up to second-order in the perturbation, enabling access to a tractable solution of electronic current.

The system's density matrix can be decoupled into two parts,

$$\rho_I(t) = \rho_C(t)\rho_{\text{leads}}(0), \tag{4.11}$$

where $\rho_I(t)$ is the density matrix of the system in the interaction picture, $\rho_C(t)$ is the density matrix of the central region, and $\rho_{\text{leads}}(0)$ is the density matrix of the leads before the perturbation term is turned on. As a consequence of the weak lead-central region interaction and CB, the time-dependent spin entanglement predicted in Ref. [22, 23] will not be accessible. In order for equation Eq. (4.11) to hold, the entanglement information between an electron coupled with the central region must be lost after some time $t = t_c$, where t_c is on the order of the coherence time of the system.

Because the reservoir is split into two leads, they are presumed to not interact with each other nor possess spin levels that interact with each other. The density matrix of the leads can then be separated by lead and by spin,

$$\rho_{\text{leads}}(0) = \rho_{L\uparrow}(0) \otimes \rho_{L\downarrow}(0) \otimes \rho_{R\uparrow}(0) \otimes \rho_{R\downarrow}(0). \tag{4.12}$$

The constant density matrix of the leads essentially means that the central region does not have an appreciable effect on the leads, and the leads maintain a thermal equilibrium. This is a statement of irreversibility of the system considered in this work.

Next we assume the Markov approximation, in that the behavior of the central region is not related to its behavior at any past time. This is justified because we assume that the coupling of the central region to the leads is at least strong enough to dampen any long-term correlations. To allow the Markov approximation to hold, we consider times longer than the natural frequency of oscillations between two central region energy states n and n', $t \gg \hbar/\left|\omega_{n'n}\right|$.

We assume that the coupling of the central region to the environment of the leads is weak enough in which the change of the total density matrix in the interaction picture is slow. By choosing a long time in which the Redfield relaxation tensor is approximately independent of time, we use the secular approximation by maximizing the exponential factor in front of the Redfield relaxation tensor to be unity. The surviving secular terms are bound by energies that satisfy $\omega_{n'n} - \omega_{N'N} = 0$ where the difference is defined between the natural frequency of between two states of the central region $\omega_{n'n}$ and the natural frequency of two states in the leads $\omega_{N'N}$.

4.2.3 Generalized Master Equation

We next follow the well-known Fermi golden rule approach to Coulomb blockade transport and construct the generalized master equation. We assume that quasiparticle lifetime τ_q within those manifolds greatly depends on their relative energies, i.e., $\tau_q \ll \hbar/|\Delta E^{(i,j)}_{N,N+1}|$. By inspecting the magnitude of $\Delta E^{(0,2)}_{N,N+1}$, the quasiparticle lifetime of this excitation is likely too short to participate in transport across the leads. Higher-order excitations with energy differences $\Delta E^{(i,j)}_{N,N+1}$ for $i > 1$ or $j > 1$ do not participate in electron transport if the transport channel involving $\Delta E^{(0,2)}_{N,N+1}$ does not participate.

For our model, the generalized master equation is then,

$$\dot{\rho}_{n'n}(t) = \frac{i}{\hbar}\left[\rho(t), \mathcal{H}_0\right]_{n'n} + \delta_{n'n} \sum_{m,n\neq m} \rho_{mm}(t) W_{n'm} - \gamma_{n'n}\rho_{n'n}(t), \tag{4.13}$$

where $\rho(t)$ refers to the *central region's* density matrix, $\rho(t) = \rho_C(t)$, and with the notation $\mathcal{H}_{n'n} \equiv \langle n'|\mathcal{H}_0|n\rangle$, $\rho_{n'n} \equiv \langle n'|\rho(t)|n\rangle$. Each term in Eq. (4.13) is explained as follows.

The first term on the right-hand side of Eq. (4.13) is the usual evolution of the central region's Hamiltonian containing the QD and multi-spin system, and the lead Hamiltonian. The dynamics of the system due to the coupling of the leads is given in the next two terms. The second term contains the transition rates between eigenstates of the system $W_{n'm}$ from state $|m\rangle$ to $|n'\rangle$ and is a sum of the contributions from each lead and spin polarization, i.e., $W_{n'm} = \sum_{\alpha\sigma} W^{\alpha\sigma}_{n'm}$. These rates are derived in Appendix B. The result for the $N \to N+1$ ("absorption") electron manifold transitions are,

$$W^{\alpha\sigma}_{c_i u_j} = w_{\alpha\sigma}\nu_{\alpha\sigma} \left|\langle c_i|\hat{c}^\dagger_{\alpha\sigma}|u_j\rangle\right|^2 f_\alpha(\Delta E^{(i,j)}_{N+1,N}), \tag{4.14}$$

where $w_{\alpha\sigma} = 2\pi|t_{\alpha\sigma}|^2 D(E_f)/\hbar$ are the lead and polarization dependent transition rate constants, $f_\alpha(E)$ is the Fermi function of lead α, $D(E_f)$ is the density of states at the Fermi energy, and $\nu_{\alpha\sigma}$ is the fractional polarization of lead α constrained to the normalization condition $\nu_{\alpha\uparrow} + \nu_{\alpha\downarrow} = 1$. For example, the leads can be chosen to be fully polarized, e.g, $\nu_{L\downarrow} = \nu_{R\uparrow} = 1.0$ and $\nu_{R\downarrow} = \nu_{L\uparrow} = 0.0$, or non-polarized, i.e., $\nu_{\alpha\sigma} = 0.5 \;\forall\; \alpha, \sigma$. The transition rates for $N+1 \to N$ ("emission") electron manifold transitions are similarly,

$$W^{\alpha\sigma}_{u_i c_j} = w_{\alpha\sigma}\nu_{\alpha\sigma} \left|\langle u_i|\hat{c}_{\alpha\sigma}|c_j\rangle\right|^2 \left(1 - f_\alpha(\Delta E^{(j,i)}_{N+1,N})\right). \tag{4.15}$$

The last term on the right-hand side of Eq. (4.13) contains a damping factor $\gamma_{n'n}$, also derived in Appendix B. This factor is a consequence of the lead's interaction with the central region, and is defined for states $n' \neq n$ as,

$$\gamma_{n'n} = \frac{1}{2}\sum_{m}\left(W_{mn'} + W_{mn}\right) + \frac{1}{T_2}, \tag{4.16}$$

where T_2 is the spin decoherence time. This T_2 time can be due to a variety of sources such as spin-spin coupling with the system and the reservoir, e.g., between the magnetic moment of the spin particles and the magnetic moment of the atoms in the surrounding substrate. T_2 times have a range of magnitudes depending on the spin system of interest at low temperatures $T \approx 1$ K, such as 10^{-7} s for magnetic adatoms on surfaces, 10^{-7} to 10^{-5} s for QDs, and 10^{-4} to 10^{-1} s for systems of donor electrons embedded in silicon [42].

To produce relevant predictions from the generalized master equation, we look at a time range in which the overall relaxation time due to transitions τ, e.g., phonon-induced, is much longer than the decay of the off diagonal elements $\tau_d = 1/\gamma_{mm'}$. This means that for $\rho_{n'n}(t) \propto e^{-t/\tau_d} \rightarrow \dot{\rho}_{n'n}(t) = -(1/\tau_d)e^{-t/\tau_d}$, so we choose a long enough time such that $t >> \tau_d$ so that $\dot{\rho}_{n'n}(t) \rightarrow 0$. We find that to in order to have non-zero electronic current, this condition is equivalent to the requirement that the off-diagonal terms of each electron manifold must be non-zero, agreeing with the conditions of non-zero current of a similar model in Ref. [33, 34]. Finally, the diagonal elements of the differential density matrix are solved by assuming the steady-state case, i.e., choosing some time $t_s >> 1/W_{mm'}$ to obtain closed equations of the density matrix elements $\rho_{nn} \equiv \rho_{nn}(t_s)$. We define the current through the central region as the transition from the charged to uncharged state across lead α and polarization σ. The long-time steady-state current is then,

$$I_T = \left(I_{R\uparrow} - I_{L\uparrow}\right) + \left(I_{R\downarrow} - I_{L\downarrow}\right), \tag{4.17}$$

where,

$$I_{\alpha\sigma} = e\left(W^{\alpha\sigma}_{u_0c_0} + W^{\alpha\sigma}_{u_1c_0}\right)\rho_{c_0c_0} + e\left(W^{\alpha\sigma}_{u_0c_1} + W^{\alpha\sigma}_{u_1c_1}\right)\rho_{c_1c_1}, \tag{4.18}$$

is the steady-state current through lead α with spin polarization σ.

4.3 Results

4.3.1 Field-Dependent Energy Level Shifts

We first choose a system with parameters that will incorporate all dynamics presented in prior sections, while simplifying some parameter choices in order to highlight the role of each interaction in the total Hamiltonian. To this end, we assume an easy axis anisotropy for S_2 and S_3, $D = -0.6$ cm^{-1}, an isotropic antiferromagnetic coupling between the centers with $J_{23} = 0.6$ cm^{-1}, an isotropic ferromagnetic coupling of the itinerant electron with each center, $J_{1i} = -0.8$ cm^{-1}, and a charging energy of $E_C = 1$ meV. To obtain non-zero current within a chosen bias window, we set the charge-state decoherence to 10 μeV. The gate voltage is initially set to $V_G = 0$ mV. For simplicity, the g factors of the three spin particles are assigned the same value 2.2. A small longitudinal magnetic field, parallel to the zero-field easy axis, is applied to aid in numerical convergence, $B_z = 0.1$ mT. The temperature is set to be sufficiently low for the CB to hold, at $T = 0.1$ K. For our figures, we choose non-polarized leads. The tunneling rates are chosen to be $w_{\alpha\sigma} = 10$ GHz. The spin decoherence time is set to be on the order of some magnetic molecules at $T_2 = 5.0$ ns [43].

We diagonalize each block of the uncharged and charged sectors for various choices of applied transverse magnetic field B_x and B_y, B_x, $B_y \geq 0$. We find that the energetics and transport behavior of this system are dependent on the magnitude of the applied transverse

magnetic field, and not the direction of the field on the plane perpendicular to the shared easy axis of spin particle 2 and 3. This contrasts the energy differences and asymmetric transport as a function of applied magnetic field predicted in Ref. [33, 34] because our transport equations are derived to use the eigenstates of the central region Hamiltonian, allowing us to consider additional transitions. We also do not see a dependence on the direction of the transverse field because there is no energetic preference towards a particular direction in any of the spin Hamiltonian terms (e.g., the lack of a $E(\hat{S}_x^2 - \hat{S}_y^2)$ term).

The transition rates of Eq. (4.14) and Eq. (4.15) used in the transport equation crucially depend on the energy differences between electron manifolds $\pm\Delta E_{N,N+1}^{(i,j)}$. The validity of the form of the transition rates is also dependent on maintaining the CB, which in turn is dependent on the energy levels of the central region and applied bias. Each contribution in the total Hamiltonian, then, will play a role in the transport equations. To elaborate on the roles of the Hamiltonian terms, we inspect the first four energy levels for each charge sector in Fig. 4.2 for a fixed transverse field of $B_{trans} = 2.0$ T. For these choices of parameters, if the $\mathcal{H}_{23}$ and $\mathcal{H}_E$ interactions are turned on and the other interactions are off, the uncharged sector contains a non-degenerate ground state, and a three-fold degenerate first excited state. The ground and first-excited state of the charged sector are each two-fold degenerate. When the zero-field splitting $\mathcal{H}_A$ is turned on, the three-fold degeneracy of the uncharged sector is broken. The energy differences between ground and excited states of both manifolds are shifted as a result, and appear to approach a shared value. Turning on the transverse magnetic field H_Z completely breaks the degeneracy of both charge sectors. The resulting energy differences, however, become degenerate. We find that this degeneracy occurs around 0.2 T for the parameters used for Fig. 4.2, and persists for fields up to 2.0 T. When the exchange interaction of the electron is included, the energy difference symmetry is broken.

We further investigate the dependency of the energy levels and energy differences,

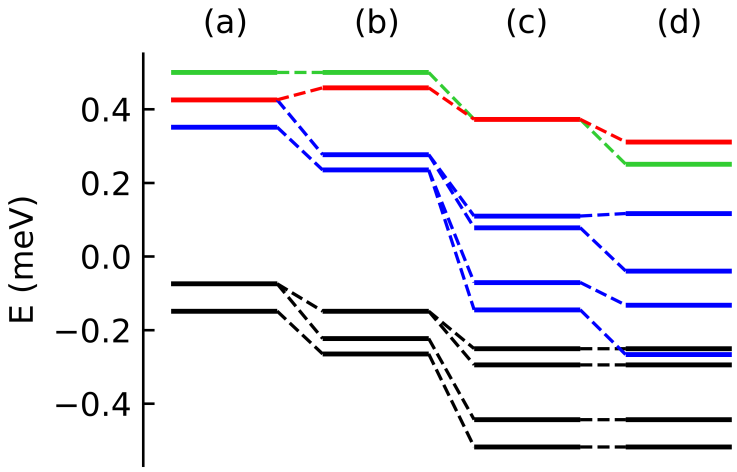

Figure 4.2: First four energy levels of the N (black) and $N+1$ (blue) central region electron manifolds. Energy differences $\Delta E^{(0,0)}_{N+1,N}$ (green) and $\Delta E^{(1,1)}_{N+1,N}$ (red) are also plotted. (a) Only $\mathcal{H}_{23}$ and $\mathcal{H}_E$ interactions are turned on, with $J_{23} = 0.6$ cm^{-1} and $E_C = 1$ meV. (b) The zero-field splitting term $\mathcal{H}_A$ is turned on with $D = -0.6$ cm^{-1}. (c) The applied magnetic field term $\mathcal{H}_Z$ is turned on with a sufficiently high field, $B_x = 0.5$ T, resulting in degenerate energy differences. (d) Finally, the exchange interaction $\mathcal{H}_{eS}$ is turned on, $J_{1i} = -0.8$ cm^{-1}, breaking the degeneracy.

as a function of the applied transverse field, as shown in Fig. 4.3 and Fig. 4.4, respectively. Fig. 4.3 displays interesting level crossing and avoided crossing behavior for applied fields in the range of $B_{trans} = 0$ T and $B_{trans} = 1.5$ T. The interesting level crossing and avoided crossing behavior also appears in the energy differences as shown in Fig. 4.4. The same level crossings in the range of $B_{trans} = 0$ T and $B_{trans} = 1.5$ T result in a flip of energetic ordering of the excited state $\Delta E^{(1,1)}_{N+1,N}$ and ground state $\Delta E^{(0,0)}_{N+1,N}$ transitions. Using the eigenstates projected onto the axis corresponding to the magnetic anisotropy Hamiltonian term, the transverse magnetic field mixes states with different total S^2 and m_S spin quantum numbers. The resulting spin eigenvectors are found to primarily have $m_S = 0$ and a non-trivial S^2 value as shown in Fig. 4.5.

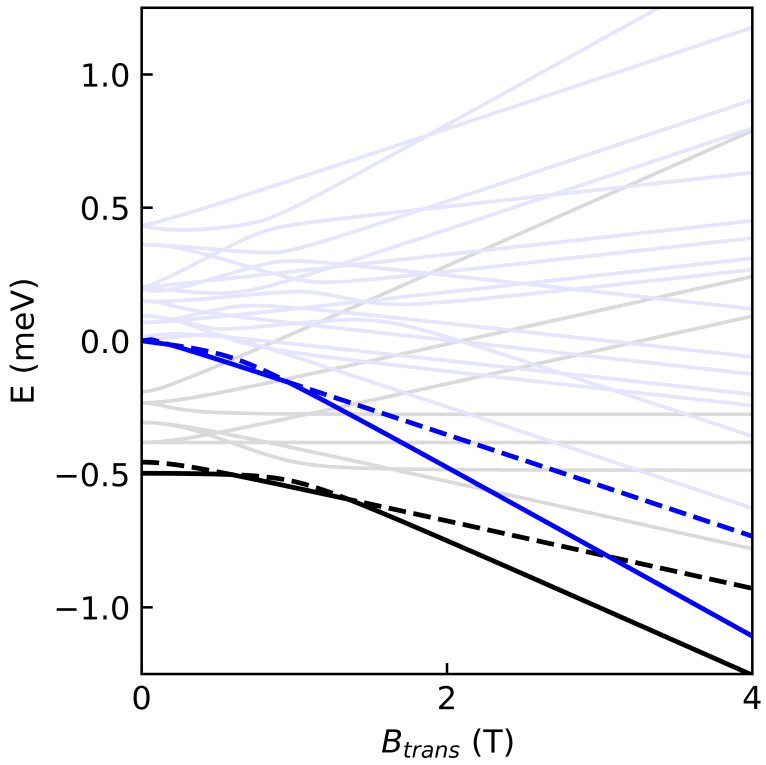

Figure 4.3: Energy levels E of the N (black) and $N+1$ (blue) central region electron manifold. The ground (solid), first excited (dashed), and higher-order (light solid) states are plotted using the parameters given in the text, as a function of applied transverse magnetic field B_{trans}.

4.3.2 Impact on Differential Conductance

Next we solve the current equation Eq. (4.18) for the system used in the prior section in order to demonstrate the impact of the spin Hamiltonian eigenvalue differences on differential conductance. We apply a transverse field of 2.0 T, sweep the bias voltage from -1 mV to +1 mV, and numerically differentiate the current with respect to the bias voltage to obtain predicted differential conductance. The results are shown in Fig. 4.6. Changing the spin Hamiltonian parameters results in different conductance spectra. Using the magnitude of J_{1i} parameter as an example, we find two conductance peaks when the electron-dimer exchange

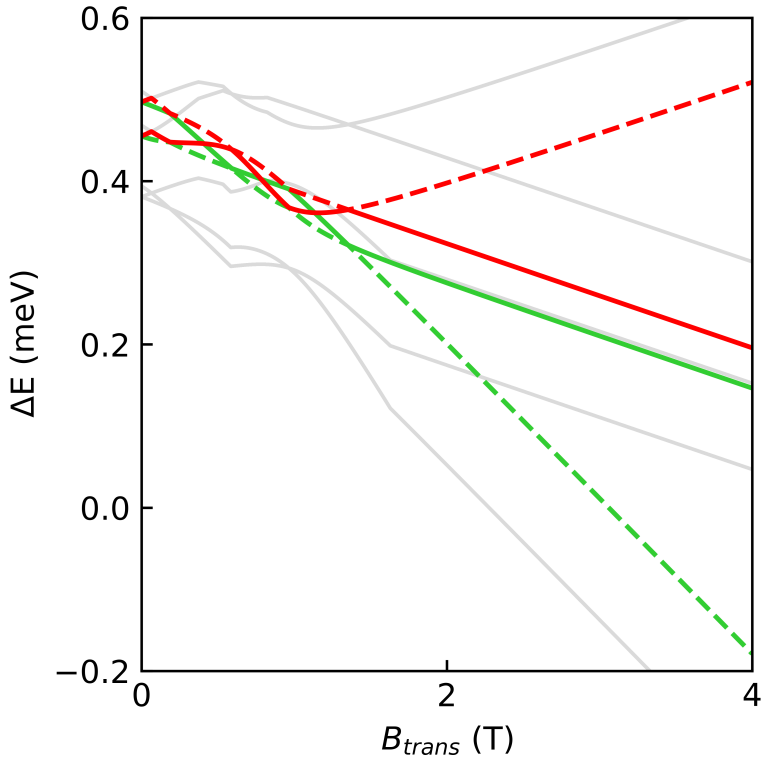

Figure 4.4: Energy difference ΔE values for the $N \to N+1$ electron manifold transitions. Energy differences are plotted by their transition type: $\Delta E^{(0,0)}_{N+1,N}$ (green solid), $\Delta E^{(0,1)}_{N+1,N}$ (green dashed), $\Delta E^{(1,0)}_{N+1,N}$ (red dashed), $\Delta E^{(1,1)}_{N+1,N}$ (red solid), and the subset of differences involving the second excited state of both manifolds (gray).

coupling is turned off, as would be expected for a system within CB conditions. As the absolute magnitude of the exchange coupling is increased, additional peaks appear. Each peak is found to correspond with the energy differences of the ground states $\Delta E^{(0,0)}_{N+1,N}$ and excited states $\Delta E^{(1,1)}_{N+1,N}$ as the energy differences enter the bias window. If the magnitude of J_{1i} is increased, the peaks become more aligned with the value $\pm 2\Delta E^{(k,k)}_{N+1,N}$ involving the k'th energy states.

Next we investigate the differential conductance as a function of both gate and bias voltage. The results are shown in Fig. 4.7. A Coulomb diamond-like feature appears in the

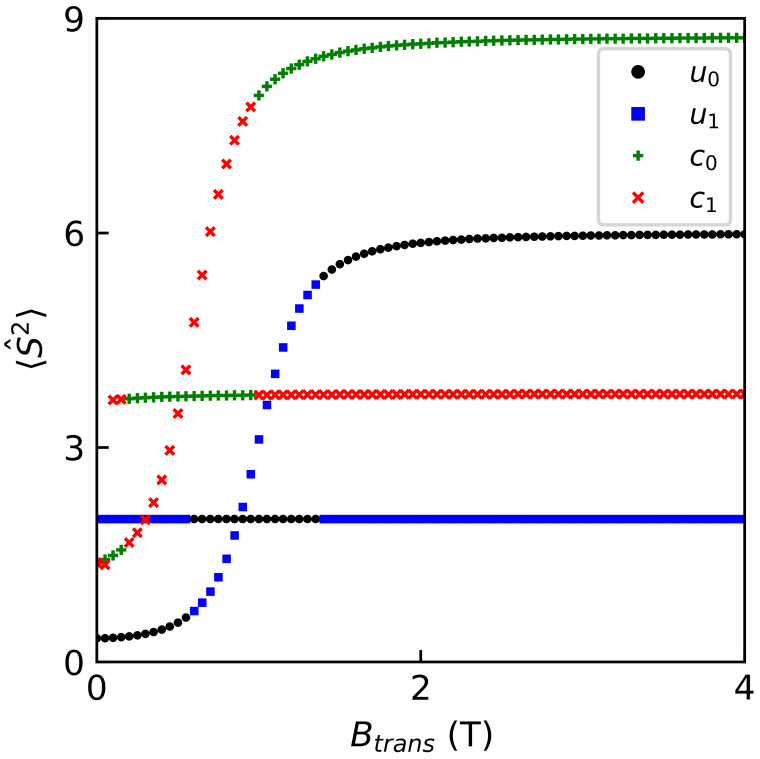

Figure 4.5: S^2 projections of the first two states in the uncharged and charged manifolds.

plot, with more than one conductance maxima lines proportional to the magnitude of the bias and gate voltages. When the exchange interaction of the itinerant electron with the dimer is turned off and the excitation energies become degenerate, these features disappear, and the typical Coulomb diamond plot is reproduced.

4.3.3 Mapping of Spin Hamiltonian Parameters

The finding from the prior section suggests that one could use differential conductance measurements to characterize and parameterize the spin Hamiltonian. The mapping procedure to the model in this work is complicated by four parameter types, J_{1i}, J_{23}, D, and g_i. To make the procedure tractable, we first assume the same simplifications of the last section,

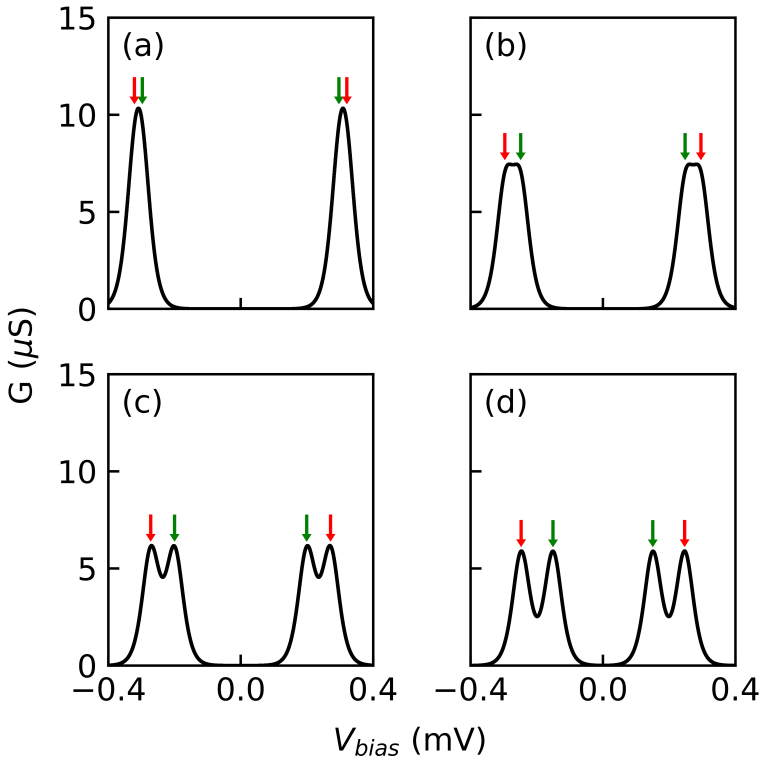

Figure 4.6: Differential conductance G as a function of bias voltage for $V_{gate} = 0.2$ mV. Four peaks of conductance correspond with key energy difference values entering the bias window, $\pm 2\Delta E^{(0,0)}_{N+1,N}$ (green arrow) and $\pm 2\Delta E^{(1,1)}_{N+1,N}$ (red arrow), broadened by temperature. The values of J_{1i} (in units of cm^{-1}) are (a) -0.2, (b) -0.4, (c) -0.6, and (d) -0.8.

but now allow D, J_{23}, and J_{1i} to take on reasonable values. The range of values chosen are provided as an example of the energy range relevant for MMs and QDs. The magnetic anisotropy is allowed to take on a representative "easy" axis, no axis, and "hard" axis values: $D \in \{-0.6,\ 0.0,\ 0.6\}$ cm^{-1}. Similarly, we choose the dimer exchange coupling to be either ferromagnetic or antiferromagnetic: $J_{23} \in \{-0.6,\ 0.6\}$ cm^{-1}. Last, we choose the dot-dimer exchange coupling to be either ferromagnetic, "weakly" ferromagnetic, weakly antiferromagnetic, or antiferromagnetic: $J_{1i} \in \{-0.8,\ -0.08,\ 0.08,\ 0.8\}$ cm^{-1}. We assume that the J_{1i} value is non-zero to ensure the QD's coupling to the spin space of the dimer. We also assume

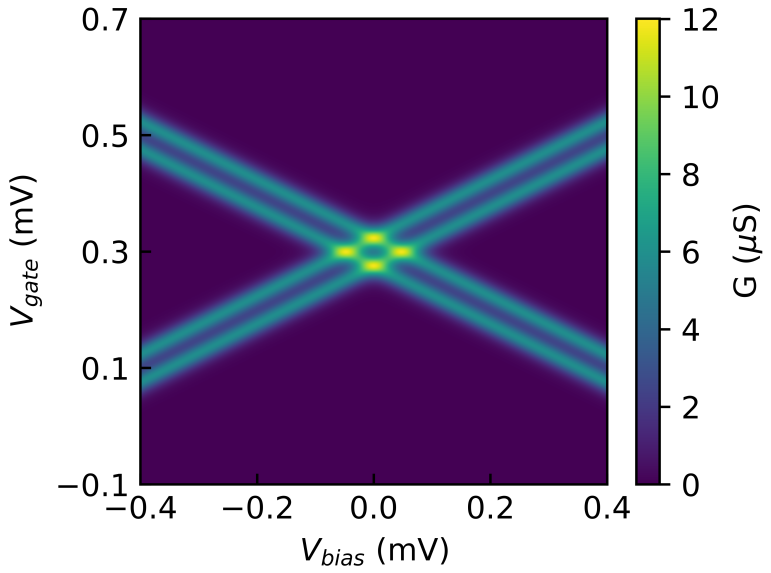

Figure 4.7: Differential conductance G as a function of bias voltage and gate voltage. For the parameter set chosen, four conductance lines are clearly seen, associated with the inclusion of four energy difference values as bias is increased.

that the g factor of each spin center in the dimer has the same value, but can be different from the QD's effective g factor of 2.2: $g_{23} \in \{2.2,\ 3.2,\ 4.2\}$.

The first stage in the mapping of the parameters is to make differential conductance measurements without the use of an applied magnetic field. By doing so, the Zeeman term of the Hamiltonian disappears, and the g factor does not need to be parameterized in this stage. We explore the parameter space of J_{1i}, J_{23}, and D using the V_{gate} and V_{bias} independent variables. The key highlights of the dependency of the conductance spectra on the sign of J_{1i} and the sign of D is highlighted in Fig. 4.8.

The next stage in mapping of the parameters is to utilize the Zeeman field to investigate Hamiltonian terms that should be sensitive to the field magnitude. We also set $B_{trans} = 2.0$ T for those independent variable combinations that do not involve it, such as the dependence of conductance on B_z and V_{bias}. We find important changes in the conductance

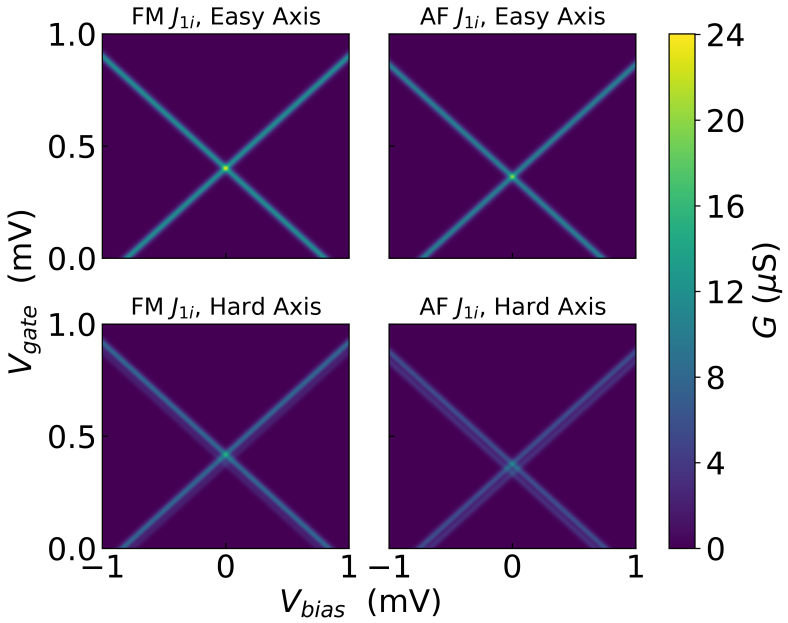

Figure 4.8: Differential conductance G as a function of bias voltage and gate voltage, with a ferromagnetic J_{23} parameter. The correspondence of plot labels to numerical parameters can be found in the text of Section 4.3.3.

to identify the sign and magnitude of J_{1i} and the sign of J_{23} as shown in Fig. 4.9.

Once the signs and magnitudes of J_{1i}, J_{23}, and D have been determined, we create a third stage of measurements to get information on the g factor. We find in Fig. 4.10 that it is relatively easy to see changes in the conductance spectra at the resolution of our example using the parallel-aligned applied magnetic field and bias voltage because the change in location and magnitude of the peaks is dependent on the magnitude of the g factor.

Finally, noting that the sensitivity of the magnitude of the exchange coupling strength of the QD and the spin system is apparent in the prior figures, we further explore the role of the magnitude and sign of J_{1i} in Fig. 4.11. As the absolute magnitude of the exchange coupling is increased from $J_{1i} = 0.0$ cm^{-1}, the double peak feature is broken into four peaks. If a gate voltage is applied, one can access the three-peak regime within a chosen bias window,

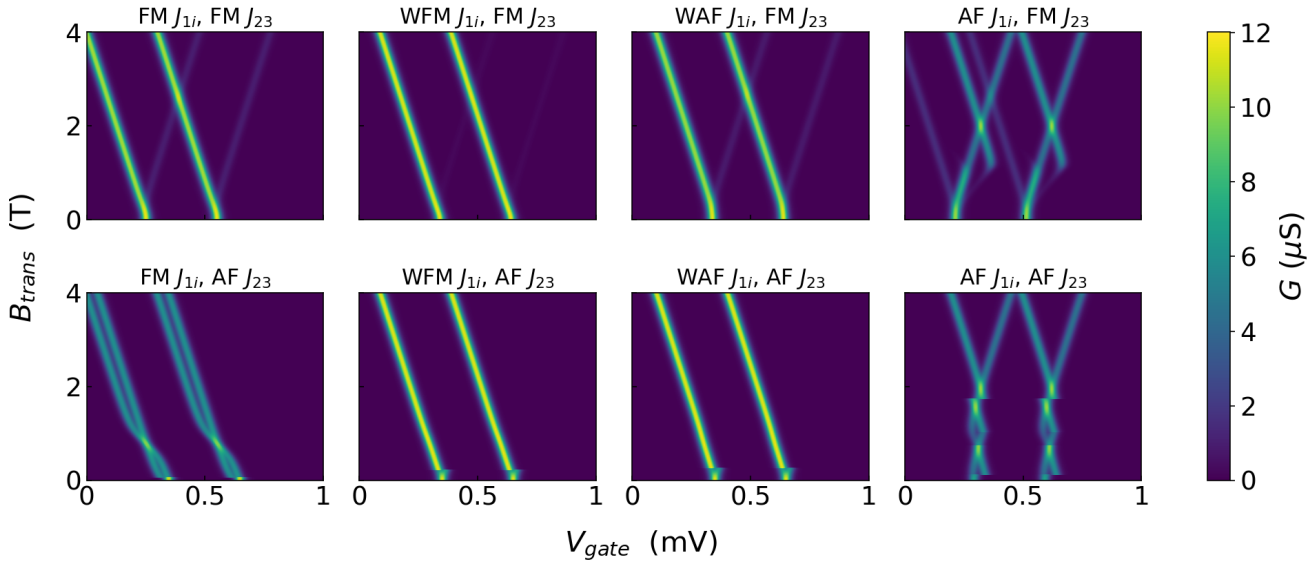

Figure 4.9: Differential conductance G as a function of gate voltage and transverse applied magnetic field, with an easy axis D. The correspondence of plot labels to numerical parameters can be found in the text of Section 4.3.3.

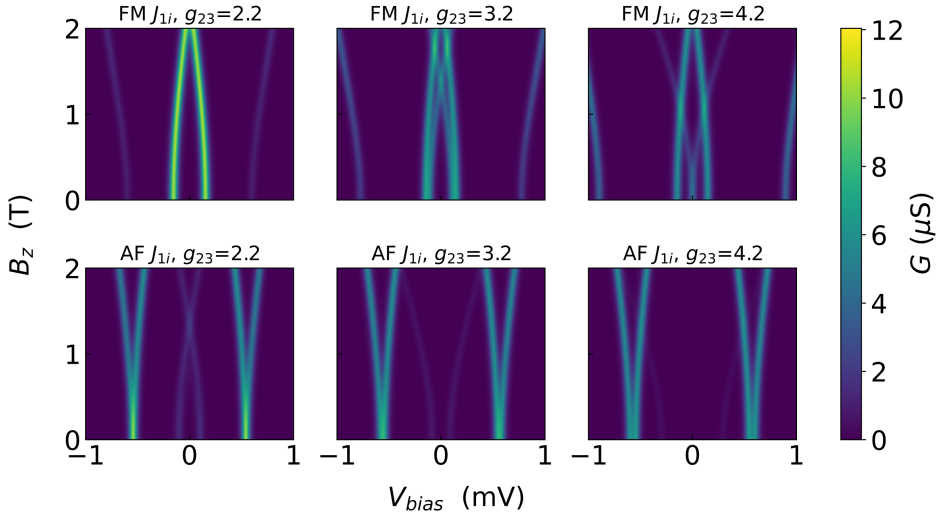

Figure 4.10: Differential conductance G as a function of bias voltage and parallel applied magnetic field, with an easy axis D and a ferromagnetic J_{23}. The correspondence of plot labels to numerical parameters can be found in the text of Section 4.3.3.

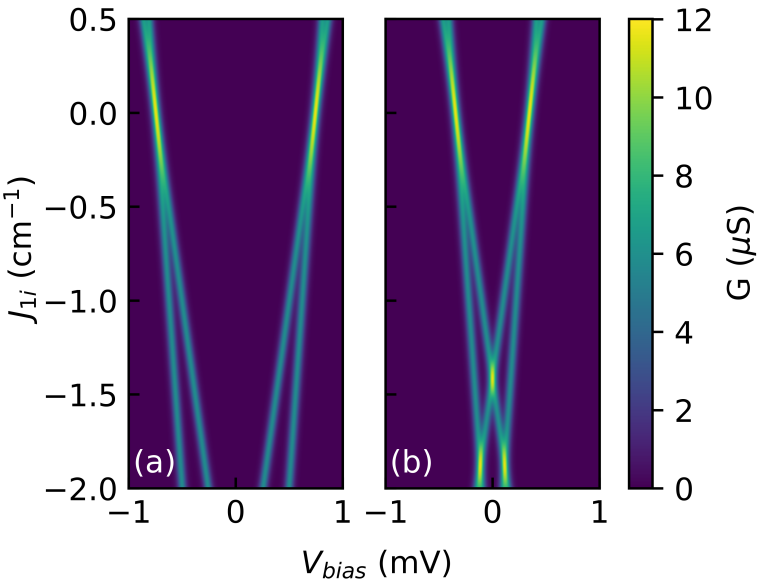

Figure 4.11: Differential conductance G as a function of bias voltage and exchange coupling J_{1i}. The exchange coupling breaks the symmetry of the conductance peaks as the absolute magnitude is increased from $J_{1i} = 0.0$ cm^{-1}. Different gate voltage V_{gate} at (a) 0.0 mV and (b) 0.2 mV changes the bias needed to split the conductance peaks.

and even revert to two conductance peaks for large enough J_{1i}. The choice of gate voltage is equivalent to accessing different parts of the Coulomb diamond shown in Fig. 4.7.

4.4 Discussion

The dependency of the conductance splitting on each spin Hamiltonian parameter is evident in Figures 4.8-4.11. The measurement scheme, involving each of the three stages, is the main result of this paper. Parameterizing all four spin Hamiltonian terms at once is a difficult task, and so we find that the three-stage process listed here is a method to constrain the parameter search by simplifying the parameter space at each stage. We first note the reason why different peaks and lines appear in the differential conductance plots. The splitting of conductance peaks are explained by the inclusion of additional energy differences (and thus

additional transport channels) in the bias window, as shown in Fig. 4.6. Both the $\Delta E^{(0,0)}_{N+1,N}$ and $\Delta E^{(1,1)}_{N+1,N}$ energy differences are degenerate at zero exchange coupling, which leads to only two peaks appearing in the differential conductance plots. We have found that this degeneracy appears only when a critical threshold of B_{trans} is reached depending on the parameters of J_{23}, D, and g.

The features resulting from energy difference degeneracy and change of ordering of the ground states for each charge manifold appear to allow one to probe different regimes for a chosen parameter combination. In Fig. 4.8, we find that for ferromagnetic J_{23}, one can determine the sign of D and J_{1i} by comparing the peak magnitude and location of the differential conductance and the number of conductance lines. When comparing the lower-left corner of Fig. 4.9 to Fig. 4.5, we see that the re-ordering of the ground state leads to observed changes in the conductance spectra. That particular conductance plot is unique to the parameter choices we explore, in comparison to the other combinations of ferromagnetic and antiferromagnetic J_{1i} and J_{23} for an easy D axis. There are still challenges, however, when searching for particular parameter combinations in each stage. For example, if J_{23} is antiferromagnetic, it is difficult to discern differences in the conductance spectra within the first stage with zero applied magnetic field (see Fig. 2 in B).

While an analytical solution for the eigenenergies is not trivial, Fig. 4.11 demonstrates that one can still infer important information regarding the contribution of each parameter in the system to the additional conductance peaks. It's important to note the role of temperature. For example, with the small J_{1i} in 4.6, the peaks of conductance do not align with the energy difference values because of the finite temperature broadening induced by the Fermi functions in Eq. (4.14) and Eq. (4.15). Because of the temperature dependence in the transition rates equation, higher temperatures smooth out the energy differences, and thus the four peak features may be difficult to resolve in a conductance measurement. High enough temperature, however, will result in moving out of the regime that utilizes the CB,

in which our results are no longer applicable.

We also compare the results of this work to a similar approach that was used for systems that contained a few of the elements of our model Hamiltonian, but not its entirety. In the double dot model of Ref. [20], conductance peak splitting was found as a function of the interdot coupling. Comparing to our work, a similar type of coupling is accomplished through the $\mathcal{H}_{eS}$ Hamiltonian term. Instead of transport between the two dots in their work, our model has an effective spin interaction mediated between the two centers via $\mathcal{H}_{23}$ and onsite zero-field splitting terms $\mathcal{H}_A$, which establishes an energetic preference of states, and thus ordering of preferable transport channels.

An interesting feature can be seen in the energy differences shown in Fig. 4.4. Sweeping the transverse magnetic field within the parameter space changes the number of state transitions within a given bias window. If one were to extend our two electron manifold and eigenstate model to include the new transport channels, additional features in the electronic current should appear. Based on the results of Fig. 4.6, as long as the lowest transition $\Delta E^{(i,0)}_{N+1,N}$ for $i > 2$ is within the bias window, these additional state transitions would result in a change of the width and number of the predicted conductance peaks.

Our model can be extended to include more effects found in systems consisting of a QD coupled to a molecular complex or impurity. For example, one could introduce the effects of charging on the coupled spin system. It's known that the SMM Mn_{12} zero-field splitting parameter and other spin parameters change upon charging [44]. We find that accommodating for a charge state anisotropy in zero-field splitting results in similar or different conductance peak behavior depending on the parameter range. If we use the same parameters in Fig. 4.7, and instead choose an uncharged $D_0 = -0.6$ cm^{-1} and charged $D_1 \gtrapprox -1.2$ cm^{-1}, the four peak feature is retained. If one instead chooses $D_1 \lessapprox -1.2$ cm^{-1}, the four peak feature disappears.

4.5 Summary and Outlook

As has been shown, within the CB for the model of an itinerant electron originating from leads passing into a QD connected to a multi-spin complex, conductance peak splitting appears within a range of parameters related to the magnetic response of the central region. We have also shown that one may match the location and number of differential conductance peaks as a function of bias voltage, gate voltage, and anisotropically-applied magnetic field in order to effectively measure each parameter of the model spin Hamiltonian. This provides a mapping to experimentally determine these magnetic properties for increasingly small nanoscale devices, such as molecular transistors, using only electronic differential conductance.

One challenge with this mapping is the number of Hamiltonian parameters. Machine-learning methods may be used to help fit experimental differential conductance measurements to the model Hamiltonian explored in this work, using the results from this work as the starting point for a training set. In addition, sources of decoherence, the role of the magnitude of decoherence, and the impacts of higher spin $S_i > 1$ were not studied in this work. Investigations are needed to determine the relative impact of each property on the measured conductance and location of conductance peak splitting. Furthermore, this work assumes a steady-state transport measurement with unpolarized leads. From prior studies [22, 23], one can hypothesize that the itinerant electron will entangle the spin system and produce a time-dependent coherent current in short timescales. This time-dependent entanglement may be useful to quantum information science applications. Nano- and femto-timescale electron and spin current studies with polarized (and possibly asymmetric) leads are needed to fully explore that possibility.

4.6 List of References

[1] A. Wilson, J. Lawrence, E.-C. Yang, M. Nakano, D. N. Hendrickson, and S. Hill, Physical Review B **74**, 140403 (2006).

[2] A. Wilson, E.-C. Yang, D. N. Hendrickson, and S. Hill, Polyhedron Proceedings of the 10th International Conference on Molecule-based Magnets (ICMM 2006), **26**, 2065 (2007).

[3] S. Hill, S. Datta, J. Liu, R. Inglis, C. J. Milios, P. L. Feng, J. J. Henderson, E. d. Barco, E. K. Brechin, and D. N. Hendrickson, Dalton Transactions **39**, 4693 (2010).

[4] N. Roch, R. Vincent, F. Elste, W. Harneit, W. Wernsdorfer, C. Timm, and F. Balestro, Physical Review B **83**, 081407 (2011).

[5] E. Burzurí, R. Gaudenzi, and H. S. J. v. d. Zant, Journal of Physics: Condensed Matter **27**, 113202 (2015).

[6] A. Noiri, T. Nakajima, J. Yoneda, M. R. Delbecq, P. Stano, T. Otsuka, K. Takeda, S. Amaha, G. Allison, K. Kawasaki, Y. Kojima, A. Ludwig, A. D. Wieck, D. Loss, and S. Tarucha, Nature Communications **9**, 5066 (2018).

[7] T. Nakajima, A. Noiri, J. Yoneda, M. R. Delbecq, P. Stano, T. Otsuka, K. Takeda, S. Amaha, G. Allison, K. Kawasaki, A. Ludwig, A. D. Wieck, D. Loss, and S. Tarucha, Nature Nanotechnology **14**, 555 (2019).

[8] A. Noiri, K. Takeda, T. Nakajima, T. Kobayashi, A. Sammak, G. Scappucci, and S. Tarucha, Nature **601**, 338 (2022).

[9] R. C. C. Leon, C. H. Yang, J. C. C. Hwang, J. Camirand Lemyre, T. Tanttu, W. Huang,

J. Y. Huang, F. E. Hudson, K. M. Itoh, A. Laucht, M. Pioro-Ladrière, A. Saraiva, and A. S. Dzurak, Nature Communications **12**, 3228 (2021).

[10] E. Moreno Pineda, N. F. Chilton, R. Marx, M. Dörfel, D. O. Sells, P. Neugebauer, S.-D. Jiang, D. Collison, J. van Slageren, E. J. L. McInnes, and R. E. P. Winpenny, Nature Communications **5**, 5243 (2014).

[11] S. Hill, R. S. Edwards, N. Aliaga-Alcalde, and G. Christou, Science **302**, 1015 (2003).

[12] D. Gatteschi, R. Sessoli, and J. Villain, *Molecular nanomagnets*, Vol. 5 (Oxford University Press on Demand, 2006).

[13] N. Motoyama, H. Eisaki, and S. Uchida, Physical Review Letters **76**, 3212 (1996).

[14] S. Carretta, J. van Slageren, T. Guidi, E. Liviotti, C. Mondelli, D. Rovai, A. Cornia, A. L. Dearden, F. Carsughi, M. Affronte, C. D. Frost, R. E. P. Winpenny, D. Gatteschi, G. Amoretti, and R. Caciuffo, Physical Review B **67**, 094405 (2003).

[15] S. Piligkos, L. D. Slep, T. Weyhermüller, P. Chaudhuri, E. Bill, and F. Neese, Coordination Chemistry Reviews Deutsche Forschungsgemeinschaft Molecular Magnetism Research Report, **253**, 2352 (2009).

[16] F. R. Waugh, M. J. Berry, D. J. Mar, R. M. Westervelt, K. L. Campman, and A. C. Gossard, Physical Review Letters **75**, 705 (1995).

[17] J. M. Golden and B. I. Halperin, Physical Review B **53**, 3893 (1996).

[18] F. R. Waugh, M. J. Berry, C. H. Crouch, C. Livermore, D. J. Mar, R. M. Westervelt, K. L. Campman, and A. C. Gossard, Physical Review B **53**, 1413 (1996).

[19] J. Q. You and H. Z. Zheng, Physical Review B **60**, 13314 (1999).

[20] X. G. Zhang and T. Xiang, International Journal of Quantum Chemistry **112**, 28 (2012).

[21] D. V. Averin and K. K. Likharev, Journal of Low Temperature Physics **62**, 345 (1986).

[22] E. D. Switzer, X.-G. Zhang, and T. S. Rahman, Physical Review A **104**, 052434 (2021).

[23] E. D. Switzer, X. G. Zhang, and T. S. Rahman, Journal of Physics Communications **6**, 075007 (2022).

[24] F. Elste and C. Timm, Physical Review B **71**, 155403 (2005).

[25] F. Elste and C. Timm, Physical Review B **73**, 235305 (2006).

[26] C. Timm and F. Elste, Physical Review B **73**, 235304 (2006).

[27] M. Misiorny and J. Barnaś, Physical Review B **75**, 134425 (2007).

[28] M. Misiorny and J. Barnaś, Physical Review B **76**, 054448 (2007).

[29] K. Hymas and A. Soncini, Physical Review B **99**, 245404 (2019).

[30] S. Thiele, F. Balestro, R. Ballou, S. Klyatskaya, M. Ruben, and W. Wernsdorfer, Science **344**, 1135 (2014).

[31] K. Najafi, A. L. Wysocki, K. Park, S. E. Economou, and E. Barnes, The Journal of Physical Chemistry Letters **10**, 7347 (2019).

[32] H. Biard, E. Moreno-Pineda, M. Ruben, E. Bonet, W. Wernsdorfer, and F. Balestro, Nature Communications **12**, 4443 (2021).

[33] G. González and M. N. Leuenberger, Physical Review Letters **98**, 256804 (2007).

[34] G. González, M. N. Leuenberger, and E. R. Mucciolo, Physical Review B **78**, 054445 (2008).

[35] K. Hymas, *Quantum Spin Dynamics of Molecular Spintronic Devices Based on Single-molecule Nanomagnets*, Doctoral dissertation, The University of Melbourne (2020).

[36] Z. Zhang, Y. Wang, H. Wang, H. Liu, and L. Dong, Nanoscale Research Letters **16**, 77 (2021).

[37] C.-I. Kim, N.-C. Kim, C.-S. Yun, and C.-J. Kang, Physica B: Condensed Matter **646**, 414297 (2022).

[38] C.-I. Kim, N.-C. Kim, C.-S. Yun, and C.-J. Kang, Physics Letters A **453**, 128474 (2022).

[39] P. W. Anderson, Physical Review Letters **17**, 95 (1966).

[40] J. R. Schrieffer and P. A. Wolff, Physical Review **149**, 491 (1966).

[41] L. P. Kouwenhoven, C. M. Marcus, P. L. McEuen, S. Tarucha, R. M. Westervelt, and N. S. Wingreen, Electron transport in quantum dots, in *Mesoscopic Electron Transport* (Springer Netherlands, Dordrecht, 1997) pp. 105–214.

[42] F. Delgado and J. Fernández-Rossier, Progress in Surface Science **92**, 40 (2017).

[43] E. del Barco, A. D. Kent, E. C. Yang, and D. N. Hendrickson, Physical Review Letters **93**, 157202 (2004).

[44] R. Basler, A. Sieber, G. Chaboussant, H. U. Güdel, N. E. Chakov, M. Soler, G. Christou, A. Desmedt, and R. Lechner, Inorganic Chemistry **44**, 649 (2005).

CHAPTER 5: EQUILIBRIUM GREEN'S FUNCTIONS FORMALISM APPLIED TO EXCHANGE COUPLED TRIPARTITE SYSTEMS

5.1 Introduction

In prior chapters, I established the spin-space interactions that can occur when two of the spins possess magnetic anisotropy. I also explored the impact of incorporating leads and the use of perturbation theory to extract quantities like current and conductance, which are found to be strongly dependent on the spin structure. To go further in the model, so that it may be applied more readily to more complicated systems, one must look at the energy dependence and time dependence of spin states. One of the techniques to do so is the Green's function formalism, as described in Chapter 1. I will do so now, using an important and simple example of a toy three-spin particle model that accounts for the momentum of the electron and spin exchange coupling, compared to known results for the model [1–3].

5.2 Theoretical Method

5.2.1 1D Wire and Two Magnetic Impurity Model

Cicarrello *et al.* explored the toy model of an electron in 1D wire interacting with two magnetic impurities separated by a distance x_0 through a contact exchange interaction, with the Hamiltonian,

$$\mathcal{H} = \frac{\hat{p}^2}{2m^*} + J\hat{\boldsymbol{\sigma}} \cdot \hat{\mathbf{S}}_1 \delta(x) + J\hat{\boldsymbol{\sigma}} \cdot \hat{\mathbf{S}}_1 \delta(x - x_0), \tag{5.1}$$

where $\hat{p}$ is the momentum operator, m^* is the effective electron mass, J the exchange coupling constant, $\hat{\boldsymbol{\sigma}}$ is the electron spin operator, and $\hat{\mathbf{S}}_i$ the spin of the i'th $S = 1/2$ impurity [2]. The impurities in this model behave statically, and so spin-flip scattering processes are not accounted for. By imposing boundary conditions at the impurities and solving the time-independent Schrödinger equation for the eight stationary states, $\mathcal{H}\left|\Psi_{i,\mathrm{stat}}\right\rangle = E_i\left|\Psi_{i,\mathrm{stat}}\right\rangle$, the electron transmissivity T can be calculated. The authors found that the transmission was dependent on two dimensionless quantities: kx_0 where $k > 0$ is the quantum number associated with the eigenvalues $E = \hbar^2k^2/2m^*$, and $\rho(E)J$, where $\rho(E) = (\sqrt{2m^*/E})/\pi\hbar$ is the density of states per unit length of the wire. They also found that transmission was dependent on the static spin state of the impurities. For example, if the impurities were prepared in the entangled spin triplet configuration $\left(|\uparrow\downarrow\rangle + |\downarrow\uparrow\rangle\right)/\sqrt{2}$, there were no conditions of the two dimensionless quantities that led to perfect transmission. Surprisingly, they found that if the impurities were prepared in the entangled spin singlet configuration $\left(|\uparrow\downarrow\rangle - |\downarrow\uparrow\rangle\right)/\sqrt{2}$, there existed conditions in which perfect transmission could be achieved. Their result was also generalized for any spin S impurities [3].

The toy model of reference [1–3] is a jumping point from which one can construct a Green's function formalism for the tripartite spin problem, before attempting the more complicated non-equilibrium Green's function method found in Chapter 6. I convert the problem into the well-known double-well potential and show the method of solving with first-quantized Green's functions and the Lippman-Schwinger equation. I then apply this to the toy-model of Ref. [1, 2] to demonstrate that one can easily obtain the solutions without solving the boundary-problem explicitly. I then extend the results by considering anisotropic exchange coupling and comment on the modulation of transmission. Finally, I summarize the challenges of using this method to solve for the model in which the two impurities are exchange coupled.

5.2.2 Spinless First Quantization Green's Function Solution

The first step is to convert the problem into a spin-independent delta-function potential problem to ensure that well-known results can be reproduced. The modified Hamiltonian is,

$$\mathcal{H} = \frac{\hat{p}^2}{2m^*} + J_1\delta(x) + J_2\delta(x - x_0), \tag{5.2}$$

Next, the problem is converted into a Dyson-like time-independent Green's function equation in first-quantized form,

$$G(x, x') = G_0(x, x') + \int \mathrm{d}y \int \mathrm{d}z\, G_0(x, y)V(y, z)G(z, x'), \tag{5.3}$$

where,

$$V(y, z) = V(y) = J_1\delta(y) + J_2\delta(y - x_0), \tag{5.4}$$

and the first-quantized Green's function is defined as,

$$G(x, x') \equiv G(E, x, x') = \frac{\hbar^2}{2m^*} \langle x| \frac{1}{E - \mathcal{H} \pm i\eta} |x'\rangle \,. \tag{5.5}$$

The Dyson equation is then,

$$G(x, x') = G_0(x, x') + J_1G_0(x, 0)G(0, x') + J_2G_0(x, x_0)G(x_0, x'). \tag{5.6}$$

The method of substitution is used to solve this equation in Appendix C.1. The result is,

$$G_{\text{two-delta}}(x, x') = G_{\text{one-delta}}(x, x') + G_{\text{corrections}}(x, x'), \tag{5.7}$$

where,

$$G_{\text{one-delta}}(x,x') = G_0(x,x') + \frac{G_0(x,0)G_0(0,x')}{\beta_1(0)}, \tag{5.8}$$

$$\beta_i(x) = \frac{1}{J_i} - G_0(x,x), \tag{5.9}$$

$$\lambda = \left[\beta_2(x_0)\beta_1(0) - G_0(x_0,0)G_0(0,x_0)\right]^{-1}, \tag{5.10}$$

and,

$$G_{\text{corrections}}(x,x') = \lambda\Bigg(G_0(x,0)G_0(0,x_0)G_0(x_0,x') + G_0(x,x_0)G_0(x_0,0)G_0(0,x') + \beta_1(0)G_0(x,x_0)G_0(x_0,x') + \frac{G_0(x,0)G_0(0,x_0)G_0(x_0,0)G_0(0,x')}{\beta_1(0)}\Bigg). \tag{5.11}$$

5.2.3 Scattering Problem from Lippmann-Schwinger Formalism

The scattering problem can now be solved by making use of the Lippmann-Schwinger equation expressed in the position basis and solved for a particular energy E,

$$\psi(x) = \psi_0(x) + \int \mathrm{d}y\, G_0^r(x,y)V(y)\psi(y), \tag{5.12}$$

with $\psi_0(x) \equiv \langle x|\psi_0\rangle$ as the solution of the free Schrödinger's equation and $G_0^r(x,x') \equiv \langle x|G_0^r(x,x')|x'\rangle$ and $G_0^r(x,x') \equiv G_0(E+i\eta,x,x')$. Inserting the spin-less potential gives,

$$\psi(x) = \psi_0(x) + J_1 G_0^r(x,0)\psi(0) + J_2 G_0^r(x,x_0)\psi(x_0). \tag{5.13}$$

As expected, this form is similar to the form determined from the Green's function approach. Following the procedure in Appendix C.2, one obtains in the case when $x > x_0$ and x_0 is positive (i.e., looking at the region to the right of the second potential barrier),

$$\psi_{\text{one-delta}}(x)\Big|_{x>x_0} = e^{ikx} + \frac{\gamma_1}{1-\gamma_1}e^{ikx} = \frac{1}{1-\gamma_1}e^{ikx}, \tag{5.14}$$

and,

$$\psi_{\text{corrections}}(x)\Big|_{x>x_0} = \left[\left(\frac{1}{\gamma_1}-1\right)\left(\frac{1}{\gamma_2}-1\right) - e^{2ikx_0}\right]^{-1}\left[\frac{1}{\gamma_1} + \left(\frac{1}{1-\gamma_1}\right)e^{2ikx_0}\right]e^{ikx}, \tag{5.15}$$

where,

$$\gamma_i \equiv \frac{J_i m^*}{ik\hbar^2} \tag{5.16}$$

Using $\psi_{\text{one-delta}}(x)$, one obtains the transmission amplitude,

$$t_{\text{one-delta}} = \frac{1}{1-\gamma_1} = \frac{1}{1-\frac{Jm^*}{ik\hbar^2}}, \tag{5.17}$$

matching textbook solutions for the transmission of a single delta function potential with $E > 0$. Obtaining the probability for transmission is trivial,

$$T_{\text{one-delta}} = |t_{\text{one-delta}}|^2 = \frac{1}{1+\frac{J^2(m^*)^2}{k^2\hbar^4}}. \tag{5.18}$$

Similarly for the double-delta problem with the same conditions and $J_1 = J_2$, the transmission coefficient is,

$$t_{\text{two-delta}} = \left(1 - 2\gamma_1 + \gamma_1^2\left(1 - e^{2ikx_0}\right)\right)^{-1}. \tag{5.19}$$

The transmission probability tends towards 1 as $kx_0 \to \infty$, and is zero when $kx_0 = 0$.

5.2.4 First-Quantized Green's Function Solution with Spin

Now that the double-potential problem has been solved using the Green's function method, spin is reintroduced into the problem. One can extend the momentum space to the tensor product of the momentum and spin space site representation as,

$$|k\rangle \to |k, s_1, s_2, s_3, m_1, m_2, m_3\rangle \equiv |k\rangle \otimes |s_1, s_2, s_3, m_1, m_2, m_3\rangle \,. \tag{5.20}$$

One can also use the product basis through the use of the appropriate standard procedure involving Clepsch-Gordon coefficients, to describe a state with spin s and spin quantum number m_s:

$$|k\rangle \to |k, s, m_s\rangle \equiv |k\rangle \otimes |s, m_s\rangle \,. \tag{5.21}$$

As an example of this extension, for the free Green's function with spin,

$$\begin{aligned}
G_0(\mathbf{r}, s, m_s; \mathbf{r}', s', m'_{s'}) &= \langle \mathbf{r}, s, m_s | \, \hat{G}_0 \, | \mathbf{r}', s', m'_{s'} \rangle & \text{(5.22a)} \\
&= \langle \mathbf{r}, s, m_s | \, \hat{G}_0 \left(\int \mathrm{d}^d k' \, |\mathbf{k}'\rangle \, \langle \mathbf{k}'| \right) |\mathbf{r}', s', m'_{s'}\rangle & \text{(5.22b)} \\
&= \int \mathrm{d}^d k' \, \langle \mathbf{r}|\mathbf{k}'\rangle \, \frac{1}{E - \frac{\hbar^2 |\mathbf{k}'|^2}{2m^*}} \, \langle \mathbf{k}'|\mathbf{r}'\rangle \, \delta_{s,s'} \delta_{m_s, m'_{s'}} & \text{(5.22c)} \\
&= \frac{2m^*}{\hbar^2} \frac{1}{(2\pi)^d} \int \mathrm{d}^d k' \frac{e^{i\mathbf{k}'\cdot(\mathbf{r}-\mathbf{r}')}}{k^2 - |\mathbf{k}'|^2} \delta_{s,s'} \delta_{m_s, m'_{s'}}. & \text{(5.22d)}
\end{aligned}$$

It is immediately clear that a free Green's function will maintain the spin state of the particle because there are no spin interactions that induce a spin flip.

Turning now to the problem at hand, one converts the problem into a Dyson-like

time-independent Green's function equation in first-quantized form,

$$G(x,\sigma;x',\sigma') = G_0(x,\sigma;x',\sigma') + \sum_{\sigma_y,\sigma_z}\int \mathrm{d}y \int \mathrm{d}z\, G_0(x,\sigma;y,\sigma_y)V(y,\sigma_y;z,\sigma_z)G(z,\sigma_z;x',\sigma'), \tag{5.23}$$

where σ contains all the information that is needed for the spin space. Because of the one-body nature of the potential V, the Dyson equation simplifies to,

$$G(x,\sigma;x',\sigma') = G_0(x,\sigma;x',\sigma') + \sum_{\sigma_y}\int \mathrm{d}y\, G_0(x,\sigma;y,\sigma_y)V(y,\sigma_y)G(y,\sigma_y;x',\sigma'). \tag{5.24}$$

5.3 Results

I apply this Green's function result to the contact exchange model with strengths J_1 and J_2. Defining the total spin $\mathbf{S} = \boldsymbol{\sigma} + \mathbf{S}_1 + \mathbf{S}_2$ and electron-impurity spin $\mathbf{S}_{ei} = \boldsymbol{\sigma} + \mathbf{S}_i$, and noting that spin-flip processes are not allowed to occur, one can inspect each spin subspace as follows.

5.3.1 Isotropic Exchange s=3/2 Subspace

In the $s = 3/2$ spin subspace, both s_{e1} and s_{e2} take on the value of 1, and so the equation models the spin free case with a modified uniform strength J. For completeness, I indicate the spin wave functions for this space using the same spin basis as Ref. [1, 2] of $|s_{e2}, s, m_s\rangle$

and their equivalent $|m_e, m_1, m_2\rangle$ form,

$$|1, 3/2, +3/2\rangle = |\uparrow,\uparrow,\uparrow\rangle\,, \tag{5.25}$$

$$|1, 3/2, +1/2\rangle = \sqrt{\frac{1}{3}}\,|\uparrow,\uparrow,\downarrow\rangle + \sqrt{\frac{1}{3}}\,|\uparrow,\downarrow,\uparrow\rangle + \sqrt{\frac{1}{3}}\,|\downarrow,\uparrow,\uparrow\rangle\,, \tag{5.26}$$

$$|1, 3/2, -1/2\rangle = \sqrt{\frac{1}{3}}\,|\downarrow,\uparrow,\downarrow\rangle + \sqrt{\frac{1}{3}}\,|\downarrow,\downarrow,\uparrow\rangle + \sqrt{\frac{1}{3}}\,|\uparrow,\downarrow,\downarrow\rangle\,, \tag{5.27}$$

$$|1, 3/2, -3/2\rangle = |\downarrow,\downarrow,\downarrow\rangle\,. \tag{5.28}$$

Converting the Green's function to the Lippman-Schwinger wave function form,

$$\psi(x, \tfrac{3}{2}, m_s) = \psi_0(x, \tfrac{3}{2}, m_s) + \frac{J_1\hbar^2}{4}G_0^r(x, 0)\psi(0, \tfrac{3}{2}, m_s) + \frac{J_2\hbar^2}{4}G_0^r(x, x_0)\psi(x_0, \tfrac{3}{2}, m_s). \tag{5.29}$$

one sees that the form is similar to the spin-free case, and thus one needs to simply tack on the information of the total s, m_s space. The transmission for the case when $J_1 = J_2$ (i.e., the result in Ref. [1, 2]) can be calculated using the wave function result for a double-delta function to obtain,

$$t_{\text{two-delta}} = \left(1 - 2\gamma_1 + \gamma_1^2\left(1 - e^{2ikx_0}\right)\right)^{-1} \tag{5.30a}$$

$$= \frac{64}{64 + \pi\rho(E)J\left[16i + \left(e^{2ikx_0} - 1\right)\pi\rho(E)J\right]}. \tag{5.30b}$$

where,

$$\gamma_1 = \frac{1}{4i}J\frac{m^*}{k\hbar^2} = \frac{1}{4i}J\frac{\pi}{2}\rho(E) = \frac{\pi}{8i}J\rho(E), \tag{5.31}$$

has been used.

5.3.2 Isotropic Exchange s=1/2 Subspace

The $s = 1/2$ case is more complicated because now s_{e1} and s_{e2} are no longer good quantum numbers. Expressing the $\mathbf{S}_{e1}^2$ operator using the four s_{e2} states,

$$\mathbf{S}_{e1}^2 \left|0; 1/2, m\right\rangle = \frac{3}{2} \left|0; 1/2, m\right\rangle + \frac{\sqrt{3}}{2} \left|1; 1/2, m\right\rangle, \tag{5.32}$$

$$\mathbf{S}_{e1}^2 \left|1; 1/2, m\right\rangle = \frac{\sqrt{3}}{2} \left|0; 1/2, m\right\rangle + \frac{1}{2} \left|1; 1/2, m\right\rangle. \tag{5.33}$$

and for the $\mathbf{S}_{e2}^2$ operator,

$$\mathbf{S}_{e2}^2 \left|0; 1/2, m\right\rangle = 0, \tag{5.34}$$

$$\mathbf{S}_{e2}^2 \left|1; 1/2, m\right\rangle = 2 \left|1; 1/2, m\right\rangle. \tag{5.35}$$

As one can see, these spin eigenstates mix upon action of the spin operator. One must solve,

$$\begin{aligned} G(x, s_{e2}; x', s'_{e2}) = G_0(x, s_{e2}; x', s'_{e2}) + \sum_{s_{e2}^y} \int \mathrm{d}y \, G_0(x, s_{e2}; y, s_{e2}) \\ \times \left(\frac{J_1}{2} \left[\mathbf{S}_{e1}^2 - \frac{3}{2} \right] \delta(y) + \frac{J_2}{2} \left[\mathbf{S}_{e2}^2 - \frac{3}{2} \right] \delta(y - x_0) \right) G(y, s_{e2}^y; x', s'_{e2}), \end{aligned} \tag{5.36}$$

with the understanding that the spin s_{e2}^y is connected to the s_{e2} spin through the interactions of the $\mathbf{S}_{ei}^2$ operators. Because s'_{e2} is not a good quantum number, the action of the operators will necessarily split the Green's function into contributions of all possible values of s_{e2}. In the case of $s = 1/2$ impurities, the span of the possible s_{e2} values are 0 and 1. The action of the contact exchange coupling is to connect these distinct spin spaces. This is seen in the

form of the Green's functions,

$$G(x, s_{e2}; x', s'_{e2}) = G_0(x, s_{e2}; x', s'_{e2}) + \int \mathrm{d}y\, G_0(x, s_{e2}; y, s_{e2}) \langle s_{e2}| V |0\rangle G(y, 0; x', s'_{e2}) + \int \mathrm{d}y\, G_0(x, s_{e2}; y, s_{e2}) \langle s_{e2}| V |1\rangle G(y, 1; x', s'_{e2}) \tag{5.37}$$

Substituting the interaction V,

$$\begin{aligned} G(x, s_{e2}; x', s'_{e2}) = G_0(x, s_{e2}; x', s'_{e2}) &+ \int \mathrm{d}y\, G_0(x, s_{e2}; y, s_{e2}) \left(J_{e1}^{s_{e2},0}\delta(y) + J_{e2}^{s_{e2},0}\delta(y - x_0)\right) G(y, 0; x', s'_{e2}) \\ &+ \int \mathrm{d}y\, G_0(x, s_{e2}; y, s_{e2}) \left(J_{e1}^{s_{e2},1}\delta(y) + J_{e2}^{s_{e2},1}\delta(y - x_0)\right) G(y, 1; x', s'_{e2}), \end{aligned} \tag{5.38}$$

where the modulated strength $J_{e1/e2}^{s_{e2},s_{e2}^z}$ is determined by the result of the operation,

$$J_{ei}^{s_{e2},n} \equiv \langle s_{e2}| \frac{J_i}{2} \left[\mathbf{S}_{ei}^2 - \frac{3}{2}\right] |n\rangle . \tag{5.39}$$

For the $s_{e2}^y = 0$, $m = \pm 1/2$ spin states,

$$\langle 0| \frac{J_1}{2} \left[\mathbf{S}_{e1}^2 - \frac{3}{2}\right] |0\rangle = J_{e1}^{0,0} = 0, \tag{5.40}$$

$$\langle 0| \frac{J_2}{2} \left[\mathbf{S}_{e2}^2 - \frac{3}{2}\right] |0\rangle = J_{e2}^{0,0} = -\frac{3}{4} J_2, \tag{5.41}$$

$$\langle 0| \frac{J_1}{2} \left[\mathbf{S}_{e1}^2 - \frac{3}{2}\right] |1\rangle = J_{e1}^{0,1} = \frac{\sqrt{3}}{4} J_1, \tag{5.42}$$

$$\langle 0| \frac{J_2}{2} \left[\mathbf{S}_{e2}^2 - \frac{3}{2}\right] |1\rangle = J_{e2}^{0,1} = 0, \tag{5.43}$$

and for the $s^y_{e2} = 1$, $m = \pm 1/2$ spin states,

$$\langle 1| \frac{J_1}{2} \left[\mathbf{S}^2_{e1} - \frac{3}{2} \right] |0\rangle = J^{1,0}_{e1} = \frac{\sqrt{3}}{4} J_1, \tag{5.44}$$

$$\langle 1| \frac{J_2}{2} \left[\mathbf{S}^2_{e2} - \frac{3}{2} \right] |0\rangle = J^{1,0}_{e2} = 0, \tag{5.45}$$

$$\langle 1| \frac{J_1}{2} \left[\mathbf{S}^2_{e1} - \frac{3}{2} \right] |1\rangle = J^{1,1}_{e1} = -\frac{1}{2} J_1, \tag{5.46}$$

$$\langle 1| \frac{J_2}{2} \left[\mathbf{S}^2_{e2} - \frac{3}{2} \right] |1\rangle = J^{1,1}_{e2} = \frac{1}{4} J_2. \tag{5.47}$$

One can exploit the delta function in the contact exchange coupling and simplify the integrals, resulting in,

$$\begin{aligned} G(x, s_{e2}; x', s'_{e2}) = G_0(x, s_{e2}; x', s'_{e2}) &+ J^{s_{e2},0}_{e1} G_0(x, s_{e2}; 0, s_{e2}) G(0, 0; x', s'_{e2}) \\ &+ J^{s_{e2},0}_{e2} G_0(x, s_{e2}; x_0, s_{e2}) G(x_0, 0; x', s'_{e2}) \\ &+ J^{s_{e2},1}_{e1} G_0(x, s_{e2}; 0, s_{e2}) G(0, 1; x', s'_{e2}) \\ &+ J^{s_{e2},1}_{e2} G_0(x, s_{e2}; x_0, s_{e2}) G(x_0, 1; x', s'_{e2}). \end{aligned} \tag{5.48}$$

Solving this equation by substitution can be done with the aid of a computational algebra software, such as Mathematica [4], whose resultant expanded form has over 1000 terms. One can then convert the Green's function to the Lippman-Schwinger wave function form, and calculate transmission probabilities, obtaining the same results as Ref. [1, 2].

5.3.3 Anisotropic Exchange

Instead of assuming an isotropic J as in Ref. [1, 2], I assume an anisotropic J_1 and J_2 for the coupling of the electron to the magnetic impurities. First, I explore the $s = 3/2$ subspace. Taking $\rho(E)J_1 = 2$ as an example, the ratio of the magnitude of J_1 and J_2 results in different transmission behavior, as seen in Fig. 5.1. The relative sign of the exchange coupling results

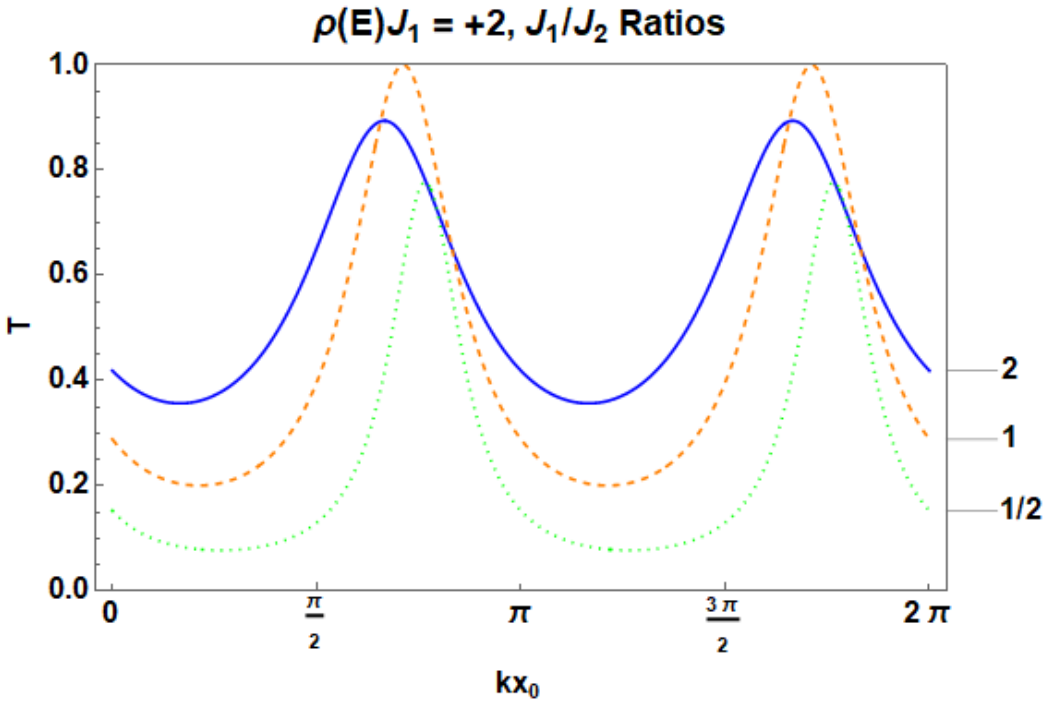

Figure 5.1: Transmission as a function of the dimensionless quantity kx_0 for $\rho(E)J_1 = 2$ for any state preparation in the $s = 3/2$ spin space, for a range of different exchange coupling ratios.

in a shift of the transmission curve, as shown in Fig. 5.2.

Moving now to the $s = 1/2$ spin subspace, I repeat the same explore of the ratios and signs of the $\rho(E)J_i$ quantities. The case when the electron is injected as $\uparrow$ and the impurities are prepared in the non-entangled $|\uparrow\downarrow\rangle$ state results in different transmission profiles, dependent on the ratio of the different exchange coupling strengths, as shown in Fig. 5.3. I also look at the difference in transmission profiles for singlet (in Fig. 5.4 and Fig. 5.5) and triplet-prepared impurity spin states (in Fig. 5.4 and Fig. 5.5) for both different ratios and relative signs of the exchange coupling.

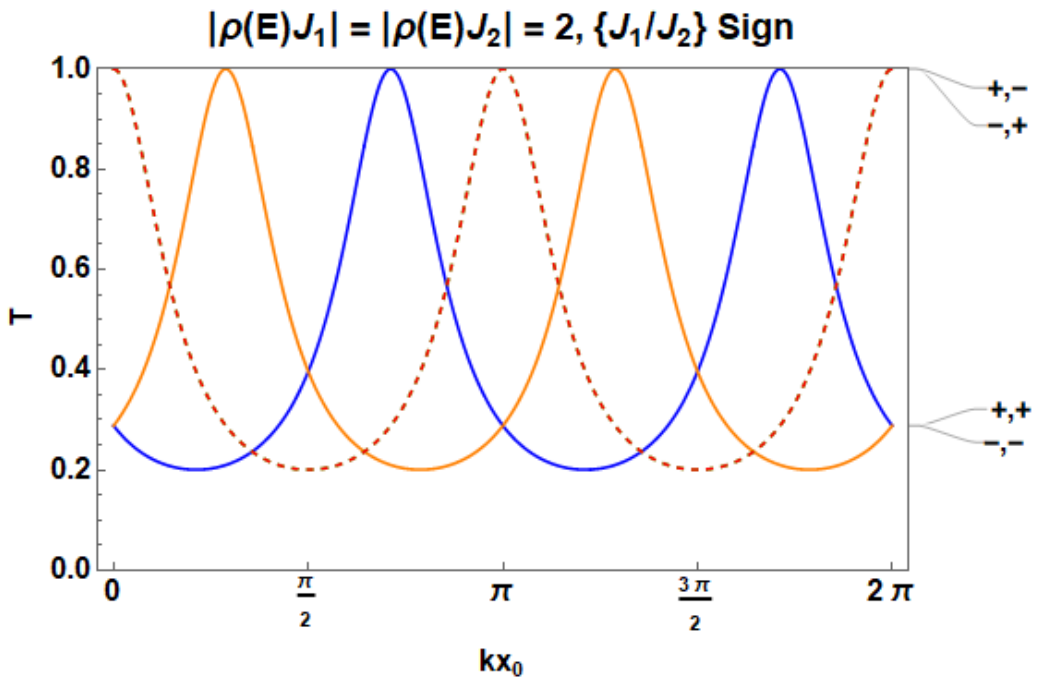

Figure 5.2: Transmission as a function of the dimensionless quantity kx_0 for $\rho(E)J_1 = \rho(E)J_2 = 2$ for any state preparation in the $s = 3/2$ spin space, for a range of different relative signs of the exchange coupling.

5.4 Discussion and Summary

In Fig. 5.1, when the coupling is equal, perfect transmission is possible, agreeing with the results from Ref. [2]. When the coupling has different magnitudes, but the same sign, there are no conditions in which perfect transmission can occur because the spin states are no longer eigenstates of the Hamiltonian. The effect of sign is clearly seen in Fig. 5.2. The point at which perfect transmission is shifted symmetrically about the condition $kx_0 = \pi$ when the exchange-coupling constant for each impurity carries the same sign. The case for opposite sign (e.g., a ferromagnetic J_1 and antiferromagnetic J_2 coupling) shows that the same principle holds as for similar magnitude and sign coupling. This also says that the use of an electron transmission to ascribe the sign of exchange coupling of a particular impurity

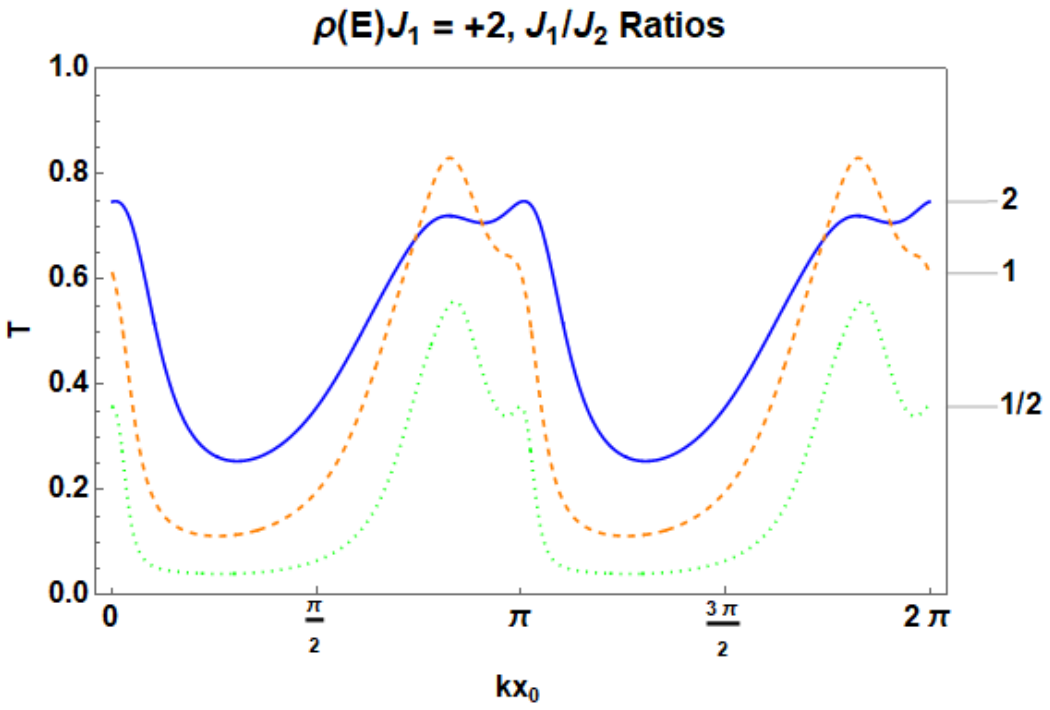

Figure 5.3: Transmission as a function of the dimensionless quantity kx_0 for $\rho(E)J_1 = 2$. The electron is injected as $|\uparrow\rangle$, and the spin impurities are prepared with the spin state $|\uparrow\downarrow\rangle$, for a range of different exchange coupling ratios.

is not possible in this toy model if at least one of the impurities has opposite sign.

As I have shown, the Green's function formalism is a powerful tool to explore spin-dependent problems and avoid some complexities of using solving the time-independent Schrödinger equation using the boundary condition method, but there are limitations in the first-quantized form. For example, if one wants to include an exchange coupling term of spin 1 and 2, the potential is no longer single body. A different formalism is needed to solve the problem, like the many-body Green's function method. In addition, a Dyson-like equation must be solved self-consistently in that scenario to obtain a steady-state solution (if it exists). The method of using a many-body Green's function, and exploring the time-dependent behavior of such a system will be explored in the next chapter.

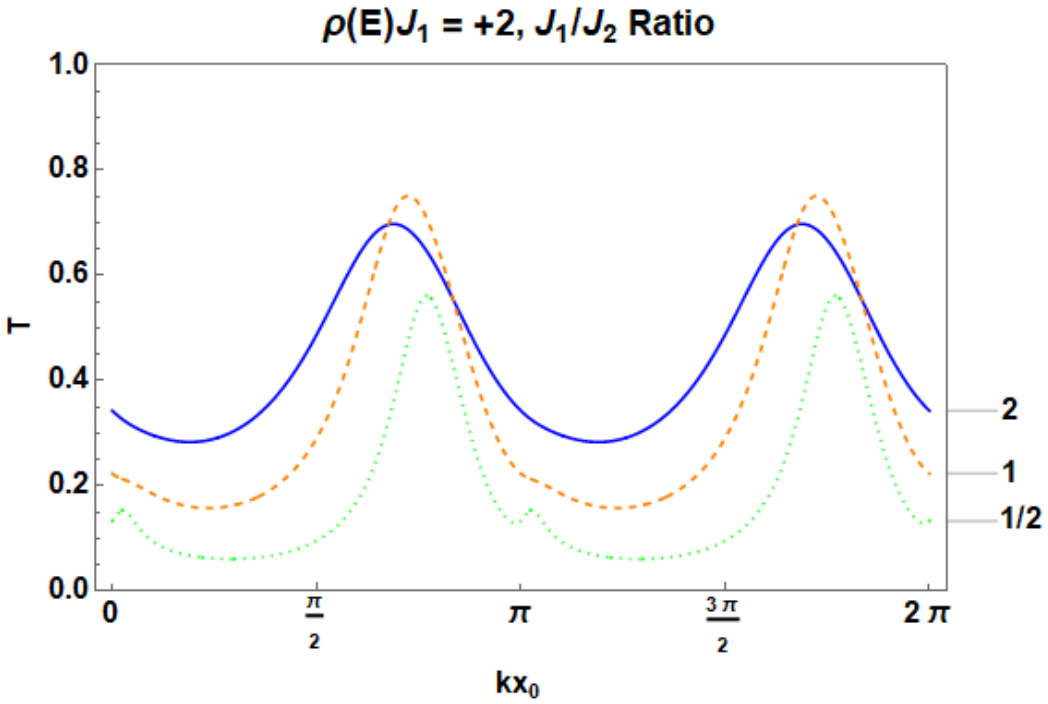

Figure 5.4: Transmission as a function of the dimensionless quantity kx_0 for $\rho(E)J_1 = 2$. The electron is injected as $|\uparrow\rangle$, and the spin impurities are prepared as a spin triplet $(|\uparrow\downarrow\rangle + |\downarrow\uparrow\rangle)/\sqrt{2}$ state, for a range of different exchange coupling ratios.

5.5 List of References

[1] F. Ciccarello, G. M. Palma, M. Zarcone, Y. Omar, and V. R. Vieira, New Journal of Physics **8**, 214 (2006).

[2] F. Ciccarello, G. M. Palma, M. Zarcone, Y. Omar, and V. R. Vieira, Journal of Physics A: Mathematical and Theoretical **40**, 7993 (2007).

[3] F. Ciccarello, G. Massimo Palma, M. Paternostro, M. Zarcone, and Y. Omar, Solid State Sciences **11**, 931 (2009).

[4] W. R. Inc., Mathematica, Version 13.2, champaign, IL, 2022.

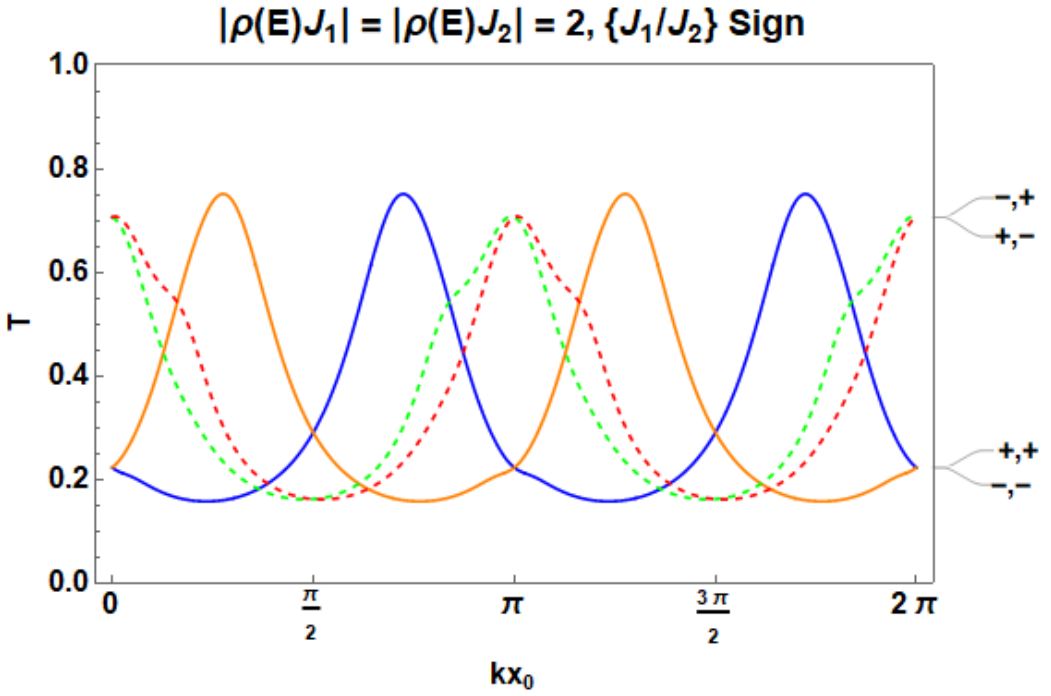

Figure 5.5: Transmission as a function of the dimensionless quantity kx_0 for $|\rho(E)J_1| = |\rho(E)J_2| = 2$. The electron is injected as $|\uparrow\rangle$, and the spin impurities are prepared as a spin triplet $\left(|\uparrow\downarrow\rangle + |\downarrow\uparrow\rangle\right)/\sqrt{2}$ state, for a range of different relative signs of the exchange coupling.

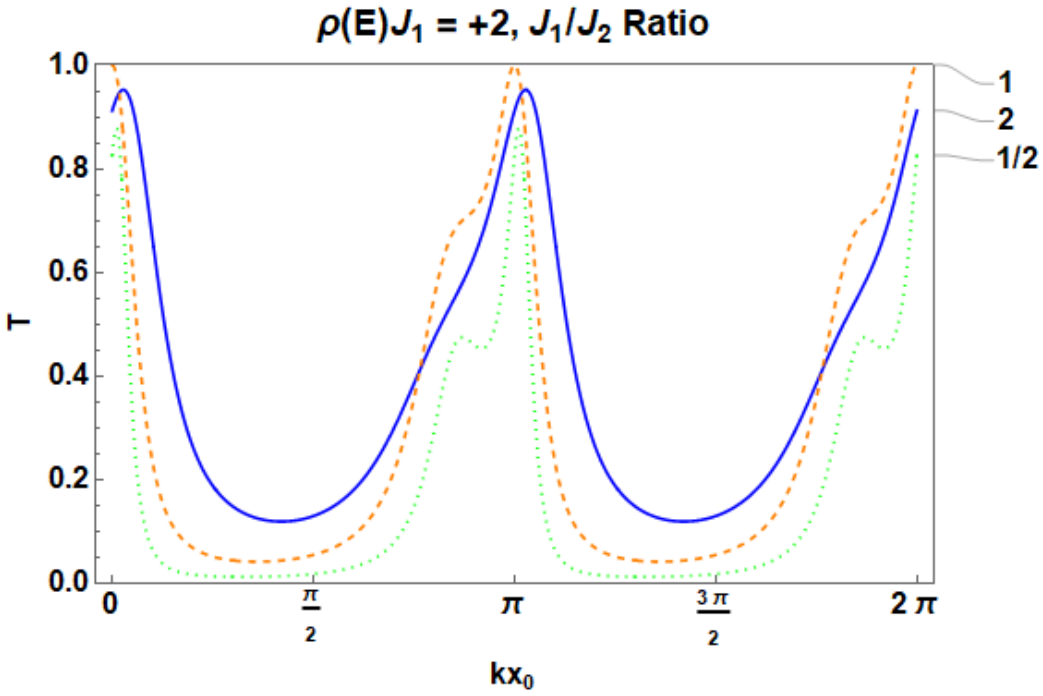

Figure 5.6: Transmission as a function of the dimensionless quantity kx_0 for $\rho(E)J_1 = 2$. The electron is injected as $|\uparrow\rangle$, and the spin impurities are prepared as a spin singlet $\left(|\uparrow\downarrow\rangle - |\downarrow\uparrow\rangle\right)/\sqrt{2}$ state, for a range of different exchange coupling ratios.

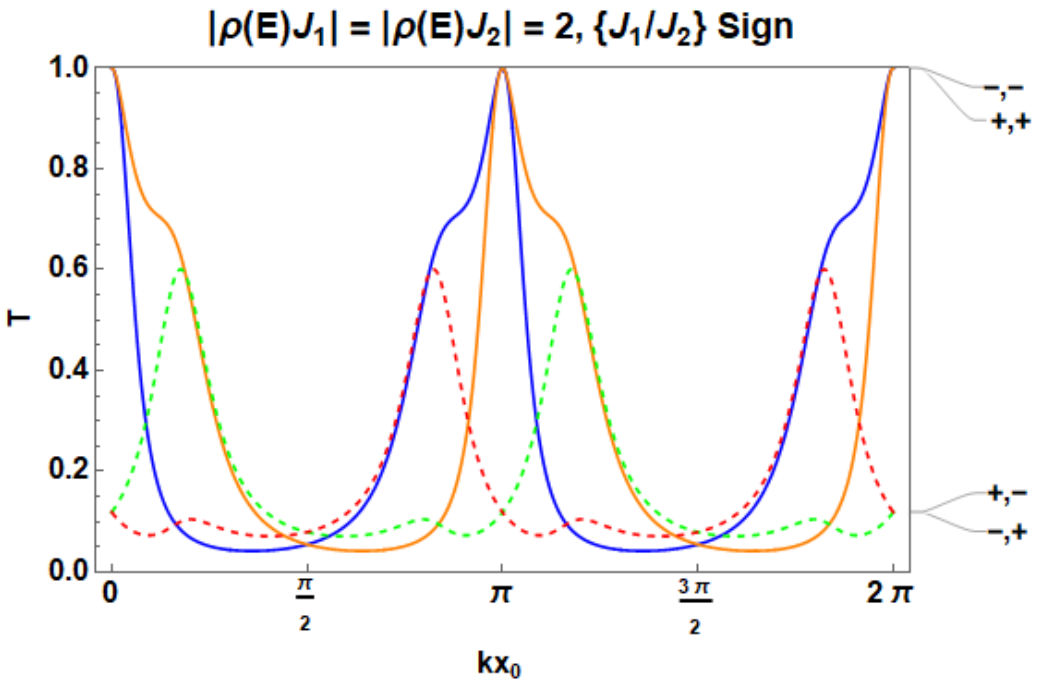

Figure 5.7: Transmission as a function of the dimensionless quantity kx_0 for $|\rho(E)J_1| = |\rho(E)J_2| = 2$. The electron is injected as $|\uparrow\rangle$, and the spin impurities are prepared as a spin singlet $\left(|\uparrow\downarrow\rangle - |\downarrow\uparrow\rangle\right)/\sqrt{2}$ state, for a range of different relative signs of the exchange coupling.

CHAPTER 6: NON-EQUILIBRIUM GREENS FUNCTIONS APPLIED TO TRIPARTITE TIGHT-BINDING MODELS

6.1 Introduction

I now extend the work from the last chapter to the many-body Green's function formalism, with the aim of also introducing the non-equilibrium paradigm. There has been much work on investigating multi-site problems using the NEGF formalism. As mentioned in Chapter 1, many of them are based on the Meir-Wingreen formalism [1], where one solves NEGFs in the energy domain for the case of a central region connected to two large leads,

$$\mathcal{I} = \frac{e}{\hbar} \sum_{k\alpha n} \int \frac{\mathrm{d}\omega}{2\pi} \left[V_{k\alpha n} G^{<}_{n,k\alpha}(\omega) - V^{*}_{k\alpha n} G^{<}_{k\alpha,n}(\omega) \right], \tag{6.1}$$

where $G^{<}_{n,k\alpha}$ is the Keldysh Green's function for the energy level n in the central region and k wave vector in lead α, and $V_{k\alpha n}$ is the interaction connecting the leads to the central region. This approach has been widely successful, and is used in the latest-generation NEGF codes [2–4] to explore steady-state transport.

Of interest is the time-*dependent* NEGF formalism, where one can attempt to model transient behavior of a quantum system. For example, the non-linear time-dependent behavior of double-dot systems that utilize a two-site Hubbard model for the scattering region with hopping from electrodes has been explored [5]. Because of the complexities involved with spin-spin interactions, I explore a relatively simple toy model of two and three tight-binding sites at finite temperature and solve it using NEGF. I present the results of several non-equilibrium conditions and the impact on the occupation number of each site as a function of time. I will then outline the procedure that one must do in order to incorporate spin and describe the equations of motion that must be solved self-consistently to model exchange

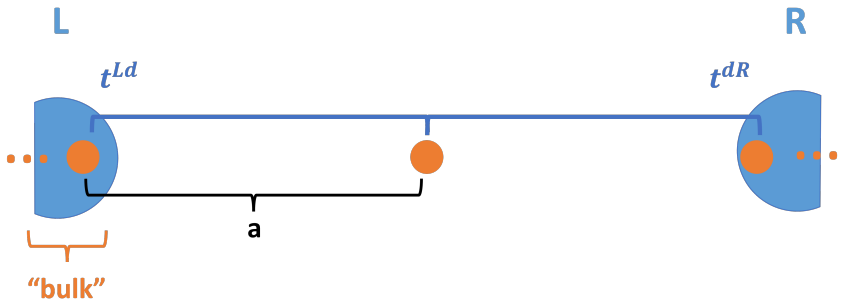

Figure 6.1: Schematic of the three-site model considered in this chapter. One site on the left and one on the right represent the sites with the surface of a bulk-like lead, with a single transition site located a distance a (leading to effective hopping terms t^{Ld} and t^{dR}) in between the leads.

coupled spins.

6.2 Tight-Binding Three-Site Model

I first consider the tight-binding model represented in Fig. 6.1. In this model, I consider one orbital site connected to orbital sites on the surface of leads without spin interactions. The lead sites are assumed to be at a particular chemical potential that mirrors the bulk properties of the lead. The electron can hop from lead orbitals into and out of a device region site's orbitals, accounted for by a hopping term in the Hamiltonian that represented the kinetic energy of the electron and is in principle directly related to the spacing of the site from the leads. In this model, an electron hops from one lead to the site and onto the next lead if a chemical potential difference or electric field has been created between both leads. The full Hamiltonian is

$$\hat{\mathcal{H}} = \hat{\mathcal{H}}_L + \hat{\mathcal{H}}_C + \hat{\mathcal{H}}_R + V. \tag{6.2}$$

Each Hamiltonian term is described as follows. For lead $\alpha \in \{L, R\}$, the Hamiltonian after the bias has been turned on is,

$$\hat{\mathcal{H}}_\alpha = \sum_\sigma \left(\varepsilon_\alpha - \mu_\alpha\right) \hat{c}^\dagger_{\alpha\sigma} \hat{c}_{\alpha\sigma}, \tag{6.3}$$

where $c^\dagger_\sigma$ creates an electron in lead α whose eigenvalue upon action of the spin projection operator $\hat{S}^z$ is $+\hbar/2$ or $-\hbar/2$ (this will be notated as $\uparrow, \downarrow$, respectively), the spin-independent onsite energy is given by ε_α, and the chemical potential of the lead is μ_α. For the central region, the Hamiltonian is simply,

$$\mathcal{H}_C = \sum_\sigma \varepsilon_d \hat{d}^\dagger_\sigma \hat{d}_\sigma, \tag{6.4}$$

where $d^\dagger_\sigma$ creates an electron in the single-orbital site, and ε_d is the spin-independent onsite energy. Importantly, this model does not include the interaction energy $U\hat{n}_\uparrow \hat{n}_\downarrow$ of two oppositely polarized electrons on a single site, as is done in other theoretical treatments [5]. Including the interaction energy could lead to an energetic preference of singly-occupied sites. I assume that one is already in the regime in which the low energy states of singly-occupied sites dominate the dynamics, and thus I do not include U. The coupling between the central site and the leads is given by a perturbation term that turns on after some time $t = 0$,

$$V = \sum_{\alpha\sigma} \left(t_{\alpha d} \hat{c}^\dagger_{\alpha\sigma} \hat{d}_\sigma + h.c. \right), \tag{6.5}$$

where $t_{\alpha d}$ is the hopping parameter and $h.c.$ denotes the Hermitian conjugate of every term in the parenthesis. In essence, the system in the infinite past is decoupled and in equilibrium, and after $t = 0$, the coupling V is turned on. As can be seen in the form of the total Hamiltonian, there are no spin-interaction terms, and thus the Hamiltonian can be block-

diagonalized into separate spin polarization blocks.

6.2.1 Fermion Operator Equation of Motion

The time-dependent nature of the fermion operators can be solved. For the lead operators, the equation of motion (EOM) reads,

$$i\hbar\frac{\mathrm{d}}{\mathrm{d}t}\hat{c}_{\alpha\sigma} = \left[\hat{c}_{\alpha\sigma}, \hat{\mathcal{H}}\right], \tag{6.6}$$

where the commutator has been defined $\left[\hat{A}, \hat{B}\right] = \hat{A}\hat{B} - \hat{B}\hat{A}$, and the anticommutator $\left\{\hat{A}, \hat{B}\right\} = \hat{A}\hat{B} + \hat{B}\hat{A}$. To solve the right-hand side (RHS) of Eq. (6.6), I quote the result of the commutation relations in Appendix D.1, and obtain,

$$\left[\hat{c}_{\alpha'\sigma'}, \hat{\mathcal{H}}\right] = \sum_{\alpha\sigma}\left\{\left(\varepsilon_\alpha - \mu_\alpha\right)\left[\hat{c}_{\alpha'\sigma'}, \hat{c}^\dagger_{\alpha\sigma}\hat{c}_{\alpha\sigma}\right] + \left(t_{\alpha d}\left[\hat{c}_{\alpha'\sigma'}, \hat{c}^\dagger_{\alpha\sigma}\hat{d}_\sigma + h.c.\right]\right)\right\} + \sum_\sigma \varepsilon_d\left[\hat{c}_{\alpha'\sigma'}, \hat{d}^\dagger_\sigma\hat{d}_\sigma\right] \tag{6.7a}$$

$$= \sum_{\alpha\sigma}\left\{\left(\varepsilon_\alpha - \mu_\alpha\right)\delta_{\alpha'\alpha}\delta_{\sigma'\sigma}\hat{c}_{\alpha\sigma} + t_{\alpha d}\delta_{\alpha\alpha'}\delta_{\sigma\sigma'}\hat{d}_\sigma\right\} \tag{6.7b}$$

$$= \left(\varepsilon_{\alpha'} - \mu_{\alpha'}\right)\hat{c}_{\alpha'\sigma'} + t_{\alpha' d}\hat{d}_{\sigma'}. \tag{6.7c}$$

The equation of motion for the $\hat{c}$ operators are then,

$$i\hbar\frac{\mathrm{d}}{\mathrm{d}t}\hat{c}_{\alpha\sigma} = \left(\varepsilon_\alpha - \mu_\alpha\right)\hat{c}_{\alpha\sigma} + t_{\alpha d}\hat{d}_\sigma. \tag{6.8}$$

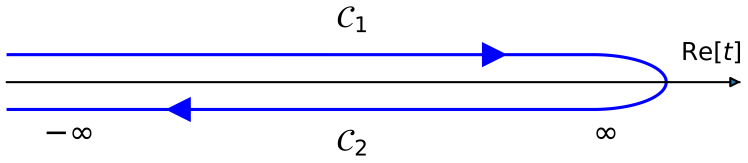

Figure 6.2: The two-branch contour considered for the zero-temperate non-equilibrium Green's functions considered in this chapter.

Performing the same procedure for the $\hat{d}$ operator results in,

$$\left[\hat{d}_{\sigma'}, \hat{\mathcal{H}}\right] = \sum_{\alpha\sigma} \left\{ (\varepsilon_\alpha - \mu_\alpha) \left[\hat{d}_{\sigma'}, \hat{c}^\dagger_{\alpha\sigma}\hat{c}_{\alpha\sigma}\right] + \left(t_{\alpha d}\left[\hat{d}_{\sigma'}, \hat{c}^\dagger_{\alpha\sigma}\hat{d}_\sigma + h.c.\right]\right)\right\} + \sum_\sigma \varepsilon_d \left[\hat{d}_{\sigma'}, \hat{d}^\dagger_\sigma \hat{d}_\sigma\right] \tag{6.9a}$$

$$= \sum_{\alpha\sigma} t^*_{\alpha d}\delta_{\sigma\sigma'}\hat{c}_{\alpha\sigma} + \sum_\sigma \varepsilon_d \delta_{\sigma'\sigma}\hat{d}_\sigma \tag{6.9b}$$

$$= \sum_\alpha t^*_{\alpha d}\hat{c}_{\alpha\sigma'} + \varepsilon_d \hat{d}_{\sigma'}, \tag{6.9c}$$

with an equation of motion,

$$i\hbar\frac{\mathrm{d}}{\mathrm{d}t}\hat{d}_\sigma = t^*_{Ld}\hat{c}_{L\sigma} + t^*_{Rd}\hat{c}_{R\sigma} + \varepsilon_d\hat{d}_\sigma. \tag{6.10}$$

6.2.2 NEGF Equation of Motion

The EOM for the NEGFs can now be calculated. One should use the contour-ordered Green's functions, as defined in Appendix D.4. For this simple model, I set the temperature at $T = 0$, and use the two branch contour defined in Fig. 6.2. The NEGFs are evaluated on the two-branch contour for variable z that describes the location on the contour. The z and z' coordinate arguments may be on different branches of the time contour, and so I designate

the time variable t^+ for times on the upper branch ($\mathcal{C}_1$) and t^- for the lower branch ($\mathcal{C}_2$).

Using the results of Appendix D.5, in general the contour Green's function EOM, with respect to the contour variable z is,

$$i\hbar\frac{\mathrm{d}}{\mathrm{d}z}G^c_{ab}(z,z') = \delta(z-z')\left\langle\left\{a_k(z), b_q^\dagger(z')\right\}\right\rangle - \frac{i}{\hbar}\left\langle\mathcal{T}\left([a_k(z),\mathcal{H}]\, b_q^\dagger(z')\right)\right\rangle, \tag{6.11}$$

where z, z' contain the coordinates of interest on the contour, k and q contain other coordinates that increase the dimensionality considered (e.g., spin, momenta), and $\mathcal{T}$ is the contour-ordered operator. For the three-site tight-binding problem, there will be 9 equations in total for each spin σ. Defining the $\mathbf{B}$ vector of operators, with the entries,

$$\mathbf{B} = \begin{bmatrix}\hat{c}_{L\sigma} & \hat{d}_\sigma & \hat{c}_{R\sigma}\end{bmatrix}, \tag{6.12}$$

I index the contour Green's function as the combination of operators in the $\mathbf{B}$ vector with the indices i and j,

$$i\hbar\frac{\mathrm{d}}{\mathrm{d}z}G^c_{ij}(z,z') = \delta(z-z')\left\langle\left\{B_i(z), B_j^\dagger(z')\right\}\right\rangle - \frac{i}{\hbar}\left\langle\mathcal{T}\left([B_i(z),\mathcal{H}]\, B_j^\dagger(z')\right)\right\rangle. \tag{6.13}$$

As an example, for the $\hat{c}_{L\sigma}\hat{c}^\dagger_{L\sigma}$ combination, the contour Green's functions EOM are,

$$i\hbar\frac{\mathrm{d}}{\mathrm{d}z}G^c_{11}(z,z') = \delta(z-z') + \epsilon_L G^c_{11}(z,z') + t_{Ld}G^c_{21}(z,z'), \tag{6.14}$$

where I have transformed the onsite energies to effective onsite energy $\epsilon_i = \varepsilon_i - \mu_i$. Performing the same for the rest of the operator combinations, and dropping the contour c index for brevity, results in,

$$i\hbar\frac{\mathrm{d}}{\mathrm{d}z}\mathbf{G}(z,z') = \delta(z-z')\mathbf{1} + \mathbf{H}(z)\mathbf{G}(z,z'), \tag{6.15}$$

where the Green's function vector $\mathbf{G}(z, z')$ is defined as (and dropping the (z, z') as well for brevity),

$$\mathbf{G} = \begin{bmatrix} \mathbf{G}_L^c \\ \mathbf{G}_d^c \\ \mathbf{G}_R^c \end{bmatrix}, \quad \mathbf{G}_L^c = \begin{bmatrix} G_{LL}^c \\ G_{Ld}^c \\ G_{LR}^c \end{bmatrix} \quad \mathbf{G}_d^c = \begin{bmatrix} G_{dL}^c \\ G_{dd}^c \\ G_{dr}^c \end{bmatrix} \quad \mathbf{G}_R^c = \begin{bmatrix} G_{RL}^c \\ G_{Rd}^c \\ G_{RR}^c \end{bmatrix}, \tag{6.16}$$

$\mathbf{1}$ is the unit vector, and the one-body part of the Hamiltonian $\mathbf{H}(z)$ (which in general depends on time, but for our case does not) has the form,

$$\mathbf{H} = \begin{bmatrix} \mathbf{H}_{LL} & \mathbf{H}_{Ld} & \\ \mathbf{H}_{dL} & \mathbf{H}_{dd} & \mathbf{H}_{dR} \\ & \mathbf{H}_{Rd} & \mathbf{H}_{RR} \end{bmatrix}, \tag{6.17}$$

where the empty entries are zero. The nine-dimensional representation of $\mathbf{H}$ is,

$$\mathbf{H} = \begin{bmatrix} \epsilon_L & & & t_{Ld} & & & & & \\ & \epsilon_L & & & t_{Ld} & & & & \\ & & \epsilon_L & & & t_{Ld} & & & \\ t_{Ld}^* & & & \varepsilon_d & & & t_{Rd} & & \\ & t_{Ld}^* & & & \varepsilon_d & & & t_{Rd} & \\ & & t_{Ld}^* & & & \varepsilon_d & & & t_{Rd} \\ & & & t_{Rd}^* & & & \epsilon_R & & \\ & & & & t_{Rd}^* & & & \epsilon_R & \\ & & & & & t_{Rd}^* & & & \epsilon_R \end{bmatrix} \tag{6.18}$$

This form of the contour Green's function's EOM is easily translated to a computational

form. Optionally, one can express the contour Green's functions with the matrix,

$$\mathbf{G} = \begin{bmatrix} \mathbf{G}^c_{LL} & \mathbf{G}^c_{Ld} & \mathbf{G}^c_{LR} \\ \mathbf{G}^c_{dL} & \mathbf{G}^c_{dd} & \mathbf{G}^c_{dR} \\ \mathbf{G}^c_{RL} & \mathbf{G}^c_{Rd} & \mathbf{G}^c_{RR} \end{bmatrix}. \tag{6.19}$$

In this case, the unit matrix is the usual definition,

$$\mathbf{1} = \begin{bmatrix} 1 & & \\ & 1 & \\ & & 1 \end{bmatrix}. \tag{6.20}$$

The coupled matrix equation of Eq. (6.15) must be solved consistently between the time-derivative of both arguments [6], i.e.,

$$i\hbar \frac{\mathrm{d}}{\mathrm{d}z}\mathbf{G}(z,z') = \delta(z-z')\mathbf{1} + \mathbf{H}(z)\mathbf{G}(z,z'), \tag{6.21}$$

$$-i\hbar \frac{\mathrm{d}}{\mathrm{d}z'}\mathbf{G}(z,z') = \delta(z-z')\mathbf{1} + \mathbf{G}(z,z')\mathbf{H}(z'). \tag{6.22}$$

The computational procedure used in this work involves the trapezoidal rule, with details found in Appendix D.6.

6.2.3 Derived Quantities

Once $\mathbf{G}(z,z')$ has been found using Eqs. (6.21) and (6.22) for every z and z' points of the contour, one can separate the $\mathbf{G}(z,z')$ into their equivalent time components $\mathbf{G}(t,t')$ by their

position on the contour,

$$\mathbf{G}(z,z') \to \begin{bmatrix} \mathbf{G}(t_+,t'_+) & \mathbf{G}(t_+,t'_-) \\ \mathbf{G}(t_-,t'_+) & \mathbf{G}(t_-,t'_-) \end{bmatrix}. \tag{6.23}$$

A handy relation is that each of these sectors correspond with the usual Green's functions (retarded, advanced, Keldysh, lesser, and greater) and these components,

$$\mathbf{G}^R(t,t') = \mathbf{G}(t_+,t'_+) - \mathbf{G}(t_+,t'_-), \tag{6.24}$$

$$\mathbf{G}^A(t,t') = \mathbf{G}(t_+,t'_+) - \mathbf{G}(t_-,t'_+), \tag{6.25}$$

$$\mathbf{G}^K(t,t') = \mathbf{G}(t_-,t'_+) + \mathbf{G}(t_+,t'_-), \tag{6.26}$$

$$\mathbf{G}^<(t,t') = \mathbf{G}(t_+,t'_-), \tag{6.27}$$

$$\mathbf{G}^>(t,t') = \mathbf{G}(t_-,t'_+). \tag{6.28}$$

Single-particle quantities, such as density of states, can be calculated from these usual Green's functions. For example, one should first transform the retarded $\mathbf{G}^R(t,t')$ Green's function into an average (physical) time t_{avg} and relative time t_{rel},

$$\mathbf{G}^R(t,t') \to \mathbf{G}^R(t+t'/2, t-t') = \mathbf{G}^R(t_{avg}, t_{rel}), \tag{6.29}$$

and then perform a Fourier transform on t_{rel} to obtain the frequency and time-dependent density of states, and the corresponding spectral function,

$$\mathbf{G}^R(t_{avg},\omega) = \int \mathrm{d}t_{rel}\, e^{i\omega t_{rel}} \mathbf{G}^R(t_{avg}, t_{rel}), \tag{6.30}$$

$$\mathbf{A}(t_{avg},\omega) = -\frac{1}{\pi} \operatorname{Im}\big\{\mathbf{G}^R(t_{avg},\omega)\big\}. \tag{6.31}$$

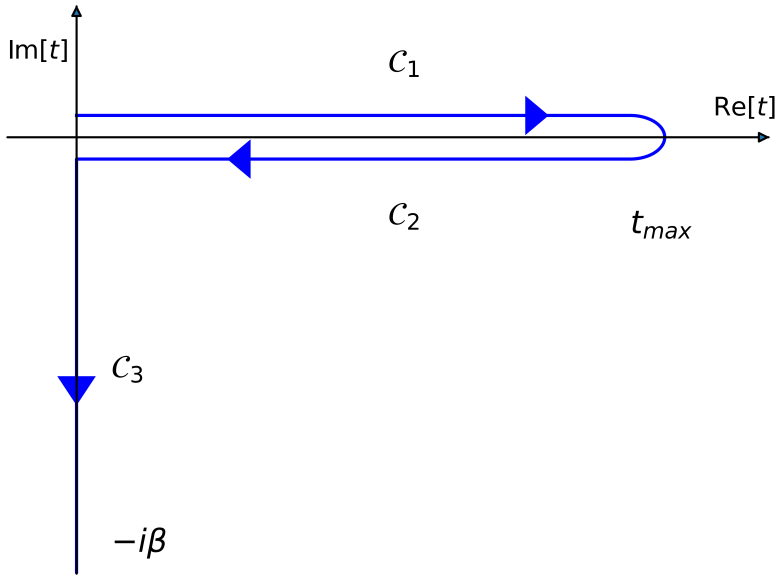

Figure 6.3: The three-branch contour considered for the finite-temperate non-equilibrium Green's functions considered in this chapter.

Important to this work, one can define the occupation number of the j'th site using the same time lesser Green's function,

$$n_j(t) = -i\mathbf{G}^{<}_{jj}(t, t+\delta), \tag{6.32}$$

where δ is an infinitesimal time.

6.2.4 Temperature and Initial Conditions

To fully include temperature, one must extend the contour method of the prior sections, in line with the Kadanoff-Baym formalism [7]. The new contour includes an imaginary time term which accounts for all initial correlations, assumed to have equilibrated at an infinite time in the past, and temperature effects through the variable $\beta \equiv 1/k_B T$. The overall contour is sketched in Fig 6.3. Accounting for this in the formalism involves computing the

Green's function for additional time point combinations along the new contour,

$$\mathbf{G}(z,z') \rightarrow \begin{bmatrix} \mathbf{G}(t_+,t'_+) & \mathbf{G}(t_+,t'_-) & \mathbf{G}(t_+,t'_\tau) \\ \mathbf{G}(t_-,t'_+) & \mathbf{G}(t_-,t'_-) & \mathbf{G}(t_-,t'_\tau) \\ \mathbf{G}(t_\tau,t'_+) & \mathbf{G}(t_\tau,t'_-) & \mathbf{G}(t_\tau,t'_\tau) \end{bmatrix}, \tag{6.33}$$

where t_τ is a time on the imaginary contour branch $\mathcal{C}_3$. The computational implementation is the same as for the two-branch contour case, but extended now with imaginary times. Discretizing the Green's function requires some care [8, 9]. I have found that 1000 real time steps and 100 imaginary time steps is sufficient to see non-linear behavior in the calculated occupation number.

6.3 Results

I first start with the two-site model, where I investigate how the occupation number changes as a function of time under non-equilibrium conditions. Because the Hamiltonian interactions do not mix spin terms, I block diagonalize a single polarization and present the occupation number results for a single spin channel. For the energy scales, I assume that the scale of the hopping term between the two sites t_{LR} sets the scale of the onsite energy of the sites, i.e., $\epsilon_L = t_{LR}$. I then apply a symmetric bias on the chemical potentials of the left and right site $\epsilon_L = -\epsilon_R$. For the units of the system, I set $\hbar = 1$, and so the timescale is chosen to be on the units of inverse energy. The temperature is chosen to be on the order of the inverse of the hopping term, $\beta = 1/t_{LR}$. The results of the occupation number as a function of time is shown in Fig. 6.4.

Next, I explore the three site model. The additional site gives us more bias options to explore. The first option, shown in Fig. 6.5, is the linear energy level difference bias with the site between the lead sites as a reference: $\epsilon_L = -\epsilon_R$ and $\varepsilon_d = 0$ with symmetric hopping

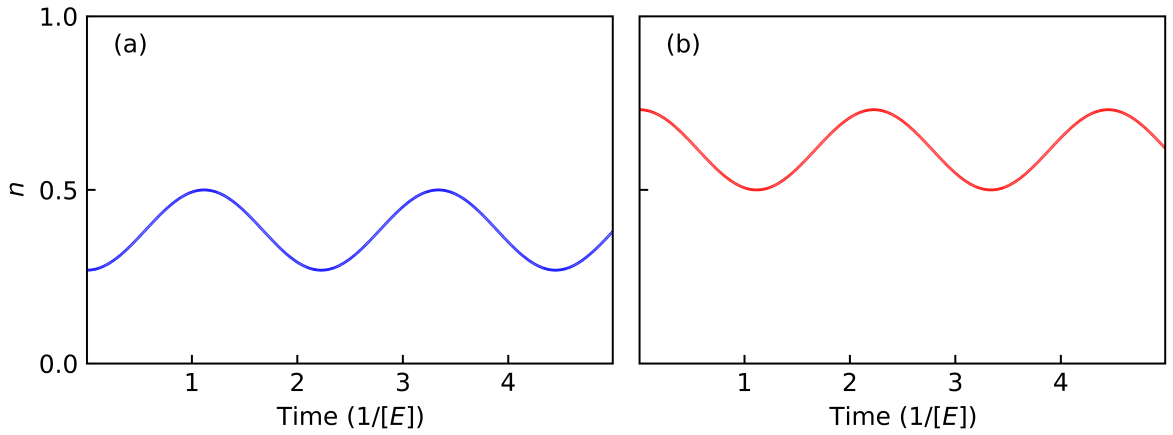

Figure 6.4: Occupation number of the left site (a) and the right site (b) in the two-site biased model as a function of time.

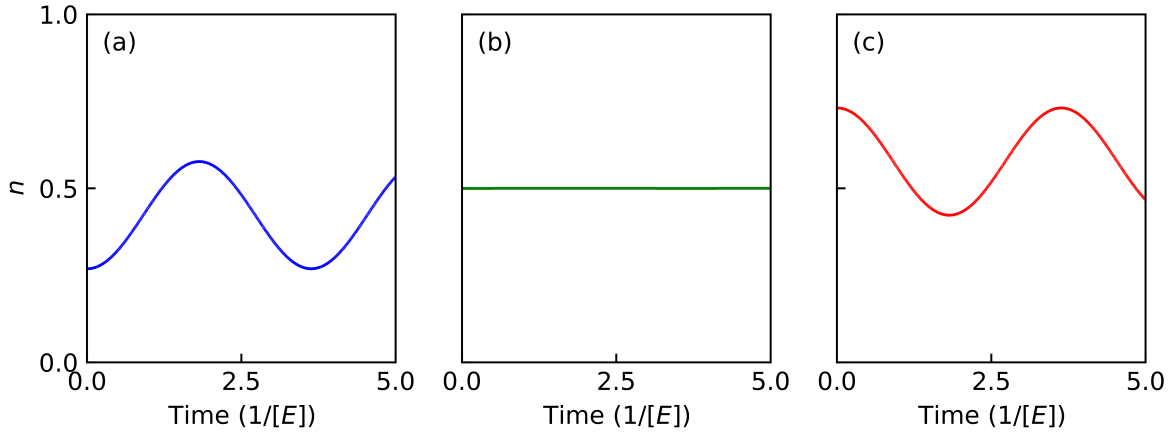

Figure 6.5: Occupation number of the left site (a), center site (b), and right site (c) in the three-site model with linear energy level differences, as a function of time.

to the center site $t_{Ld} = t_{Rd}$. Next is the so-called "armchair" bias, where the lead sites are kept at the same chemical potential $\epsilon_L = \epsilon_R$, while the middle site is set lower than the leads (e.g., through the use of a gate voltage) $\varepsilon_d = 0$. Again, the hopping terms are enforced to be symmetric $t_{Ld} = t_{Rd}$. The change in occupation number with this bias is shown in Fig. 6.6.

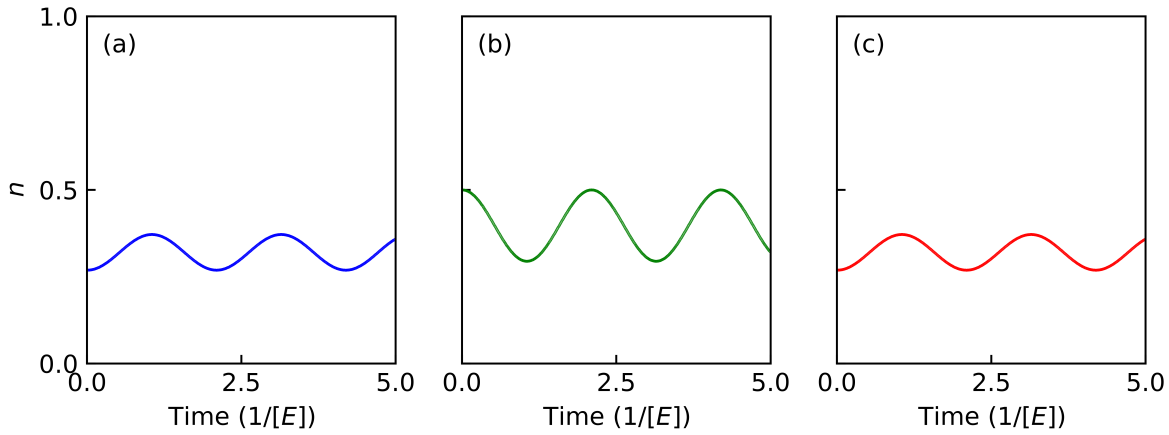

Figure 6.6: Occupation number of the left site (a), center site (b), and right site (c) in the three-site model, with chemical potentials chosen in the armchair configuration.

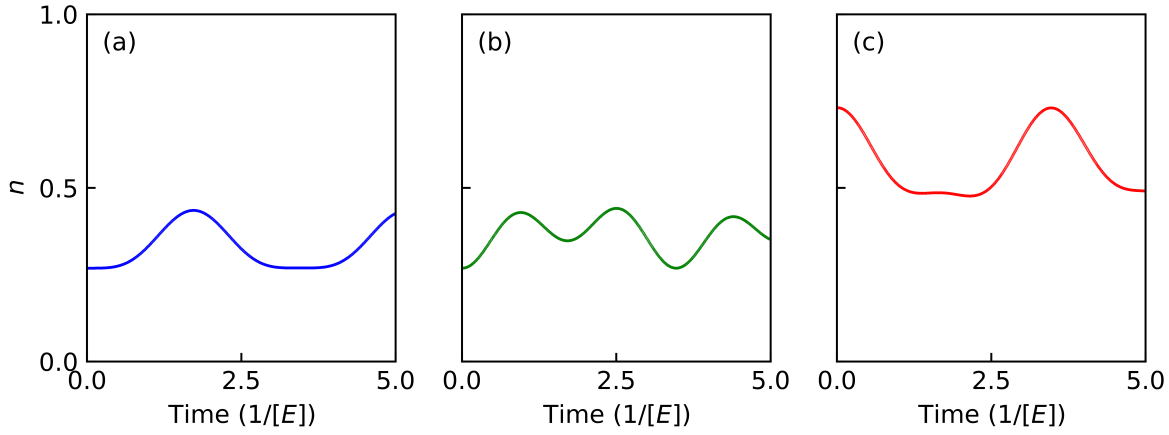

Figure 6.7: Occupation number of the left site (a), center site (b), and right site (c) in the three-site model, with asymmetric energy levels.

Asymmetric arrangements also lead to some interesting changes in the occupation numbers of each site. I first use an asymmetric bias, where $\epsilon_L = \varepsilon_d$ and $\epsilon_R = 0$, which shows non-linear effects in Fig. 6.7. Finally, I explore the case when there are asymmetric hopping terms, e.g., the central site is closer to one of the leads, while biasing the chemical potentials

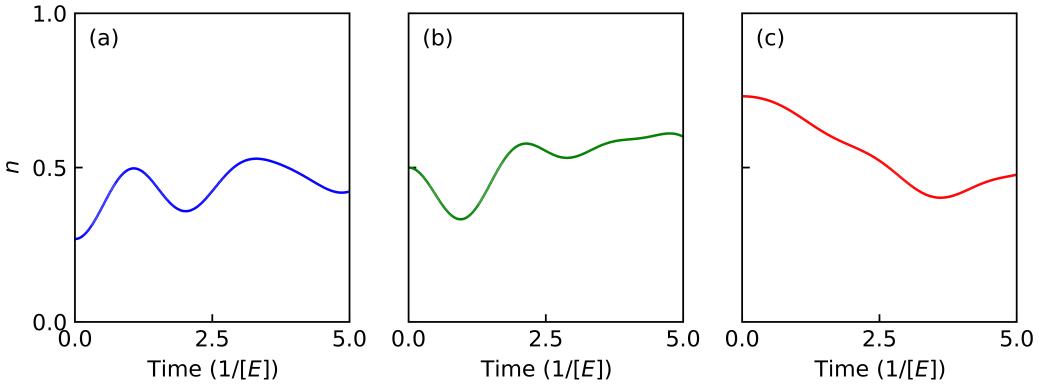

Figure 6.8: Occupation number of the left site (a), center site (b), and right site (c) in the three-site model, with asymmetric hopping terms.

linearly. I set $t_{Ld} = 1.5|\epsilon_L|$ and $t_{Rd} = 0.5|\epsilon_R|$, the results of which are shown in Fig. 6.8.

6.4 Discussion and Outlook

The results shown in Fig. 6.4 and Fig. 6.5 of the two-body and three-body linear bias is expected. The occupation of one lead will oscillate opposite of the other lead as the electron is transferred between them. In the absence of dissipative processes, the transfer will continue indefinitely. This linear bias across three sites shows this behavior, with the occupation number unchanging for the center site. This is because the same amount of occupation number changing from one lead is compensated exactly by the other through the influence of the symmetric hopping terms and symmetric position of the bias.

The behavior of the non-linear bias and hopping terms is interesting. In particular, the armchair bias in Fig. 6.6 indicates that if one holds the center site below the chemical potential, the site will experience partial charging cycles, akin to the Coulomb blockade cycling without the full zero-to-one electron occupation change. The asymmetric leads in Fig. 6.7 show nonlinear effects, and in the time range considered, do not appear to evolve

towards an equilibrium occupation number. Similarly, the asymmetric hopping arrangement in Fig. 6.8 results in asymmetric occupation versus time, and also does not appear to tend towards equilibrium.

So far, I have neglected many-body effects. By introducing interactions (either electronic or spin), the EOM is no longer a closed equation. When taking these interactions into account, solving for the Green's function EOM of Eqs. (6.21) and (6.22) as done before modifies the equations to include a many-body self energy $\mathbf{\Sigma}^{MB}(z, z'')$,

$$i\hbar\frac{\mathrm{d}}{\mathrm{d}z}\mathbf{G}(z,z') = \delta(z-z')\mathbf{1} + \mathbf{H}(z)\mathbf{G}(z,z') + \int \mathrm{d}z''\, \mathbf{\Sigma}^{MB}[\mathbf{G}](z,z'')\mathbf{G}(z'',z'), \tag{6.34}$$

$$-i\hbar\frac{\mathrm{d}}{\mathrm{d}z'}\mathbf{G}(z,z') = \delta(z-z')\mathbf{1} + \mathbf{G}(z,z')\mathbf{H}(z') + \int \mathrm{d}z''\, \mathbf{G}(z,z'')\mathbf{\Sigma}^{MB}[\mathbf{G}](z'',z'). \tag{6.35}$$

The many body self energy term is a functional of $\mathbf{G}$, and so these equations must be solved self-consistently. The form of this term is approximated for numerical work. In a first approximation, for example, one can assume that $\mathbf{\Sigma}^{MB}(z'', z')$ is known and only depends on the uncoupled $\mathbf{g}(z'', z')$ Green's functions, solved for the non-interacting case as has been done in this work.

6.4.1 Extension to Onsite Spin Interactions

I provide a concrete example of how one could extend the results of this chapter, by including an onsite Kondo interaction between two spin objects whose fields impact the central site. The central region Hamiltonian is then changed to include the term,

$$\mathcal{H}_C = \sum_\sigma \varepsilon_d \hat{d}^\dagger_\sigma \hat{d}_\sigma + \frac{1}{2}\sum_{\mu\mu'}\left(J_1\hat{\mathbf{S}}_1 + J_2\hat{\mathbf{S}}_2\right)\cdot \hat{d}^\dagger_\mu \hat{\boldsymbol{\sigma}}_{\mu\mu'}\hat{d}_{\mu'}. \tag{6.36}$$

I keep each spin term separate in anticipation of including interaction terms between them. The addition of the two spin objects naturally brings about six new operators, enlarging the

B vector,

$$\mathbf{B} = \begin{bmatrix} \hat{c}_{L\sigma} & \hat{d}_{\sigma} & \hat{c}_{R\sigma} & \hat{S}_{1\chi} & \hat{S}_{2\chi} \end{bmatrix}, \tag{6.37}$$

where $\sigma \in [\uparrow, \downarrow]$ and $\chi \in [x,\ y,\ z]$.

As before, I solve for the commutation relations of each operator with the Hamiltonian. For the $\hat{c}$ operators,

$$\left[\hat{c}_{\alpha'\sigma'}, \hat{\mathcal{H}}\right] = \left[\hat{c}_{\alpha'\sigma'}, \hat{\mathcal{H}}_{TB}\right] + \left[\hat{c}_{\alpha'\sigma'}, \frac{1}{2}\sum_{\mu\mu'}\left(J_1\hat{\mathbf{S}}_1 + J_2\hat{\mathbf{S}}_2\right)\cdot \hat{d}^{\dagger}_{\mu}\hat{\boldsymbol{\sigma}}_{\mu\mu'}\hat{d}_{\mu'}\right] \tag{6.38a}$$

$$= \left(\varepsilon_{\alpha'} - \mu_{\alpha'}\right)\hat{c}_{\alpha'\sigma'} + t_{\alpha' d}\hat{d}_{\sigma'}. \tag{6.38b}$$

Performing the same procedure for the $\hat{d}$ operator results in,

$$\left[\hat{d}_{\sigma'}, \hat{\mathcal{H}}\right] = \left[\hat{d}_{\sigma'}, \hat{\mathcal{H}}_{TB}\right] + \left[\hat{d}_{\sigma'}, \frac{1}{2}\sum_{\mu\mu'}\left(J_1\hat{\mathbf{S}}_1 + J_2\hat{\mathbf{S}}_2\right)\cdot \hat{d}^{\dagger}_{\mu}\hat{\boldsymbol{\sigma}}_{\mu\mu'}\hat{d}_{\mu'}\right] \tag{6.39a}$$

$$= \sum_{\alpha}\left(t^{*}_{\alpha d}\hat{c}_{\alpha\sigma'} + \varepsilon_d\hat{d}_{\sigma'}\right) + \frac{1}{2}\sum_{\mu}\left(J_1\hat{\mathbf{S}}_1 + J_2\hat{\mathbf{S}}_2\right)\cdot\hat{\boldsymbol{\sigma}}_{\sigma'\mu}\hat{d}_{\mu}. \tag{6.39b}$$

Immediately one sees that because of the many-body interaction, the commutator results in three-operator objects, rather than the two-operator averages considered in the prior model. In this form, a new Green's function is created, and the Green's function equations are no

longer closed, e.g.,

$$i\hbar\frac{\mathrm{d}}{\mathrm{d}z}G^c_{d_\sigma d_\sigma}(z,z') = \delta(z-z') + t^*_{Ld}G^c_{L_\sigma d_\sigma}(z,z') + t^*_{Rd}G^c_{R_\sigma d_\sigma}(z,z') + \varepsilon_d G^c_{d_\sigma d_\sigma}(z,z') - \frac{1}{2}\sum_{i\mu\chi}\frac{i}{\hbar}\left\langle \mathcal{T}\left(J_i\hat{S}_{i\chi}(z)\sigma^\chi_{\sigma\mu}\hat{d}_\mu(z)\hat{d}^\dagger_\sigma(z')\right)\right\rangle \tag{6.40a}$$

$$= \delta(z-z') + t^*_{Ld}G^c_{L_\sigma d_\sigma}(z,z') + t^*_{Rd}G^c_{R_\sigma d_\sigma}(z,z') + \varepsilon_d G^c_{d_\sigma d_\sigma}(z,z') - \sum_{i\mu\chi}\frac{J_i}{2}\sigma^\chi_{\sigma\mu}\frac{i}{\hbar}\left\langle \mathcal{T}\left(\hat{S}_{i\chi}(z)\hat{d}_\mu(z)\hat{d}^\dagger_\sigma(z')\right)\right\rangle \tag{6.40b}$$

$$= \delta(z-z') + t^*_{Ld}G^c_{L_\sigma d_\sigma}(z,z') + t^*_{Rd}G^c_{R_\sigma d_\sigma}(z,z') + \varepsilon_d G^c_{d_\sigma d_\sigma}(z,z') + \sum_{i\mu\chi}\frac{J_i}{2}\sigma^\chi_{\sigma\mu}G^c_{S_{i\chi}d_\mu;d_\sigma}(z,z'), \tag{6.40c}$$

where $G^c_{ab;c}(z,z')$ is the new three-operator Green's function. This is the source of the many-body self-energy term in Eqs. (6.34) and (6.35). If one continues the procedure with this new Green's function, one will derive an infinite set of equations. Similarly, one can derive the Green's functions for the spin-spin correlations, using the $\hat{S}_{1\chi}$ and $\hat{S}_{2\chi}$ commutators,

$$\left[\hat{S}_{i'\chi'},\hat{\mathcal{H}}\right] = \left[\hat{S}_{i'\chi'},\hat{\mathcal{H}}_{TB}\right] + \left[\hat{S}_{i'\chi'},\frac{1}{2}\sum_{\mu\mu'}\left(J_1\hat{\mathbf{S}}_1 + J_2\hat{\mathbf{S}}_2\right)\cdot\hat{d}^\dagger_\mu\hat{\boldsymbol{\sigma}}_{\mu\mu'}\hat{d}_{\mu'}\right] \tag{6.41}$$

$$= \frac{i}{2}\sum_{\mu\mu' mn}\left(J_1\delta_{i'1}\epsilon^{\chi' mn}\hat{S}_{1n} + J_2\delta_{i'2}\epsilon^{\chi' mn}\hat{S}_{2n}\right)\hat{m}\cdot\hat{\boldsymbol{\sigma}}_{\mu\mu'}\hat{d}^\dagger_\mu\hat{d}_{\mu'}. \tag{6.42}$$

The final equation of motion that needs to be solved has the form,

$$i\hbar\frac{\mathrm{d}}{\mathrm{d}z}G^c_{ij}(z,z') = \delta(z-z')\left\langle\left\{B_i(z),B^\dagger_j(z')\right\}\right\rangle - \frac{i}{\hbar}\left\langle\mathcal{T}\left(\left[B_i(z),\mathcal{H}\right]B^\dagger_j(z')\right)\right\rangle, \tag{6.43}$$

where,

$$\mathbf{G} = \begin{bmatrix} \mathbf{G}^c_{LL} & \mathbf{G}^c_{Ld} & \mathbf{G}^c_{LR} & \mathbf{G}^c_{LS_1} & \mathbf{G}^c_{LS_2} \\ \mathbf{G}^c_{dL} & \mathbf{G}^c_{dd} & \mathbf{G}^c_{dR} & \mathbf{G}^c_{dS_1} & \mathbf{G}^c_{dS_2} \\ \mathbf{G}^c_{RL} & \mathbf{G}^c_{Rd} & \mathbf{G}^c_{RR} & \mathbf{G}^c_{RS_1} & \mathbf{G}^c_{RS_2} \\ \mathbf{G}^c_{S_1L} & \mathbf{G}^c_{S_1d} & \mathbf{G}^c_{S_1R} & \mathbf{G}^c_{S_1S_1} & \mathbf{G}^c_{S_1S_2} \\ \mathbf{G}^c_{S_2L} & \mathbf{G}^c_{S_2d} & \mathbf{G}^c_{S_2R} & \mathbf{G}^c_{S_2S_1} & \mathbf{G}^c_{S_2S_2} \end{bmatrix}, \tag{6.44}$$

and where the $\mathbf{G}_{ij}$ blocks are no longer equal size, as they take on the dimension of the spin for each operator. One can introduce approximations to truncate the number of new Green's functions that one must solve for in Eq. (6.40c), for example, by considering a mean-level theory. A comparison of contact-spin exchange interaction in the time-domain could then be made to the results of Chapter 5 to establish the applicability of static versus transient pictures for these type of models.

As mentioned in Chapter 1, there exists other numerical NEGF codes that can tackle the tripartite spin problem. One code that I have helped develop is the TimeESR code `https://github.com/qphensurf/TimeESR`. TimeESR is derived from the NEGF formalism and is applied to the quantum master equation scheme [10, 11]. This allows one to probe low-temperature transport features for a variety of interactions under applied fields, like those relevant to scanning tunneling microscopy (STM) on exchange-coupled magnetic atoms. In the next chapters, I utilize other numerical implementations of *ab initio* codes (including an NEGF code) to explore two examples of novel quantum systems that may be a precursor to the tripartite systems described in this thesis.

6.5 List of References

[1] Y. Meir and N. S. Wingreen, Physical Review Letters **68**, 2512 (1992).

[2] M. Brandbyge, J.-L. Mozos, P. Ordejón, J. Taylor, and K. Stokbro, Physical Review B **65**, 165401 (2002).

[3] N. Papior, N. Lorente, T. Frederiksen, A. García, and M. Brandbyge, Computer Physics Communications **212**, 8 (2017).

[4] A. García, N. Papior, A. Akhtar, E. Artacho, V. Blum, E. Bosoni, P. Brandimarte, M. Brandbyge, J. I. Cerdá, F. Corsetti, R. Cuadrado, V. Dikan, J. Ferrer, J. Gale, P. García-Fernández, V. M. García-Suárez, S. García, G. Huhs, S. Illera, R. Korytár, P. Koval, I. Lebedeva, L. Lin, P. López-Tarifa, S. G. Mayo, S. Mohr, P. Ordejón, A. Postnikov, Y. Pouillon, M. Pruneda, R. Robles, D. Sánchez-Portal, J. M. Soler, R. Ullah, V. W.-z. Yu, and J. Junquera, The Journal of Chemical Physics **152**, 204108 (2020).

[5] A. Dey, D. S. Bhakuni, B. K. Agarwalla, and A. Sharma, Journal of Physics: Condensed Matter **32**, 075603 (2019).

[6] P. Myöhänen, A. Stan, G. Stefanucci, and R. van Leeuwen, Physical Review B **80**, 115107 (2009).

[7] G. Kadanoff, Leo. P; Baym, *Quantum statistical mechanics; Green's function methods in equilibrium and nonequilibrium problems* (W.A. Benjamin, New York, 1962).

[8] J. K. Freericks, Physical Review B **77**, 075109 (2008).

[9] J. K. Freericks, An introduction to many-body green's functions in and out of equilibrium (2019).

[10] B. Bhandari, R. Fazio, F. Taddei, and L. Arrachea, Physical Review B **104**, 035425 (2021).

[11] J. Reina-Gálvez, N. Lorente, F. Delgado, and L. Arrachea, Physical Review B **104**, 245435 (2021).

CHAPTER 7: COMPARISON OF EXCITATION ENERGIES AND STATES IN QUBIT CANDIDATE H-BN VB- PREDICTED BY DENSITY FUNCTIONAL THEORY AND QUANTUM DEFECT EMBEDDING THEORY

(Adapted from Eric D. Switzer, Christian Vorwerk, Volodymyr Turkowski, Duy Le, Giulia Galli, and Talat S. Rahman, "Comparison of Excitation Energies and States in Qubit Candidate h-BN $V_B{}^-$ Predicted by Density-Functional Theory and Quantum Defect Embedding Theory." *In preparation* (2023))

7.1 Introduction

Considerable effort is underway to find new and improved solid-state qubits, e.g., spin qubits derived from defects in bulk hexagonal boron nitride (h-BN) [1–6]. h-BN is a van der Waals material that has desirable insulating properties when used as a substrate for 2D materials [7]. Progress has been made in developing qubits from defected h-BN, namely the boron vacancy (h-BN $V_B{}^-$) [8]. Recent experimental work has found that coherence times of up to 4 μs are possible for h-BN $V_B{}^-$ using a strong continuous microwave field, making it a competitive candidate compared to qubits made of nitrogen-vacancy centers in nanodiamonds [6].

To characterize the defects, theoretical work has focused on identifying the excitation properties of h-BN $V_B{}^-$. Density matrix renormalization group and Kohn-Sham (KS) density-functional theory (DFT) have been used to characterize optically detected magnetic resonance for single-sheet h-BN V_B [9]. Group theory analysis and DFT has also been used to characterize single-photon emission for several types of vacancies in 2D h-BN [10]. Coupled cluster theory, DFT, time-dependent DFT (TDDFT) and complete-active-space self-consistent field methods were used to describe ODMR for single-flake h-BN V_B [11].

Our study furthers this research by calculating the excitation energies using quantum defect embedding theory (QDET) [12] for the qubit h-BN $V_B{}^-$, using KS wave functions obtained from traditional DFT using Quantum Espresso [13, 14] at the GGA PBE and GGA HSE exchange-correlation functional level incorporating van der Waal corrections and calculations. In this work, we characterize the ground state energies and symmetries of the defect geometry. Our results show that the choice of functional leads to significant differences in point-group symmetry labels and energetic ordering of defect states for the spin polarized system. We also show that the choice of functional level dictates the overall energy range of transitions as calculated by QDET. We find that QDET predicts singlet-triplet splittings of the fourth and fifth excitations, and the sixth and seventh excitations, at 23 meV and 25 meV for the PBE level of theory. We also find that the HSE level of theory gives splittings of 22 meV and 2 meV for these singlet-triplet pairs.

The chapter is organized as follows. First in Section 7.2, we describe the DFT and QDET method and relevant computational parameters. In Section 7.3.1, we present our results on the electronic ground state. In Section 7.3.2, we show our calculated QDET excitation states. Finally, in Sections 7.4 and 7.5, we present an analysis of the excitation types and a future outlook for using QDET to characterize excitations.

7.2 Methodology

7.2.1 DFT Computational Details

Our first-principles calculations were carried out using Quantum Espresso [13, 14]. Exchange and correlation effects were included at the generalized gradient approximation (GGA) level for two separate simulations: one using the PBE [15] and the other using the HSE [16, 17] potentials. For the GGA PBE calculations, we used the revised van der Waal density functional [18]. For GGA HSE, we used van der Waal Grimme D3 semi-empirical corrections

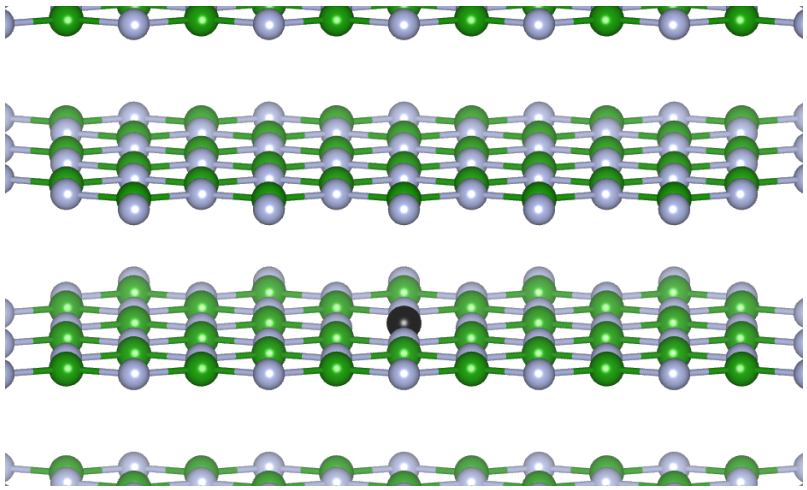

Figure 7.1: Schematic of the h-BN $V_B{}^-$ supercell used in this work. Green: Boron, silver: Nitrogen, black: charged Boron vacancy

[19] and the Gygi-Baldereschi scheme to handle divergences of the Coulomb integral [20]. Both spin polarized and spin-unpolarized calculations were carried out. The single-electron wave functions were expanded in a plane-wave basis using the SG15 optimized norm-conserving Vanderbilt (ONCV) scalar relativistic pseudopotentials [21, 22], a kinetic energy cutoff of 85 Ry, and charge density cutoff of 340 Ry.

To simulate an isolated defect in the h-BN bulk structure, we used a cubic 239 atom supercell built from an orthorhombic 4-atom unit cell with a Boron atom removed. A schematic of the defected structure is shown in Fig. 7.1. The relaxed cell dimensions were 12.89 Å x 12.41 Å x 13.49 Å for the structure using the HSE potential, and 13.03 Å x 12.54 Å x 13.10 Å for the structure using the PBE potential. The k-point sampling of the total energy was restricted to the Γ point of the Brillouin zone. The tolerance of the self-consistent loops was set to 10^{-7} Ry. Relaxation of generated structures was achieved when all force components were smaller than 3×10^{-4} Ry/Bohr, and the estimated energy error between relaxation steps was less than 10^{-4} Ry. To simulate the charged defect, a total charge of $-e$

per supercell and a net magnetic moment of $-2\ \mu_B$ per supercell was enforced during the relaxation procedure.

7.2.2 QDET Details

QDET belongs to a classic of techniques, named embedding theories, which are designed to solve for the electronic structure of a region of interest surrounded by an environment [12, 23–27]. QDET specifically describes a condensed system in which the electronic excitations occur within a small active subspace of the full Hilbert space of the system [12]. The active region is taken in the dilute limit, i.e., the supercell representing the system is large enough to ensure that the active space in neighboring images do not interact with each other. This active space is represented by an orthogonal set of functions, typically a restricted set of the Kohn-Sham (KS) Hamiltonian states $\psi_i^{\mathrm{KS}}(\mathbf{x})$ describing the solid. One may select the active orbital space in calculations of defects in solids by manually identifying orbitals induced by the defect. We use the following localization function to identify these orbitals,

$$L(\psi_i^{\mathrm{KS}}) = \int_V \mathrm{d}\mathbf{x} \left|\psi_i^{\mathrm{KS}}(\mathbf{x})\right|^2, \tag{7.1}$$

where the integration volume is chosen to include the defect and at most is bounded by the volume of the supercell, and thus $L \in [0, 1]$. We define the active space for the defect by choosing orbital that have an L value larger than a chosen threshold.

Utilizing the Born-Oppenheimer and non-relativistic approximation, the effective many-body Hamiltonian of the chosen active space is defined as,

$$\hat{\mathcal{H}} = \sum_{ij} t_{ij} \hat{a}_i^\dagger \hat{a}_j + \frac{1}{2} \sum_{ijkl} v_{ijkl} \hat{a}_i^\dagger \hat{a}_j^\dagger \hat{a}_l \hat{a}_k, \tag{7.2}$$

where t_{ij} is the effective one-body interaction strength, v_{ijkl} the effective two-body interaction

strength, $\hat{a}_i$ is the annihilation operator for the i'th active space orthogonal wave function $\phi_i(\mathbf{x})$, and the sum is over all orthogonal wave functions in the active space. The v_{ijkl} elements are taken to be the matrix elements of the partially screened static Coulomb potential, screening the bare Coulomb potential v with the active space reduced polarizability χ_0^R,

$$v_{ijkl} = \left[W_0^R(\omega = 0)\right]_{ijkl}, \tag{7.3}$$

where,

$$W_0^R(\omega = 0) = v + v\chi_0^R W_0^R(\omega = 0). \tag{7.4}$$

The reduced polarizability χ_0^R is calculated by first computing the KS polarizability χ_0, and then subtracting out the active space polarizability χ_0^A, which is simply the KS polarizability projected onto the active space. Within the random-phase approximation, the active space polarizability is given by,

$$\begin{aligned} P_0^A(\mathbf{x}_1, \mathbf{x}_2; \omega) = \sum_i \sum_j & \left(f^A \psi_v^{\mathrm{KS}}\right)(\mathbf{x_1}) \left(f^A \psi_c^{\mathrm{KS}}\right)(\mathbf{x_1}) \\ & \times \left(f^A \psi_c^{\mathrm{KS}}\right)(\mathbf{x_2}) \left(f^A \psi_v^{\mathrm{KS}}\right)(\mathbf{x_2}) \\ & \times \left(\frac{1}{\omega - (\varepsilon_j - \varepsilon_i) + i\eta} + \frac{1}{\omega + (\varepsilon_j - \varepsilon_i) + i\eta}\right). \end{aligned} \tag{7.5}$$

Here f^A is the active space projector $\sum_k |\phi_k\rangle \langle\phi_k|$, ε_i is the i'th KS eigenvalue, the sum over v is over occupied states, and the sum over c is over unoccupied KS states. Once the reduced polarizability is found, the Dyson equation Eq. (7.3) is solved, and one obtains the v_{ijkl} elements. Because the definition of the two-body elements involves contributions of the Hartree and exchange correlations energies, which are also included in the calculations of the KS energies and states, the elements contain so-called double counting terms. The correction

Table 7.1: Symmetry labels for the defect levels at the PBE and HSE functional level (D1 to D5) for each spin channel (↑ and ↓). Labels belong to the C_{2v} point-group symmetry.

Level	PBE (↑)	PBE (↓)	HSE (↑)	HSE (↓)
D1	b_1	b_1	b_2	b_1
D2	b_1	b_1	b_2	b_2
D3	b_2	b_2	b_1	a_1
D4	a_1	a_1	b_1	a_1
D5	b_2	b_2	b_2	b_2

is removed in the calculation of the single-body terms,

$$t_{ij} = \mathcal{H}_{ij}^{\mathrm{KS}} - t_{ij}^{\text{double-count}}, \tag{7.6}$$

where $\mathcal{H}^{\mathrm{KS}}$ is the KS Hamiltonian. The method to calculate and remove the double-counting from the t_{ij} elements can be found in the literature describing the computational implementation [12, 26]. The QDET calculations and diagonalization of the many-body Hamiltonian were carried out using the WEST code [28], yielding the many-body eigenspectrum.

7.3 Results

7.3.1 Ground State Calculations

First we find the energy levels of the PBE structure, as shown in Fig. 7.2. The defect levels for the PBE level are identified by analyzing the charge density maps in Fig. 7.4 and 7.4, and the localization function in Fig. 7.8. We similarly plot the defect energy levels at the HSE functional level in Fig. 7.3. We plot the charge density of the spin up channel for PBE in Fig. 7.4, and HSE in Fig. 7.5. We plot the other spin channel in Fig. 7.6 and Fig. 7.6.

Visual analysis of the charge density allows us to ascribe the symmetry label for the local point-group symmetry C_{2v}, with results shown in Table 7.1. Using the localization function

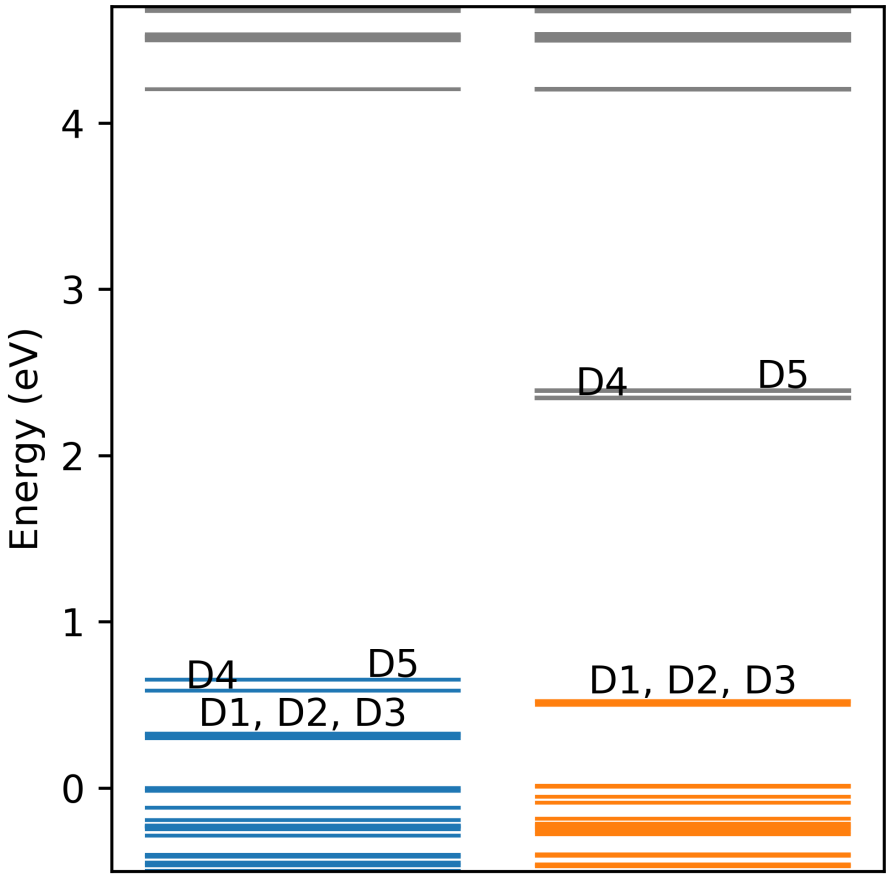

Figure 7.2: Energy diagram for the V_B^- structure at the PBE functional level with defect orbitals labeled. The zero of the energy is the maximum non-defect band energy in the spin up channel. The spin up channel is colored blue, while the spin down channel is colored orange. Gray energy levels are unoccupied levels.

as determined by QDET for the spin polarized calculation with radius of half the interlayer distance, centered about the center of the defect and with a threshold of 0.1, we find five localized orbitals that are within the band gap of bulk h-BN in the PBE functional level. Though a localized level exists below the five considered in this work for one of the spin channels, we find that this orbital's energy is situated at a similar value to bulk bands. We assume that this level will most likely not contribute to spin excitations.

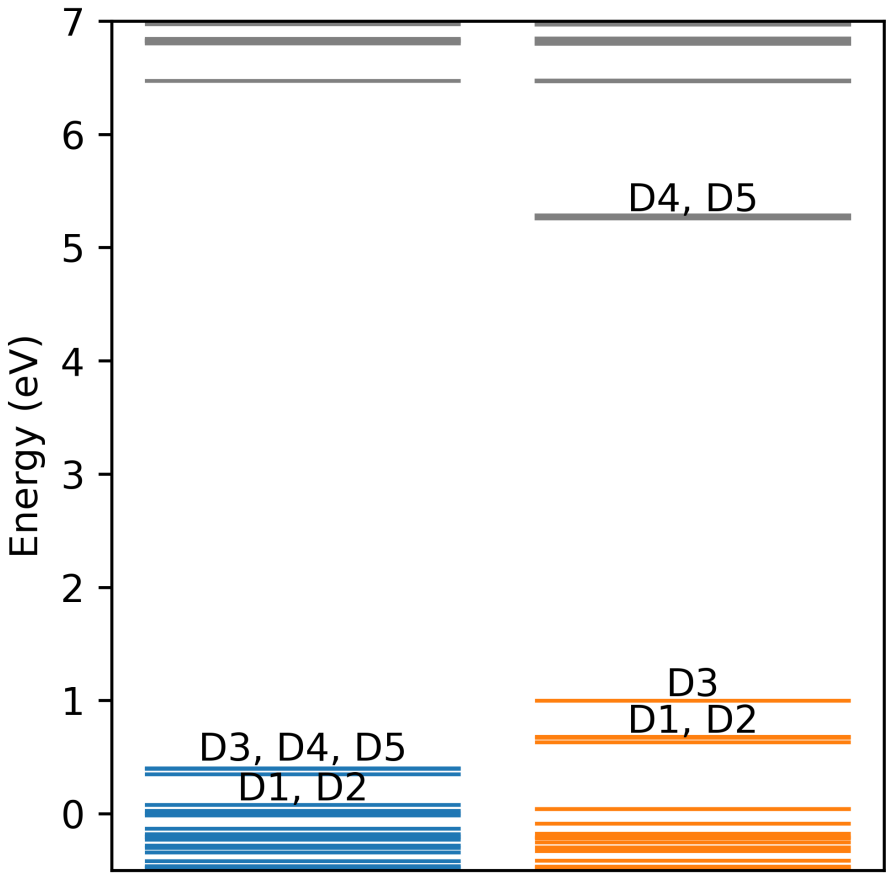

Figure 7.3: Energy diagram for the V_B^- structure at the HSE functional level with defect orbitals labeled. The zero of the energy is the maximum non-defect band energy in the spin up channel. The spin up channel is colored blue, while the spin down channel is colored orange. Gray energy levels are unoccupied levels.

7.3.2 QDET Excited States

The same localization function and threshold is used as the spin-polarized case, and is shown in Fig. 7.9. We determine that only five levels belong to the localized defect, supporting the defect level identification of the spin-polarized case. QDET uses a spin-unpolarized mean-field starting point to reduce spin contamination in the generation of the parameters for the effective Hamiltonian. The orbital energies of both functional levels are shown in Table 7.2.

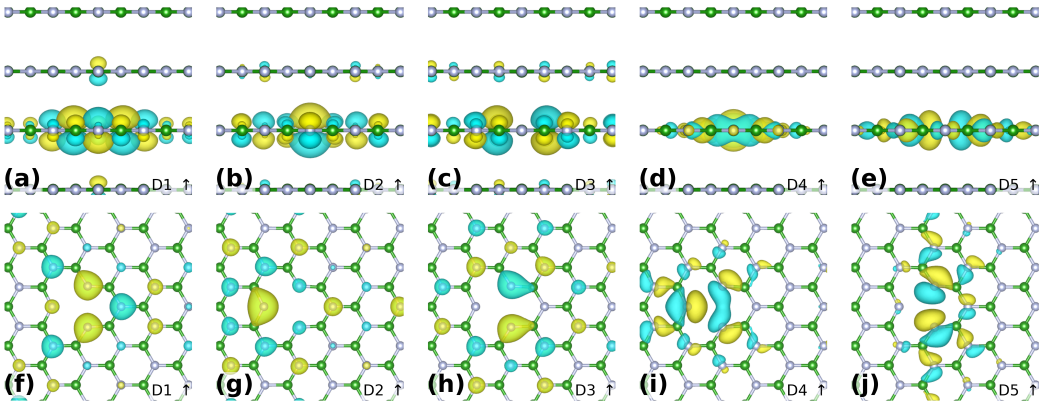

Figure 7.4: Charge density of the five defect bands at the PBE functional level for the spin up channel, as described in the text. (a)-(e) are maps in the a cell direction, and (f)-(j) are in the c cell direction. The phase of wave function contributed to the charge density is colored green and yellow.

Table 7.2: Defect Kohn-Sham (KS) orbital energies of the PBE and HSE spin-unpolarized structures (D1 to D5) and energy of the first bulk-like conduction band. The orbital energies are taken with respect to the energy of the maximum non-defect band, similar to the spin polarized case.

Level	PBE KS Energy (eV)	HSE KS Energy (eV)
D1	0.442	0.487
D2	0.448	0.518
D3	0.452	0.528
D4	1.429	2.532
D5	1.484	2.570
CB	4.220	6.446

The many-body excited states are then calculated using the five defect states. The first eight excitation energies are given in Table 7.3. Last, we inspect the two-spin channel, five-state Slater determinant per spin channel, state for each excitation. We define the nomenclature for the state as $|\chi_{D1}, \chi_{D2}, \chi_{D3}, \chi_{D4}, \chi_{D5}\rangle$ where $\chi_i \in \{0, \uparrow, \downarrow, \uparrow\downarrow\}$, with a total occupation of 4 electrons in each channel. The results are given in Table 7.4.

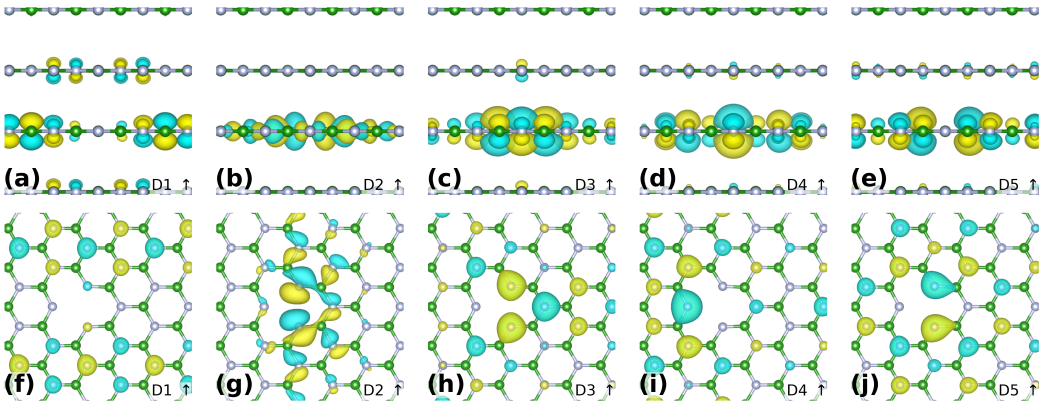

Figure 7.5: Charge density of the five defect bands at the HSE functional level for the spin up channel, as described in the text. (a)-(e) are maps in the a cell direction, and (f)-(j) are in the c cell direction.

Table 7.3: Excitation energies and spin multiplicity of the first eight excitations for the PBE and HSE structures, measured with respect to the ground state (GS) energy. The ground state multiplicity is also given.

Excitation Number	Spin Multiplicity	PBE Energy (eV)	HSE Energy (eV)
GS	3	0.000	0.000
1	1	0.694	2.099
2	1	0.734	2.153
3	1	1.428	-
4	3	3.789	3.761
5	1	3.812	3.783
6	3	3.901	3.889
7	1	3.926	3.891

7.4 Discussion

We first find that the defect energy levels shift significantly between PBE and HSE spin polarized calculations. The band gap is 4.189 eV and 5.841 eV for PBE and HSE respectively, when the defect orbitals identified later in this discussion are neglected, and are thus with

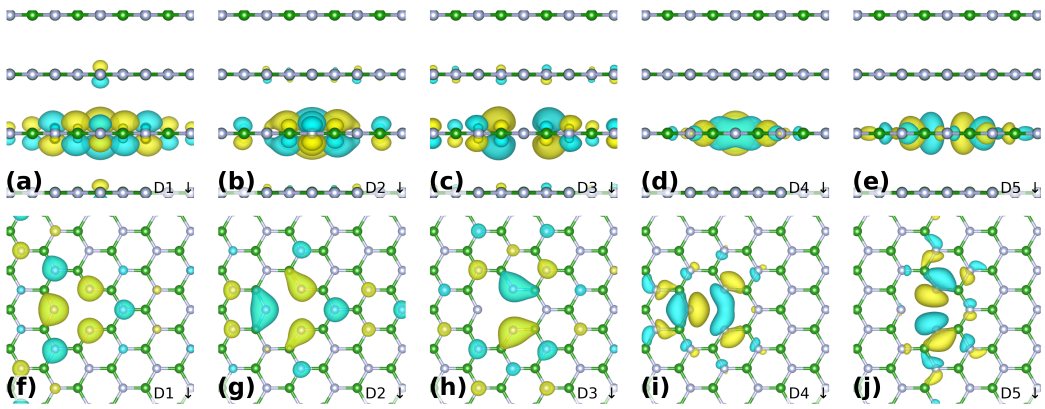

Figure 7.6: Charge density of the five defect bands at the PBE functional level for the spin down channel, as described in the text. (a)-(e) are maps in the a cell direction, and (f)-(j) are in the c cell direction. The phase of wave function contributed to the charge density is colored green and yellow.

Table 7.4: Excitation states in the $|\chi_{D1}, \chi_{D2}, \chi_{D3}, \chi_{D4}, \chi_{D5}\rangle$ nomenclature for the ground state and first four excitations of the PBE structure as calculated by QDET.

Excitation Number	State
GS	$0.707\,\|\uparrow\downarrow,\uparrow\downarrow,\uparrow\downarrow,\uparrow,\downarrow\rangle - 0.707\,\|\uparrow\downarrow,\uparrow\downarrow,\uparrow\downarrow,\downarrow,\uparrow\rangle$
1	$0.719\,\|\uparrow\downarrow,\uparrow\downarrow,\uparrow\downarrow,\uparrow\downarrow,0\rangle - 0.695\,\|\uparrow\downarrow,\uparrow\downarrow,\uparrow\downarrow,0,\uparrow\downarrow\rangle$
2	$0.707\,\|\uparrow\downarrow,\uparrow\downarrow,\uparrow\downarrow,\uparrow,\downarrow\rangle + 0.707\,\|\uparrow\downarrow,\uparrow\downarrow,\uparrow\downarrow,\downarrow,\uparrow\rangle$
3	$0.695\,\|\uparrow\downarrow,\uparrow\downarrow,\uparrow\downarrow,\uparrow\downarrow,0\rangle - 0.719\,\|\uparrow\downarrow,\uparrow\downarrow,\uparrow\downarrow,0,\uparrow\downarrow\rangle -$ $0.015\,\|\uparrow\downarrow,\uparrow\downarrow,0,\uparrow\downarrow,\uparrow\downarrow\rangle - 0.016\,\|\uparrow\downarrow,0,\uparrow\downarrow,\uparrow\downarrow,\uparrow\downarrow\rangle -$ $0.015\,\|0,\uparrow\downarrow,\uparrow\downarrow,\uparrow\downarrow,\uparrow\downarrow\rangle$
4	$0.230\,\|\uparrow\downarrow,\uparrow\downarrow,\uparrow,\uparrow\downarrow,\downarrow\rangle + 0.014\,\|\uparrow\downarrow,\uparrow\downarrow,\uparrow,\downarrow,\uparrow\downarrow\rangle - 0.482\,\|\uparrow\downarrow,\uparrow,\uparrow\downarrow,\downarrow,\uparrow\downarrow\rangle -$ $0.462\,\|\uparrow,\uparrow\downarrow,\uparrow\downarrow,\downarrow,\uparrow\downarrow\rangle - 0.230\,\|\uparrow\downarrow,\uparrow\downarrow,\downarrow,\uparrow\downarrow,\uparrow\rangle -$ $0.014\,\|\uparrow\downarrow,\uparrow\downarrow,\downarrow,\uparrow,\uparrow\downarrow\rangle + 0.483\,\|\uparrow\downarrow,\downarrow,\uparrow\downarrow,\uparrow,\uparrow\downarrow\rangle - 0.463\,\|\uparrow\downarrow,\downarrow,\uparrow\downarrow,\uparrow,\uparrow\downarrow\rangle$

respect to the valence band maximum of the bulk KS orbitals. Including the defect states, the gap is 3.551 eV for the spin up channel and 1.822 eV for the spin down in the PBE functional. It is 6.072 eV for the spin up channel and 4.263 eV for the spin down channel for the HSE functional. These define the KS same-spin excitations.

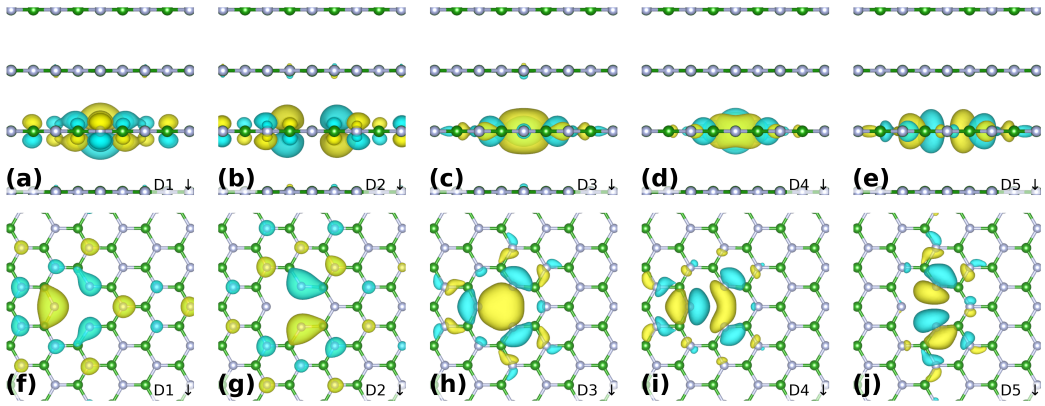

Figure 7.7: Charge density of the five defect bands at the HSE functional level for the spin down channel, as described in the text. (a)-(e) are maps in the a cell direction, and (f)-(j) are in the c cell direction.

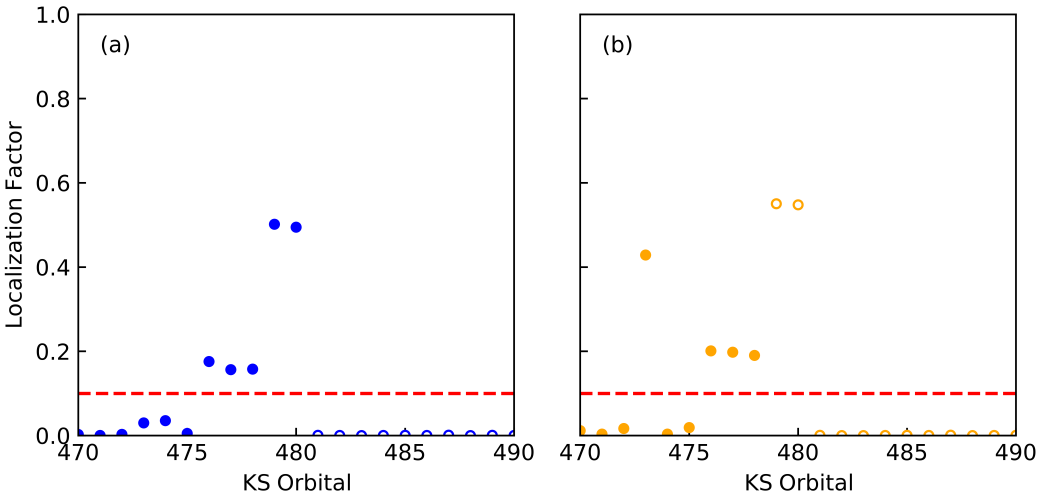

Figure 7.8: Localization function for selected Kohn-Sham orbitals for the (a) spin up and (b) spin down channel, at the PBE functional level. The threshold guideline is shown (red dashed). Filled circles represent filled orbitals, while empty orbitals are not filled.

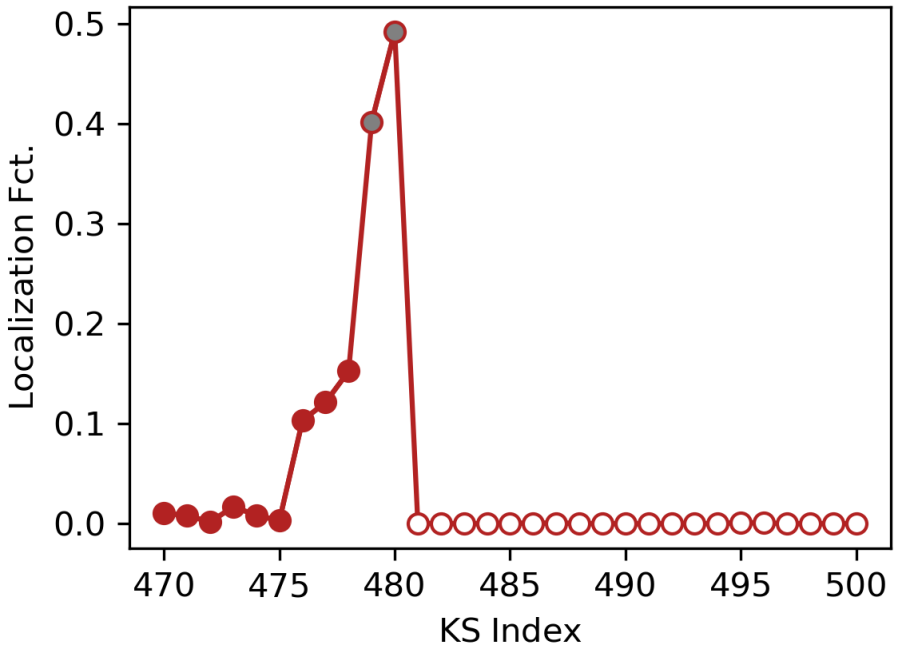

Figure 7.9: Localization function for selected Kohn-Sham orbitals for the unpolarized PBE functional level calculation, used as the basis for the QDET excitation calculation. The threshold guideline is shown (red dashed). Filled circles represent filled orbitals (2 electrons), gray-filled orbitals are partially filled orbitals (1 electron), while empty orbitals are not filled.

The first two KS spin-flip excitations, where an electron is promoted from the defect's highest occupied molecular orbital (HOMO) to the opposite spin channel defect's lowest unoccupied molecular orbital (LUMO), at the PBE functional level are 3.678 eV for spin up HOMO to spin down LUMO, and 1.695 eV for spin down HOMO for spin up LUMO. The corresponding HSE functional level spin-flip excitations are at 5.475 eV and 4.860 eV, respectively. In this way, based solely on the ground-state electron density and the predicted conduction bands, the lowest energy excitation would be a spin flip transition from the spin up HOMO to the spin down LUMO at the PBE level of theory. At the HSE level, the lowest energy excitation would be a same-spin excitation in the down channel.

We note that there are common trends of the defect levels in both levels of theory.

The first two defect levels in both spin channels are nearly degenerate. In addition, the spin down channel's unoccupied defect levels are nearly degenerate. This behavior is replicated in the non-spin polarized calculations given in Table 7.2.

Looking now to the symmetry of the orbitals, at the PBE level, the symmetry label of each spin polarization channel is the same. For the HSE level, the symmetry labels are different for the D1, D3 and D4 defect levels. In the PBE spin-unpolarized case, QDET predicts a triplet ground state which results in two partially occupied defect orbitals, while the bottom three defect orbitals are fully occupied. For the PBE excitations calculated by QDET, there are two nearly degenerate singlet excitations (separated by a splitting of 40 meV), and then another singlet 694 meV higher. According to the results of Table 7.4, the degenerate singlet states have almost even mixtures $(1/\sqrt{2})$ of two states. In particular, the ground state and second excitation are opposite in phase. The PBE functional results, however, appear to indicate that if one excites the system from the ground state to the second excited state, there may be significant contamination of pumping to the first excited state if one does not have fine-tuned control and resolution at the meV scale. The third excitation larger excitation energy can be attributed to the mixing of states that promote both electrons from one of the bottom three defect orbitals. This excitation, however, has a low mixing coefficient (< 0.1).

The fourth excitation is the first triplet excitation. This excitation involves mixing states that promote a single electron from one of the bottom three defect orbitals. The triplet excitation is paired with a nearly degenerate singlet excitation (the fifth excitation), leading to a singlet-triplet splitting of 23 meV. A similar singlet-triplet splitting is found for the sixth and seven excitations, with the sixth excitation lying only 89 meV away from the fifth excitation, and having a splitting of 25 meV.

The HSE excitation energies show a large contrast with the PBE ones. The first two excitations occur at much larger energies, and have a slightly larger splitting of their

degeneracy (54 meV). The third singlet transition, however, is missing, and instead the triplet excitation occurs 1.608 eV larger. The singlet-triplet pairs are also found in the HSE results, with splitting of 22 meV and 2 meV, respectively.

7.5 Summary and Conclusions

h-BN V_B^- is a promising spin qubit. In this work, we have attempted to address the challenge of characterizing the ground state energies and symmetries of the defect geometry. Our results show that the choice of functional leads to significant differences in point-group symmetry labels and energetic ordering of defect states for the spin polarized system. We have shown that the choice of functional level dictates the overall energy range of transitions as calculated by QDET. We have also shown that the many-body excitations exhibit a similar pattern between the choice of functionals used in this paper. Last, we show that the singlet-triplet splitting predicted by QDET is very small and may be difficult to experimentally access. Work may be needed in the future to further characterize the many-body states through time-dependent DFT methods.

7.6 List of References

[1] J. Bhang, H. Ma, D. Yim, G. Galli, and H. Seo, ACS Applied Materials and Interfaces **13**, 45768 (2021).

[2] W. Liu, V. Ivády, Z.-P. Li, Y.-Z. Yang, S. Yu, Y. Meng, Z.-A. Wang, N.-J. Guo, F.-F. Yan, Q. Li, J.-F. Wang, J.-S. Xu, X. Liu, Z.-Q. Zhou, Y. Dong, X.-D. Chen, F.-W. Sun, Y.-T. Wang, J.-S. Tang, A. Gali, C.-F. Li, and G.-C. Guo, Nature Communications **13**, 5713 (2022).

[3] F. F. Murzakhanov, G. V. Mamin, S. B. Orlinskii, U. Gerstmann, W. G. Schmidt,

T. Biktagirov, I. Aharonovich, A. Gottscholl, A. Sperlich, V. Dyakonov, and V. A. Soltamov, Nano Letters **22**, 2718 (2022).

[4] J. Lee, H. Park, and H. Seo, npj 2D Materials and Applications **6**, 1 (2022).

[5] A. Haykal, R. Tanos, N. Minotto, A. Durand, F. Fabre, J. Li, J. H. Edgar, V. Ivády, A. Gali, T. Michel, A. Dréau, B. Gil, G. Cassabois, and V. Jacques, Nature Communications **13**, 4347 (2022).

[6] A. J. Ramsay, R. Hekmati, C. J. Patrickson, S. Baber, D. R. M. Arvidsson-Shukur, A. J. Bennett, and I. J. Luxmoore, Nature Communications **14**, 461 (2023).

[7] C. R. Dean, A. F. Young, I. Meric, C. Lee, L. Wang, S. Sorgenfrei, K. Watanabe, T. Taniguchi, P. Kim, K. L. Shepard, and J. Hone, Nature Nanotechnology **5**, 722 (2010).

[8] A. Gottscholl, M. Diez, V. Soltamov, C. Kasper, A. Sperlich, M. Kianinia, C. Bradac, I. Aharonovich, and V. Dyakonov, Science Advances **7**, eabf3630 (2021).

[9] V. Ivády, G. Barcza, G. Thiering, S. Li, H. Hamdi, J.-P. Chou, O. Legeza, and A. Gali, npj Computational Materials **6**, 1 (2020).

[10] M. Abdi, J.-P. Chou, A. Gali, and M. B. Plenio, ACS Photonics **5**, 1967 (2018).

[11] J. R. Reimers, J. Shen, M. Kianinia, C. Bradac, I. Aharonovich, M. J. Ford, and P. Piecuch, Physical Review B **102**, 144105 (2020).

[12] N. Sheng, C. Vorwerk, M. Govoni, and G. Galli, Journal of Chemical Theory and Computation **18**, 3512 (2022).

[13] P. Giannozzi, S. Baroni, N. Bonini, M. Calandra, R. Car, C. Cavazzoni, D. Ceresoli, G. L. Chiarotti, M. Cococcioni, I. Dabo, A. D. Corso, S. d. Gironcoli, S. Fabris,

G. Fratesi, R. Gebauer, U. Gerstmann, C. Gougoussis, A. Kokalj, M. Lazzeri, L. Martin-Samos, N. Marzari, F. Mauri, R. Mazzarello, S. Paolini, A. Pasquarello, L. Paulatto, C. Sbraccia, S. Scandolo, G. Sclauzero, A. P. Seitsonen, A. Smogunov, P. Umari, and R. M. Wentzcovitch, Journal of Physics: Condensed Matter **21**, 395502 (2009).

[14] P. Giannozzi, O. Andreussi, T. Brumme, O. Bunau, M. B. Nardelli, M. Calandra, R. Car, C. Cavazzoni, D. Ceresoli, M. Cococcioni, N. Colonna, I. Carnimeo, A. D. Corso, S. d. Gironcoli, P. Delugas, R. A. DiStasio, A. Ferretti, A. Floris, G. Fratesi, G. Fugallo, R. Gebauer, U. Gerstmann, F. Giustino, T. Gorni, J. Jia, M. Kawamura, H.-Y. Ko, A. Kokalj, E. Küçükbenli, M. Lazzeri, M. Marsili, N. Marzari, F. Mauri, N. L. Nguyen, H.-V. Nguyen, A. Otero-de-la Roza, L. Paulatto, S. Poncé, D. Rocca, R. Sabatini, B. Santra, M. Schlipf, A. P. Seitsonen, A. Smogunov, I. Timrov, T. Thonhauser, P. Umari, N. Vast, X. Wu, and S. Baroni, Journal of Physics: Condensed Matter **29**, 465901 (2017).

[15] J. P. Perdew, K. Burke, and M. Ernzerhof, Physical Review Letters **77**, 3865 (1996).

[16] J. Heyd, G. E. Scuseria, and M. Ernzerhof, The Journal of Chemical Physics **118**, 8207 (2003).

[17] J. Heyd, G. E. Scuseria, and M. Ernzerhof, The Journal of Chemical Physics **124**, 219906 (2006).

[18] I. Hamada, Physical Review B **89**, 121103 (2014).

[19] S. Grimme, J. Antony, S. Ehrlich, and H. Krieg, The Journal of Chemical Physics **132**, 154104 (2010).

[20] F. Gygi and A. Baldereschi, Physical Review B **34**, 4405 (1986).

[21] D. R. Hamann, Physical Review B **88**, 085117 (2013).

[22] D. R. Hamann, Physical Review B **95**, 239906 (2017).

[23] Q. Sun and G. K.-L. Chan, Accounts of Chemical Research **49**, 2705 (2016).

[24] L. O. Jones, M. A. Mosquera, G. C. Schatz, and M. A. Ratner, Journal of the American Chemical Society **142**, 3281 (2020).

[25] H. Ma, M. Govoni, and G. Galli, npj Computational Materials **6**, 1 (2020).

[26] H. Ma, N. Sheng, M. Govoni, and G. Galli, Journal of Chemical Theory and Computation **17**, 2116 (2021).

[27] C. Vorwerk, N. Sheng, M. Govoni, B. Huang, and G. Galli, Quantum Embedding Theories to Simulate Condensed Systems on Quantum Computers (2022).

[28] M. Govoni and G. Galli, Journal of Chemical Theory and Computation **11**, 2680 (2015).

CHAPTER 8: ELECTRONIC TRANSPORT PROPERTIES OF A GRAPHENE-SUPPORTED SPIN CROSSOVER FEBIPY COMPLEX THROUGH GOLD ELECTRODES: AN AB INITIO STUDY.

8.1 Introduction

There has been renewed investigation into the use of molecular complexes for spintronics: solid state architectures that take advantage of both the spin and electronic degrees of freedom. Spintronics are primarily made of metals and semiconductors, and they may offer the ability to deliver greater efficiency in terms of power and performance [1, 2]. A class of spintronic candidates, spin-crossover (SCO) molecules, appears to be an attractive option due to their relatively easy fabrication and tailorable ligands. SCO molecules, often observed within first-row transition metal complexes, are so called because of their ability to switch between two or more defined total S spin states that are accessed upon application of light, temperature, pressure, or magnetic field [3]. One example are Fe^{2+} complexes, which have a diamagnetic low spin (LS) state and a paramagnetic high spin (HS) state. There are still challenges that remain in order for SCO molecule-based spintronics to be competitive with silicon-based devices, including desired electronic control and demonstration of high on/off ratios [4].

The thin film $Fe[H_2B(Pz)_2]_2(bipy)$ SCO complex (referred to as "FeBipy") has been recently identified as a good candidate for nonvolatile voltage-controlled spin state switching between its LS ($S = 0$) and HS ($S = 2$) states, and current measurements of spin state [4–7]. The spintronics operation for that film comes from exploiting the conductance-molecular spin state relationship and high on/off ratios, which appear to persist even beyond room tempera-

ture. There is a desire to predict the transport properties of SCO complexes such as FeBipy in order to identify new electrode-SCO geometries to enhance on/off ratios, and a complete picture of the conductance channels is missing. Quantum transport calculations have been made for other iron(II) complexes, such as trans-bis(3-(2-pyridyl)[1,2,3]triazolo[1,5-a]-pyridine)bis(isothiocyanato) which shows substantial HS/LS current ratios that may be assisted from contributions of minority spin channel transmission [8].

In this chapter, I aim to characterize the transport properties of the FeBipy SCO molecule using *ab initio* transport methods based on non-equilibrium Green's functions. I show that there is qualitatively similar behavior with experiments of FeBipy devices with the transport predictions of the FeBipy SCO molecule connected to graphene supports, attached to Au leads. I find that different spin channels play a role in the transmission, and comment on future work aimed at uncovering a more quantitative picture.

The chapter is organized as follows. In Section 8.2 I describe the geometry of the FeBipy complex connected to leads and computational parameters used to model transport through the complex. I then present qualitative transport predictions in Section 8.3. In Section 8.4, I show the correspondence with recent experiments around FeBipy SCO molecules, and discuss the use of a more complete basis set to get better quantitative agreement with experiment.

8.2 Methods

The geometry used in the simulation is shown in Fig. 8.1. I use both the LS and HS geometries of the 59-atom $Fe[H_2B(Pz)_2]_2(bipy)$ SCO molecule relaxed with the *ab initio* plane wave basis density functional theory (DFT) software Quantum Espresso [9, 10]. The FeBipy SCO molecule is centered away from a 42-atom graphene layer placed 2.5 Å on either side. The graphene layer is layered on top of a 4x4x1 Au layer with 3.4 Å separation. The

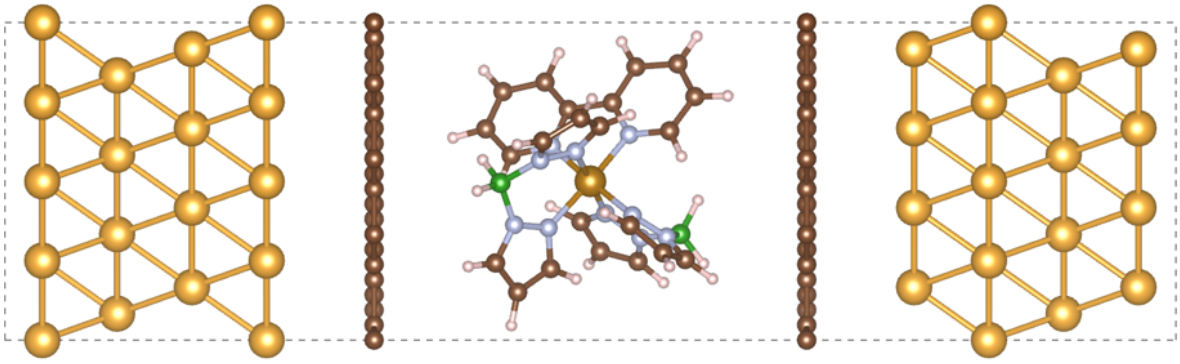

Figure 8.1: Representation of the optimized unit cell for the LS system. Yellow: Au, Gold: Fe, Light-Blue: N, Green: B, Brown: C, White: H.

4x4 in-plane periodicity is used to avoid artificial interactions between repeating images of molecules due to the periodic boundary conditions. Defining the stacked direction as the transport direction, the gold layer is repeated for four vertical layers, with an Au-Au bond length of 2.897 Å. The graphene layer's C-C bond length is 1.460 Å. The graphene layer is used in this geometry because of its demonstrated trade-off between junction stability and SCO switching capability [11], allowing the SCO-Au interface to possibility avoid unwanted coupling effects [12].

I consider the effective 4L 4x4 Au layer structure as a bulk electrode to be used in the *ab initio* DFT-based transport code TranSiesta [13–15], which utilizes the non-equilibrium Green's function method and the localized atomic orbital basis set DFT software Siesta [15, 16]. The GGA PBE exchange-correlation functional is used [17], with the numerical orbital SZP basis generated by Siesta for each element. An energy shift of 0.02 Ry is applied to the basis set, with a mesh cutoff of 250 Ry. The complex contour contains 28 points for the circle portion of the contour, and 10 points for the tail. The density matrix and Green's functions were converged self-consistently using the Γ point, while for transmission calculations, a denser 2×2 k-point mesh was employed. Transmission and I-V characteristics

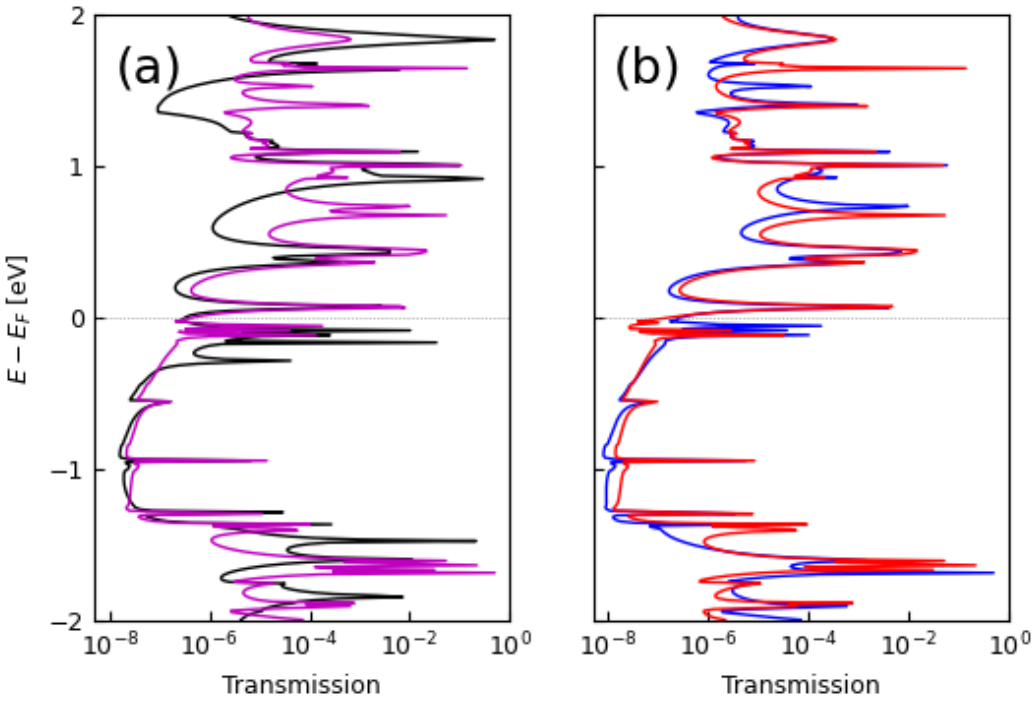

Figure 8.2: Zero-bias transmission of the (a) LS (black) and HS (magenta) SCO transport geometry. The transmission is spin-resolved (b) for majority (red) and minority (blue) channels.

were extracted using TBTrans [14] and SISL [18].

8.3 Results

I first plot the transmission for both the LS and HS structures in Fig. 8.2. The results show that for the HS structure, the majority versus minority transmission differs significantly. Next, I perform transmission calculations at several bias points for both structures. The resulting current, shown in Fig. 8.3, also shows differences based on spin state.

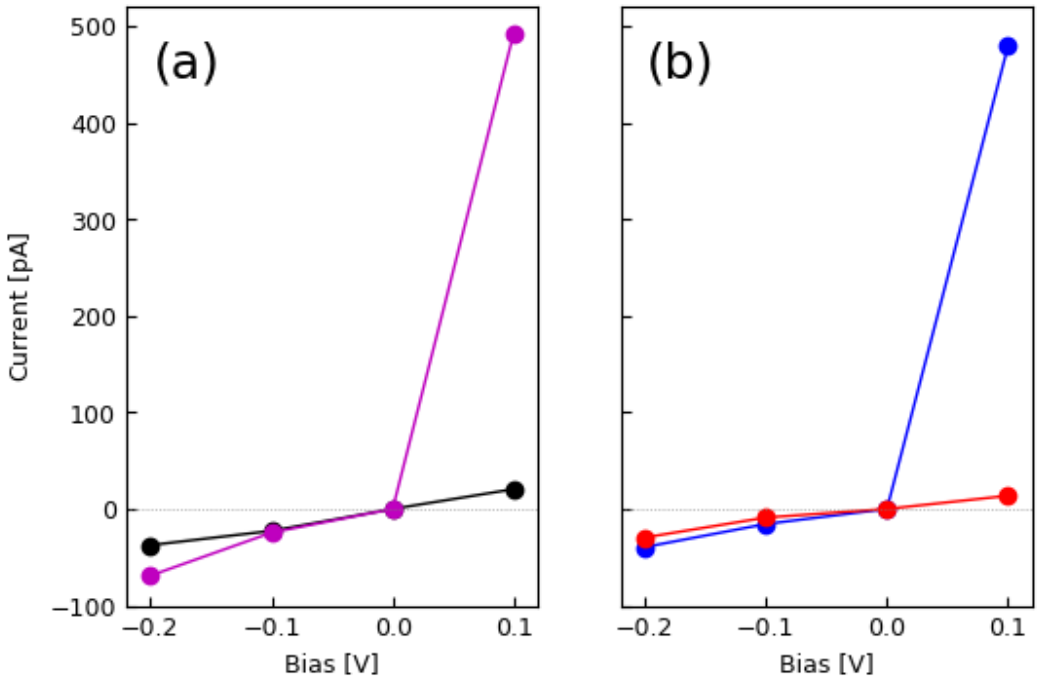

Figure 8.3: Current versus voltage for the (a) LS (black) and HS (magenta) SCO transport geometry. Current contributions are spin-resolved (b) for majority (red) and minority (blue) channels.

8.4 Discussion

It is clear in Fig. 8.2 that the spin state of the SCO molecule impacts transmission significantly. Within the range of 0 to -200 meV, there are sharp peaks in transmission that are orders of magnitude different between the LS and HS states. The onset of different orbitals within the bias window appears to correspond with jumps in current in Fig. 8.3. Looking at each spin channel in both figures, there is a significant difference of transmission between the majority and minority channel for the HS structure. Most of the current for the HS structure comes from minority spin channel. This appears to be consistent with the results of other Fe(II) complexes [8].

I note that the negative bias regime is not symmetric with the positive bias regime.

The effective on/off ratio between the two spin states in that regime is small. In contrast, the on/off ratio is found to be 24.015 for the $V = 100$ meV bias. Qualitatively, this matches the behavior of different FeBipy thin film devices, such as the one considered in Ref. [5]. Quantitatively, the order of magnitude for both the onset of such a high on/off ratio and the current is higher than the experimental result of Ref. [5]. This may be due to the basis set chosen, as optimized based sets designed to mimic all-electron bulk results (like the one in Ref. [19]) may give different quantitative results. The basis set dependency on calculated transmission is well known for TranSiesta [20]. Simulations using an optimized basis set and finer sampling of the density matrix and Green's functions may result in a more quantitative agreement. Work along this direction for the FeBipy SCO complex is ongoing.

8.5 Summary

In this chapter, I have qualitatively characterized the transport properties of the FeBipy SCO molecule supported by graphene supports connected to Au leads using *ab initio* transport methods for a small bias window. I have shown that there is similar behavior with experiments of FeBipy devices with the transport predictions of both LS and HS geometries. The calculated on/off ratio indicates that the FeBipy-graphene-Au complex is capable of large on/off ratios, and it may be a viable candidate geometry for spintronic applications.

8.6 List of References

[1] A. Fert, Reviews of Modern Physics **80**, 1517 (2008).

[2] K. S. Kumar and M. Ruben, Angewandte Chemie International Edition **60**, 7502 (2021).

[3] J.-P. Tuchagues, A. Bousseksou, G. Molnár, J. J. McGarvey, and F. Varret, in *Spin Crossover in Transition Metal Compounds III*, Topics in Current Chemistry, edited by P. Gütlich and H. Goodwin (Springer, Berlin, Heidelberg, 2004) pp. 84–103.

[4] T. K. Ekanayaka, G. Hao, A. Mosey, A. S. Dale, X. Jiang, A. J. Yost, K. R. Sapkota, G. T. Wang, J. Zhang, A. T. N'Diaye, A. Marshall, R. Cheng, A. Naeemi, X. Xu, and P. A. Dowben, Magnetochemistry **7**, 37 (2021).

[5] A. Mosey, A. S. Dale, G. Hao, A. N'Diaye, P. A. Dowben, and R. Cheng, The Journal of Physical Chemistry Letters **11**, 8231 (2020).

[6] A. Mosey, A. S. Dale, G. Hao, A. N'Diaye, P. A. Dowben, and R. Cheng, The Journal of Physical Chemistry Letters **12**, 2463 (2021).

[7] T. K. Ekanayaka, K. P. Maity, B. Doudin, and P. A. Dowben, Nanomaterials **12**, 1742 (2022).

[8] D. Aravena and E. Ruiz, Journal of the American Chemical Society **134**, 777 (2012).

[9] P. Giannozzi, S. Baroni, N. Bonini, M. Calandra, R. Car, C. Cavazzoni, D. Ceresoli, G. L. Chiarotti, M. Cococcioni, I. Dabo, A. D. Corso, S. d. Gironcoli, S. Fabris, G. Fratesi, R. Gebauer, U. Gerstmann, C. Gougoussis, A. Kokalj, M. Lazzeri, L. Martin-Samos, N. Marzari, F. Mauri, R. Mazzarello, S. Paolini, A. Pasquarello, L. Paulatto, C. Sbraccia, S. Scandolo, G. Sclauzero, A. P. Seitsonen, A. Smogunov, P. Umari, and R. M. Wentzcovitch, Journal of Physics: Condensed Matter **21**, 395502 (2009).

[10] P. Giannozzi, O. Andreussi, T. Brumme, O. Bunau, M. B. Nardelli, M. Calandra, R. Car, C. Cavazzoni, D. Ceresoli, M. Cococcioni, N. Colonna, I. Carnimeo, A. D. Corso, S. d. Gironcoli, P. Delugas, R. A. DiStasio, A. Ferretti, A. Floris, G. Fratesi, G. Fugallo, R. Gebauer, U. Gerstmann, F. Giustino, T. Gorni, J. Jia, M. Kawamura, H.-Y. Ko, A. Kokalj, E. Küçükbenli, M. Lazzeri, M. Marsili, N. Marzari, F. Mauri, N. L. Nguyen, H.-V. Nguyen, A. Otero-de-la Roza, L. Paulatto, S. Poncé, D. Rocca, R. Sabatini, B. Santra, M. Schlipf, A. P. Seitsonen, A. Smogunov, I. Timrov, T. Thonhauser,

P. Umari, N. Vast, X. Wu, and S. Baroni, Journal of Physics: Condensed Matter **29**, 465901 (2017).

[11] S. K. Karuppannan, A. Martín-Rodríguez, E. Ruiz, P. Harding, D. J. Harding, X. Yu, A. Tadich, B. Cowie, D. Qi, and C. A. Nijhuis, Chemical Science **12**, 2381 (2021).

[12] D. Li, Y. Tong, K. Bairagi, M. Kelai, Y. J. Dappe, J. Lagoute, Y. Girard, S. Rousset, V. Repain, C. Barreteau, M. Brandbyge, A. Smogunov, and A. Bellec, The Journal of Physical Chemistry Letters **13**, 7514 (2022).

[13] M. Brandbyge, J.-L. Mozos, P. Ordejón, J. Taylor, and K. Stokbro, Physical Review B **65**, 165401 (2002).

[14] N. Papior, N. Lorente, T. Frederiksen, A. García, and M. Brandbyge, Computer Physics Communications **212**, 8 (2017).

[15] A. García, N. Papior, A. Akhtar, E. Artacho, V. Blum, E. Bosoni, P. Brandimarte, M. Brandbyge, J. I. Cerdá, F. Corsetti, R. Cuadrado, V. Dikan, J. Ferrer, J. Gale, P. García-Fernández, V. M. García-Suárez, S. García, G. Huhs, S. Illera, R. Korytár, P. Koval, I. Lebedeva, L. Lin, P. López-Tarifa, S. G. Mayo, S. Mohr, P. Ordejón, A. Postnikov, Y. Pouillon, M. Pruneda, R. Robles, D. Sánchez-Portal, J. M. Soler, R. Ullah, V. W.-z. Yu, and J. Junquera, The Journal of Chemical Physics **152**, 204108 (2020).

[16] J. M. Soler, E. Artacho, J. D. Gale, A. García, J. Junquera, P. Ordejón, and D. Sánchez-Portal, Journal of Physics: Condensed Matter **14**, 2745 (2002).

[17] J. P. Perdew, K. Burke, and M. Ernzerhof, Physical Review Letters **77**, 3865 (1996).

[18] N. Papior, sisl: v0.13.0 (2022).

[19] P. Rivero, V. M. García-Suárez, D. Pereñiguez, K. Utt, Y. Yang, L. Bellaiche, K. Park, J. Ferrer, and S. Barraza-Lopez, Computational Materials Science **98**, 372 (2015).

[20] C. García-Fernández and N. Lorente, Surface Science Surface Structure and Dynamics – in Honor of Karl-Heinz Rieder, **678**, 201 (2018).

CHAPTER 9: CONCLUSION AND OUTLOOK

In this thesis, I have explored the theoretical framework for tripartite spin systems that contain spin exchange coupling and MA. The spin space, investigated in chapter 2 and 3 has a rich structure which can be exploited for QIS applications. Connecting such a system to leads in chapter 4 uncovered important information about spin interactions through conductance measurements. Investigating the time-(in)dependent nature of representative toy models is possible as shown in chapter 5 and 6, but a more thorough treatment of the spin terms in the exchange-coupled tripartite system is needed. Finally, exploring qubit and other quantum architecture candidates using *ab initio* methods in chapter 7 and 8 highlights some of the challenges that need to be overcome in order to adequately characterize the more complicated three-spin exchange+MA paradigm.

A challenge not completely addressed in this thesis is how to realize the three-spin model Hamiltonian in experiment. Such an experiment is needed in order to confirm the theoretical results presented so far, such as the DJ resonance conditions in chapters 2 and 3. There are several experimental setups that one could use for inspiration. For example, it's been recently theorized that double quantum dots and the Pauli spin blockade can be used to generate entangled states [1]. Effective multi-spin particle setups connected to a transport channel have also been experimentally explored, such as magnetic molecule dimers exchanged coupled to carbon nanotubes [2].

One possibility is the use of spin interferometry measurements using two molecular channels placed on a substrate [3]. Each molecular channel hosts a current of mobile electrons, which precess because of their interaction with the underlying molecular electronic structure. The two channels controllable interact through a gate-enabled exchange interaction, entangling the spin states of the mobile electrons. The polarization of the electrons of each channel is then measured in a stochastic manner in order to build a confirmation of the

entanglement state prior to measurement.

Another experimental possibility is the coherent manipulation of atomic spins [4]. In the experiment, spin rotations have been achieved at the nanosecond timescale utilizing a scanning tunneling microscope (STM). Control of an individual atomic qubit's spin state has shown to be possible using electron spin resonance (ESR) coupled with STM [5]. Utilizing an anisotropy in the exchange coupling between atoms, in a manner similar to the conditions pointed out in chapter 3, may enable generation of multi-partite entanglement.

Another challenge is the inherent need for time and probability-resolved read out of the electron's polarization when at the DJ resonance conditions in order to prepare the entanglement of the spin centers with MA. The relatively "long time" incoherence spin polarization measurements that one could obtain in an experimental arrangement similar to chapter 4 do not appear to allow measurement of the resonances at the nanosecond scale. There has been theoretical work on utilizing a delocalized ancillary electron (a planewave-like electron) to address molecular spin centers [6], and experimental work is needed in order to validate such an approach. On the other hand, efforts to address coherent quantum operations are ongoing [7], for example with the achievement of ultra-fast manipulation of electron spin qubits with gate operations on the order of pico- or nano-seconds [8].

Another aspect not addressed in this thesis is the accurate parameterization of spin parameters so that one may find and use the resonance conditions of Chapter 3. There has been much work in predicting MA energy for bulk systems using DFT, such as VFe_2O_4 [9]. The strategy to find a system's MA using DFT requires comparison of the total energy of the system as a function of the direction of the magnetic moment. This noncollinear magnetism can be found in a variety of materials such as magnets at finite temperatures and molecular magnets, so the extension of DFT to describe noncollinear materials should be used. The noncollinear form of spin-DFT was formulated by Jürgen Kübler and co-workers [10], where the exchange-correlation energy functional depends on a general magnetization

density $m(\mathbf{r}) = \mu_B \sum_i^N \psi_i^{\mathrm{KS}}(\mathbf{r})\boldsymbol{\sigma}\psi_i^{\mathrm{KS}}(\mathbf{r})$, where μ_B is the Bohr magneton, and $\boldsymbol{\sigma}$ is the Pauli spin vector. This form removes the constraint of global collinearity, i.e., the global "up" and "down" spin direction assumed in Eq. (1.18). A description of the noncollinear form of spin-DFT and the approximations for $E_{xc}[n(\mathbf{r}), m(\mathbf{r})]$ (namely the use of local reference frames at each real-space point to describe the spin density), is outside the scope of this thesis. A brief review of one of the latest methods can be found in Ref. [11].

Armed with noncollinear spin-DFT, one can use it to parameterize Heisenberg-like spin interactions $J_{ij}\mathbf{S}_i \cdot \mathbf{S}_j$, and even parameterize a more general $\mathbf{S}_i\mathbf{J}\mathbf{S}_j$ for the coupling tensor $\mathbf{J}$. To obtain the tensor J and incorporate spin-orbit coupling within DFT, one must turn to the relativistic Dirac equation in order to extend the inherently non-relativistic KS Hamiltonian [12]. The three required changes to the KS Hamiltonian are straight forward: 1. modify the electron momentum operator $\mathbf{p}$ to include the vector potential $\mathbf{A}(\mathbf{r})/c$, where c is the speed of light, 2. add scalar-relativistic mass-velocity correction terms, and 3. include the spin-orbit interaction. Using Eq. (1.14), one compares calculations of different spin moment orientations to obtain the components of the $\mathbf{J}$ coupling tensor for each atom. In practice, this calculation requires care on the convergence of the DFT numerical parameters and choice of functional, such as inclusion of strong correlation effects and how one determines the "true" magnetic ground state.

By calculating the effective coupling tensor $\mathbf{J}$, one automatically obtains the J_{ij} terms found in the Heisenberg-like spin Hamiltonian. The calculation of the characteristic times for spin qubit operations (T_1 and T_2) can be calculated through the use of quantum bath theory with coupled cluster expansion (CCE) and generalized CCE techniques, as has been done in SiC qubits [13–15] and molecular qubits [16] using PyCCE [17].

Finally, work is underway to utilize NEGF-derived codes that describe the time-dependent behavior of exchange-coupled tripartite systems. Codes that have been developed to describe the dynamics of some of the aforementioned experimental realizations like STM

coupled with ESR [4, 5, 18, 19] show promise for systems in which the spin parameters can be accurately determined experimentally. Other options, like time-dependent DFT [20] explore time ranges such as femto- and nano-scale dynamics that may be inaccessible to full NEGF methods. With these promising avenues of research, exchange-coupled tripartite spin systems with MA appear to be inviting quantum architectures. It is my hope that the contents of this thesis and the developed framework will inspire further exploration of these systems.

9.1 List of References

[1] S. Bugu, F. Ozaydin, T. Ferrus, and T. Kodera, Scientific Reports **10**, 3481 (2020).

[2] M. Urdampilleta, S. Klyatskaya, J.-P. Cleuziou, M. Ruben, and W. Wernsdorfer, Nature Materials **10**, 502 (2011).

[3] A. Dhingra, X. Hu, M. F. Borunda, J. F. Johnson, C. Binek, J. Bird, A. T. N'Diaye, J.-P. Sutter, E. Delahaye, E. D. Switzer, E. d. Barco, T. S. Rahman, and P. A. Dowben, Journal of Physics: Condensed Matter **34**, 441501 (2022).

[4] K. Yang, W. Paul, S.-H. Phark, P. Willke, Y. Bae, T. Choi, T. Esat, A. Ardavan, A. J. Heinrich, and C. P. Lutz, Science **366**, 509 (2019).

[5] Y. Wang, M. Haze, H. T. Bui, W.-h. Soe, H. Aubin, A. Ardavan, A. J. Heinrich, and S.-h. Phark, npj Quantum Information **9**, 1 (2023).

[6] C. Bunker, S. Hoffman, J.-X. Yu, X.-G. Zhang, and H.-P. Cheng, Scattering solution of interacting Hamiltonian for electronic control of molecular spin qubits (2022), arXiv:2210.15747 [cond-mat, physics:quant-ph].

[7] A. J. Heinrich, W. D. Oliver, L. M. K. Vandersypen, A. Ardavan, R. Sessoli, D. Loss,

A. B. Jayich, J. Fernandez-Rossier, A. Laucht, and A. Morello, Nature Nanotechnology **16**, 1318 (2021).

[8] E. R. MacQuarrie, S. F. Neyens, J. P. Dodson, J. Corrigan, B. Thorgrimsson, N. Holman, M. Palma, L. F. Edge, M. Friesen, S. N. Coppersmith, and M. A. Eriksson, npj Quantum Information **6**, 1 (2020).

[9] H. Bushra Munir, A. Afaq, A. Bakar, I. Asif, and N. ul Aarifeen, Materials Today Communications **26**, 101763 (2021).

[10] J. Kubler, K.-H. Hock, J. Sticht, and A. R. Williams, Journal of Physics F: Metal Physics **18**, 469 (1988).

[11] Z. Pu, H. Li, N. Zhang, H. Jiang, Y. Gao, Y. Xiao, Q. Sun, Y. Zhang, and S. Shao, Physical Review Research **5**, 013036 (2023).

[12] G. Bihlmayer, in *Handbook of Materials Modeling: Methods: Theory and Modeling* (Springer, 2020) pp. 895–917.

[13] H. Seo, A. L. Falk, P. V. Klimov, K. C. Miao, G. Galli, and D. D. Awschalom, Nature Communications **7**, 12935 (2016).

[14] A. Bourassa, C. P. Anderson, K. C. Miao, M. Onizhuk, H. Ma, A. L. Crook, H. Abe, J. Ul-Hassan, T. Ohshima, N. T. Son, G. Galli, and D. D. Awschalom, Nature Materials **19**, 1319 (2020).

[15] M. Onizhuk, K. C. Miao, J. P. Blanton, H. Ma, C. P. Anderson, A. Bourassa, D. D. Awschalom, and G. Galli, PRX Quantum **2**, 010311 (2021).

[16] S. Bayliss, P. Deb, D. Laorenza, M. Onizhuk, G. Galli, D. Freedman, and D. Awschalom, Physical Review X **12**, 031028 (2022).

[17] M. Onizhuk and G. Galli, PyCCE: A Python Package for Cluster Correlation Expansion Simulations of Spin Qubit Dynamic (2021).

[18] B. Bhandari, R. Fazio, F. Taddei, and L. Arrachea, Physical Review B **104**, 035425 (2021).

[19] J. Reina-Gálvez, N. Lorente, F. Delgado, and L. Arrachea, Physical Review B **104**, 245435 (2021).

[20] C. A. Ullrich, *Time-dependent density-functional theory: concepts and applications* (OUP Oxford, Oxford, 2011).

APPENDIX A: DERIVATION OF HOPPING TERM FROM A TRANSFORMATION OF THE TWO IMPURITY ANDERSON MODEL

In this appendix, we derive the origin of the hopping term between the spin monomers found in Chapters 2 and 3, and in the process show a derivation of the total Hamiltonian. We first begin with a review of the two impurity Anderson model (TIAM), which is an extension of the single impurity Anderson model [1]. The Hamiltonian of the TIAM model is,

$$\mathcal{H} = \mathcal{H}_{\text{imp}} + \mathcal{H}_{\text{band}} + V_{\text{band-imp}}, \tag{A.1}$$

where, for simplicity, the impurity has only two accessible levels (one for each spin). The first term is the impurity energy term,

$$\mathcal{H}_{\text{imp}} = \sum_{i\sigma} \epsilon_i \hat{n}_{d_{i\sigma}} + U_i \hat{n}_{d_{i\uparrow}} \hat{n}_{d_{i\downarrow}}, \tag{A.2}$$

where ϵ_i is the energy of impurity $i \in \{2, 3\}$, U_i is the Coulombic repulsion of that impurity, $\hat{n}_{d_{i\sigma}} = \hat{d}^\dagger_{i\sigma}\hat{d}_{i\sigma}$ is the number operator of impurity i with state σ, and $\hat{d}^\dagger_{i\sigma}/\hat{d}_{i\sigma}$ the second-quantization creation/annihilation operators of that state, respectively. The second term describes the electrons in a metal

$$\mathcal{H}_{\text{band}} = \sum_{\mathbf{k}\sigma} \epsilon_{\mathbf{k}} \hat{c}^\dagger_{\mathbf{k}\sigma} \hat{c}_{\mathbf{k}\sigma}, \tag{A.3}$$

where $\epsilon_{\mathbf{k}}$ is the energy of the band $\mathbf{k}$, and $\hat{c}^\dagger_{\mathbf{k}\sigma}/\hat{c}_{\mathbf{k}\sigma}$ create/annihilate an electron with wave number $\mathbf{k}$ and spin σ in that band, respectively. The last term describes the coupling of the bands to the impurities,

$$V_{\text{band-imp}} = \sum_{i\mathbf{k}\sigma} t_{i\mathbf{k}} \hat{c}^\dagger_{\mathbf{k}\sigma} \hat{d}_{i\sigma} + h.c., \tag{A.4}$$

where $t_{i\mathbf{k}}$ is the coupling constant. When one applies a generalized form of the Schrieffer-Wolff transformation [2] to the TIAM model, one obtains a transformed Hamiltonian $\mathcal{H}'$

that can be separated into six terms,

$$\mathcal{H}' = \mathcal{H}_0 + \mathcal{H}'_0 + \mathcal{H}_{\text{dir}} + \mathcal{H}_{\text{exch}} + \mathcal{H}_{\text{pair-tunnel}} + \mathcal{H}_{\text{imp-imp}}. \tag{A.5}$$

The first two terms are diagonal in the spin space of the impurities,

$$\mathcal{H}_0 = \mathcal{H}_{\text{imp}} + \mathcal{H}_{\text{band}}, \tag{A.6}$$

and,

$$\mathcal{H}'_0 \equiv -\sum_{i\mathbf{k}\sigma} \left(W^{ii}_{\mathbf{kk}} + \frac{1}{2} J^{ii}_{\mathbf{kk}} \hat{n}_{\hat{d}_{i-\sigma}} \right) \hat{n}_{\hat{d}_{i\sigma}}, \tag{A.7}$$

where the coupling constants are defined as,

$$W^{i'i}_{\mathbf{k'k}} \equiv \frac{1}{2} t_{i'\mathbf{k}'} t^*_{i\mathbf{k}} \left(\frac{1}{\epsilon_{\mathbf{k}'} - \epsilon_{i'}} + \frac{1}{\epsilon_{\mathbf{k}} - \epsilon_i} \right), \tag{A.8}$$

$$J^{i'i}_{\mathbf{k'k}} \equiv t_{i'\mathbf{k}'} t^*_{i\mathbf{k}} \left(\frac{1}{\epsilon_{\mathbf{k}'} - \epsilon_{i'} - U_{i'}} + \frac{1}{\epsilon_{\mathbf{k}} - \epsilon_i - U_i} - \frac{1}{\epsilon_{\mathbf{k}'} - \epsilon_{i'}} - \frac{1}{\epsilon_{\mathbf{k}} - \epsilon_i} \right). \tag{A.9}$$

The third term is the direct (spin-independent) interaction,

$$\mathcal{H}_{\text{dir}} \equiv \sum_{i\mathbf{kk}'} \left(W^{ii}_{\mathbf{k'k}} + \frac{1}{4} J^{ii}_{\mathbf{k'k}} \left(\hat{\Psi}^\dagger_i \hat{\Psi}_i \right) \right) \left(\hat{\Psi}^\dagger_{\mathbf{k}'} \hat{\Psi}_{\mathbf{k}} \right), \tag{A.10}$$

where the following generalized creation/annihilation operators have been defined,

$$\hat{\Psi}_{\mathbf{k}} \equiv \begin{pmatrix} \hat{c}_{\mathbf{k}\uparrow} \\ \hat{c}_{\mathbf{k}\downarrow} \end{pmatrix}, \tag{A.11}$$

$$\hat{\Psi}_i \equiv \begin{pmatrix} \hat{d}_{i\uparrow} \\ \hat{d}_{i\downarrow} \end{pmatrix}. \tag{A.12}$$

The fourth term is the Kondo exchange interaction

$$\mathcal{H}_{\text{exch}} \equiv -\sum_{i\mathbf{k}\mathbf{k}'} J^{ii}_{\mathbf{k}'\mathbf{k}} \left(\hat{\Psi}^{\dagger}_{\mathbf{k}'} \frac{\hat{\boldsymbol{\sigma}}}{2} \hat{\Psi}_{\mathbf{k}} \cdot \hat{\Psi}^{\dagger}_{i} \frac{\hat{\boldsymbol{\sigma}}}{2} \hat{\Psi}_{i} \right) = -\sum_{i\mathbf{k}\mathbf{k}'} J^{ii}_{\mathbf{k}'\mathbf{k}} \left(\hat{\Psi}^{\dagger}_{\mathbf{k}'} \hat{\mathbf{S}} \hat{\Psi}_{\mathbf{k}} \cdot \hat{\Psi}^{\dagger}_{i} \hat{\mathbf{S}} \hat{\Psi}_{i} \right). \tag{A.13}$$

The fifth term is the pair-tunneling interaction where two electrons or two holes are created at once.

$$\mathcal{H}_{\text{pair-tunnel}} \equiv \frac{1}{4} \sum_{i\mathbf{k}\mathbf{k}'\sigma} J^{ii}_{\mathbf{k}'\mathbf{k}} \hat{c}^{\dagger}_{\mathbf{k}-\sigma} \hat{c}^{\dagger}_{\mathbf{k}'\sigma} \hat{d}_{i\sigma} \hat{d}_{i-\sigma} + h.c. \tag{A.14}$$

The last term does not appear when one transforms the single-impurity Anderson model,

$$\mathcal{H}_{\text{imp-imp}} \equiv -\frac{1}{2} \sum_{i \neq j} \sum_{\mathbf{k}\sigma} \left(W^{ij}_{\mathbf{k}\mathbf{k}} + \frac{1}{2} \tilde{J}^{ij}_{\sigma} \right) \hat{d}^{\dagger}_{i\sigma} \hat{d}_{j\sigma} + h.c., \tag{A.15}$$

where,

$$\tilde{J}^{i'i}_{\sigma} \equiv t_{i'\mathbf{k}} t^{*}_{i\mathbf{k}} \left(\frac{\hat{n}_{\hat{d}_{i'-\sigma}}}{\epsilon_{\mathbf{k}} - \epsilon_{i'} - U_{i'}} + \frac{\hat{n}_{\hat{d}_{i-\sigma}}}{\epsilon_{\mathbf{k}} - \epsilon_{i} - U_{i}} - \frac{\hat{n}_{\hat{d}_{i'-\sigma}}}{\epsilon_{\mathbf{k}} - \epsilon_{i'}} - \frac{\hat{n}_{\hat{d}_{i-\sigma}}}{\epsilon_{\mathbf{k}} - \epsilon_{i}} \right). \tag{A.16}$$

This term represents a second-order hopping between sites mediated by the conduction electron levels. In other words, it represents an electron hopping away from one impurity into the conduction band, followed by an electron hopping from the conduction band to the second impurity. The first two terms of the transformed Hamiltonian adjust the energy level of the system, and can be incorporated to redefine the energy levels. The third term can be absorbed into the bands, and the fifth term can be neglected because it is energetically unfavorable in this second-order treatment. There are two surviving terms, namely the Kondo exchange interaction and impurity-impurity interaction terms, that describe the transformed

TIAM model, which we call the two-site Kondo model,

$$\mathcal{H}_{2K} \equiv \mathcal{H}_{\text{exch}} + \mathcal{H}_{\text{imp-imp}}. \tag{A.17}$$

This model can be generalized to larger spin for the impurities. First, a simple notation change is made,

$$\hat{\Psi}^{\dagger}_{\mathbf{k}'}\hat{\mathbf{S}}\hat{\Psi}_{\mathbf{k}} \equiv \hat{\Psi}^{\dagger}_{\mathbf{k}'}\mathbf{S_1}\hat{\Psi}_{\mathbf{k}}, \tag{A.18}$$

and then the spin sum over σ is expanded to a sum over all μ spin degrees of freedom in the impurities of any spin S,

$$\mathcal{H}_{2K} = -\sum_{i,\mathbf{k},\mathbf{k}'} J^{ii}_{\mathbf{k}'\mathbf{k}} \left(\hat{\Psi}^{\dagger}_{\mathbf{k}'}\mathbf{S_1}\hat{\Psi}_{\mathbf{k}} \cdot \hat{\Psi}^{\dagger}_{i}\hat{\mathbf{S}}_i\hat{\Psi}_i\right) - \frac{1}{2}\sum_{i\neq j}\sum_{\mathbf{k},\mu}\left(W^{ij}_{\mathbf{k}\mathbf{k}} + \frac{1}{2}\tilde{J}^{ij}_{\mu}\right)\hat{d}^{\dagger}_{i\mu}\hat{d}_{j\mu} + h.c. \tag{A.19}$$

In order to isolate the spin space of this model, the momentum index $\mathbf{k}$ is dropped,

$$\mathcal{H}_{2K} = -\sum_{\mu,\mu',i} J^{ii}\hat{\mathbf{S}}_i \cdot \hat{d}^{\dagger}_{\mu,i}\hat{\boldsymbol{\sigma}}_{\mu,\mu'}\hat{d}_{\mu',i} - \frac{1}{2}\sum_{i\neq j}\sum_{\mu}\left(W^{ij} + \frac{1}{2}\tilde{J}^{ij}_{\mu}\right)\hat{d}^{\dagger}_{i\mu}\hat{d}_{j\mu} + h.c. \tag{A.20}$$

The constants can then be redefined, e.g., $J_{Ki} \equiv -2J^{ii}$ and $t_{\mu,ij} = -1/2(W^{ij} + \tilde{J}^{ij}_{\mu}/2)$, so that,

$$\mathcal{H}_{\text{three-spin}} = \frac{1}{2}\sum_{\mu,\mu',i} J_{Ki}\hat{\mathbf{S}}_i \cdot \hat{d}^{\dagger}_{\mu,i}\hat{\boldsymbol{\sigma}}_{\mu,\mu'}\hat{d}_{\mu',i} + \sum_{\mu} t_{\mu,23}\hat{d}^{\dagger}_{\mu,2}\hat{d}_{\mu,3} + h.c. \tag{A.21}$$

Finally one can see that the problem in spin space is now constructed of interactions between three spin operators: $\hat{\mathbf{S}}_1$, $\hat{\mathbf{S}}_2$, and $\hat{\mathbf{S}}_3$, and a hopping term. Assuming that the hopping term

is independent of the spin of the impurities, $t_{\mu,23} = t \; \forall \; \mu$, one finds,

$$\mathcal{H}_{\text{three-spin}} = \mathcal{H}_{\text{K}} + \mathcal{H}_{\text{t}}, \tag{A.22}$$

where,

$$\mathcal{H}_{\text{K}} = \frac{1}{2} \sum_{\mu,\mu',i=2,3} J_{\text{Ki}} \hat{\mathbf{S}}_i \cdot \hat{d}^{\dagger}_{\mu,i} \hat{\boldsymbol{\sigma}}_{\mu,\mu'} \hat{d}_{\mu',i}, \tag{A.23}$$

and,

$$\mathcal{H}_{\text{t}} = \sum_{\mu} \left\{ t \hat{d}^{\dagger}_{\mu,2} \hat{d}_{\mu,3} + h.c. \right\}. \tag{A.24}$$

Spin interactions between the impurities and other dynamics can be included, like magnetic anisotropy, to obtain the total Hamiltonian used in Chapters 2 and 3,

$$\mathcal{H} = \mathcal{H}_{\text{H}} + \mathcal{H}_{\text{K}} + \mathcal{H}_{\text{A}} + \mathcal{H}_{\text{t}}. \tag{A.25}$$

A.1 List of References

[1] P. W. Anderson, Physical Review Letters **17**, 95 (1966).

[2] J. R. Schrieffer and P. A. Wolff, Physical Review **149**, 491 (1966).

APPENDIX B: MAPPING SPIN INTERACTIONS DERIVATIONS AND SUPPLEMENTARY FIGURES

B.1 Derivation of Steady-State Current for the Generalized Master Equation

To obtain the density matrix equations and transition rates of our GME model, we express the coupling terms of V as products of the lead and central region operators. We designate an index notation that tracks all combinations of different $\hat{c}$ and $\hat{d}$ operators,

$$V = \sum_i t_i \hat{F}_i \hat{Q}_i, \tag{B.1}$$

where $\hat{F}_i$ refers to a possible form of the $\hat{c}$ operator, $\hat{Q}_i$ refers to a possible form of the $\hat{d}$ operator, and t_i is the coupling constant for that combination.

In this form, the correlators are defined [1],

$$\begin{aligned}\Gamma^{+}_{mkln} = &-\frac{1}{\hbar^2}\sum_{ij} t_i t_j \langle m|Q_i|k\rangle \ \langle l|Q_j|n\rangle \\ &\times \int_0^\infty \mathrm{d}t\, e^{-i\omega_{ln}t} \langle F_i(t) F_j\rangle\,, \end{aligned} \tag{B.2}$$

$$\begin{aligned}\Gamma^{-}_{mkln} = &-\frac{1}{\hbar^2}\sum_{ij} t_i t_j \langle m|Q_j|k\rangle \ \langle l|Q_i|n\rangle \\ &\times \int_0^\infty \mathrm{d}t\, e^{-i\omega_{mk}t} \langle F_j F_i(t)\rangle\,, \end{aligned} \tag{B.3}$$

with the Q operators acting on the Fock spin space of the central region, on the system eigenstates m, k, l, and n with eigenenergies E_m, E_k, E_l, and E_n, respectively. The leading contribution of the transition rates from central region eigenstate n to m (corresponding to

sequential tunneling) is then,

$$\begin{aligned} W_{n'n} &= \Gamma^{+}_{nn'n'n} + \Gamma^{-}_{nn'n'n} \\ &= \frac{2\pi}{\hbar} \sum_{iNN'} \left| \langle n'N'|t_i \hat{F}_i \hat{Q}_i|nN\rangle \right|^2 \langle N|\rho_{\text{leads}}(0)|N\rangle \\ &\qquad \times \delta\left(E_N - E_{N'} - \hbar\omega_{n'n}\right), \end{aligned} \tag{B.4}$$

where $\omega_{n'n} \equiv (E_{n'} - E_n)/\hbar$, and the system eigenstates have been expanded in terms of the combined lead N', N and central region n', n eigenstate indices. Because of the form of V, the only non-zero $W_{n'n}$ elements are those from a charged to an uncharged state or vice versa (i.e., $W_{u_i u_j} = W_{c_i c_j} = 0 \; \forall \; i, j$). The damping factor has the form,

$$\gamma_{n'n} = \sum_m \left[\Gamma^{+}_{n'mmn'} + \Gamma^{-}_{nmmn}\right] - (\Gamma^{+}_{nnn'n'} + \Gamma^{-}_{nnn'n'}). \tag{B.5}$$

This is simplified by redefining $\gamma_{mm'}$ as is done in Ref. [2] to the form of Eq. (4.16) in the main text.

Finally, clarifying the diagonal versus the off-diagonal terms of the system density matrix, one obtains,

$$\begin{aligned} \dot{\rho}_{nn}(t) &= \frac{i}{\hbar}\left[\rho(t), \mathcal{H}_0\right]_{nn} + \sum_{m,n\neq m} \rho_{mm}(t) W_{nm} \\ &\qquad - \rho_{nn}(t) \sum_{m,n\neq m} W_{mn}, \end{aligned} \tag{B.6}$$

$$\dot{\rho}_{n'n}(t) = \frac{i}{\hbar}\left[\rho(t), \mathcal{H}_0\right]_{n'n} - \gamma_{n'n}\rho_{n'n}(t). \tag{B.7}$$

The equation for the dynamics of $\rho(t)$ is given by the Pauli master equation for the diagonal elements, while the off-diagonal elements contain the decoherence of the system with the surrounding reservoir.

As mentioned in the main text, in order to produce relevant predictions from the generalized master equation, we look at a time range in which the overall relaxation time due to transitions is much longer than the decay of the off-diagonal elements. Because of the time range concerned, $\lim_{t\to\tau} \dot{\rho}_{n'n}(t) = 0$, and so,

$$\rho_{n'n}(t) = \frac{i}{\hbar\gamma_{n'n}} \left[\rho(t), \mathcal{H}_0\right]_{n'n}. \tag{B.8}$$

Substituting the central region and leads Hamiltonian into Eq. (B.7), one obtains closed equations for the off-diagonal density matrix elements. The off-diagonal terms in the same charge sector, i.e., $n, n' \in \{u_0, u_1\}$ or $n, n' \in \{c_0, c_1\}$, are,

$$\rho_{n'n}(t) = \frac{\mathcal{H}_{n'n}\left(\rho_{n'n'}(t) - \rho_{nn}(t)\right)}{\mathcal{H}_{n'n'} - \mathcal{H}_{nn} - i\hbar\gamma_{n'n}}. \tag{B.9}$$

Inserting this result into the generalized master equation's diagonal elements, and noting that $\gamma_{nn'} = \gamma_{n'n}$, results in,

$$\begin{aligned}\dot{\rho}_{n'n'}(t) = \Gamma_{n'n}\left(\rho_{nn}(t) - \rho_{n'n'}(t)\right) \\ + \sum_{m,n'\neq m} \rho_{mm} W_{n'm} - \rho_{n'n'} \sum_{m,n'\neq m} W_{mn'},\end{aligned} \tag{B.10}$$

where the Lorentzian decoherence factor is defined as,

$$\Gamma_{n'n} = \frac{\left|\mathcal{H}_{n'n}\right|^2}{\hbar^2} \frac{2\gamma_{n'n}}{\left(\mathcal{H}_{n'n'} - \mathcal{H}_{nn}\right)^2/\hbar^2 + \gamma_{n'n}^2}. \tag{B.11}$$

The quantity $\gamma_{n'n}^2$ can now be interpreted as the broadening factor of the Lorentzian, and the peak of the Lorentzian is maximized if $\mathcal{H}_{n'n'} = \mathcal{H}_{nn}$. We point out that while the $n'n$ elements in Eq. (B.10) are constrained to the same charge sector, the sums over the index m include only those terms that connect different charge sectors, with the form $W_{u_i c_j}$ and $W_{c_j u_i}$.

This means that the transition rates between any of the different levels between different charge states should be accounted for, if not forbidden by transition rules (e.g., through spin conservation). The transition rates from an uncharged eigenstate u_j to charged eigenstate c_i is derived to be,

$$W_{c_i u_j} = \sum_{\alpha\sigma} W^{\alpha\sigma}_{c_i u_j}, \tag{B.12}$$

where,

$$\begin{aligned} W^{\alpha\sigma}_{c_i u_j} = & \frac{2\pi}{\hbar}\nu_{\alpha\sigma}|t_{\alpha\sigma}|^2 \left| \langle c_i|\hat{c}^\dagger_{\alpha\sigma}|u_j\rangle \right|^2 \\ & \times \int \mathrm{d}E\, D(E) f_\alpha(\Delta E^{(i,j)}_{N+1,N} + E). \end{aligned} \tag{B.13}$$

In the rate equation, $D(E) \equiv D_{\alpha\sigma}(E) D_{\alpha\sigma}(\Delta_{ij} + E)$, and the zero of the chemical potential is measured against the zero of the charged sector. The reverse process has a similar form,

$$\begin{aligned} W^{\alpha\sigma}_{u_i c_j} = & \frac{2\pi}{\hbar}\nu_{\alpha\sigma}|t_{\alpha\sigma}|^2 \left| \langle u_i|\hat{c}_{\alpha\sigma}|c_j\rangle \right|^2 \\ & \times \int \mathrm{d}E\, D(E) \left(1 - f_\alpha(\Delta E^{(j,i)}_{N+1,N} + E)\right). \end{aligned} \tag{B.14}$$

These rates are further simplified by assuming that transport primarily occurs with electrons near the Fermi level of the leads, and so we assign the tunneling rate $w_{\alpha\sigma} = 2\pi|t_{\alpha\sigma}|^2 D(E_f)/\hbar$. Inserting these results along with the steady-state case assumption allows us to obtain closed equations of the density matrix elements. The derived density matrix elements using

Eq. (B.10) are,

$$\begin{aligned}\eta\rho_{u_0u_0} = {} & W_{c_0u_1}\left(W_{u_0c_0}\left(\Gamma_{c_0c_1}+W_{u_0c_1}+W_{u_1c_1}\right)+\Gamma_{c_0c_1}W_{u_0c_1}\right)\\ & + W_{c_1u_1}\left(\Gamma_{c_0c_1}\left(W_{u_0c_0}+W_{u_0c_1}\right)+W_{u_0c_1}\left(W_{u_0c_0}+W_{u_1c_0}\right)\right)\\ & + \Gamma_{u_0u_1}\left(\Gamma_{c_0c_1}\left(W_{u_0c_0}+W_{u_0c_1}+W_{u_1c_0}+W_{u_1c_1}\right)+\left(W_{u_0c_0}+W_{u_1c_0}\right)\left(W_{u_0c_1}+W_{u_1c_1}\right)\right),\end{aligned} \tag{B.15}$$

$$\begin{aligned}\eta\rho_{u_1u_1} = {} & W_{c_0u_0}\left(\Gamma_{c_0c_1}\left(W_{u_1c_0}+W_{u_1c_1}\right)+W_{u_1c_0}\left(W_{u_0c_1}+W_{u_1c_1}\right)\right)\\ & + W_{c_1u_0}\left(\Gamma_{c_0c_1}\left(W_{u_1c_0}+W_{u_1c_1}\right)+W_{u_1c_1}\left(W_{u_0c_0}+W_{u_1c_0}\right)\right)\\ & + \Gamma_{u_0u_1}\left(\Gamma_{c_0c_1}\left(W_{u_0c_0}+W_{u_0c_1}+W_{u_1c_0}+W_{u_1c_1}\right)+\left(W_{u_0c_0}+W_{u_1c_0}\right)\left(W_{u_0c_1}+W_{u_1c_1}\right)\right),\end{aligned} \tag{B.16}$$

$$\begin{aligned}\eta\rho_{c_0c_0} = {} & W_{c_0u_0}\left(W_{c_0u_1}\left(\Gamma_{c_0c_1}+W_{u_0c_1}+W_{u_1c_1}\right)+W_{c_1u_1}\left(\Gamma_{c_0c_1}+W_{u_0c_1}\right)+\Gamma_{u_0u_1}\left(\Gamma_{c_0c_1}+W_{u_0c_1}+W_{u_1c_1}\right)\right)\\ & + W_{c_0u_1}\left(\left(\Gamma_{c_0c_1}+W_{u_1c_1}\right)\left(W_{c_1u_0}+\Gamma_{u_0u_1}\right)+W_{u_0c_1}\Gamma_{u_0u_1}\right)\\ & + \Gamma_{c_0c_1}\left(\Gamma_{u_0u_1}\left(W_{c_1u_0}+W_{c_1u_1}\right)+W_{c_1u_0}W_{c_1u_1}\right),\end{aligned} \tag{B.17}$$

and,

$$\begin{aligned}\eta\rho_{c_1c_1} = {} & W_{c_0u_1}\left(\Gamma_{c_0c_1}\left(W_{c_0u_0}+\Gamma_{u_0u_1}\right)+W_{c_1u_0}\left(\Gamma_{c_0c_1}+W_{u_0c_0}\right)\right)\\ & + \Gamma_{u_0u_1}\left(\Gamma_{c_0c_1}W_{c_0u_0}+\left(W_{c_1u_0}+W_{c_1u_1}\right)\left(\Gamma_{c_0c_1}+W_{u_0c_0}+W_{u_1c_0}\right)\right)\\ & + W_{c_1u_1}\left(W_{c_0u_0}\left(\Gamma_{c_0c_1}+W_{u_1c_0}\right)+W_{c_1u_0}\left(\Gamma_{c_0c_1}+W_{u_0c_0}+W_{u_1c_0}\right)\right),\end{aligned} \tag{B.18}$$

where η is a normalization constant.

B.2 Plots of Conductance For No Applied Magnetic Field

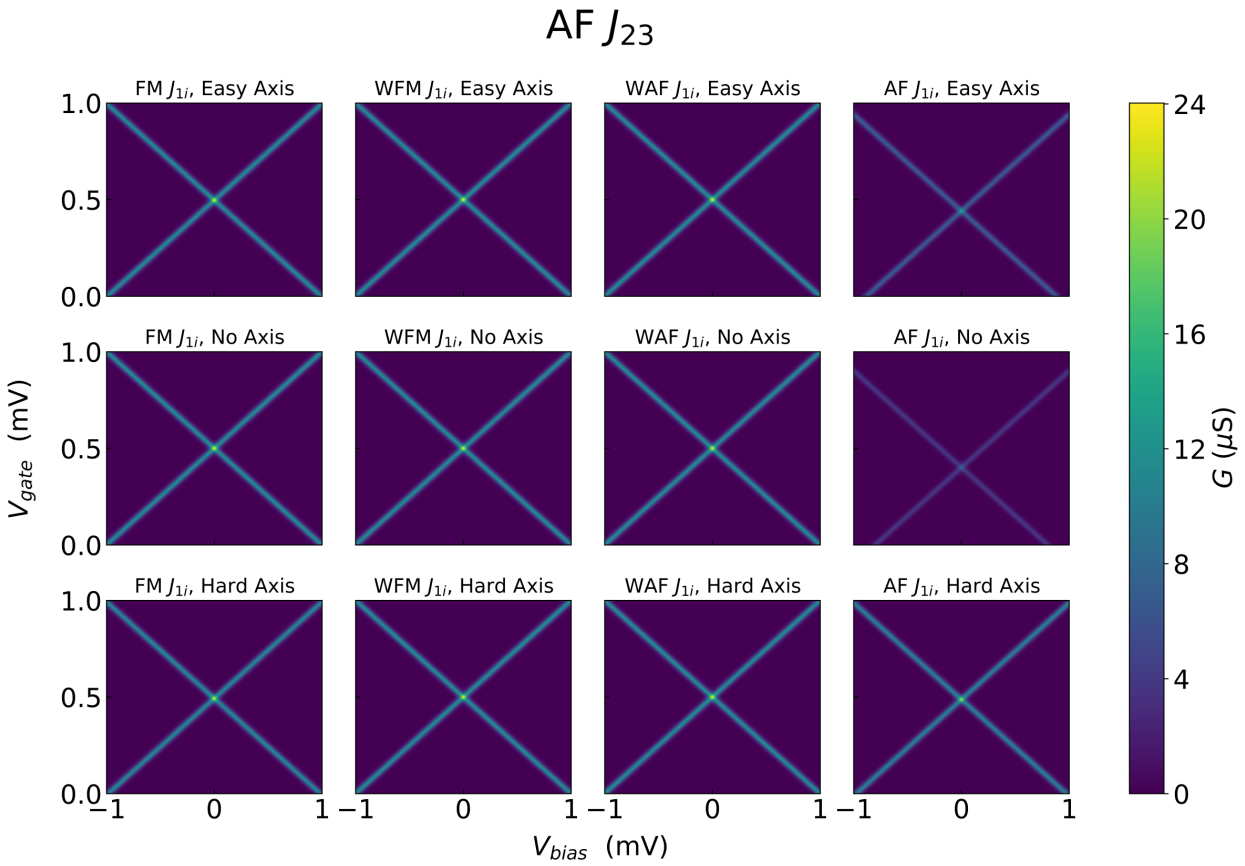

Figure B.1: Differential conductance G as a function of bias voltage and gate voltage for antiferromagnetic J_{23}. The correspondence of plot labels to numerical parameters can be found in the main text.

B.3 Plots of Conductance With an Applied Magnetic Field

B.4 List of References

[1] K. Blum, *Density Matrix Theory and Applications* (Springer Berlin Heidelberg, Berlin, Heidelberg, 2012).

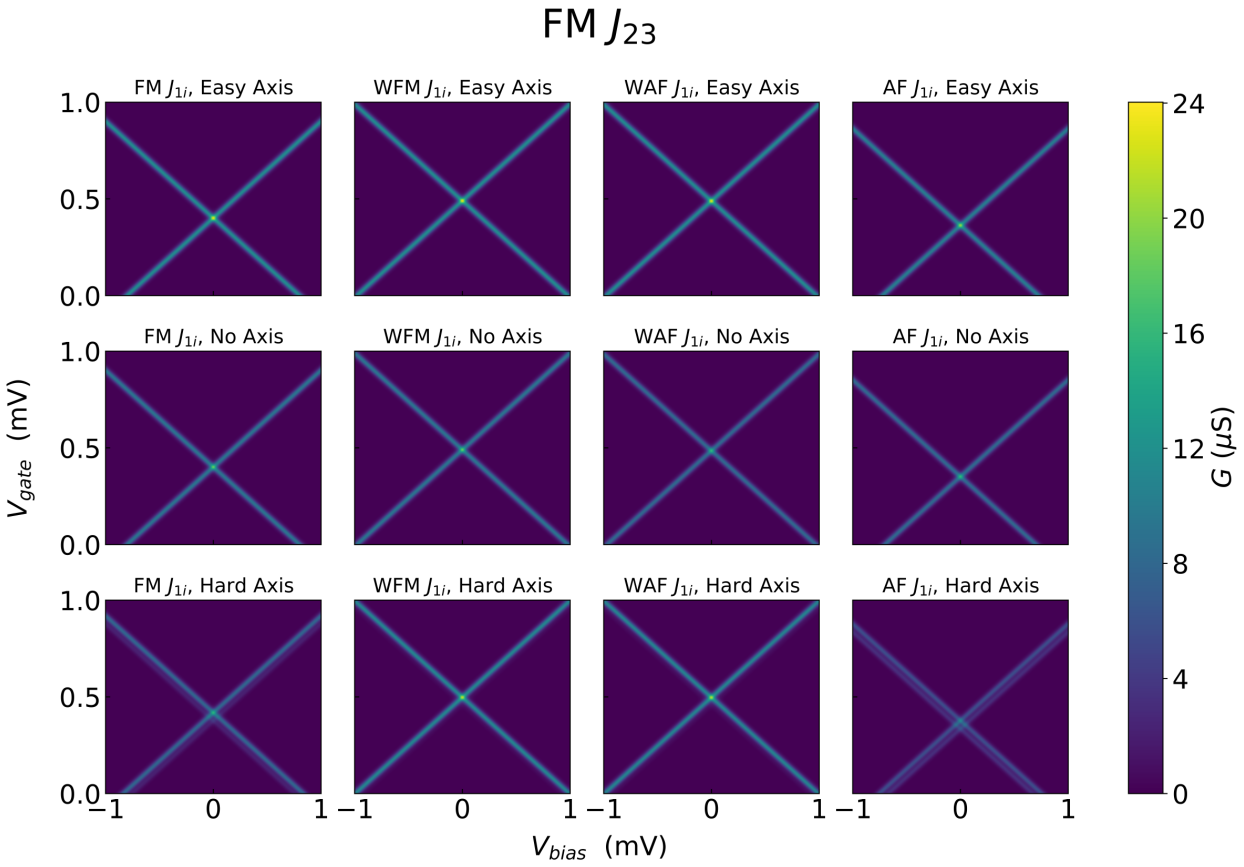

Figure B.2: Differential conductance G as a function of bias voltage and gate voltage for ferromagnetic J_{23}. The correspondence of plot labels to numerical parameters can be found in the main text.

[2] G. González and M. N. Leuenberger, Physical Review Letters **98**, 256804 (2007).

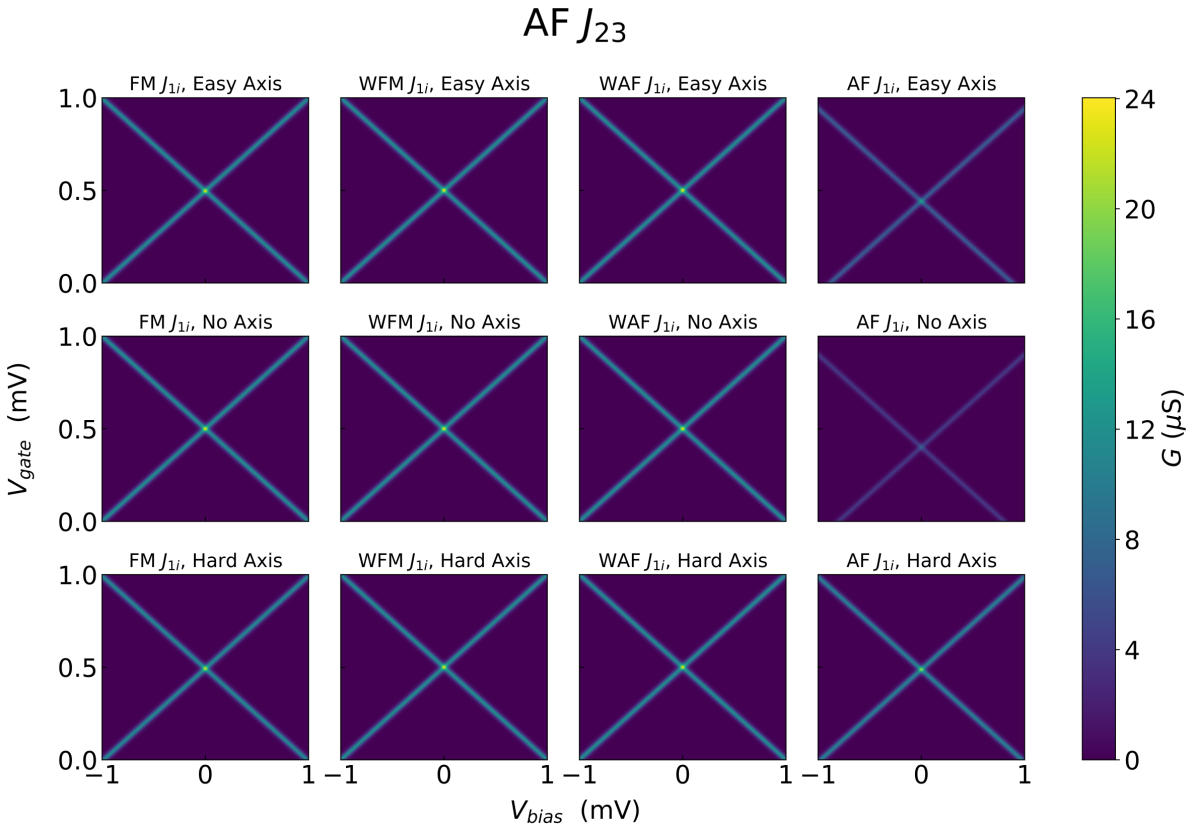

Figure B.3: Differential conductance G as a function of gate voltage and transverse applied magnetic field for ferromagnetic J_{23}. The correspondence of plot labels to numerical parameters can be found in the main text.

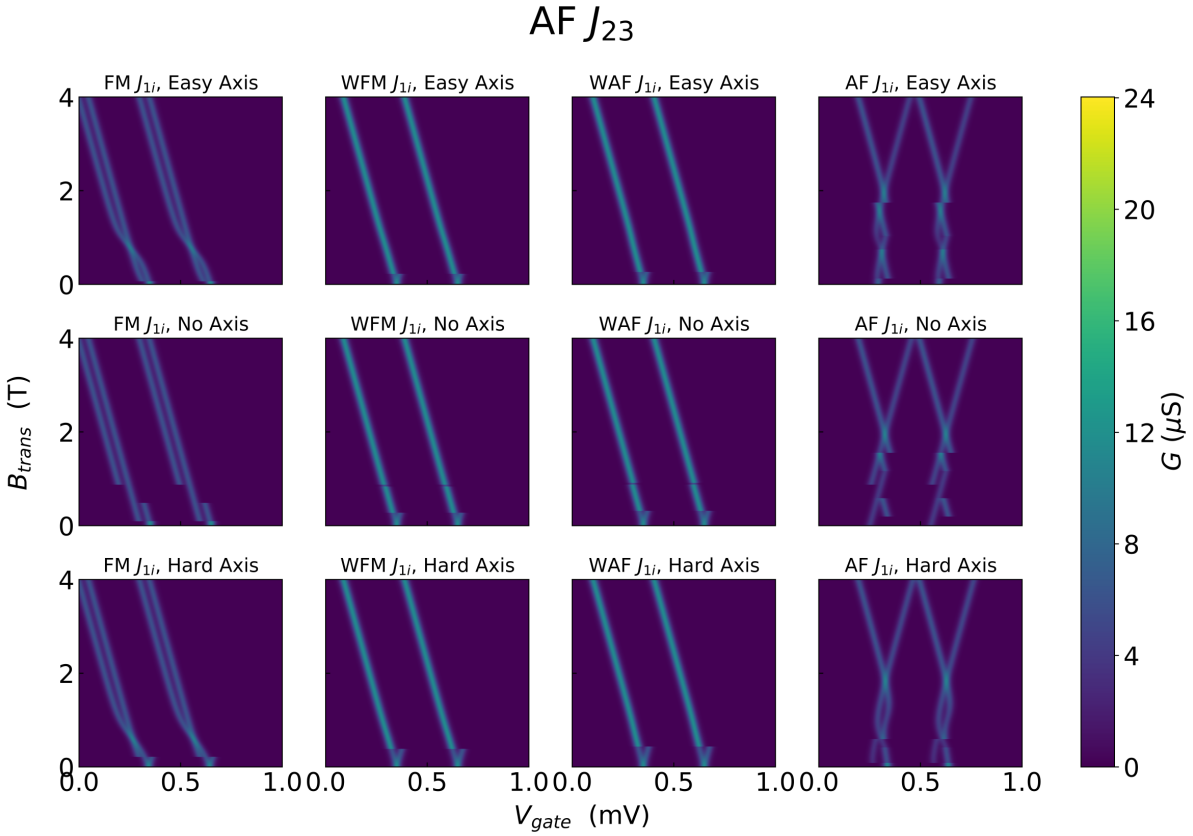

Figure B.4: Differential conductance G as a function of gate voltage and transverse applied magnetic field for antiferromagnetic J_{23}. The correspondence of plot labels to numerical parameters can be found in the main text.

APPENDIX C: EQUILIBRIUM GREENS FUNCTIONS FOR AN ELECTRON EXCHANGE COUPLED WITH TWO SPIN IMPURITIES

C.1 Double-Delta First Quantization Green's Function Solution

From Eq. 5.6, I solve for $G(0,x')$ and $G(x_0,x')$ by setting $x \in \{0, x_0\}$. One obtains,

$$G(0,x') = \frac{G_0(0,x') + J_2 G_0(0,x_0) G(x_0,x')}{\alpha_1(0)}, \tag{C.1}$$

where,

$$\alpha_i(x) = 1 - J_i G_0(x,x). \tag{C.2}$$

and

$$G(x_0,x') = \left[G_0(x_0,x') + \frac{J_1 G_0(x_0,0) G_0(0,x')}{\alpha_1(0)}\right]\left[\frac{\alpha_1(0)}{\alpha_2(x_0)\alpha_1(0) - J_1 J_2 G_0(x_0,0) G_0(0,x_0)}\right], \tag{C.3}$$

Reinserting this result back into Eq. (5.6),

$$\begin{aligned} G(x,x') = G_0(x,x') &+ \frac{J_1 G_0(x,0) G_0(0,x')}{\alpha_1(0)} \\ &+ \gamma\Bigg(J_1 J_2 G_0(x,0) G_0(0,x_0) G_0(x_0,x') + \frac{J_1^2 J_2 G_0(x,0) G_0(0,x_0) G_0(x_0,0) G_0(0,x')}{\alpha_1(0)} \\ &\quad + J_2 \alpha_1(0) G_0(x,x_0) G_0(x_0,x') + J_1 J_2 G_0(x,x_0) G_0(x_0,0) G_0(0,x') \Bigg), \end{aligned} \tag{C.4}$$

where,

$$\gamma = \left[\alpha_2(x_0)\alpha_1(0) - J_1 J_2 G_0(x_0,0) G_0(0,x_0)\right]^{-1}. \tag{C.5}$$

Defining the new terms,

$$\beta_i(x) = \frac{1}{J_i} - G_0(x,x), \tag{C.6}$$

$$\lambda = \left[\beta_2(x_0)\beta_1(0) - G_0(x_0,0)G_0(0,x_0)\right]^{-1}, \tag{C.7}$$

and inserting into Eq. (C.4), one obtains,

$$\begin{aligned} G(x,x') = G_0(x,x') &+ \frac{G_0(x,0)G_0(0,x')}{\beta_1(0)} \\ &+ \lambda\Bigg(G_0(x,0)G_0(0,x_0)G_0(x_0,x') + \frac{G_0(x,0)G_0(0,x_0)G_0(x_0,0)G_0(0,x')}{\beta_1(0)} \\ &+ \beta_1(0)G_0(x,x_0)G_0(x_0,x') + G_0(x,x_0)G_0(x_0,0)G_0(0,x')\Bigg), \end{aligned} \tag{C.8}$$

Note that the first two terms on the right-hand side of this Green's function looks like the Green's function for a single delta function.

C.2 Double-Delta Lippmann-Schwinger Solution

Starting from Eq. (5.13), and inserting the double-well potential for anisotropic strength J,

$$\psi(0) = \frac{\psi_0(0) + J_2 G_0^r(0,x_0)\psi(x_0)}{J_1\beta_1^r(0)}, \tag{C.9}$$

where I have defined,

$$\alpha_i^r(x) = 1 - J_i G_0^r(x,x) \tag{C.10}$$

$$\beta_i^r(x) = \frac{1}{J_i}\alpha_i^r(x) = \frac{1}{J_i} - G_0^r(x,x). \tag{C.11}$$

Comparing to the Green's function solution, one can perform the following starting from the Green's function formalism,

1. Substitute any Green's function that contains x' (i.e., $G(\alpha, x')$ and $G_0(\alpha, x')$) with its wave function counterpart: $\psi(\alpha)$ and $\psi_0(\alpha)$.

2. Substitute any other $G_0(x, y)$ with $G_0^r(x, y)$.

Using this substitution method, one finds,

$$\psi_{\text{two-delta}}(x) = \psi_{\text{one-delta}}(x) + \psi_{\text{corrections}}(x), \tag{C.12}$$

where,

$$\psi_{\text{one-delta}}(x) = \psi_0(x) + \frac{G_0^r(x,0)\psi_0(0)}{\beta_1^r(0)}, \tag{C.13}$$

$$\begin{aligned}\psi_{\text{corrections}}(x) = \lambda\Bigg(& G_0^r(x,0)G_0^r(0,x_0)\psi_0(x_0) + G_0^r(x,x_0)G_0^r(x_0,0)\psi_0(0) \\ & + \beta_1(0)G_0^r(x,x_0)\psi_0(x_0) + \frac{G_0^r(x,0)G_0^r(0,x_0)G_0^r(x_0,0)\psi_0(0)}{\beta_1(0)}\Bigg),\end{aligned} \tag{C.14}$$

and,

$$\beta_i(x) = \frac{1}{J_i} - G_0^r(x,x), \tag{C.15}$$

$$\lambda = \left[\beta_2(x_0)\beta_1(0) - G_0^r(x_0,0)G_0^r(0,x_0)\right]^{-1}. \tag{C.16}$$

Now I analyze the behavior as $x \to \infty$. The free Green's function becomes,

$$\lim_{x\to\infty} G_0^r(x,x') = \frac{2m^*}{\hbar^2}\frac{1}{2ik}e^{ikx}e^{-ik\hat{\mathbf{n}}_x\cdot\mathbf{x}'} \tag{C.17}$$

In our case, $\hat{\mathbf{n}}_x = -\hat{\mathbf{n}}_{x'}$, and so for the cases of the retarded free Green's function that is

outside an integral over x' or x, I obtain,

$$\lim_{x\to\infty} G_0^r(x,x') = \frac{2m^*}{\hbar^2}\frac{1}{2ik}e^{ikx}. \tag{C.18}$$

Because a general solution is desired, I begin by assuming the general form of the free-electron Green's function. I then impose the initial condition of,

$$\psi_0(x) = e^{ikx}, \tag{C.19}$$

and define both,

$$c_k \equiv \frac{m^*}{ik\hbar^2}, \tag{C.20}$$

$$\gamma_i \equiv \frac{J_i m^*}{ik\hbar^2} = J_i c_k, \tag{C.21}$$

to obtain for the one-delta function potential,

$$\psi_{\text{one-delta}}(x) = e^{ikx} + \frac{\gamma_1}{1-\gamma_1}e^{ik|x|}. \tag{C.22}$$

For the corrections,

$$\psi_{\text{corrections}}(x) = \lambda\left(e^{ik(|x|+|x_0|+x_0)} + e^{ik(|x-x_0|+|x_0|)} + \left(\frac{1}{\gamma_1}-1\right)e^{ik(|x-x_0|+x_0)} + \frac{\gamma_1}{1-\gamma_1}e^{ik(|x|+|2x_0|)}\right), \tag{C.23}$$

where,

$$\lambda = \left[\left(\frac{1}{\gamma_1}-1\right)\left(\frac{1}{\gamma_2}-1\right) - e^{2ik|x_0|}\right]^{-1}. \tag{C.24}$$

APPENDIX D: NON-EQUILIBRIUM GREENS FUNCTION MODEL FOR TIGHT-BINDING TRIPARTITE SPIN SYSTEMS

D.1 Fermion Operator Algebra

The important fermion operator anticommutator rules are stated,

$$\{c_k, c_q^\dagger\} = c_k c_q^\dagger + c_q^\dagger c_k = \delta_{kq}, \tag{D.1}$$

$$\{c_k, c_q\} = \{c_k^\dagger, c_q^\dagger\} = 0. \tag{D.2}$$

These rules naturally lead to the operator commutator rules,

$$[c_k, c_q^\dagger] = \{c_k, c_q^\dagger\} - 2c_q^\dagger c_k = \delta_{kq} - 2c_q^\dagger c_k \tag{D.3}$$

$$[c_k, c_q] = -2c_q c_k \tag{D.4}$$

$$[c_k^\dagger, c_q^\dagger] = -2c_q^\dagger c_k^\dagger. \tag{D.5}$$

One can extend the prior result to a product of three creation operators,

$$\begin{aligned}
\big[c_i, c_j^\dagger c_k\big] &= \big[c_i, c_j^\dagger\big] c_k + c_j^\dagger \big[c_i, c_k\big] && \text{(D.6a)}\\
&= \Big(\big\{c_i, c_j^\dagger\big\} - 2c_j^\dagger c_i\Big) c_k + c_j^\dagger \Big(\big\{c_i, c_k\big\} - 2c_k c_i\Big) && \text{(D.6b)}\\
&= \Big(\delta_{ij} - 2c_j^\dagger c_i\Big) c_k - 2c_j^\dagger c_k c_i && \text{(D.6c)}\\
&= \delta_{ij} c_k. && \text{(D.6d)}
\end{aligned}$$

D.2 Spin Operator Algebra

The spin operator rules are also stated for general spin S,

$$\left(S^{+}\right)^{\dagger} = S^{-} \tag{D.7}$$

$$\left(S^{-}\right)^{\dagger} = S^{+} \tag{D.8}$$

$$\left[S^{+}_{\beta}, S^{-}_{\beta'}\right] = \delta_{\beta\beta'} 2\hbar S^{z}_{\beta} \tag{D.9}$$

$$\left[S^{z}_{\beta}, S^{\pm}_{\beta'}\right] = \pm\delta_{\beta\beta'} \hbar S^{\pm}_{\beta'} \tag{D.10}$$

$$\left\{S^{+}_{\beta}, S^{-}_{\beta'}\right\} = \left[S^{+}_{\beta}, S^{-}_{\beta'}\right] + 2S^{-}_{\beta'} S^{+}_{\beta} = \delta_{\beta\beta'} 2\hbar S^{z}_{\beta} + 2S^{-}_{\beta'} S^{+}_{\beta}, \tag{D.11}$$

$$\left\{S^{z}_{\beta}, S^{\pm}_{\beta'}\right\} = \left[S^{z}_{\beta}, S^{\pm}_{\beta'}\right] + 2S^{\pm}_{\beta'} S^{z}_{\beta} = \pm\delta_{\beta\beta'} \hbar S^{\pm}_{\beta'} + 2S^{\pm}_{\beta'} S^{z}_{\beta}. \tag{D.12}$$

It is interesting to note the action of the conjugate transpose operation on the Cartesian spin operators for any spin S,

$$\left(S^{x}_{\beta}\right)^{\dagger} = \left[\frac{1}{2}\left(S^{+}_{\beta} + S^{-}_{\beta}\right)\right]^{\dagger} = S^{x}_{\beta}, \tag{D.13}$$

$$\left(S^{y}_{\beta}\right)^{\dagger} = -\left[\frac{i}{2}\left(S^{+}_{\beta} - S^{-}_{\beta}\right)\right]^{\dagger} = S^{y}_{\beta}, \tag{D.14}$$

$$\left(S^{z}_{\beta}\right)^{\dagger} = \left[\frac{1}{2\hbar}\left(S^{+}_{\beta} S^{-}_{\beta} - S^{-}_{\beta} S^{+}_{\beta}\right)\right]^{\dagger} = S^{z}_{\beta}. \tag{D.15}$$

For the Cartesian spin operators, the commutator relation for any spin S is more easily obtained,

$$\left[S^{l}_{\beta}(t), S^{m}_{\beta'}(t)\right] = \delta_{\beta\beta'} i\hbar \sum_{n} \epsilon^{lmn} S^{n}_{\beta}(t). \tag{D.16}$$

In the case when calculating the commutator relation of a spin vector $\mathbf{S}$ with another spin operator, one obtains,

$$\left[S^l_\beta(t), \mathbf{S}_{\beta'}(t)\right] = \sum_m \left[S^l_\beta(t), S^m_{\beta'}(t)\right] \hat{m} \tag{D.17a}$$

$$= \delta_{\beta\beta'} i\hbar \sum_{mn} \epsilon^{lmn} S^n_\beta(t) \hat{m}, \tag{D.17b}$$

where $\hat{m}$ is the *direction* of the vector component, and not an operator. The anticommutator relation for any spin S is then,

$$\left\{S^l_\beta(t_i), S^m_{\beta'}(t_i)\right\} = \left[S^l_\beta(t_i), S^m_{\beta'}(t_i)\right] + 2S^m_{\beta'}(t_i)S^l_\beta(t_i) = i\hbar\delta_{\beta\beta'} \sum_n \epsilon^{lmn} S^n_\beta(t_i) + 2S^m_{\beta'}(t_i)S^l_\beta(t_i). \tag{D.18}$$

The following anticommutator is true for the Cartesian representation of the spin operators,

$$\left\{S^l_\beta(t_i), S^{m\dagger}_{\beta'}(t_i)\right\} = \left[S^l_\beta(t_i), S^{m\dagger}_{\beta'}(t_i)\right] + 2S^{m\dagger}_{\beta'}(t_i)S^l_\beta(t_i) \tag{D.19a}$$

$$= i\hbar\delta_{\beta\beta'} \sum_n \epsilon^{lmn} S^n_\beta(t_i) + 2S^m_{\beta'}(t_i)S^l_\beta(t_i). \tag{D.19b}$$

and thus for three spin operators for any spin S,

$$\left[S^l_\beta(t), S^m_{\beta'}(t)S^n_{\beta''}(t)\right] = \left[S^l_\beta(t), S^m_{\beta'}(t)\right] S^n_{\beta''}(t) + S^m_\beta(t) \left[S^l_{\beta'}(t), S^n_{\beta''}(t)\right] \tag{D.20a}$$

$$= \delta_{\beta\beta'} i\hbar \sum_p \epsilon^{lmp} S^p_\beta(t) S^n_{\beta''}(t) + \delta_{\beta'\beta''} i\hbar \sum_p \epsilon^{lnp} S^m_\beta(t) S^p_{\beta''}(t) \tag{D.20b}$$

$$= i\hbar \sum_p \left(\delta_{\beta\beta'}\epsilon^{lmp} S^p_\beta(t) S^n_{\beta''}(t) + \delta_{\beta'\beta''}\epsilon^{lnp} S^m_\beta(t) S^p_{\beta''}(t)\right). \tag{D.20c}$$

In the special case when $m = n = z$ and $\beta' = \beta''$, this relation becomes,

$$\left[S^l_\beta(t), S^z_{\beta'}(t)S^z_{\beta'}(t)\right] = i\hbar \sum_p \left(\delta_{\beta\beta'}\epsilon^{lzp}S^p_\beta(t)S^z_\beta(t) + \epsilon^{lzp}S^z_\beta(t)S^p_{\beta'}(t)\right) \tag{D.21a}$$

$$= i\hbar \left(\delta_{ly}\left[\delta_{\beta\beta'}S^x_\beta(t)S^z_\beta(t) + S^z_\beta(t)S^x_{\beta'}(t)\right] - \delta_{lx}\left[\delta_{\beta\beta'}S^y_\beta(t)S^z_\beta(t) + S^z_\beta(t)S^y_{\beta'}(t)\right]\right). \tag{D.21b}$$

D.3 Green's Function Definitions

The total Green's function G is a thermodynamic average of the product of two Heisenberg operators $\psi(\mathbf{1})$ and $\psi(\mathbf{1}')$. The one-particle Green's function is defined as,

$$G(\mathbf{1}, \mathbf{1}') = -\frac{i}{\hbar}\left\langle \mathcal{T}\left(\psi(\mathbf{1})\psi^\dagger(\mathbf{1}')\right)\right\rangle, \tag{D.22}$$

where $\mathcal{T}$ is the Wick time-ordering operator, designed to place the "earliest" operator on the right-most side of the equation, and the "latest" on the left-most side [1],

$$\mathcal{T}\left(\psi(\mathbf{1})\psi^\dagger(\mathbf{1}')\right) = \psi(\mathbf{1})\psi^\dagger(\mathbf{1}') \text{ for } t_1 > t_{1'}, \tag{D.23a}$$

$$= -\psi^\dagger(\mathbf{1}')\psi(\mathbf{1}) \text{ for } t_1 < t_{1'}. \tag{D.23b}$$

The Green's functions are expressed in coordinates $\mathbf{1} \equiv (\mathbf{x}, t, \sigma)$ (or $\mathbf{1} \equiv (\mathbf{x}, \tau, \sigma)$ for complex time τ as appropriate). It is often easier, especially when differentiating time-ordered products, to introduce a more compact form of the Wick time-ordering operator,

$$\mathcal{T}\left(\psi(\mathbf{1})\psi^\dagger(\mathbf{1}')\right) = \theta(t_1 - t_{1'})\psi(\mathbf{1})\psi^\dagger(\mathbf{1}') - \theta(t_{1'} - t_1)\psi^\dagger(\mathbf{1}')\psi(\mathbf{1}) \tag{D.23c}$$

The two-particle Green's function is defined as,

$$G(\mathbf{1},\mathbf{2},\mathbf{1}',\mathbf{2}') = -\frac{1}{\hbar^2}\left\langle \mathcal{T}\left(\psi(\mathbf{1})\psi(\mathbf{2})\psi^\dagger(\mathbf{2}')\psi^\dagger(\mathbf{1}')\right)\right\rangle, \tag{D.24}$$

The lesser and greater Green's functions are,

$$G^<(\mathbf{1},\mathbf{1}') = \frac{i}{\hbar}\left\langle \psi^\dagger(\mathbf{1}')\psi(\mathbf{1})\right\rangle, \tag{D.25}$$

$$G^>(\mathbf{1},\mathbf{1}') = -\frac{i}{\hbar}\left\langle \psi(\mathbf{1})\psi^\dagger(\mathbf{1}')\right\rangle, \tag{D.26}$$

where the $<$ and $>$ notation remind one that for $t_1 > t_{1'}$. To explore the connection of observable to Green's functions, first look at the number density,

$$\langle n(\mathbf{1})\rangle = \left\langle \psi^\dagger(\mathbf{1})\psi(\mathbf{1})\right\rangle = -i\hbar G^<(\mathbf{1},\mathbf{1}), \tag{D.27}$$

for particle density $n(\mathbf{1})$. The reason why the lesser Green's function is used is because of the obfuscation,

$$\langle n(\mathbf{1})\rangle = \left\langle \psi^\dagger(\mathbf{1})\psi(\mathbf{1}^+)\right\rangle = -i\hbar G(\mathbf{1},\mathbf{1}^+), \tag{D.28}$$

where $\mathbf{1}^+ \equiv \lim_{\varepsilon\to 0}(\mathbf{x}, t+\varepsilon)$. One can then determine the connection with Green's functions and density matrices,

$$\rho_{ij}(\tau) = -i\hbar G^<(\mathbf{1}_i(\tau),\mathbf{1}_j(\tau+\varepsilon)) \tag{D.29}$$

It is also useful to define two additional Green's functions: the retarded and advanced, which are given as

$$G^r(\mathbf{1},\mathbf{1}') = -\frac{i}{\hbar}\theta(t-t')\left\langle\left\{\psi(\mathbf{1}),\psi^\dagger(\mathbf{1}')\right\}\right\rangle, \tag{D.30}$$

$$G^a(\mathbf{1},\mathbf{1}') = \frac{i}{\hbar}\theta(t'-t)\left\langle\left\{\psi(\mathbf{1}),\psi^\dagger(\mathbf{1}')\right\}\right\rangle. \tag{D.31}$$

It can be easily proven that with these definitions of the Green's functions, the following relation exists,

$$G^r - G^a = G^> - G^<. \tag{D.32}$$

D.4 Non-Equilibrium Green's Function

The non-equilibrium Green's functions are defined along a contour [2]. Instead of using a Wick time-ordering operator, one must now use a contour-ordered operator $\mathcal{T}_C$. Because it is useful later, the additional Green's functions, the causal (time-ordered) and anti-causal (anti-time ordered) Green's functions, are defined on the contour as,

$$G^c(\mathbf{1},\mathbf{1}') = -\frac{i}{\hbar}\theta(t_1-t_{1'})\left\langle\psi(\mathbf{1})\psi^\dagger(\mathbf{1}')\right\rangle + \frac{i}{\hbar}\theta(t_{1'}-t_1)\left\langle\psi^\dagger(\mathbf{1}')\psi(\mathbf{1})\right\rangle, \tag{D.33}$$

$$G^{\tilde{c}}(\mathbf{1},\mathbf{1}') = -\frac{i}{\hbar}\theta(t_{1'}-t_1)\left\langle\psi(\mathbf{1})\psi^\dagger(\mathbf{1}')\right\rangle + \frac{i}{\hbar}\theta(t_1-t_{1'})\left\langle\psi^\dagger(\mathbf{1}')\psi(\mathbf{1})\right\rangle. \tag{D.34}$$

D.5 Equation of Motion

To obtain the dynamics, one approach is to calculate the partial time derivative of the causal Green's function. Doing so for the electron operators as an example, one obtains,

$$\begin{aligned}
\frac{\partial G^c(\mathbf{1},\mathbf{1}')}{\partial t} &= -\frac{i}{\hbar}\delta(t-t')\left\langle c_k(t)c_q^\dagger(t')\right\rangle - \frac{i}{\hbar}\theta(t-t')\frac{\partial}{\partial t}\left\langle c_k(t)c_q^\dagger(t')\right\rangle \\
&\quad - \frac{i}{\hbar}\delta(t'-t)\left\langle c_q^\dagger(t')c_k(t)\right\rangle + \frac{i}{\hbar}\theta(t'-t)\frac{\partial}{\partial t}\left\langle c_q^\dagger(t')c_k(t)\right\rangle && \text{(D.35a)} \\
&= -\frac{i}{\hbar}\delta(t-t')\left(\left\langle c_k(t)c_q^\dagger(t')\right\rangle + \left\langle c_q^\dagger(t')c_k(t)\right\rangle\right) \\
&\quad - \frac{i}{\hbar}\theta(t-t')\left(\left\langle \frac{\partial c_k(t)}{\partial t}c_q^\dagger(t')\right\rangle + \left\langle c_k(t)\frac{\partial c_q^\dagger(t')}{\partial t}\right\rangle\right) && \text{(D.35b)} \\
&\quad + \frac{i}{\hbar}\theta(t'-t)\left(\left\langle \frac{\partial c_q^\dagger(t')}{\partial t}c_k(t)\right\rangle + \left\langle c_q^\dagger(t')\frac{\partial c_k(t)}{\partial t}\right\rangle\right) && \text{(D.35c)} \\
&= -\frac{i}{\hbar}\delta(t-t')\left\langle\left\{c_k(t),c_q^\dagger(t')\right\}\right\rangle - \frac{i}{\hbar}\left\langle\mathcal{T}\left(\frac{\partial c_k(t)}{\partial t}c_q^\dagger(t')\right)\right\rangle. && \text{(D.35d)}
\end{aligned}$$

Next the equation of motion of the electron operators is,

$$i\hbar\frac{\partial c_k(t)}{\partial t} = \left[c_k(t),\mathcal{H}\right], \tag{D.36}$$

for a Hamiltonian $\mathcal{H}$. Inserting this into the result of the time derivative of the causal Green's function, and multiplying by another factor of $i\hbar$, one obtains,

$$i\hbar\frac{\partial G^c(\mathbf{1},\mathbf{1}')}{\partial t} = \delta(t-t')\left\langle\left\{c_k(t),c_q^\dagger(t')\right\}\right\rangle - \frac{i}{\hbar}\left\langle\mathcal{T}\left(\left[c_k(t),\mathcal{H}\right]c_q^\dagger(t')\right)\right\rangle. \tag{D.37}$$

As will be used later, the equation of motion is also needed for the retarded and

advanced Green's functions. For the former,

$$\frac{\partial G^r(\mathbf{1},\mathbf{1}')}{\partial t} = \frac{\partial}{\partial t}\left(-\frac{i}{\hbar}\theta(t-t')\left\langle\left\{c_k(t), c_q^\dagger(t')\right\}\right\rangle\right) \tag{D.38a}$$

$$= -\frac{i}{\hbar}\delta(t-t')\left\langle\left\{c_k(t), c_q^\dagger(t')\right\}\right\rangle - \frac{i}{\hbar}\theta(t-t')\left\langle\left\{\frac{\partial c_k(t)}{\partial t}, c_q^\dagger(t')\right\}\right\rangle \tag{D.38b}$$

$$= -\frac{i}{\hbar}\delta(t-t')\left\langle\left\{c_k(t), c_q^\dagger(t')\right\}\right\rangle - \frac{i}{\hbar}\theta(t-t')\left\langle\left\{-\frac{i}{\hbar}\left[c_k(t),\mathcal{H}\right], c_q^\dagger(t')\right\}\right\rangle, \tag{D.38c}$$

and so,

$$i\hbar\frac{\partial G^r(\mathbf{1},\mathbf{1}')}{\partial t} = \delta(t-t')\left\langle\left\{c_k(t), c_q^\dagger(t')\right\}\right\rangle - \frac{i}{\hbar}\theta(t-t')\left\langle\left\{\left[c_k(t),\mathcal{H}\right], c_q^\dagger(t')\right\}\right\rangle. \tag{D.39}$$

Performing the same on the advanced Green's functions results in,

$$i\hbar\frac{\partial G^a(\mathbf{1},\mathbf{1}')}{\partial t} = \delta(t'-t)\left\langle\left\{c_k(t), c_q^\dagger(t')\right\}\right\rangle + \frac{i}{\hbar}\theta(t'-t)\left\langle\left\{\left[c_k(t),\mathcal{H}\right], c_q^\dagger(t')\right\}\right\rangle. \tag{D.40}$$

Repeating the same for the $G^<$ function (because the current through a device depends on that function), one finds that the equation of motion is,

$$\frac{\partial G^<(\mathbf{1},\mathbf{1}')}{\partial t} = \frac{i}{\hbar}\frac{\partial}{\partial t}\left(\left\langle c_q^\dagger(t')c_k(t)\right\rangle\right) \tag{D.41a}$$

$$= \frac{i}{\hbar}\left\langle c_q^\dagger(t')\frac{\partial}{\partial t}c_k(t)\right\rangle \tag{D.41b}$$

$$= \frac{i}{\hbar}\left\langle c_q^\dagger(t')\frac{-i}{\hbar}\left[c_k(t),\mathcal{H}\right]\right\rangle, \tag{D.41c}$$

which leads to,

$$i\hbar\frac{\partial G^<(\mathbf{1},\mathbf{1}')}{\partial t} = \frac{i}{\hbar}\left\langle c_q^\dagger(t')\left[c_k(t),\mathcal{H}\right]\right\rangle, \tag{D.42}$$

D.6 Time Propagation using the Trapezoidal Rule for Green's Functions

I state the numerical implementation of time propagation of a Green's function that does not contain a self-energy term, using the trapezoidal rule, the computational time step Δt, the Green's function computational matrix $\mathbf{G}$ and the Hamiltonian matrix $\mathbf{H}$. One first starts with the equation of motion,

$$i\hbar\frac{\mathrm{d}\mathbf{G}}{\mathrm{d}t} = \delta(t-t')\mathbf{I} + \mathbf{H}\mathbf{G}. \tag{D.43}$$

Applying the trapezoidal rule,

$$\begin{aligned}\mathbf{G}(t+\Delta t) &= \mathbf{G}(t) + \frac{1}{2}\left[\frac{\mathrm{d}\mathbf{G}(t)}{\mathrm{d}t} + \frac{\mathrm{d}\mathbf{G}(t+\Delta t)}{\mathrm{d}t}\right]\Delta t \\ &= \mathbf{G}(t) - \frac{i}{2\hbar}\left[\delta(t-t')\mathbf{I} + \mathbf{H}\mathbf{G}(t) + \delta(t+\Delta t-t')\mathbf{I} + \mathbf{H}\mathbf{G}(t+\Delta t)\right]\Delta t, \qquad \text{(D.44)} \\ &= \mathbf{G}(t) - \frac{i}{2\hbar}\left[\delta(t-t') + \delta(t+\Delta t-t')\right]\mathbf{I}\Delta t - \frac{i}{2\hbar}\mathbf{H}\left[\mathbf{G}(t) + \mathbf{G}(t+\Delta t)\right]\Delta t. \qquad \text{(D.45)}\end{aligned}$$

Solving for $\mathbf{G}(t+\Delta t)$,

$$\left(\mathbf{I} + \frac{i}{2\hbar}\mathbf{H}\Delta t\right)\mathbf{G}(t+\Delta t) = \mathbf{G}(t) - \frac{i}{2\hbar}\left[\delta(t-t') + \delta(t+\Delta t-t')\right]\mathbf{I}\Delta t - \frac{i}{2\hbar}\mathbf{H}\mathbf{G}(t)\Delta t, \tag{D.46}$$

so,

$$\mathbf{G}(t+\Delta t) = \left(\mathbf{I} + \frac{i}{2\hbar}\mathbf{H}\Delta t\right)^{-1}\left[\left(\mathbf{I} - \frac{i}{2\hbar}\mathbf{H}\Delta t\right)\mathbf{G}(t) + \left(-\frac{i}{2\hbar}\Delta t\left[\delta(t-t') + \delta(t+\Delta t-t')\right]\right)\mathbf{I}\right]. \tag{D.47}$$

Repeating the same procedure for t',

$$-i\hbar\frac{\mathrm{d}\mathbf{G}}{\mathrm{d}t'} = \delta(t-t')\mathbf{I} + \mathbf{G}\mathbf{H}, \tag{D.48}$$

so,

$$\frac{\mathrm{d}\mathbf{G}}{\mathrm{d}t'} = \left(\frac{i}{\hbar}\right)\Big(\delta(t-t')\mathbf{I} + \mathbf{G}\mathbf{H}\Big). \tag{D.49}$$

Again, applying the trapezoidal rule,

$$\begin{aligned}\mathbf{G}(t'+\Delta t') &= \mathbf{G}(t') + \frac{1}{2}\left[\frac{\mathrm{d}\mathbf{G}(t')}{\mathrm{d}t'} + \frac{\mathrm{d}\mathbf{G}(t'+\Delta t')}{\mathrm{d}t'}\right]\Delta t' \\ &= \mathbf{G}(t') + \frac{i}{2\hbar}\left[\delta(t-t')\mathbf{I} + \mathbf{G}(t')\mathbf{H} + \delta(t-t'-\Delta t')\mathbf{I} + \mathbf{G}(t'+\Delta t')\mathbf{H}\right]\Delta t', \end{aligned} \tag{D.50}$$

$$= \mathbf{G}(t') + \frac{i}{2\hbar}\left[\delta(t-t') + \delta(t-\Delta t'-t')\right]\mathbf{I}\Delta t' + \frac{i}{2\hbar}\left[\mathbf{G}(t') + \mathbf{G}(t'+\Delta t')\right]\mathbf{H}\Delta t'. \tag{D.51}$$

Solving for $\mathbf{G}(t'+\Delta t')$,

$$\mathbf{G}(t'+\Delta t')\left(\mathbf{I} - \frac{i}{2\hbar}\mathbf{H}\Delta t'\right) = \mathbf{G}(t') + \frac{i}{2\hbar}\left[\delta(t-t') + \delta(t-\Delta t'-t')\right]\mathbf{I}\Delta t' + \frac{i}{2\hbar}\mathbf{G}(t')\mathbf{H}\Delta t', \tag{D.52}$$

so,

$$\mathbf{G}(t'+\Delta t') = \left[\mathbf{G}(t')\left(\mathbf{I} + \frac{i}{2\hbar}\mathbf{H}\Delta t'\right) + \left(\frac{i}{2\hbar}\Delta t'\left[\delta(t-t') + \delta(t-\Delta t'-t')\right]\right)\mathbf{I}\right]\left(\mathbf{I} - \frac{i}{2\hbar}\mathbf{H}\Delta t'\right)^{-1}. \tag{D.53}$$

D.7 List of References

[1] G. Kadanoff, Leo. P; Baym, *Quantum statistical mechanics; Green's function methods in equilibrium and nonequilibrium problems* (W.A. Benjamin, New York, 1962).

[2] H. Haug and A. Jauho, *Quantum Kinetics in Transport and Optics of Semiconductors* (Springer Berlin Heidelberg, 2007).